



HAL
open science

Mechanism and quantification of natural hydrogen generation within intracratonic areas: the case of the Mid-Rift System (Kansas, USA)

Valentine Combaudon

► **To cite this version:**

Valentine Combaudon. Mechanism and quantification of natural hydrogen generation within intracratonic areas: the case of the Mid-Rift System (Kansas, USA). Earth Sciences. Université de Pau et des Pays de l'Adour, 2023. English. NNT: 2023PAUU3047 . tel-04639861

HAL Id: tel-04639861

<https://theses.hal.science/tel-04639861>

Submitted on 9 Jul 2024

HAL is a multi-disciplinary open access archive for the deposit and dissemination of scientific research documents, whether they are published or not. The documents may come from teaching and research institutions in France or abroad, or from public or private research centers.

L'archive ouverte pluridisciplinaire **HAL**, est destinée au dépôt et à la diffusion de documents scientifiques de niveau recherche, publiés ou non, émanant des établissements d'enseignement et de recherche français ou étrangers, des laboratoires publics ou privés.

IFP Energies Nouvelles - Université de Pau et des Pays de l'Adour

Département Sciences du Sol et du Sous-Sol (IFPEN) – LFCR (UPPA)

Ecole doctorale des Sciences Exactes et leurs Applications (ED211)



Thèse présentée le 23 octobre 2023

par Valentine Combaudon

pour obtenir le grade de docteur en géosciences de l'Université de Pau et des Pays de l'Adour

Mécanismes et quantification de la génération d'hydrogène naturel en contexte intracratonique : le cas du *Mid-Rift System* (USA)

Membres du jury

Laurent Truche (Professeur, Université Grenoble Alpes) - **Rapporteur**

Manuel Muñoz (Professeur, Université de Montpellier) - **Rapporteur**

Isabelle Moretti (HDR, UPPA) – **Présidente du jury**

Barbara Sherwood-Lollar (Professeur, Université de Toronto) – **Examinatrice**

Emanuelle Fréry (Ingénieure de recherche, CSIRO) - **Examinatrice**

Hannelore Derluyn (Chargée de recherche CNRS, UPPA) – **Directrice de thèse**

Éric Deville (HDR, IFPEN) – **Directeur de thèse**

Olivier Sissmann (Docteur, IFPEN) – **Co-encadrant de thèse**

Remerciements

Trois ans et vingt-trois jours, une mission de terrain et deux conférences aux Etats-Unis, cinq jours au synchrotron SOLEIL, des missions partout en France à la recherche de nouvelles techniques d'analyses, des centaines de rencontres, des rires, des énervements, des pleurs, mais surtout une aventure inoubliable. Trois ans et vingt-trois jours pour réaliser cette thèse mais ce n'est pas une question de temps, c'est une question de rencontre et de partage et le voyage compte tout autant que l'arrivée. C'est donc le moment tant attendu de mettre sur le papier toutes ces rencontres et de vous remercier, sincèrement, du fond du cœur.

Je ne pourrai pas écrire ces remerciements sans commencer par mes encadrants, Olivier, Hannelore et Éric.

Olivier, le promoteur de cette thèse IFPEN, tu as encadré ce projet de A à Z pendant ces trois années, tu l'as nourri de tes connaissances, de tes milliers de contacts à travers le monde (j'exagère à peine), de ta curiosité et de ton optimisme (sauf avec les objets type ordinateurs, câbles, connexion internet, autoclaves ...) ! Je dois une partie de ma réussite à ton encadrement c'est certains. J'ai beaucoup râlé, notamment sur le terrain (je suis sûre que tu t'en souviens) mais je sais la chance que j'ai eu d'apprendre à tes côtés et je suis très contente de savoir que l'on continuera à travailler ensemble !

Hannelore, Éric, mes directrice et directeur de thèse, je me considère particulièrement chanceuse d'avoir été votre étudiante en thèse. Je vous remercie pour votre confiance des 2020, pendant les trois années qui ont suivi et notamment lors de cette dernière année de thèse. De nombreux défis se sont présentés et je vous suis reconnaissante de votre patience et de votre bienveillance.

Je pense que c'est aussi le moment adéquat pour te remercier François. Je garderai en mémoire les nombreuses séances de MET réalisées à Jussieu pendant ces trois années de thèse. Toutes nos conversations m'ont énormément appris et ont enrichi mon travail. Je te suis extrêmement reconnaissante d'avoir pris part à ce projet de recherche et de m'avoir initié à la microscopie. Merci pour tout.

Je souhaiterais aussi vivement remercier Laurent Truche et Manuel Munoz qui ont accepté de rapporter mon manuscrit avec beaucoup de bienveillance et de curiosité scientifique. Je remercie chaleureusement Barbara Sherwood-Lollar, ainsi que Emanuelle Fréry, toutes deux examinatrices de ce travail. Enfin, un merci tout particulier à Isabelle Moretti qui a accepté de présider ce jury de thèse et qui m'accompagne professionnellement depuis bientôt quatre ans.

Merci pour tous ces échanges et toutes ces opportunités qui m'auront fait grandir en tant que chercheuse et géologue.

Mes remerciements vont ensuite à l'ensemble des Parisiens qui ont participé de près ou de loin à cette thèse. Julia, merci pour les conseils, les congrès, les relectures et pour bien d'autres choses. Sonia, je mesure ma chance d'avoir pu travailler avec toi et d'avoir tant appris à tes côtés. Et puis surtout merci pour ta gentillesse et pour tout le temps que tu n'avais pas mais que tu as dédié à ce projet. Merci à toutes les personnes de l'IFPEN avec qui j'ai eu la chance de travailler, Stéphane, Caroline, Patiente, Hermann, Saïd, Elodie, Joel. Merci aussi à toutes les personnes croisées en salle de « convivialité » de Myosotis, vous vous reconnaitrez j'en suis sûre !! The last but not the least à l'IFPEN, Djaméla, je te remercie chaleureusement pour ton travail, ta gentillesse, toutes les petites discussions que l'on a pu avoir en trois ans. On n'irait pas bien loin, nous les scientifiques de l'IFPEN, sans toi.

A Paris, j'ai aussi eu la chance de collaborer avec des chercheurs de tous les horizons : Sylvain, Jean-Christophe, Corentin, Valentine M, je vous remercie très chaleureusement pour nos échanges, vos conseils et le temps passé au synchrotron. Cette collaboration m'a permis de pousser ma réflexion dans des endroits inattendus et cela fait la richesse de cette thèse ! Merci aussi à Stefan. B à l'IPGP pour l'accueil et le travail réalisé ensemble.

Ces travaux de thèse ont aussi été rendu possible grâce aux échanges France – Etats-Unis avec Dean Rossell, l'équipe de Talon metals, Latisha Brengman, Amy Radakovitch Block, Tony Runkel, Don McKeever, et Doug Wick que je remercie chaleureusement.

A Pau, capitale du Béarn et du bus à hydrogène, mes remerciements se dirigent vers Kanchana ainsi que tout le reste de l'équipe du DMEX. J'y aurai découvert l'art de la tomographie mais aussi de nombreux conseils et itinéraires de randonnées en été, comme en hiver. Je remercie aussi très chaleureusement Stephen C. Merci pour le travail entrepris ensemble, les nombreuses heures de boulot et ta disponibilité exceptionnelle ! Je considère aussi Pau comme le siège de la team H₂ même si maintenant tout le monde est plus ou moins dispersé aux quatre coins de la France. Dan, Vincent, Gabriel, Keanu, merci pour les échanges, j'ai hâte de travailler de nouveau avec vous ! Enfin, merci à Patricia qui a géré les multiples complexités administratives, les budgets, les congrès, et tout ça en restant disponible et attentive. Mille mercis !

Et maintenant le cœur de l'histoire, celles et ceux qui font partie intégrante de l'aventure et de bien plus encore. Les doctorants qui dépotent ; Camille, Ugo, Elliot, Théo, Anne-Sophie, Emma, Alexis, Jean-Lou ou *Jean-Fou*, Marc. Vous avez égaillé ces trois années, et Dieu sait qu'elles en avaient besoin. J'ai déjà hâte de la suite ! Les amis de toujours avec qui j'ai tout vécu (et je n'exagère pas); Pierre, Lucile, Nicolas, François, Maéva. Je sais que vous n'êtes pas étonnés de me voir devenir docteure en géologie étant donné mes aspirations professionnelles plus qu'étrangères depuis le collège... Manon, Oriane, Lola, merci pour les concerts, les randos, et pour m'avoir supporté ces trois dernières années. Sachez tous que je pense à vous, et que je chérie notre amitié si fortement.

Toutes ces lignes ne seraient pas écrites aujourd'hui sans le soutien de ma famille. Je ne peux pas nommer tout le monde, mais je me dois de parler plus longuement de ma cousine Stéphanie et de ma mère Catherine. Steph ta présence ces vingt-sept dernières années, ton franc parlé de punk et ton caractère exceptionnel (j'ai en tête quelques punchlines exquises que je ne peux pas écrire ici) m'ont toujours encouragé à chercher le meilleur et cette thèse en est le résultat. Maman, on en a vécu des histoires ces dernières années, qui aurait pu prédire notre point d'arrivée en cette fin d'année 2023... Pourtant tu as toujours cru en moi, tu m'as toujours incité à aller de l'avant et aller chercher ce qui était soi-disant inaccessible. Si j'ai appris quelques choses ces dernières années, et grâce à toi, c'est qu'en se donnant les moyens tout est possible, alors je te remercie de m'avoir permis de rêver. Je vais m'employer à continuer de faire des choses dingues et c'est grâce à toi.

Je voudrai terminer ces remerciements en dédiant cette thèse à mon père. Ce n'est pas grand-chose en comparaison de tout ce qu'il m'a apporté pendant ces vingt-sept années mais je sais que le plus important est de continuer à aller de l'avant et à chérir le temps qui passe.

**Rédigé dans un TGV Paris-Bordeaux, bien évidemment*

*Tout ce qui est or ne brille pas,
Tous ceux qui errent ne sont pas perdus*

J.R.R. Tolkien

Table of contents (summarized)

CHAPTER I. Introduction	18
CHAPTER II. State of art	23
CHAPTER III. Presentation of the study case	36
CHAPTER IV. Methodology of the study	47
CHAPTER V. Mineralogy of the DR1-A well rock samples	67
CHAPTER VI. Mass transfer study of a fayalite-bearing gabbro from the Kansas Precambrian basement (USA) and implications for natural hydrogen generation....	101
CHAPTER VII. Composition and origin of gases associated with high pH waters within the Mid-Rift System in Minnesota (USA).....	129
CHAPTER VIII. Synthesis and discussion on the H ₂ -potential of the Mid-Rift System	161
CHAPTER IX. Conclusions and perspectives	179
CHAPTER X. Supplementary 1: Methodology.....	186
CHAPTER XI: Supplementary 2: Supplementary works.....	190
CHAPTER XII: Bibliography	196

Table of contents (detailed)

CHAPTER I. Introduction	18
I. Natural H ₂ generation: a challenge for the energy sector.....	19
II. Scientific problem and scope of the thesis.....	20
CHAPTER II. State of art	23
I. Introduction.....	24
II. The search for natural hydrogen: from plate boundaries to intracratonic areas	24
II.i. Precambrian cratons: peralkaline massifs and BIFs have been spotted for H ₂ exploration	25
II.ii. Sedimentary basins.....	29
III. Synthesis of the mechanisms allowing to generate H ₂ in intracratonic contexts	30
III.i. Iron oxidation with water reduction.....	31
III.ii. Radiolysis of water	31
III.iii. Organic matter decomposition.....	32
III.iv. Silicates cataclasis: the role of faults	32
III.v. Current estimates of the intracratonic hydrogen generation	33
IV. Focus on the alteration of ferrous silicates and the redox reaction of iron	33
V. Conclusion of the chapter	35
CHAPTER III. Presentation of the study case	36
I. Geological context	37
I.i. The Precambrian basement.....	37
I.ii. The Mesoproterozoic Mid-Rift System	38
I.iii. The Paleozoic and Cenozoic	40
II. Pre-existing wells data	40
II.i. CFA Oil#1 Scott well and CFA Oil#1 Heins well	40
II.ii. WTW Operating LLC#1 Wilson, well.....	43

II.iii.	CFA Oil#1 Scott well, CFA Oil#1 Heins well, and CFA Oil Sue Duroche#2 well (2008-2016 study).....	44
II.iv.	Doe Run DR1-A well.....	46
III.	Conclusion of the chapter	46
CHAPTER IV. Methodology of the study		47
I.	Overview of the chosen methodology and analytical tools	48
II.	Mineralogical analysis	49
II.i.	Optical microscopy	49
II.ii.	Scanning electron microscopy.....	49
II.iii.	Sample preparation by Focused Ion beam.....	51
II.iv.	Scanning Transmission X-ray Microtomography and X-ray Absorption Near Edges Structures (STXM-XANES).....	52
II.v.	Transmitted electron microscopy (TEM)	54
II.vi.	Electron probe micro-analyzer (EPMA).....	56
II.vii.	X-ray microtomography (μ CT)	56
II.viii.	Synthesis: input and limitations	58
III.	Hydrogen quantification workflow	59
IV.	Field sampling.....	62
IV.i.	In-situ analysis of gas and water	62
IV.ii.	Sampling of gas and water	62
V.	Geochemical analysis.....	63
V.i.	Gas Chromatography (GC).....	63
V.ii.	Synthesis: input and limitations	65
VI.	Conclusion of the chapter	66
CHAPTER V. Mineralogy of the DR1-A well rock samples.....		67
I.	Introduction of the chapter.....	69
II.	Mineralogy study	71
III.	Conclusion on the selection of K1 and K2 samples.....	76

IV.	Are Fe-rich-clay veins related to H ₂ generation in the Kansas (USA) Precambrian crust? 77	77
IV.i.	Abstract.....	77
IV.ii.	Introduction.....	78
IV.iii.	Materials and methods	81
IV.iv.	Results.....	82
IV.v.	Discussion	93
IV.vi.	Conclusion	98
IV.vii.	Appendix A. Supplementary Material.....	99
V.	Conclusion of the chapter	99

CHAPTER VI. Mass transfer study of a fayalite-bearing gabbro from the Kansas Precambrian basement (USA) and implications for natural hydrogen generation.... 101

I.	Introduction of the chapter.....	102
II.	Mass transfer study of a fayalite-bearing gabbro from the Kansas Precambrian basement (USA) and implications for natural hydrogen generation.....	102
II.i.	Abstract.....	102
II.ii.	Introduction.....	103
II.i.	Geological context	106
II.ii.	Material and methods.....	107
II.iii.	Results.....	110
II.iv.	Discussion	119
II.iv.i.	Density decreases and solid volume variation during mineral replacement reaction 119	
II.v.	Conclusion	127
II.vi.	Acknowledgments.....	128
II.vii.	Authors contributions.....	128
II.viii.	Declaration of interest	128

CHAPTER VII. Composition and origin of gases associated with high pH waters within the Mid-Rift System in Minnesota (USA)..... 129

I.	Introduction of the chapter.....	131
II.	Article 3: Composition and origin of gases associated with high pH waters within the Mid-Rift System in Minnesota (USA)	131
II.i.	Abstract.....	131
II.ii.	Introduction.....	133
II.iii.	Geological context	134
II.iv.	Materials and methods	138
II.v.	Results.....	140
II.vi.	Discussion	148
II.vii.	Conclusion	158
III.	Supplementary	159

CHAPTER VIII. Synthesis and discussion on the H₂-potential of the Mid-Rift System161

I.	Introduction.....	162
II.	Synthesis of the thesis results	162
II.i.	Previous gas study: why did we choose to study the Kansas Precambrian basement? 162	
II.ii.	Sample material.....	163
II.iii.	Microscopy: mineralogy of the deepest samples of the DR1-A well.....	163
II.iv.	Other samples from the DR1-A well and their H ₂ potential.....	164
II.v.	Estimation of quantities of hydrogen generated by the Kansas Precambrian rocks 166	
II.vi.	Minnesota: Synthesis of the gas study.....	167
III.	Take home messages	168
IV.	Remaining questions and perspectives	168
V.	Discussion on the MRS potential for hydrogen generation	170
V.i.	Previous studies on the Lake Superior part of the MRS (Minnesota, USA) and links with potential H ₂ generation	171

V.ii.	The H ₂ potential of the MRS.....	177
VI.	Conclusion of the chapter	177
CHAPTER IX. Conclusions and perspectives		179
I.	Potential of natural hydrogen generation within intracratonic areas and perspectives 180	
I.i.	Other studies with similarities but in different geological contexts.....	180
I.ii.	Other reactions occurring in intracratonic rocks with potential hydrogen generation 182	
I.iii.	The required characteristics of an H ₂ system	183
CHAPTER X. Supplementary 1: Methodology.....		186
I.	GC-C-Isotope Ratio Mass Spectrometry.....	187
I.i.	Principle	187
I.i.	Analytical conditions and post-processing of the data	187
II.	Noble gas spectroscopy.....	188
II.i.	Principle	188
II.ii.	Analytical conditions and post-processing of the data	188
CHAPTER XI: Supplementary 2: Supplementary works.....		190
I.	Combaudon, V., Moretti, I., Kleine, B. I., & Stefánsson, A. (2022). Hydrogen emissions from hydrothermal fields in Iceland and comparison with the Mid-Atlantic Ridge. <i>International Journal of Hydrogen Energy</i> , 47(18), 10217-10227.....	191
II.	Geymond, U., Briolet, T., Combaudon, V., Sissmann, O., Martinez, I., Duttine, M., & Moretti, I. (2023). Reassessing the role of magnetite during natural hydrogen generation. <i>Frontiers in Earth Science</i> , 11, 1169356.....	192
III.	Lévy, D., Roche, V., Pasquet, G., Combaudon, V., Geymond, U., Loiseau, K., & Moretti, I. (2023). Natural H ₂ exploration: tools and workflows to characterize a play. <i>Science and Technology for Energy Transition (in press)</i>	193
IV.	Kularatne, K., Senechal, P., Combaudon, V., Darouich, O., Subirana, M.A., Proietti, A., Delhaye, C., Schaumlöffel, D., Sissmann, O., Deville, E., & Derluyn, H. (<i>in prep</i>). X-ray	

micro-computed tomography-based approach to quantify natural H₂ generation by Fe(II) oxidation in the intracratonic lithologies. 194

CHAPTER XII: Bibliography 196

I.	Chapter 1.....	196
II.	Chapter 2.....	197
III.	Chapter 3.....	204
IV.	Chapter 4.....	207
V.	Chapter 5.....	212
VI.	Chapter 6.....	216
VII.	Chapter 7.....	224
VIII.	Chapter 8.....	231
IX.	Chapter 9.....	236
X.	Supplementary 1.....	240

ABSTRACT (English version)

Mechanisms and quantification of natural hydrogen emissions within intracratonic areas: the case of the Mid-Rift System (Kansas, USA)

Natural hydrogen (H_2) has been associated, for a long time, with the serpentinization of ultramafic and mafic rocks located at current lithospheric plate boundaries, in mid-oceanic ridges (MOR) and ophiolitic contexts. Such hydrogen is also found on the continent and is located within intracratonic areas that were not subjected to any significant magmatic or tectonic events over the last hundreds of millions of years. As the exploitation of hydrogen emitted at the MOR is excluded because of its location, intracratonic hydrogen could be considered more attractive. However, the lack of knowledge is still too high for this H_2 to be regarded as a reliable energy source.

Kansas (right in the middle of the USA) is home to H_2 -emitting wells where hydrogen was previously characterized as a flux and associated with the underlying Precambrian basement rocks. The Kansas Precambrian basement was intruded 1.1 Ga ago by the Mid-Rift System (MRS), an aborted rift with a kilometric-scale accumulation of iron-rich rocks being potential H_2 -generating rocks. The rift is buried below Paleozoic sediments in Kansas and extends over more than 2000 km up to the Lake Superior Province (Minnesota, USA), where the basement rocks are outcropping.

To overcome the global lack of knowledge on intracratonic H_2 , a mineralogy study on rock samples from the Kansas part of the MRS was conducted. The aim was to identify the potential mechanisms responsible for hydrogen generation. Subsequently, a multimodal and multiscale workflow was proposed to quantify hydrogen generation by combining EPMA analysis, a mass transfer evaluation, and X-ray microtomography. Finally, a field study was conducted in the Minnesota part of the MRS to acquire additional data, including the sampling of emitted gas and their associated waters on which geochemistry analyses were performed.

Indeed, the Kansas Precambrian basement in the vicinity of the H_2 -emitting wells is made of fayalite-bearing monzo-gabbros with evidence of at least, two events of water-rock interactions (WRI): (1) a deuteric alteration of fayalites during a late magmatic episode, (2) a late episode of fluid circulation at lower temperatures. They both could have led to hydrogen generation. In the Minnesota part of the MRS, significant contents of methane (CH_4), helium (He), carbon dioxide (CO_2), heavier hydrocarbons, and H_2 up to 500 ppm are found in dissolved gas and free-gas phases. They have complex isotopic signatures, and it is difficult to distinguish the

different isotopic trends. They are, however, associated with reduced (negative Eh) and basic waters typical of WRI, such as serpentinization. These results suggest that a part of this hydrogen is generated in the subsurface by serpentinization of the iron-rich rocks of the MRS and consumed with CO₂ to produce CH₄.

This work provides new information on hydrogen related to the Mid-Rift System as well as key elements to better understand the more global subject of intracratonic hydrogen.

Keywords: hydrogen; Mid-Rift System; fayalite; iron-rich clay minerals; iron oxidation; deuteric alteration; mineral replacement; abiotic methane; crustal helium; STXM-XANES; EPMA; X-ray microtomography; carbon and deuterium isotopy

RESUME (Version française)

Mécanismes et quantification de la génération d'hydrogène naturel en contexte intracratonique : le cas du *Mid-Rift System* (Kansas, USA)

L'hydrogène naturel (H_2) a longtemps été associé uniquement à la serpentinisation des roches ultrabasiques et basiques en contexte de limites de plaques lithosphériques (rides médio-océaniques ou massifs ophiolitiques). Un tel hydrogène a aussi été identifié au milieu des continents, dans des zones qualifiées d'intracratoniques, et caractérisées par une quasi-absence d'activité tectonique et magmatique depuis plusieurs millions d'années. L'exploitation de l'hydrogène généré au niveau de dorsales océaniques étant exclu, l'hydrogène continental, et plus particulièrement intracratonique, pourrait être considéré comme plus attractif. Cependant, l'état actuel des connaissances scientifiques sur cet hydrogène est relativement limité et ne permet pas d'assurer une production à moindres risques et moindres coûts.

Le Kansas abrite d'actuels puits émetteurs d'hydrogène naturel. Cet H_2 a été, lors de précédentes études, caractérisé comme un flux et associé aux roches sous-jacentes appartenant au socle Précambrien. Ce socle a été intrudé, il y a 1.1 milliards d'années, par le Mid-Rift System (MRS), un rift avorté associé à une accumulation kilométrique de roches riches en fer et potentiellement génératrices d' H_2 . Ce rift qui est enfoui sous des sédiments paléozoïques au Kansas, s'étend sur plus de 2000 km, jusqu'à la région des grands lacs (Minnesota) où les roches affleurent.

Pour combler le déficit de connaissance concernant l'hydrogène intracratonique une étude minéralogique poussée des échantillons de roches provenant de la partie du rift situé au Kansas a été réalisée. L'objectif était d'identifier le mécanisme principal de génération d' H_2 . Ensuite, une méthodologie d'étude multi-échelle combinant données de microsonde, bilan de transfert de masse, et données de microtomographie par rayons X a été développée, dans le but de quantifier l' H_2 généré. Enfin une mission d'échantillonnage d'eau et de gaz dans la zone nord du MRS (Minnesota) a été effectuée. L'objectif était d'acquérir des données additionnelles et de fournir des analyses géochimiques destinées à mieux comprendre le système H_2 lié au MRS.

Le socle Précambrien du Kansas, dans la zone des puits émetteurs d' H_2 , est composé de monzogabbros riches en fayalites portant des marques d'au moins deux événements d'interactions eau-roche : (1) un épisode tardi-magmatique d'altération deutérique des fayalites, (2) un épisode tardif de circulation de fluide à plus basse température. Ces événements pourraient avoir conduit, chacun, à une génération d' H_2 . Dans la partie du rift se situant au Minnesota,

des quantités significatives de méthane (CH_4), d'hélium (He), de dioxyde de carbone (CO_2), d'hydrocarbures lourds, et d' H_2 (jusqu'à 500 ppm) ont été mesurés dans des gaz dissous et des gaz libres. Leur signature isotopique est complexe et il est difficile de distinguer les différents pôles isotopiques. Il est important de noter que ces gaz sont associés, en partie, à des eaux réduites et basiques typiques des réactions eaux-roches comme la serpentinisation. Ainsi, ces résultats suggèrent qu'une partie de l' H_2 est généré en subsurface par serpentinisation des roches riches en fer du rift puis consommé avec le CO_2 présent pour produire du CH_4 .

Ce travail de thèse a permis de produire de nouvelles données essentielles pour mieux comprendre la génération d'hydrogène dans le MRS mais aussi de manière plus générale dans les zones intracratoniques.

Keywords : hydrogène, Mid-Rift System, phyllosilicates riches en fer, oxydation du fer, altération deutérique, remplacement minéralogique, méthane abiotique, hélium crustal, STXM-XANES, EPMA, microtomographie par rayons X, isotopie du carbone et de l'hydrogène

CHAPTER I

CHAPTER I. Introduction

This chapter aims at putting natural hydrogen in a more global energy context and introduces the fundamental questions about intracratonic hydrogen. In addition, this chapter aims to explain the thesis's goals and scope.

Ce chapitre a pour objectif de situer l'hydrogène naturel dans un contexte énergétique plus général et ainsi d'introduire les grandes questions fondamentales qui devront être adressées dans le futur à propos de cet hydrogène naturel généré dans les zones intracratoniques.

I. Natural H₂ generation: a challenge for the energy sector

Dihydrogen (H₂), or as it is commonly called in the energy industry (and will be in the rest of this manuscript), "hydrogen", is one of the most abundant known molecules in the Universe. It is very mobile because of its small size, but also very reactive. On Earth, it is considered one of the precursors to forming more complex organic molecules, such as the first "bricks" of life (short-chain alcohols, fatty acids, aldehydes, hydrocarbons...). The combustion of hydrogen does not emit CO₂ since the only product is a molecule of H₂O. Moreover, this gas has a very high energy density: it is estimated that one kilogram of H₂ equals as much energy as three kilograms of oil. Within the energy transition framework, which must answer the major climatic challenges of the 21st century, hydrogen as a "green" fuel is, thus, in strong development. It should also be noted that hydrogen is easily transformed into electricity and vice versa. Within the framework of the storage of intermittent energy surpluses (such as wind or solar power), the conversion of the excess electricity produced in the form of hydrogen is strongly envisaged and under development.

Today, H₂ is mainly used in the industrial sector for the production of fertilizers or for refining heavy oils, but also as an energy carrier. This hydrogen is produced through different processes, such as steam reforming of hydrocarbons, coal gasification, water electrolysis, or biomass. This industrial production is costly and requires significant energy input. In the case of steam reforming and gasification, the production of H₂ is also responsible for greenhouse gas emissions since the process releases CO₂. On the other hand, the electrolysis of water requires a source of electricity and a significant supply of pure water. Although in constant technical evolution, the industrial production of hydrogen has many technical and environmental limits.

The current annual world production of H₂ is about 94 million tons (Global Hydrogen Review, 2022, IEA), the vast majority of which is intended for the oil and fertilizer industries. The transition from energy carrier to energy source is currently limited.

However, more and more studies highlight the existence of natural hydrogen emissions, i.e., H₂ leaks coming from the ground. These emissions have been recorded worldwide as they occur in different geological contexts, at the bottom of the oceans, and in the middle of the continents, and are due to various reactions.

Studies of H₂ emanations within the oceanic lithosphere tried to characterize the rocks involved, the gases, the associated fluids, and their conditions Temperature/ Pressure/ redox of formation (Moody., 1976; Welhan and Craig., 1979; Campbell., 1988; Charlou et al., 1996; McCollom et al., 2009; Marcaillou et al., 2011; Malvoisin et al., 2012, amongst others). Some chemical reactions generating H₂ have been described and will be discussed in detail in the following chapter.

Still, many emissions, notably the continental ones and especially the intracratonic ones, remain unexplained and unquantified. As natural hydrogen is of major interest in the energy transition framework, it appears fundamental to better characterize H₂ emissions within the continents to facilitate its exploration and exploitation.

II. Scientific problem and scope of the thesis

In light of the current state of knowledge about natural hydrogen, fundamental questions about intracratonic emissions remain to be solved. They are the following:

- What type of rocks and minerals must be present to find a potential H₂ system (in the sense of an exploitable hydrocarbon system) within intracratonic areas?
- What are the mechanisms responsible for such H₂ generation within intracratonic areas?
- Under which P/T/redox conditions are these mechanisms occurring?
- Which quantity of hydrogen is generated?

This thesis aims to use the North American Mid-Rift System (MRS) as a case study and thus to provide a guideline for intracratonic hydrogen exploration. The MRS, in the scope of hydrogen emissions, was first studied during a previous thesis focused on the gas and water samples of the Kansas part of the MRS (Guélard, 2016). The MRS is considered an NNE-SSW Mesoproterozoic aborted rift expanding over 2000 km from Kansas to Minnesota and Minnesota to Wisconsin (USA). It is one of the main geological features of the Central Midcontinent and represents a kilometeric-scale accumulation of mafic rocks. It is part of the Precambrian North American craton, which makes it an inactive area in terms of tectonic and seismic activities. In the southernmost part of the rift in Kansas, H₂-proven emissions have already been recorded, and studies have shown that their origin is located within the Precambrian basement. A few exploration wells have reached this basement, and core samples have been collected in some wells. In Minnesota, the northernmost part of the rift, literature on petrological studies of the rocks belonging to the rift highlights potential mineralogical markers of H₂ production. In addition, the basement is outcropping and has been highly studied and exploited for ore mineralization. A lot of literature is available, and under U.S. law, every mining company must provide access to the rock cores extracted from every well drilled. These are made accessible for scientists to study. Since H₂ emissions have been recorded in the past and rock samples are accessible, the MRS appears as an interesting intracratonic area to study natural hydrogen generation. In addition, the rift is over 2000 km long, 100 km large, and several kilometers deep, making the potential for H₂ exploration tremendous.

Thus, the aim is to propose a model for H₂ generation within the MRS and propose a well-characterized example of an H₂ system within intracratonic areas to guide future H₂ cratonic exploration.

The fundamental questions cited above are addressed in this thesis through a specific methodology which will be detailed later (Figure 1):

- To perform a petrological study of core samples associated with the Kansas emissions to spot the mechanisms responsible for H₂ generation within the basement
- To develop and apply an imaging workflow combining microscopy data and microcomputed tomography (μCT) to quantify the H₂ generation within the basement
- To add new samples by field sampling of gas, water, and outcropping rocks in the Minnesota part of the rift to have better coverage and compare both ends.
- To perform geochemical analysis of the gas and water samples to highlight a potential gas production related to the MRS in the Minnesota part of the rift

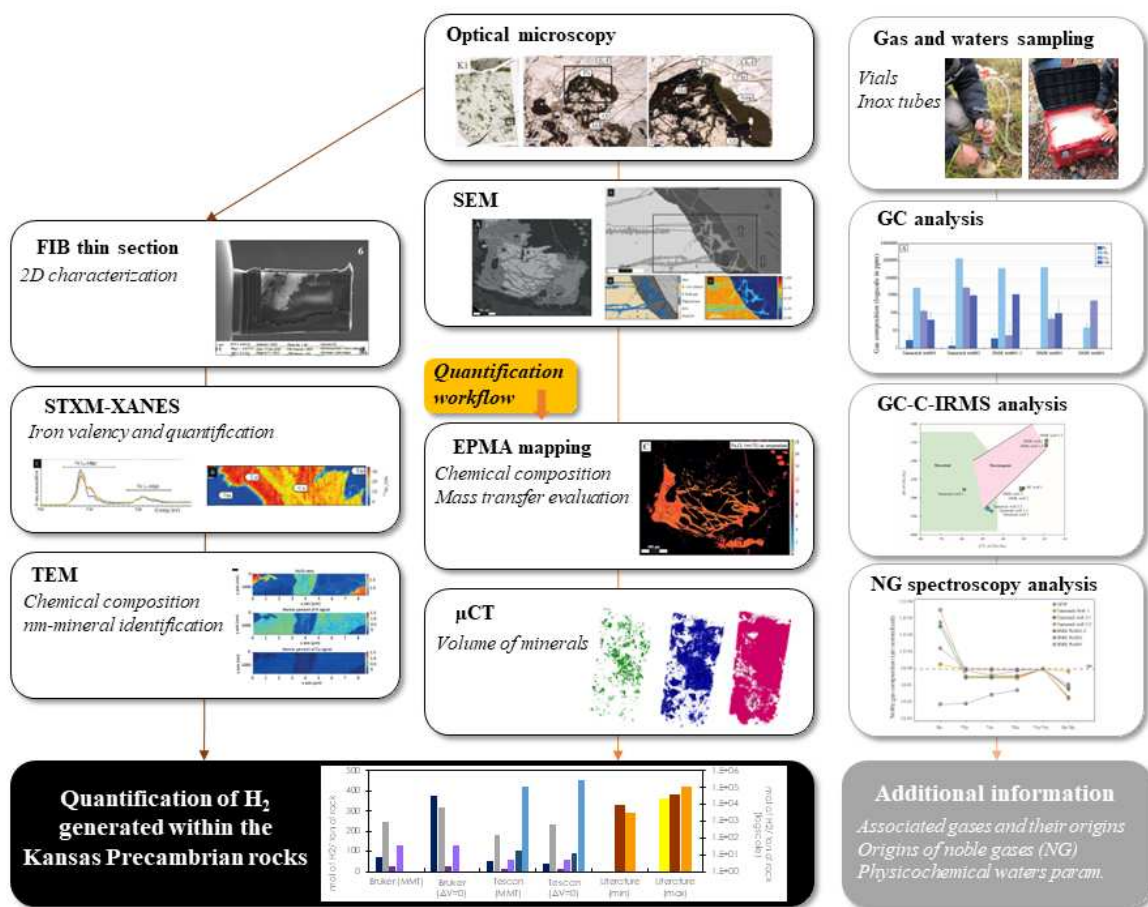


Figure 1: Illustration of the methodology used in this thesis

After discussing the state of the art in Chapter 2 and the case study of the Kansas Precambrian basement in Chapter 3, the methods used to address the research questions are described in Chapter 4. Then, the first point is addressed in Chapter 5 with the description of the DR1-A well core samples by optical microscopy and the selection, for further analyses, of two samples representative of the studied zone. The study of these latter is the subject of a submitted

manuscript to *Lithos*, presented in Chapter 5. The second point is addressed in Chapter 6 as a manuscript that will be submitted to a petrological journal. The third and last points are addressed in Chapter 7, written to be submitted in a geochemistry journal. Finally, the last chapters of this manuscript are an overview of the principal results and a comparison with previous studies and analogies found in the literature to establish the fundamentals of a model of H₂ generation within the MRS. The final goal of the manuscript is to take a step back from the studied area and to provide more general guidelines for future intracratonic H₂ studies.

CHAPTER II

CHAPTER II. State of art

This chapter aims to illustrate the interest of intracratonic areas in the scope of H₂ emissions and prospection. The goal is to focus on H₂-generating reactions occurring in this continental context, i.e., redox reaction, radiolysis, late maturation of organic matter, and cataclasis in fault zones. This chapter also aims to provide a short overview of oxidation reactions by looking at the minerals commonly involved, their kinetics of alteration, and finally, the role of pH on hydrogen generation.

Ce chapitre a dans un premier temps pour objectif d'illustrer l'intérêt des zones intracratoniques dans la prospection en hydrogène naturel. Dans un second temps ce chapitre s'intéresse aux réactions génératrices d'H₂ dans ce contexte en proposant une courte synthèse sur la réaction d'oxydation du fer.

I. Introduction

This chapter introduces the first discoveries of natural hydrogen in a plate boundary context. Intracratonic areas and associated geological contexts already linked to hydrogen generation, such as Precambrian cratons and sedimentary basins, are discussed. In addition, a synthesis of the H₂-generating mechanisms within these contexts and current estimates of intracratonic hydrogen generation are presented. As it is at the heart of this work, a zoom on the redox reaction within ferrous silicates is proposed.

II. The search for natural hydrogen: from plate boundaries to intracratonic areas

For many years, a large part of the scientific interest in natural H₂ has been focused on the boundary zones of present or past lithospheric plates, offshore or onshore. The first studies have been conducted in the Pacific Ocean (Moody., 1976; Welhan and Craig., 1979), followed by the discoveries of black smokers along the Mid-Atlantic ridge (Campbell., 1988; Charlou et al., 1996). At over 60,000km in length, oceanic ridges are the site of extension associated with mantle upwelling. These latter result in significant volcanic and seismic activity along the rifts and, in places, in the exhumation of basic and ultrabasic rocks, i.e., gabbros, and peridotites. Outcropping gabbroic rocks and especially peridotites, are rich in ferromagnesian minerals, mainly olivines. These rocks are also highly fractured and are the site of fluid circulation in the form of convective cells. Seawater seeps through the rock and hydrothermal circulation occurs in the rocks thanks to fracturing and temperature gradients between the seawater and the heat released by the magma. Significant transformations of the fluids and surrounding rocks occur, and in the case of peridotites, composed of over 70% olivine (Fo₉₀), the iron is oxidized, and the rock itself is transformed according to the following reaction of serpentinization (Malvoisin et al., 2012):

Olivine + Water → Serpentine + Brucite + Magnetite + H₂

(Equation 1): $30\text{Mg}_{1.8}\text{Fe}_{0.2}\text{SiO}_4 + 41\text{H}_2\text{O} \rightarrow 15\text{Mg}_3\text{SiO}_5(\text{OH})_4 + 9\text{Mg}(\text{OH})_2 + 2\text{Fe}_3\text{O}_4 + 2\text{H}_2$

Pyroxenes in peridotites can also be oxidized. The difference lies in the absence of brucite crystallization, which is replaced by silica in the following reaction (Malvoisin et al., 2012):

Orthopyroxene + Water → Serpentine + Magnetite + Silica + H₂

(Equation 2): $15\text{Mg}_{1.8}\text{Fe}_{0.2}\text{Si}_2\text{O}_6 + 19\text{H}_2\text{O} \rightarrow 9\text{Mg}_3\text{SiO}_5(\text{OH})_4 + \text{Fe}_3\text{O}_4 + 12\text{SiO}_2 + 2\text{H}_2$

In addition, the presence of aluminum in some pyroxenes (such as augite) can instead lead to the formation of Al-rich phyllosilicates instead of serpentine (Kularatne et al., 2023).

The focus has long been put on the Mid Oceanic Ridges (MOR). However, we now know that many natural hydrogen emissions can also occur on continent in settings with weaker-than-average geothermal gradients and low seismic activity, in North America (Coveney et al, 1987; Newell et al., 2007; Guélard et al., 2017; Warr et al., 2019), Mali (Prinzhofer et al., 2018), Russia (Larin et al., 2014; Zgonnik., 2020) or Australia (Ward., 1933; Boreham et al., 2021; Frery et al., 2021) (Figure 2). All continents are concerned by these H₂-rich gas emissions (up to 98% H₂ in Mali), which have a higher exploration potential than the oceanic areas thanks to their accessibility. These emanations are, most often, associated with:

- Precambrian cratons
- Sedimentary basins which may or may not cover Precambrian cratons

In the rest of this chapter, we will discuss these different geological contexts associated with H₂ emanations.

II.i. Precambrian cratons: peralkaline massifs and BIFs have been spotted for H₂ exploration

Natural H₂ emissions have been recorded in the middle of continents outside areas with significant geothermal gradients. In Kansas (Coveney et al., 1987; Newell et al., 2007; Guélard et al., 2017), Mali (Prinzhofer et al., 2018), Australia (Ward., 1933; Boreham et al., 2021) but also in South Africa (Lin et al., 2005; Sherwood-Lollar et al., 2014) or Russia (Larin et al., 2014), these emissions are associated with Precambrian cratons (Figure 2).

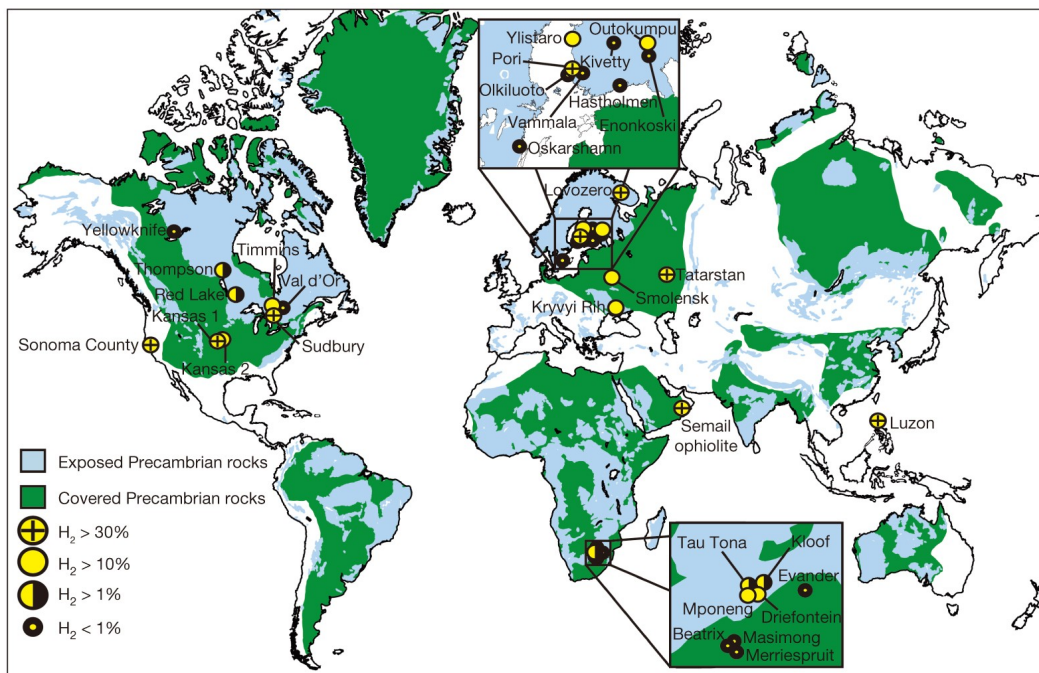


Figure 2: Map locating the various Precambrian cratons (outcropping and buried) correlated with known H₂ emissions (Sherwood-Lollar et al., 2014).

These cratons are ancient zones, older than 540 Ma, with low geothermal gradients and seismic activity. This classification arbitrarily groups together a set of geological objects, which may have undergone numerous tectonic, magmatic, and metamorphic episodes during the Precambrian, but are stable since then, except for vertical movements such as fluid weathering. Thus, we can imagine that ancient lithospheric sutures, now buried, can be found in these large cratonic complexes. Furthermore, Precambrian cratons represent more than 70% of the total continental crustal surface (Goodwin., 1996), and although almost inactive today, these cratons are strongly faulted and traversed by important aquifers, as is the case in Kansas (Guélard et al., 2017). They are composed of igneous and sedimentary rocks, mostly metamorphosed.

The proportions and compositions of gases related to H₂-seepages within these cratons greatly vary from one site to another with 98% of H₂ in Mali (Prinzhofer et al., 2018) versus less than 1% in some sites in the Canadian craton (Sherwood-Lollar et al., 1988). Hydrogen is often associated with CH₄, N₂, and He, and sometimes with more complex hydrocarbons and CO₂ (Etiope et al., 2014). H₂ isotopic composition often excludes the idea of thermogenic origin.

Hydrogen and its associated gases are found in Precambrian rocks:

- as dissolved in brines contained in fractures running through the basement (Sherwood-Lollar et al., 2014)
- as free gas (Prinzhofer et al., 2018)
- as fluid inclusions in alkaline intrusions (Salvi et al., 1992)
- as absorbed in the soil in sub-circular depressions (SCD) on the surface

These sub-circular depressions, affecting the sedimentary layers, often underlain the Precambrian basement. These structures have been mapped on most continents, in Russia (Larin et al., 2014), North America (Zgonnik et al., 2015), Brazil (Prinzhofer et al., 2019; Miagkiy et al., 2020 A and B; Moretti et al., 2021), Namibia (Moretti et al., 2022), Australia (Moretti et al., 2021; Fréry et al., 2021). Some of these have been monitored and show significant H₂ values (see references above).

These intracratonic areas are vast and a multitude of rock types can be found. In the next part of this chapter, specific intracratonic areas related to proven hydrogen emissions will be discussed. They include per alkaline massifs and banded iron formations.

II.i.i. Per alkaline massifs

The peralkaline massifs are associated with episodes of intracontinental rifting that did not result in the formation of new oceanic lithosphere (Barbarin., 1999).

These rocks have been studied by Marks and Markl (2017). The map below summarizes the various known or potential occurrences of these rocks and highlights their global distribution.

These peralkaline massifs are most often associated with Precambrian cratons. Their presence on all continents (Figure 3) and their iron enrichment make them good candidates for natural H₂ generation.

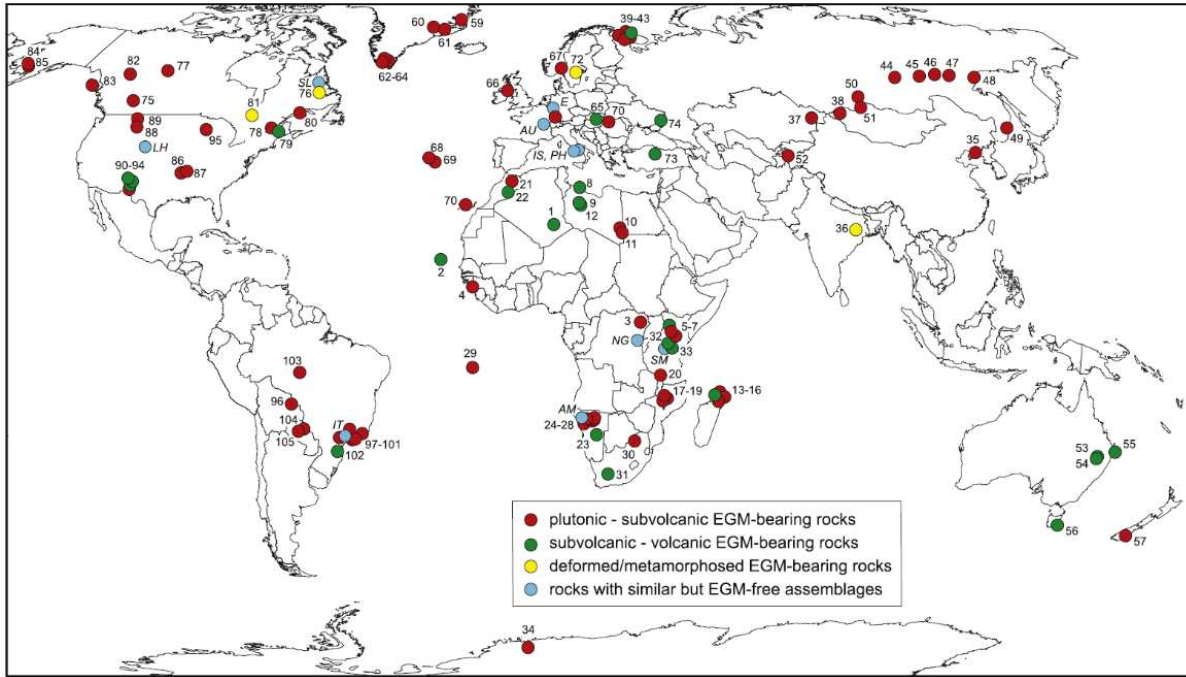


Figure 3: Map synthesizing the different occurrences of peralkaline rocks or similar mineralogical assemblages (EGM is for eudialyte-group minerals, for a more detailed legend please refer to Marks and Markl., 2017; see references).

These complexes are composed of granites poor in aluminum and calcium but rich in sodium, potassium, and iron. Their $[(Na+K)/Al]$ ratio is less than 1 (Barbarin., 1999; Marks et al., 2017). They are characterized by mineralogical assemblages (biotite, muscovite, amphibole, pyroxene, and then apatite, zircon, garnet, titanite, ilmenite, and magnetite as secondary minerals) that can only form when magmatic conditions are sufficiently reduced (low fO_2) allowing enrichment in iron and alkaline components. These characteristics are often reached at the end of the magmatic episode. The formation of these granitic complexes is attributed to magmas derived from the partial melting of mantle rocks, often combined with prolonged partial differentiation processes taking place in the crust and at shallow depths (Marks et al., 2017).

Significant concentrations of H₂ as free emissions (28 - 35 vol% at Lovozero) or as gases contained in fluid inclusions have been found at the Strange Lake peralkaline complexes in Canada (Salvi et al., 1992, 1996, 2006; Potter et al., 2013), Lovozero and Khibiny in Russia (Nivin., 2016, 2019, 2020; Potter et al., 2013), and at Ilimaussag in Greenland (Krumrei et al.,

2007). At Strange Lake but also in Russia, this hydrogen is associated with CH₄, CO₂, N₂, and more complex hydrocarbons (C₂-H₆, C₃-H₈, etc.) (Salvi et al., 1996).

Batch reactor hydrothermal experiments conducted on pure arfvedsonites (iron-rich amphiboles), and on per-alkaline granitic samples (bearing these arfvedsonites) have documented hydrogen generation by iron oxidation coupled with water reduction. The rates of H₂ generation by hydrothermal alteration at temperatures between 280 and 400°C are comparable to those known for serpentinization reactions in peridotites (Truche et al., 2021). Peralkaline complexes on all continents are good candidates for natural hydrogen generation.

II.i.ii. Banded Iron Formations

Banded Iron Formations (BIF) are sedimentary rocks from the Precambrian, formed during two distinct events: 1) during Archean to Proterozoic times, and 2) during Neoproterozoic times (Ilyin., 2009). They can be found in every continent (Figure 4) and are always associated with intracratonic areas (Klein et al., 1993, Ramanaidou et al., 2014).

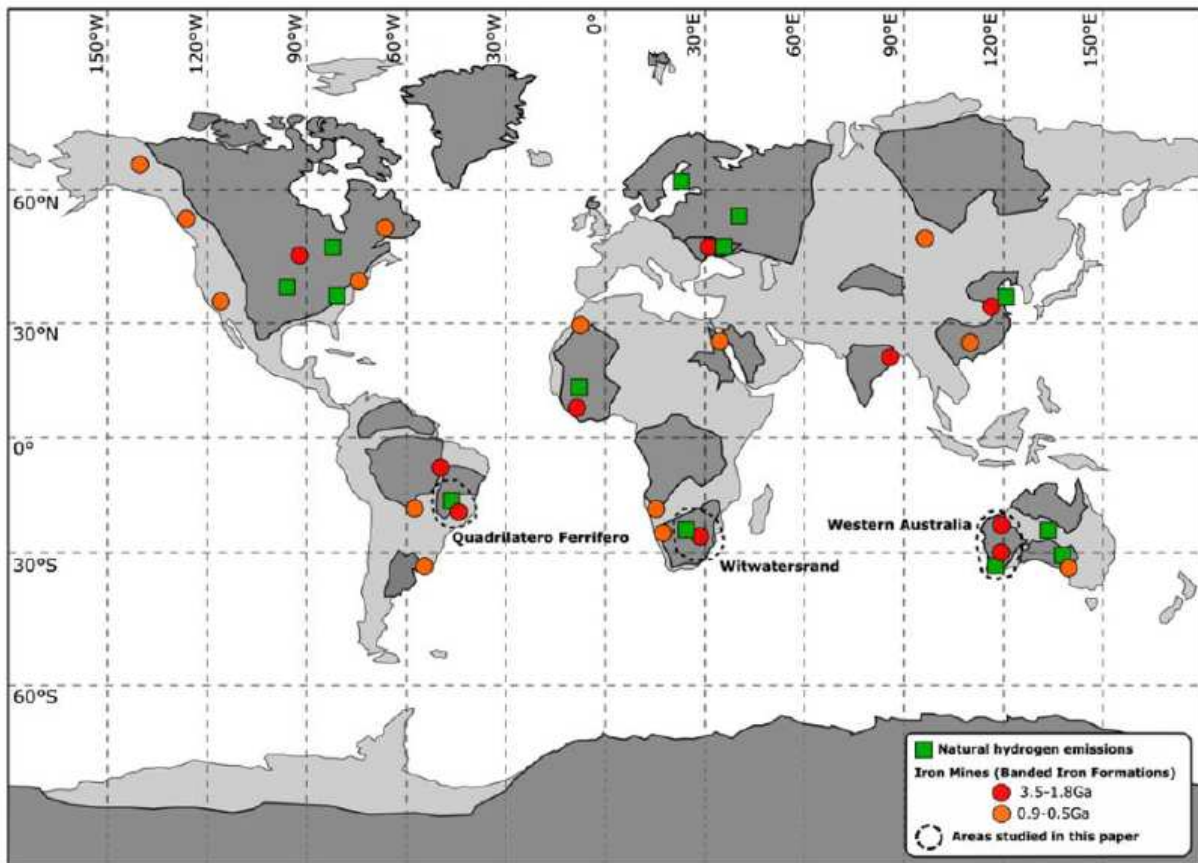


Figure 4: Map of the intracratonic areas (in dark grey) and Banded Iron Formations (Geymond et al., 2022)

The global consensus is that they were formed after the ferrous iron was dissolved in oceanic waters and then transformed into ferric iron by cyanobacteria producing O_2 . Neoproterozoic BIFs are associated with Snowball earth interglacial cycles after long periods of anoxia (Cox et al., 2013). BIFs are highly exploited by the mining industry as they represent 60% of global iron ore reserves (Zhu et al., 2014).

Geymond and co-authors (2022) highlighted the presence of sub-circular depressions above the Neoproterozoic BIF of Western Australia (Figure 4). They infer that the morphological study of these sub-circular depressions (SCD) suggests potential H_2 seeping. Their assumption is reinforced by the evidence of mineral transitions from magnetite to maghemite, hematite, and goethite and from ferrous silicates to ferric iron oxi-hydroxides which are good markers for an actual hydrogen generation by potential weathering of the BIFs and its induced iron oxidation.

II.ii. Sedimentary basins

Sedimentary basins are defined by the coupled processes of erosion and subsidence allowing for sediment deposits and burying. They can be found in passive margins, extensional or convergent settings, subduction, and even in intracratonic areas (Figure 5). For the last decades, they were excluded from the potential H_2 -generating areas as the organic matter constitutive of such basins highly reacts with hydrogen, thus diminishing the amount of hydrogen potentially preserved.

However, when they are composed of highly matured organic matter, they appear to be interesting candidates for H_2 generation as new studies suggest the late maturation of organic matter in sedimentary rocks could generate H_2 as free gas (Horsfield et al., 2022; Mahlstedt et al., 2022).

In addition, Lin and co-authors (2005) and Sherwood-Lollar and co-authors (2007) proposed radiolysis as a potential mechanism for H_2 generation in U, Th, and K-rich rocks, mostly in basement rocks. If U-Th-K-rich clay minerals are numerous enough within basin sedimentary rocks, it appears reasonable to imagine a production of H_2 by radiolysis within sedimentary basins. It has already been demonstrated to happen in U-rich rocks by Truche and co-authors (2018). Sedimentary rocks appear as potentially interesting H_2 systems as they are numerous and well-known thanks to the oil & gas industry (Figure 5).

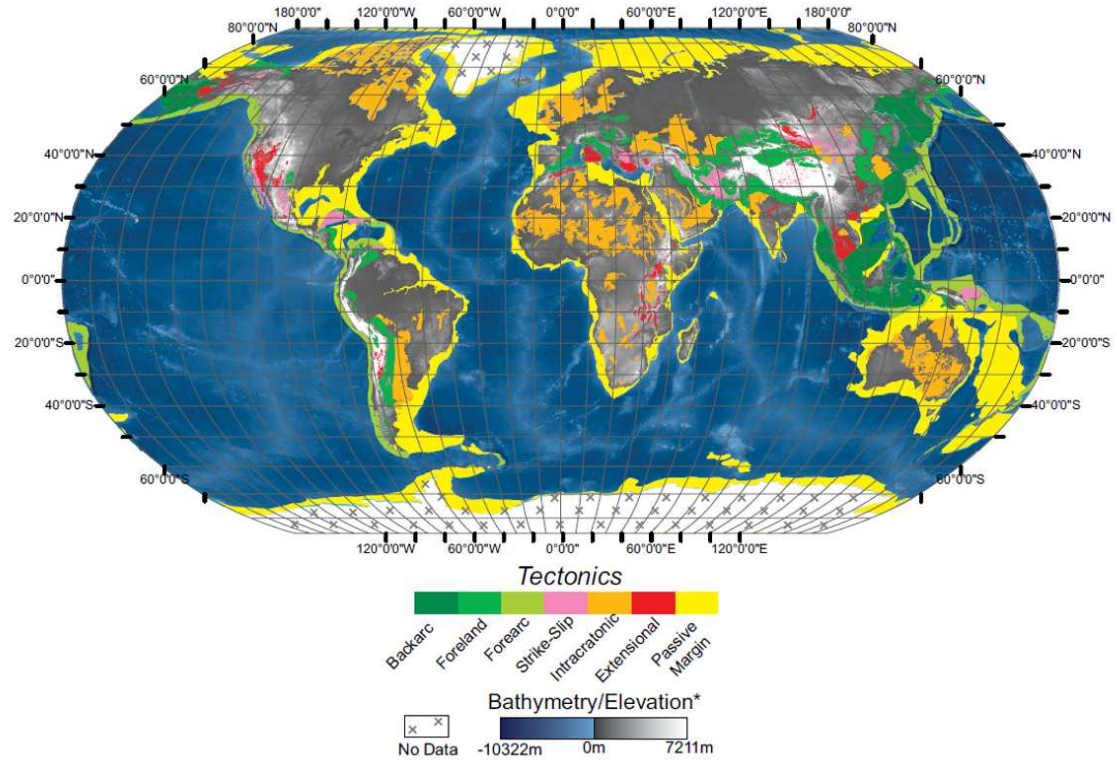


Figure 5: Location of sedimentary basins in the function of their structural regime. Intracratonic basins are represented in orange (modified from Nyberg and Howell., 2015)

III. Synthesis of the mechanisms allowing to generate H_2 in intracratonic contexts

The different geological contexts associated with intracratonic H_2 and their associated mechanisms responsible for hydrogen generation have been briefly introduced in the previous section of this chapter. The following section aims to describe the mechanisms that generate hydrogen within intracratonic areas (Table 1).

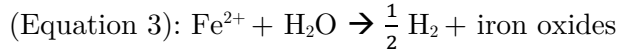
Reaction	Equation	Temperature
Redox reaction of iron ¹	$Fe^{2+} = Fe^{3+} + \bar{e}$ and $H_2O + 2\bar{e} = H_2 + O^{2-}$	(Low) to high T
Radiolysis ²	$H_2O \rightarrow OH\cdot + H\cdot$ and $H\cdot + H\cdot \rightarrow H_2$	Water stability conditions
Late OM maturation ³	...	Low to high T
Cataclasis in fault zones ⁴	$Si\cdot + H_2O \rightarrow Si-OH + H\cdot$ and $2H\cdot \rightarrow H_2$	N.D

Table 1: H_2 -generating reactions occurring in the intracratonic areas (1- Marcaillou., 2011; 2- Lin et al., 2005; Sherwood-Lollar et al., 2007; 3- Horsfield et al., 2022; Mahlstedt., 2018, Mahlstedt et al., 2022; 4- Sugisaki et al., 1983).

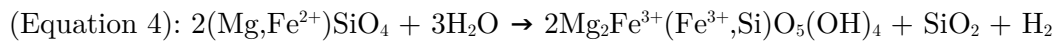
III.i. Iron oxidation with water reduction

Several hypotheses for hydrogen formation in an intracratonic context have been put forward. In the case of cratons containing mafic rocks, the most likely hypothesis is iron oxidation.

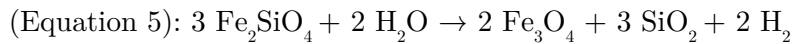
The general equation can be summed up as the reaction:



In the case of serpentinization, fluids infiltrate mafic-ultramafic rocks during hydrothermal events. This alteration leads to the oxidation of iron carried by olivine or pyroxene and its incorporation into serpentine :



Or through the precipitation of iron oxides such as magnetite:



These two processes, coupled with water reduction, lead to H_2 generation. The ferric iron is incorporated into the secondary minerals formed; the nature of these latter varies in function of the temperature and the composition of the primary mafic mineral. This reaction has been described to happen between around 100 to 400°C with an optimum of 320°C (Klein et al., 2013). It has been identified at lithospheric boundaries, in the MOR (Moody., 1976; Charlou et al., 2002), or onshore on the ophiolitic massifs (Neal and Stranger, 1983; Vacquand et al., 2018).

Redox reactions have also been highlighted in iron-rich cratonic rocks such as BIFs (Geymond et al., 2022, 2023). Even if relevant studies are lacking, it seems reasonable to believe that fluid-mediated reactions under anoxic conditions, happening within iron-rich continental rocks and leading to iron oxidation, could generate H_2 .

III.ii. Radiolysis of water

In the case of granitic cratons, or some sedimentary rocks, the hypothesis of hydrogen production by radiolysis of water has been put forward (Lin et al., 2005; Sherwood-Lollar et al., 2007). This is based on the decay of the elements U, Th, and K contained in the basement minerals. This decay produces α , β , γ radiations, which break the H-O bonds of H_2O and generate free radicals ($\text{OH}\cdot$) and ($\text{H}\cdot$), the latter of which can recombine to yield H_2 . Although geochemically simple and mediated by water, this reaction is very different from iron oxidation

reaction in that it produces both reducing (H_2) and oxidizing (H_2O_2 , O_2 , O^\cdot) compounds (Klein et al., 2020). This reaction has been primarily described in Fe-poor siliciclastic and volcanic rocks from the Witwatersrand Basin in South Africa, with rocks with up to 7410 μM of dissolved H_2 in water with pH between 7 and 9 (Sherwood-Lollar et al., 2007). H_2 enrichment has also been demonstrated in the clays-rich rocks of the Cigar Lake uranium deposit (Saskatchewan, Canada) (Truche et al., 2018). The hydrogen, which would be stored in the nanoporosity of the phyllosilicate sheets, reaches up to 500 ppm or 0.25 mol/kg of rock and is of radiolytic origin (Truche et al., 2018). Further studies are needed to better understand this radiolysis reaction and its contribution to the overall continental hydrogen production. It is important to note that craton rocks are ancient rocks, so they are the least radiogenic rocks in the lithosphere. Thus, hydrogen production by radiolysis seems to be minor in this context.

III.iii. Organic matter decomposition

Recently, H_2 was detected in several wells reaching Paleozoic mature formations part of sedimentary basins in China, Australia, Europe, and the USA. Studies (Horsfield et al., 2022; Mahlstedt et al., 2023) showed that this hydrogen is generated during the late maturation of overmature organic matter within shales and coals. This H_2 could be trapped in the porosity of marine shales (Horsfield et al., 2022). Authors infer the yield of such rocks could be close to the one of shale gas in the Barnett Shale (USA), thus making H_2 produced by organic matter thermal decomposition a significant component of global natural H_2 production. These studies are promising and deserve further investigation.

III.iv. Silicates cataclasis: the role of faults

Activity on the San Andreas and Calaveras faults (California, USA) has been correlated with peaks in H_2 emissions. Sato and co-authors (1986) suggested seismic activity, and more specifically, the application of stress on the base of the upper crust would have allowed the fault zone to expand and thus allow hydrogen (generated in this case by hydration of underlying mafic rocks) to escape (Sato et al., 1986). The role of faults in the production of natural hydrogen is also highlighted by Sugisaki et al (1983). Gases, mainly H_2 and CO_2 (up to 93570 ppm and 3.1%), are associated with active fault zones. It is observed that peak hydrogen concentrations are positively correlated with seismic activity. In addition, laboratory experiments have demonstrated that hydrogen can be generated mechanically when silica free radicals are in contact with water following the reactions (Sugisaki et al., 1983):



Some authors estimate that this H₂ generation by mechanoradical reactions at fault zones could reach nearly 1.1 mol/ kg of fluid (Hirose et al., 2011). As fault zones and seismic activities take place in both oceanic and continental settings, they could drastically influence hydrogen production rates, even in intracratonic areas where only low seismicity is recorded.

III.v. Current estimates of the intracratonic hydrogen generation

Because the reactions taking place in cratons are poorly described, the role of these rocks in global hydrogen production has probably been greatly underestimated. However, Sherwood-Lollar and co-authors' (2014) study estimates this production at 0.36 - 2.27 x 10¹¹ mol/year, i.e., an annual production comparable to what was estimated at the oceanic lithospheric boundaries. As these emissions are virtually untapped, Precambrian cratons now appear to be of significant interest in understanding the mechanisms governing H₂ production. Many questions remain open about the processes that generate hydrogen in tectonically and magmatically almost inactive domains. Their resolution is essential and would allow de-risking of the exploitation of this resource.

IV. Focus on the alteration of ferrous silicates and the redox reaction of iron

In continental rocks, the most common H₂-generating mechanism seems to be the water-rock interaction, i.e., fluid-mediated reactions happening within the rocks constitutive of the cratons and most of the time inducing iron oxidation.

The minerals suggested to be predominantly involved in such reactions are similar to those forming mafic and ultramafic rocks: i.e., olivines, amphiboles, and probably pyroxenes, garnets, or micas. However, according to specific mineralogical characteristics, the temperature of the system, and according to the composition and the redox conditions of the fluid, the kinetics of the reaction and thus the quantity of hydrogen produced can vary.

The serpentinization kinetics of peridotites is relatively well known. It has been studied in detail through autoclave alteration experiments of natural samples (Marcaillou et al., 2011; Malvoisin et al., 2012) and through numerical simulations (McCollom et al., 2009; Klein et al., 2013).

Marcaillou et al. (2011) determined that the amount of hydrogen produced is linearly dependent on the amount of ferric iron (Fe³⁺/ Fe_{total}) produced which allows for the determination of reaction kinetics and quantification of the gas emitted. They divide the serpentinization of peridotites into three stages (under optimal conditions of 300°C/300 bar):

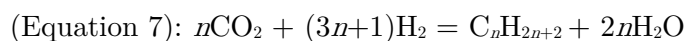
- First step/beginning of the reaction: the quantity of H₂ is controlled by the dissolution of olivine. The iron released oxidizes and precipitates as magnetite (Fe₃O₄).
- Second stage/intermediate: the amount of iron released increases, and the oxidized iron also precipitates as a trace in lizardite (a polymorph of serpentine). This increase of iron III in the neo-formed serpentine correlates with the increase of H₂ generated.
- Third step/end of the reaction: The olivines have been completely serpentinized, only the pyroxenes continue to alter. The kinetics of H₂ production decrease. The iron which is now oxidized precipitates exclusively in the magnetite (oxides). The ratio Fe³⁺/ Fe_{total} decreases in the neo-formed serpentines.

Malvoisin et al, (2012) determined that serpentinization kinetic is inversely proportional to the specific surface area of altered olivine grains. The nature of the secondary minerals, thus, depends on the initial size of the olivine grains. For instance, for grains between 5 and 150 μm, and at temperatures between 250 and 350°C, the serpentine formed is a lizardite and the dissolution of olivine is the limiting factor of the reaction. In other words, the kinetics of serpentinization, and thus H₂ production, is greatly controlled by the mineral surface in contact with the fluid, i.e., the reactive surface.

Numerical modeling also highlights the role of the temperature in the reaction, notably on the stability of certain minerals and on the distribution of ferric iron in certain species. Above 315°C, it is shown that the reaction is rapid but that the fluid approaches a thermodynamic equilibrium with respect to olivine. Above 400°C, at pressure conditions of 300/350 bar, olivine remains stable and does not alter (much higher pressures are required for serpentinization to continue). Below 150°C, the reaction is slow, and the ferrous iron re-precipitates as brucite. This magnesium hydroxide may contain traces of iron (II), which limits the production of H₂ since iron (II) reprecipitates in a secondary phase before it can oxidize. Models show that the optimum serpentinization temperature is reached between 250 and 320°C. At these temperatures, serpentinization is most capable of yielding significant amounts of hydrogen quickly.

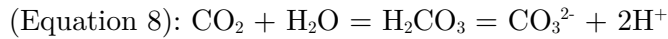
Finally, the pH of the fluid has a direct influence on the reaction. The serpentinization reaction is a redox reaction and releases [OH⁻] ions. Thus, the oxidation of iron and the reduction of water directly influence the pH of the fluid which becomes basic. The serpentinization reaction is limited, with respect to other reactions.

Depending on the other components present, it has been suggested that hydrogen can be consumed abiotically following an FFT (Fischer-Tropsch-Type) reaction of carbon fixation (Giardini et al., 1968, Holloway., 1984, Kularatne et al., 2018):



This mechanism in aqueous solution remains highly debated in experimental work, as contamination with organic carbon that can crack thermally occurs easily.

If the amounts of CO₂ are large enough carbonates can be formed through the interaction between HCO₃⁻ and CO₃²⁻ ions and Mg²⁺, Fe²⁺ ions released by serpentinization, depending on the reaction (Noel et al., 2018):



The pH of the fluid then increases and the Fe²⁺ ions are trapped in the carbonates. Iron is no longer available in solution to oxidize and to produce H₂ by reducing water.

Thus, the kinetics of H₂ generation is a complex issue that depends on the temperature, the nature of the fluid, the amount of iron present in the minerals, their dissolution kinetics, and the mineral surface in contact with the fluid. For the same rock, the quantities of hydrogen generated can vary greatly.

Few studies address the kinetics of iron oxidation related to rocks other than peridotites. Truche et al., (2021) have studied the hydrothermal alteration of peralkaline granites and show that the reaction occurs at slightly higher temperatures than the serpentinization of peridotites (280 - 400°C) but no thermodynamic modeling is currently available.

Many questions about iron oxidation remain unanswered. Understanding the factors that can impact the kinetics of this reaction in the geological environment (factors to which we can add microbial activity) remains a crucial question in understanding natural hydrogen emissions.

V. Conclusion of the chapter

Intracratonic areas represent more than 70% of the continental crust and mainly comprise Precambrian rocks undergoing various geological events.

Some hydrogen emissions have been linked to these cratons and a few hypotheses have been made about the potential mechanisms responsible for such emissions: 1) iron oxidation reaction, 2) radiolysis of water, 3) late maturation organic matter, and 4) cataclasis of silicates. Some appear to be more relevant than others but their role in the generation of intracratonic H₂ remains relatively unrestricted and unquantified.

CHAPTER III

CHAPTER III. Presentation of the study case

In order to better understand what is happening within the intracratonic areas, the study case of the Kansas Precambrian basement (USA) is presented in this chapter. The global geological context and pre-existing data regarding the H₂-emitting wells in Kansas are introduced. Gas composition, gas isotopy, and surface measurements associated with the H₂-emitting wells are accessible and help to target the lithology and processes responsible for H₂ generation.

L'objectif de ce chapitre est de présenter le cas d'étude choisi pour étudier les émissions d'hydrogène naturel en contexte intracratonique. Le contexte géologique global du Kansas, et plus précisément du socle Précambrien du Kansas (USA), est présenté. Sont aussi présentés : les données de puits préexistantes qui correspondent à des données de composition de gaz, d'isotopie de gaz, mais aussi de données de surface directement associées aux puits émetteurs d'hydrogène naturel.

I. Geological context

Kansas is located in the North American intracratonic area and belongs to the southernmost part of the Canadian craton (Goodwin, 1996). Kansas' geology is characterized by a Precambrian basement of granitic rocks intruded by the Mesoproterozoic Mid-Rift System. West of Kansas is marked by the Rocky Mountains formed between the Cretaceous and Tertiary; thus, Kansas is a foreland basin, and the rest of the state is characterized by west-dipping Paleozoic and Cenozoic sediments covering the basement and housing significant aquifers. Today, the area is non-magmatic and only marked by low seismicity.

I.i. The Precambrian basement

The Precambrian granitic basement is divided into the northern (granites, metavolcanics, and metasediments) and the southern terranes (rhyolites and epizonal granites) (Figure 6). There are no outcrops of Precambrian rocks in Kansas except for the large granite inclusions within Cretaceous mica peridotite at Rose Dome (Woodson County, southeast of Kansas) (Bickford et al., 1981).

The northern terranes are intruded by the MRS. The $^{63}\text{Rb-Sr}$ analysis gives the minimum age of these granites from 1.748 to 1.153 Ga. The U-Pb analysis gives an age of 1.650 to 1.610 Ga. The younger granite could have formed between 1.470/1.450 to 1.380/1.340 Ga. Most granitic rocks of the north Central Plain (nCP) are composed of zoned plagioclase, quartz, slightly perthitic K-feldspars, and biotite. Hornblende occurs in some samples. Accessory minerals such as zircon, apatite, sphene, and magnetite are usual. Chlorite and epidote are common. Most of these granites show partially recrystallized cataclastic textures and are highly deformed. 10 to 20% of the nCP are metasedimentary rocks such as quartzite or schists. The authors concluded that the abundance of quartzite within these rocks suggested that the basement sub-surface underwent a long period of weathering in pre-Cambrian times. Thus, only the quartzite resisted the erosion (Bickford et al., 1981). Finally, the nCP is crossed by the Nemaha ridge fault zone, responsible for uplifting some of these granites. Authors believe these nCP terranes formed at a convergent plate boundary during the mid-Proterozoic ages but cannot explain the mechanisms responsible for such abundant granite formation (Bickford et al., 1981).

The southern terranes have an age of 1.380 Ga and are mostly unmetamorphosed terranes of rhyolitic to dacitic volcanic rocks and epizonal plutons of 1.480 to 1.340 Ga. These latter are characterized by a granophyric texture and comprise quartz, perthite, sodic-plagioclase, and biotite commonly chloritized. Accessory minerals such as zircon, apatite, sphene, and magnetite are usual. The sCP formation is again associated with convergent margin, but the silicic volcanic rocks are unusual for such a context. Also, igneous and metamorphic rocks are sparse, meaning the terranes are probably not related to a past rifting episode. Consequently, authors

infer these terranes could be due to crustal thickening and heating of the previous rocks after accretion at a convergent plate boundary. The melted crust could be the origin of a granitic melt responsible for these granite formation (Bickford et al., 1981).

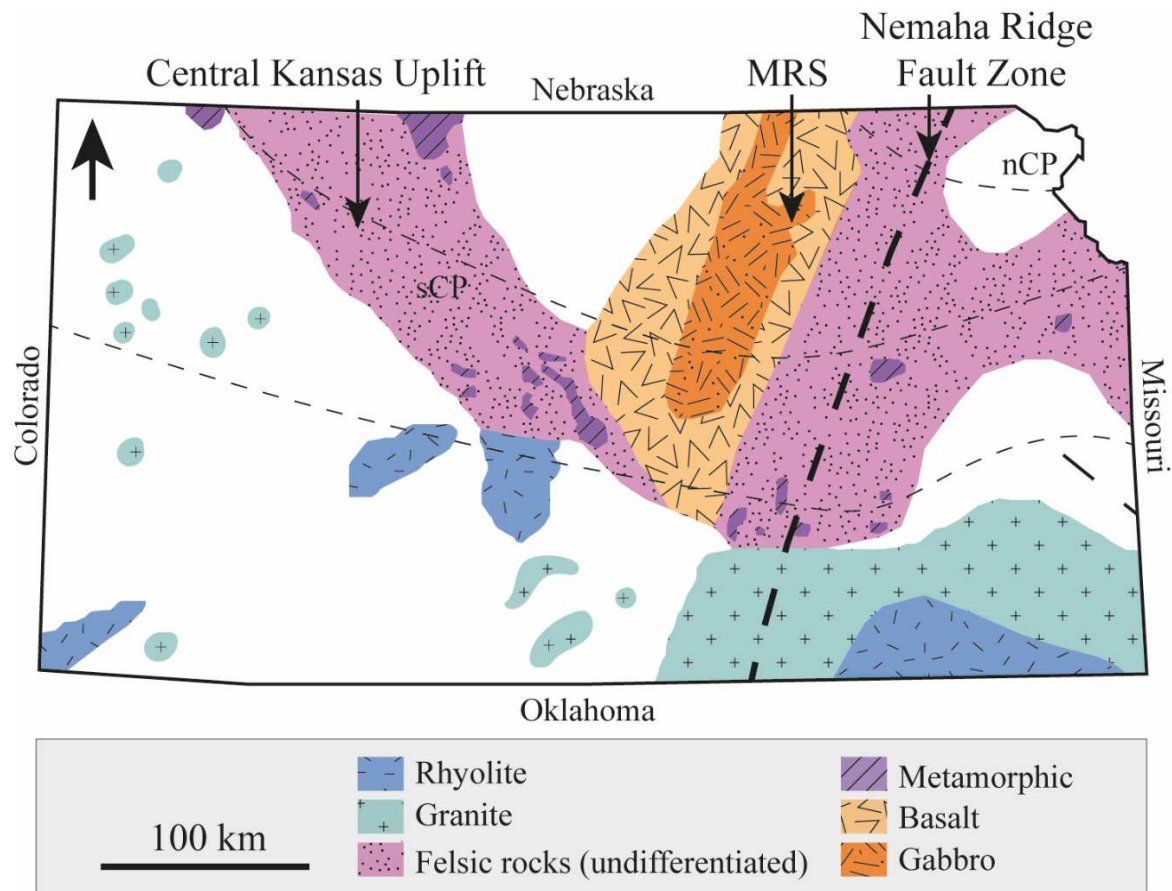


Figure 6: Synthetic map of the Kansas state with lithologies of each known portion of the Kansas basement (modified from Bickford et al., 1981).

I.ii. The Mesoproterozoic Mid-Rift System

North American geology is marked by the Mid-Rift System, a 1.1 Ga aborted rift system extending NNE-SSW from Kansas to Minnesota and southern Michigan. Only a few igneous and volcanic rocks are outcropping in the Minnesota part of the rift. The vast majority of the rocks are buried under Paleozoic and Mesozoic rocks. Thus, the structure was described using geophysical properties such as magnetic and gravity anomalies and sparse seismic data (Van Schmus and Hinze, 1985; Hinze and Braile, 1988). Indeed, gravity highs and lows within the crust are easily imaged due to the kilometeric-scale accumulation of mafic and sedimentary rocks forming the rift. The central parts of the rift, composed of igneous and volcanic rocks, have positive anomalies, while the adjacent basins have negative density and magnetic signals (Figure 7).

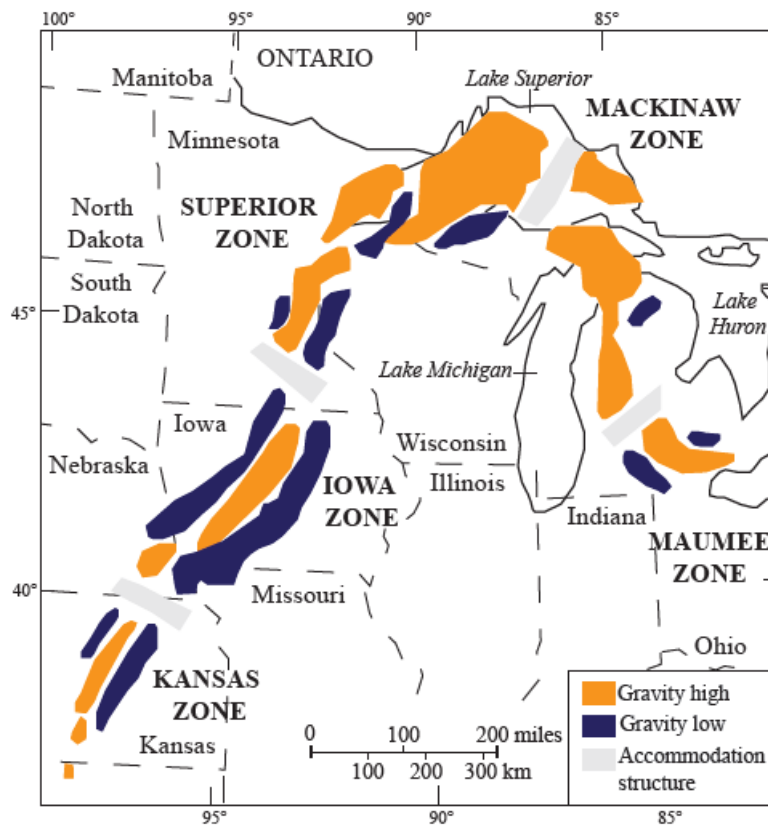


Figure 7: Simplified geological map of the Mid-Rift System gravimetric anomalies (modified from Ojakangas et al., 2001; Dickas and Mudrey, 1997).

Some authors interpreted the Kansas part of the MRS to be rift blocks rotated along eastward dipping listric faults (Serpa et al., 1984, 1989), while Woelk and co-authors (1991) believed, based on drill hole and seismic interpretations, that the MRS is an asymmetric basin bounded by reverse faults similar to what can be found in the northern part of the rift (Woelk et al., 1991). This idea was then supported by Dickas and Mudrey (1997), who infer that the rift is organized along axial blocks flanked by half-graben basins and bounded by high-angle faults (Dickas and Mudrey, 1997). Indeed, west-dipping seismic reflectors could be associated with these reverse faults. The reverse movement was applied probably during a late stage-event along primary Precambrian normal faults (Woelk et al., 1991).

The rift comprises an accumulation of igneous and volcanic rocks overlying thick clastic sediments, commonly designated as the Keweenaw Supergroup. The rifting is divided into four stages: 1) the early stage (1115- 1107 Ma) with a few mafic to ultramafic intrusions in the northern part of the rift; 2) the latent stage (1107-1100 Ma), which represents a hiatus in the magmatism, rocks associated are felsic; 3) the main stage (1110-1094 Ma) with a dominance of tholeiitic magmatism; 4) the late stage (1094-1086 Ma) which is characterized by late volcanism associated with detrital sedimentary rocks. Once the magmatism stopped because of the setup

of the Grenville orogen (1.05 Ga) east of the MRS (Cannon, 1994), the sedimentation and associated subsidence continued and explained the km-scale accumulation of sediments in several areas of the rift (Miller et al., 2011).

I.iii. The Paleozoic and Cenozoic

The Nemaha High (also called Nemaha Uplift) extends from southeast Nebraska to central Oklahoma. In Kansas, the structure separates the Forest City Basin east of Kansas and the Salina Basin west of the state. The uplift is made of several blocks, separated by faults, and is bounded to the east by the Humboldt fault zone. The Nemaha High is responsible for the uplift of the basement, which lies at less than 180 meters in the northernmost part of the High. Its formation started in the late Mississippian/ early Pennsylvanian times due to the Ouachita orogeny (or Ancestral Rocky Mountains). The area was subjected to a new and less intense compressional event after the deposition of the Permian strata and before the mid-Cretaceous, probably due to the Laramide orogeny responsible for the Rocky Mountains formation (Dolton and Finn, 1989; Burberry et al., 2015). Today, the area is deprived of magmatic or major tectonic activities, but low-intensity seismicity is still recorded along the Nemaha High and associated with the Humboldt fault. This latter is considered a complex fault zone inherited from the Precambrian (Steeple et al., 1979).

Kansas is part of the foreland basin of the Rocky Mountains. Consequently, Paleozoic strata are dipping west, and waters are circulating through the rocks due to significant aquifers. Indeed, two groups of aquifers are described: the first is the Great Plains Aquifer within the Mesozoic and Cenozoic rocks, and the second is the Western Interior Plains Aquifer, within Cambrian and Mississippian rocks (Macfarlane, 2000).

II. Pre-existing wells data

II.i. CFA Oil#1 Scott well and CFA Oil#1 Heins well

Since the eighties, hydrogen has been detected as a free gas in a dozen wells in Kansas (Table 2). Two wells have been highly studied by Coveney and co-authors (1987): the CFA Oil#1 Scott well and the CFA Oil#1 Heins well in the respective counties of Morris and Geary in northeastern Kansas.

County (Section, Township, Range)	Completion date	Well Name	Total Depth (m)
8, T12S, R6E	January 1984	Johnson	632
21, T12S, R6E	January 1984	Simpson	704
7, T13S, R7E	August 1985	Glaesner	998
17, T13S, R7E	February 1984	T.Nelson	653
29, T13S, R7E	January 1985	Amthauer	999
22, T13S, R6E	January 1984	Wolf	658
26, T13S, R6E	February 1984	L.E. Nelson	658
27, T13S, R6E	November 1981	Heins	677
20, T14S, R6E	January 1982	Scott	670
27, T14S, R6E	December 1983	R.Rindt	689
32, T1S, R17E	March 2006	Wilson	557
20, T10S, R9E	June 2009	Sue Duroche	424

Table 2: H_2 -bearing wells in Kansas (modified after Coveney et al., 1987)

The two wells are located east of the Mid-Rift System and above the Nemaha High, a few miles west of the Humboldt fault (Figure 8), which is still characterized by low-energy earthquakes (Steeple et al., 1979). The Scott and Heins wells reach 677 meters in depth, penetrate Paleozoic strata up to the Mississippian age, and are characterized by static water levels with headspaces of a few meters. A few miles west of the wells, the Precambrian basement is characterized by the Rice Formation, immature sedimentary rocks, and mafic igneous rocks (Merriam, 1963) (Figure 9).

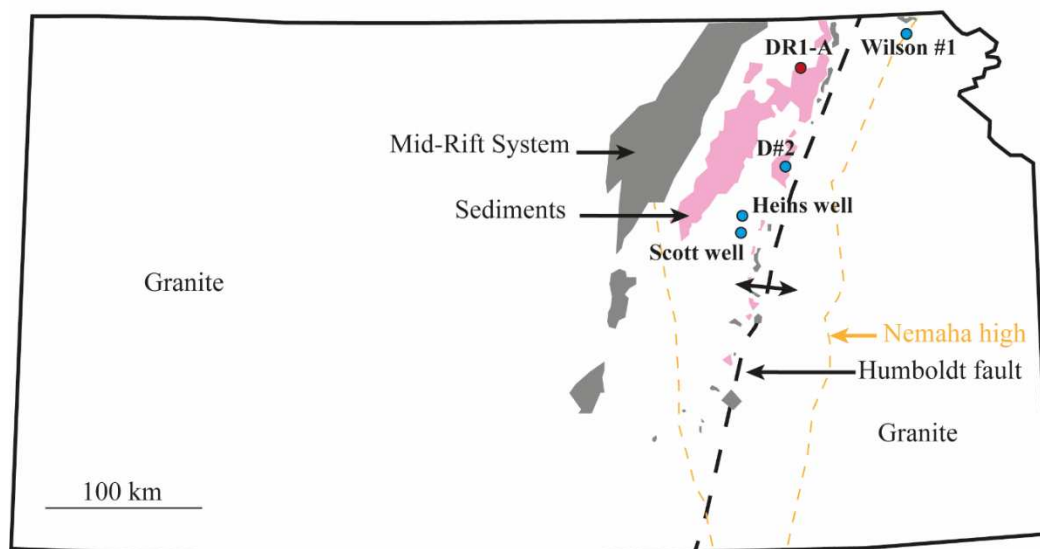


Figure 8: Simplified geological map (of the Kansas state) of the basement top with the location of the H_2 -bearing wells and DR1-A well (modified from Bickford et al., 1981; Coveney et al., 1987 and Guélard et al., 2017).

H₂ content has been quantified up to 35.1 mole%; it is associated with 60 mole% of N₂, and traces of He, CO₂, Ar, and CH₄ (Coveney et al., 1987). Deuterium isotopic values of H₂ range between -740 and -836‰ relative to SMOW (Coveney et al., 1987), ¹⁵N isotopic values range from -0.20 to -0.70 ‰ relative to an atmospheric N₂ (Coveney et al., 1987). The isotopic signature of He is of crustal origin (⁴He up to 3‰ with ⁴He/⁴⁰Ar ratios between 8.5 to 22.7) (Guélard et al., 2017). Precambrian rocks of the MRS are considered to be the kitchen of the gas. The authors consider the gas to be potentially produced by past or actual serpentinization with meteoric water circulating thanks to the high fracturation within the basement. In contrast, Paleozoic sedimentary rocks are considered to be the reservoir.

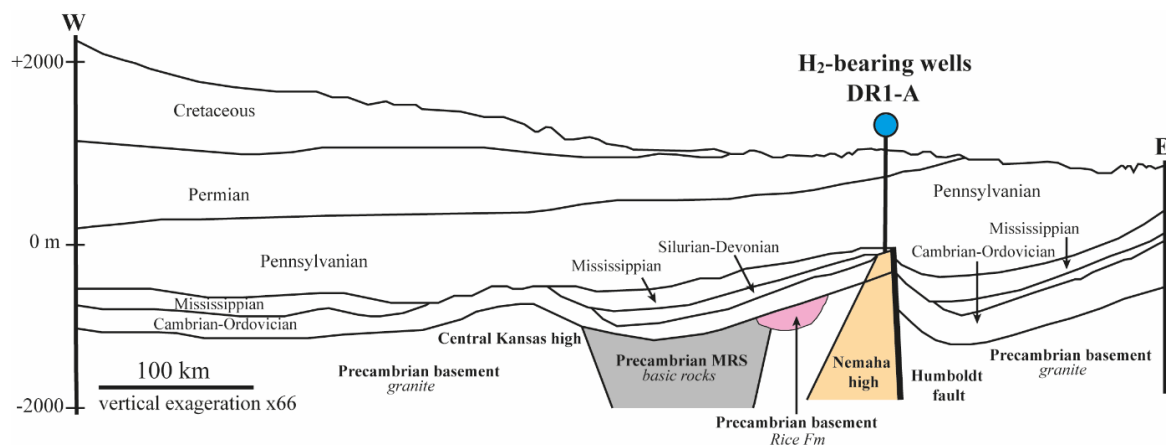


Figure 9: West-East cross-section of Kansas with the location of the H₂-bearing wells and the DR1-A well (modified from Bickford et al., 1981, Kansas Geological Survey (1984), Coveney et al., 1987, and Guélard et al., 2017).

Since Coveney and co-authors studied several Kansas wells producing Precambrian gas, only a few H₂-generating wells in Kansas have been found. The reason is that the Kansas Precambrian basement is known for lacking source rocks for petroleum. On the contrary, the Paleozoic cover is well known for its oil and gas fields, like, for example, the Hugoton-Panhandle gas field in western Kansas, where significant amounts of hydrocarbons have been found associated with N₂ and He (Hemsell., 1939, Ballentine and Sherwood Lollar., 2002). Only a few areas have characterized hydrocarbon production; the Central Kansas uplift, the Cambridge Arch, and the Nemaha uplifts are some of them, but the production comes from adjacent sedimentary rocks (Newell et al., 1987). Thus, the drilling companies do not consider the basement a target; only a small percentage of Kansas wells reach the basement (Table 3) (Cole, 1976; Cole and Watney, 1985).

County (Section, Township, Name)	Date	Precambrian lithology encountered
WA (35, T5S, R5E)	1985	arkose, basalt
NE (19, T3S, R11E)	1929	granite
MS (4, T4S, R7E)	1986	clastics
BR (32, T1S, R17E)	2005	metamorphics
RL (8, T7S, R5E)	1986	gabbro
MS (4, T4S, R57E)	1926	clastics
MS (4, T4S, R7E)	1929	metamorphics
DK (13, T13S, R2)	1932	arkose
MS (29, T2S, R9E)	1922	granite
WO (29, T26S, R17E)	1972	granite
GW (4, T24S, R10E)	1924	schist
BT (17, T19S, R11W)	1927	schist
AL (25, T24S, R18E)	1908	metamorphics
WO (29, T26S, R17E)	1923	granite
CS (2, T20S, R7E)	1917	granite
EW (3, T16S, R8W)	1926	arkose
AL (34, T23S, R21E)	2003	metamorphics

Table 3: Wells in Eastern Kansas drilled more than 300m into the Precambrian basement. AL, Allen; BR, Brown; BT, Butler; CS, Chase; DK, Dickinson; EW, Ellsworth; GW, Greenwood; MS, Marshall; NE, Nemaha; RL, Riley; WA, Washington; WO, Woodson (Newell et al., 2007)

II.ii. WTW Operating LLC#1 Wilson, well

Newell and co-authors (2007) studied the WTW Operating LLC#1 Wilson well located in the Forest City basin (Brown County), northeast of the Nemaha uplift. The well was drilled for 557 meters into the Precambrian basement and crossed a basin filled with Paleozoic sediments and thin levels of Cretaceous, Tertiary, and Pleistocene sediments. Carbonates, alternating with clastic sediments, are characteristics of the Paleozoic strata. The basement is part of the Northern Central Plains terrane (nCP), described as metamorphic gneiss and schist intruded by younger granite plutons (Carlson and Treves, 2005). The top of the Precambrian is at a depth of 1219 meters under Cambrian sandstones (Newell et al., 2007). It comprises biotite-rich schist, aplite veins, dark gray to greenish gray amphibolite, gneiss, metasediments, and no granite. Resistivity logs showed water-filled fractures within the crystalline rocks of the basement.

The bottom hole temperature of the well was 51°C (Newell et al., 2007). Water from the well after several days of swabbing was acid (pH of 5.76), with 36963 mg/L of Cl, 14883 mg/L of Na, 7181 mg/L of Ca, 1150 mg/L of Fe, and significant levels of Mg, K, Sr, HCO₃, SO₄, Al, F, and Br. SO₄ concentration was low (137 mg/L), indicating reducing conditions. When corrected from atmospheric contamination, gas from the wells was found to be composed of 42.83% of CO₂ (after acidification of the sample), 25.76% of CH₄, 19.81% of N₂, 9.84% of H₂, nearly 1% of He, and a few percent of Ar, C₂H₆, and C₃H₈.

Carbon and deuterium isotopes of CH₄ highlighted a thermogenic origin of methane. However, deuterium values in the region were more depleted than usual for this kind of gas, suggesting a mix with biotic methane (Newell et al., 2007). The isotopic signature of CH₄ was not consistent with abiogenic gases studied in Precambrian shields in South Africa or Canada by Sherwood-Lollar and co-authors (2006), where carbon isotopes are depleted while deuterium isotopes of heavier alkanes are enriched compared to methane. In addition, the C1/(C1+C2) ratio has a value of 46.3, coherent with a thermogenic origin. The He content was abundant, and the isotopic ratio of He (³He/⁴He = 0.035) indicated a radiogenic origin from continental crustal rocks.

H₂ from the Wilson, Scott, and Heins wells had the same depleted isotopic signature ($\delta D = -780$ to -798‰ relative to SMOW). However, the Wilson well was characterized by the presence of hydrocarbon phases (which is not the case for Scott and Heins wells), abundant He content, and acidic waters, which are not coherent with an H₂ generation by iron oxidation. It is worth notifying that pH measurement was done after swabbing, which modified the physicochemical characteristics of the fluid.

However, authors infer that H₂ and the hydrocarbons could have been produced by two different processes, in two different geological settings, and mixed later because of water circulation. Two compressional events and the resulting uplift of the basement could explain a past circulation of water in the Precambrian rocks, allowing gas formation and migration during a) the late Cambrian-Ordovician time and b) the late Mississippian-early Pennsylvanian time.

The WTW Operating LLC#1 Wilson well is located east of the Nemaha High (40km east) and the Humboldt crustal fault, while CFA Oil#1 Scott well and Heins well are located west of the fault and on the eastern margin of the Mid-Rift System. Thus, the three wells are located in two different basins, separated by the Nemaha uplift, which could explain the significant differences in gas composition and origins.

II.iii. CFA Oil#1 Scott well, CFA Oil#1 Heins well, and CFA Oil Sue Duroche#2 well (2008-2016 study)

From 2008 to 2016, new field measurements, gas, and water analysis were conducted on CFA Oil#1 Scott, CFA Oil#1 Heins, and CFA Oil Sue Duroche#2 (SD#2), a well drilled in 2008 (Riley County). This latter penetrates Paleozoic sediments, reaches a Pennsylvanian aquifer, and 90m of the underlying Precambrian basement. It is an artesian well with water and dissolved gas.

Julia Guélard's thesis work (2016) highlighted atypical water and gas characteristics. The water of SD#2 is reduced (Eh = -248 meV) and neutral to basic (pH = 6.9-8.6) with 1.5 times the

salinity of seawater. It has a high Fe concentration of 1.1 mM (80% is ferrous iron). Its Dissolved Organic Content (DOC) is 4.1 mg/L. The three wells show a persistent regional flux of H₂ (up to 91.7 mole%), but a decrease in H₂ and in the pressure at the wellhead is observed when the aquifer associated with the gas is produced. The gas of the H₂-bearing well is associated with N₂, He, and variable amounts of CH₄. The proportions of each gas change through time. The Sue Duroche#2 well produces three types of H₂:

- Type 1 is the first gas produced while the well is open to the fractured basement.
- Type 2 gas is produced from the aquifer in the Paleozoic strata.
- Type 3 gas is produced by the casing of the well. Guélard and co-authors (2017) have seen a massive decrease from 91.7 mole% in the free gas (in 2008) to 0.1 mole% bubbling out from the aquifer in 2014. From 2013, CH₄ appears in the wellhead.

Isotopic values of $\delta^{13}\text{C}$ of CH₄ of type 3 gas are -20.1 to -21.9‰ and -50.7 to -64.3‰ for type 2 gas. δD of H₂ is -717 to -799‰. δN_2 is of 2.5‰. SD# gas is depleted in Atmospheric Derived Noble Gases (ADNG) with ³⁶Ar ranging between 6.3 to 11.9 ppm. ⁴He is present in excess (8199 – 31.870 ppm), and the ⁴He/⁴⁰Ar ratio (mean value of 18.0 ±3.6) is higher than the mean ⁴He/⁴⁰Ar crustal ratio (4.92, determined by Ballentine et al., 1991).

The Scott# 1 well produced 25 to 56 mole%, with a decrease since June 1984. 2008 sampling showed a renewal of H₂ up to 18.3 mole% and associated with CH₄. C and H isotopic signatures of CH₄ are similar to the ones of SD#2 type 3 gas. The gas is slightly depleted in ADNG (³⁶Ar of 17.2 ppm). ⁴He is low (11 ppm) but superior to the atmospheric value (5.2 ppm).

The Heins#1 well produced 24 to 80 mole% of H₂, and no drastic decrease in the H₂ content was highlighted since then. CH₄ appears in the gas in 2008. C and H isotopic signatures of CH₄ are similar to the ones of SD type 3 gas. The ADNG values are close to the air values (³⁶Ar between 18.2 to 27.95 ppm) with a ⁴He/⁴⁰Ar ratio of 297.2. ⁴He is high (374 – 598 ppm).

Two origins for H₂ are proposed: 1) a deep crustal origin with H₂ being formed by coupled iron oxidation and water reduction within the basement, supported by the occurrence of associated radiogenic gases (⁴He and ⁴⁰Ar) and metamorphic N₂ with this H₂; 2) reactions occurring within the tubing of the well during the production because of high contents of Fe²⁺ and dissolved organic content (DOC) within the waters which provide sources elements for H₂ and CH₄ synthesis by methanogenic organisms. Type 1 gas of SD#2 probably comes from hypothesis 1. Regarding the crustal gas and N₂ contents and ¹⁵N isotopic values, type 2 gas of the aquifer come probably from the basement. Type 3 gas probably comes from hypothesis 2. Authors infer that Heins#1 and Scott#1 Wells gases are a mix of both hypotheses.

II.iv. Doe Run DR1-A well

The Doe Run DR1-A well (SE-SE-NW SEC. 1. T4S, R9E, KID: 1006461727) reaches a total depth of 457 meters and crosses the basement top at a depth of 350 meters. It is located close to the H₂-emitting wells, west of the Humboldt fault. Besides, it is one of the few wells that allow for studying the basement rock, thanks to preserved core samples. The well was drilled in 1993, and the core samples have been stored in the Kansas Geological Survey (KGS). The drilling report of P. Berenson (2003) is accessible on the KGS website. The first three hundred meters are sedimentary rocks described as limestone, shale, silty shale, sandstone, dolomite, karstic limestone with shale matrix, and oolitic rock just above the basement top. Basement rocks start from 350 meters, down to the bottom of the hole, and are described as weathered granite and mafic-rich granite with many fracture zones. These mafic-rich rocks represent potential good H₂-generating rocks as they could be the location of iron oxidation reactions.

As type 3 gas of SD#2 originates from subsurface processes related to the casing, we decided to exclude it from the rest of this study. We, therefore, focus on type 1 and type 2 gas of SD#2 and gas recorded from Heins#1 and Scott#1 wells, as all evidence suggests these gases come from the Precambrian basement and eventually from iron oxidation reactions.

The remaining questions are: Which rock from the Precambrian basement should be considered the source for H₂ generation in Kansas? What are the iron-rich minerals carried by these rocks? What processes are at stake in generating this hydrogen within the basement? Are there occurrences elsewhere in other intracratonic areas of similar H₂ emissions? If so, what are the rocks, minerals, and processes involved in generating H₂?

III. Conclusion of the chapter

In Kansas, the craton is made of a Precambrian granitoid crust intruded by a Mesoproterozoic aborted rift composed of volcanic, magmatic, and sedimentary rocks. Paleozoic sedimentary units cover the basement. Being part of the foreland basin of the Rocky Mountains (West of Kansas), the area is crossed by several aquifers that provide water down to the basement rocks. The H₂-emitting wells have been discovered a few kilometers east of the rift. They are located above the Nemaha high and aligned with the Humboldt crustal fault, which reaches the basement. Hydrogen has been directly linked to this Precambrian basement thanks to previous water and gas analysis. Still, the nature of the rock, the minerals involved, and even the reaction itself are not well known and, therefore, need to be further studied.

CHAPTER IV. Methodology of the study

This chapter presents the methodology used in this thesis to characterize and quantify the hydrogen generation within the Kansas Precambrian basement rocks. This methodology consists of examining rock samples through a multiscale and multidimensional imaging workflow, including optical microscopy (OM), scanning electron microscopy (SEM), scanning transmission X-ray microscopy X-ray absorption near edges structure (STXM-XANES), transmission electron microscopy (TEM), electron microprobe analyzer (EPMA), and X-ray microtomography (μ CT). Then, a multidimensional workflow coupling μ CT and EPMA was used to quantify the natural H_2 generation (the past and/or actual potential generation). In addition, the choice was made to add new gas and water samples associated with Precambrian basement rocks. The gas samples were characterized using gas chromatography (GC), gas chromatography linked to an isotope ratio mass spectrometer (GC-C-IRMS), and noble gas spectroscopy analyses.

L'objectif de ce chapitre est de présenter la méthodologie utilisée pour caractériser et quantifier la génération d'hydrogène au sein du socle Précambrien du Kansas. Celle-ci consiste à examiner les échantillons de roches grâce à la combinaison de la microscopie optique, de la microscopie électronique à balayage (SEM), de la microscopie à balayage par transmission des rayons X couplées à la spectroscopie de structure près du front d'absorption des rayons X (STXM-XANES), de la microscopie électronique à transmission (TEM), de la microsonde (EPMA), et de la microtomographie par rayons X (μ CT). Une méthodologie spécifique à la quantification de l' H_2 a été développée et se base sur la combinaison des données de μ CT et d'EPMA. En complément, de nouveaux échantillons de gaz et d'eau associé ont été acquis et analysés par chromatographie gazeuse (GC), par un GC couplé à un spectromètre de masse (GC-C-IRMS), et par spectroscopie des gaz rares.

I. Overview of the chosen methodology and analytical tools

This chapter presents the analytical and experimental methodology used to understand the mechanisms behind H₂ emissions in Kansas (we are focusing on iron oxidation thanks to previous works, Chapter II, section II). This methodology is applied to identify the generation zones, i.e., the rocks and minerals involved, as well as the reaction(s) that generate(s) the gas, and *in fine* to quantify the amount of gas generated. The work conducted during this thesis, which will be discussed in the following paragraphs, can be divided into three sections: 1) the rock study, 2) the gas study, and 3) the batch reactor experiments.

A microscopy workflow has been set up to describe the petrology of the Kansas rocks. It consists of gradual changes in the scale of observation, starting from the regional geological and macrometric features observed in preserved core samples, then observations at the micrometric scale on thin sections with optical microscopy (OM), progressing towards the nanometric scale with the use of scanning electron microscopy (SEM), scanning transmission x-ray microscopy (STXM), transmission electron microscopy (TEM), and electron microprobe analyzer (EPMA). The change in scale is also accompanied by a shift from a 2D to a 3D representation at the micrometric scale through X-ray microtomography (μ CT). In addition, the amount of H₂ generated by the identified processes is estimated by coupling EPMA results and μ CT.

The use of multiple microscopy techniques enables us to obtain and cross-check several types of information: the overall mineralogical assemblage and the chemical composition of each phase, as well as the speciation of elements of interest and the relationship between minerals by looking at textures at the microscopic and nanometric scales. In the first part of this chapter, we will focus on optical microscopy, SEM, TEM, STXM-XANES, EPMA, and X-ray microtomography analyses, as they are at the heart of this work. To avoid redundancy, all techniques will only be briefly described as they are also part of scientific publications in chapters 5, 6, and 7.

To have a better representativity of the H₂-generating mechanisms within the basement, a field trip was conducted on the Lake Superior part of the Mid-Rift System (USA) to acquire water and gas samples. Surface measurements of the physicochemical parameters of water and gas analysis were conducted and will be discussed in this manuscript. The gas samples were analyzed and quantified by gas chromatography (GC), gas chromatography linked to an isotope ratio mass spectrometer (GC-C-IRMS), and noble gas isotope ratio mass spectroscopy. Those measurements were performed with the goal of determining the composition and origins of the sampled gases.

It is important to highlight that adding samples from the northern part of the rift is of prime interest as it allows the comparison of two regions affected by the same geological event. In the following chapter, only gas chromatography will be discussed as this analysis has been

developed specifically for low concentrations of H₂ in gas samples. GC-C-IRMS and noble gas spectroscopy will be discussed in the supplementary material of this manuscript (Chapter 10, Supplementary 1). All techniques will be briefly summarized in Chapter 7 as they are part of a future scientific publication.

Experiments were also conducted to test hydrogen generation hypotheses and add additional gas production quantification. These experiments consist of batch reactor experiments with controlled temperature and water: rock ratios and are performed on crushed samples placed within gold capsules. Once these experiments had been completed, the gases produced were analyzed following the same protocol available for the analysis of natural gases. This part of the methodology is presented in the supplementary material of this manuscript.

Combining microscopy, gas analysis, and experiments allows for establishing a quantitative model of hydrogen generation within the Kansas basement.

II. Mineralogical analysis

Thin sections were realized on the preserved core samples of the DR1-A well. After characterization by optical microscopy, two of them were chosen for further investigations. The completed description of the thin sections is given in Chapter 5. Ultra-thin sections were then realized by the mean of a SEM equipped with a focused ion beam (FIB). The sample preparation is described in the following section of this chapter, as well as the techniques used.

II.i. Optical microscopy

Thin sections of the rocks obtained from the DR1-A well were studied under an optical microscope to characterize the minerals present in the different geological units studied. These observations were carried out using a Nikon ECLIPSE LV POL microscope available at IFPEN, which can be used to observe thin sections in both analyzed and unanalyzed polarized light. In addition, transmitted and reflected lights can be used to identify oxidized and sulfide species and cathodoluminescence analysis can be performed.

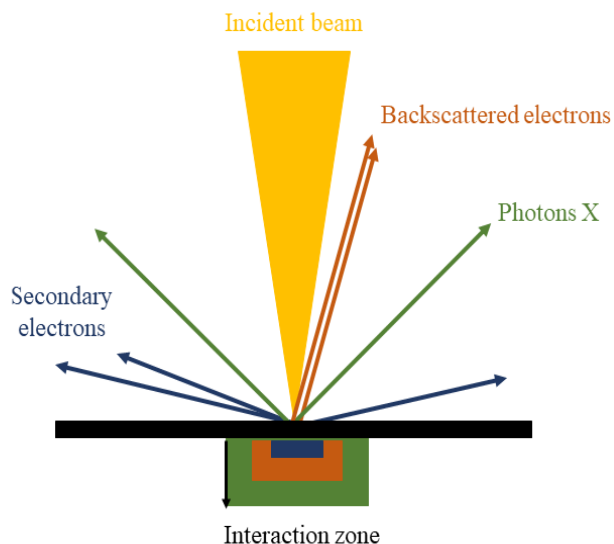
II.ii. Scanning electron microscopy

II.ii.i. Principle

Scanning electron microscopy (SEM) is used to chemically characterize the minerals in the samples studied and describe the textural relationships between these phases (Welton, 1984). It has been used many times during the past decades in order to characterize mineral assemblages and their microtextures (Putnis., 2002, Meunier et al., 2008, Malvoisin et al., 2012, Truche et al., 2021, Osselin et al., 2022 amongst others). It is based on the principle of electron-matter interactions under an electron beam.

When the electrons of an incident beam are in contact with a sample, they interact with it and are re-emitted or deviated. There are several types of interactions, resulting in the emission of different particles (

Figure 10).



When the electron cloud interacts with matter, secondary electrons excite the electron cloud. These secondary electrons are considered to be of low energy. They interact very little with matter and provide information about the sample's topography.

When the electron nucleus interacts with the material, so-called "backscattered" electrons are emitted, providing information on the sample's topography.

Figure 10: Schematization of the interactions between the beam and the sample and their associated emitted particles

The emission of secondary electrons induces ionization and the associated emission of high-energy X-ray photons. Their interaction with matter takes place in a zone of the sample called the "interaction zone", the size of which varies according to the chemical elements characterizing the sample. The energy of these photons (or their wavelength) is directly linked to the nature of the element studied and thus provides information on the chemical composition of the sample receiving the beam.

The incident beam is generated by a Field Emission Gun (FEG) and then directed through a column of lenses and diaphragms to the sample. Various detectors capture the electrons and photons emitted. The most commonly used in this study are listed below (Table 4).

Detector	Particles detected	Information acquired	Operating
SE	Secondary electrons	Topography	500 eV to 30 keV
BSD	Backscattered electron	Topography	0.5 to 30 keV
EDS	Photons X	Chemistry	>15 keV

Table 4: Summary of the detectors used during SEM analysis.

Chemical information can be acquired thanks to energy dispersive spectrometers (EDS), which analyze X-rays based on their energy level. This information remains semi-quantitative as the beam and the sample interaction generate absorption phenomena of light elements. International standards are used in order to correct the data, but it can be necessary to add an additional mapping technique to cross-check acquired chemical data.

II.ii.ii. Analytical conditions and post-processing of the data

The SEM used at IFPEN is a ZEISS Gemini with a maximum imaging resolution of 2 nm. The chemical resolution, on the other hand, depends on the elements that make up the sample studied. Most of the images and measurements were taken using a backscattered electron detector (BSD) or EDS detector with an electron acceleration voltage of 15 kV, enabling us to combine sufficient spatial and chemical resolution for the study of our samples. The corresponding working distance was 8 μm . The EDS data acquired were processed using Aztec software.

II.iii. Sample preparation by Focused Ion beam

To be studied by STXM-XANES and TEM, the samples studied must be transparent to electrons, i.e., their thickness must be around 30 to 80 nm. The samples were prepared using a SEM equipped with a FIB (Focused Ion Beam) following the methodology illustrated in Figure 11 to obtain electron-transparent sections. This technique allows to prepare nanometric scale samples that will be studied to obtain high-resolution information (Ciobanu et al., 2011). It has already been used in past studies that characterize nanometric scale minerals and their textures (Sissmann et al., 2014, Malvoisin et al., 2021 amongst others).

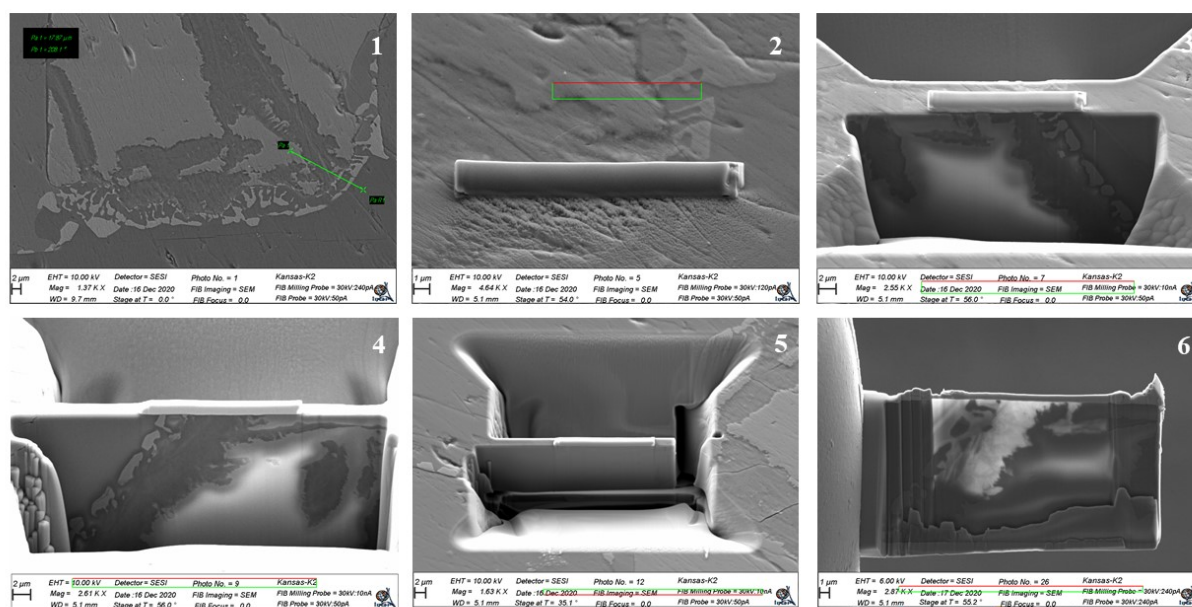


Figure 11: FIB preparation of a sample of the Kansas Precambrian basement, 1- Selection of a zone of several micrometers; 2- Deposition of a platinum layer to maintain the FIB thin section during the rest of the preparation; 3- The ion beam is used to dig around the selected area; 4- The FIB thin section is thinned by the ion beam; 5- The area around the FIB thin section is widened in order to prevent any damage during the next step; 6- The FIB thin section is extracted from the sample and fixed on a sample holder.

The Ga ion beam is first used to dig into the sample around a zone of interest before thinning it to the appropriate thickness. The sample, 10 to 80 μm long, 5 to 10 μm wide, and 30 to 80 nm thick, is then cut by the beam and welded to a sample holder. Refining to a few tens of nanometers is the most delicate stage but essential for obtaining correct electron transparency. Two 80 nm thick FIB thin sections were produced in December 2020 at the *Institut de Physique du Globe* (IPGP, Paris, France). Two additional 40 nm thick FIB thin sections were produced in spring 2021 at the *Institut Electronique, de Microélectronique et de Nanotechnologie* (IEMN) at the University of Lille. Seven additional FIB thin sections were produced in spring 2022 at the IEMN at the University of Lille. Most of these FIB thin sections will be the subject of further studies as their analysis is time-consuming and was not possible during this thesis.

II.iv. Scanning Transmission X-ray Microtomography and X-ray Absorption Near Edges Structures (STXM-XANES)

II.iv.i. Principles

STXM-XANES is a combination of two techniques of microscopy. STXM stands for Scanning Transmission X-Ray Microscopy. XANES stands for X-Ray Absorption Near Edges Structures and is based on the absorption of X-rays by the sample.

This technique is based on the focusing of an X-ray beam that scans across the sample, with a part of the X-rays being absorbed while the rest is collected by various detectors, enabling the sample to be imaged at a specific energy level (Figure 12). One absorption edge corresponds to one specific atom, which corresponds to one specific energy level (Bourdelle., 2011). Iron atoms are typically studied at the K and L edges.

The K edge can be studied using hard X-rays (i.e., the intensity of the beam > 5 keV), and by looking at the XANES spectrum's pre-edge, the atom's redox state can be determined. In order to acquire such information, high intensities of the beam and interactions are needed to obtain a signal-to-noise ratio sufficiently high to extract a good-quality spectrum.

The L edge can be studied using soft X-rays (i.e., the intensity of the beam < 5 keV), which require a lower signal intensity. As the phases within our FIB thin-section have relatively close iron abundance, thus making it complicated to obtain signals with sufficiently high and varying

intensities, we used the iron L edge. Also, the contrast obtained with the L edge comes mainly from the difference in redox. The L edge can be divided into two peaks, L₂ and L₃-edges, each of which usually displays two main absorption peaks. Their intensity can be correlated to the abundance of ferric and ferrous iron following Le Guillou, and co-authors' work (2015).

Ultimately, XANES combined with STXM enables the speciation of a chemical element (iron in this work) to be obtained in the form of an absorption spectrum, and the element of interest to be quantified and located in the form of chemical mapping of the FIB thin-section (Bourdelle et al., 2013). STXM and XANES are useful tools for characterizing hydrogen-emitting mechanisms and clay minerals evolution at a high resolution (Andreani et al., 2013; Viennet et al., 2020).

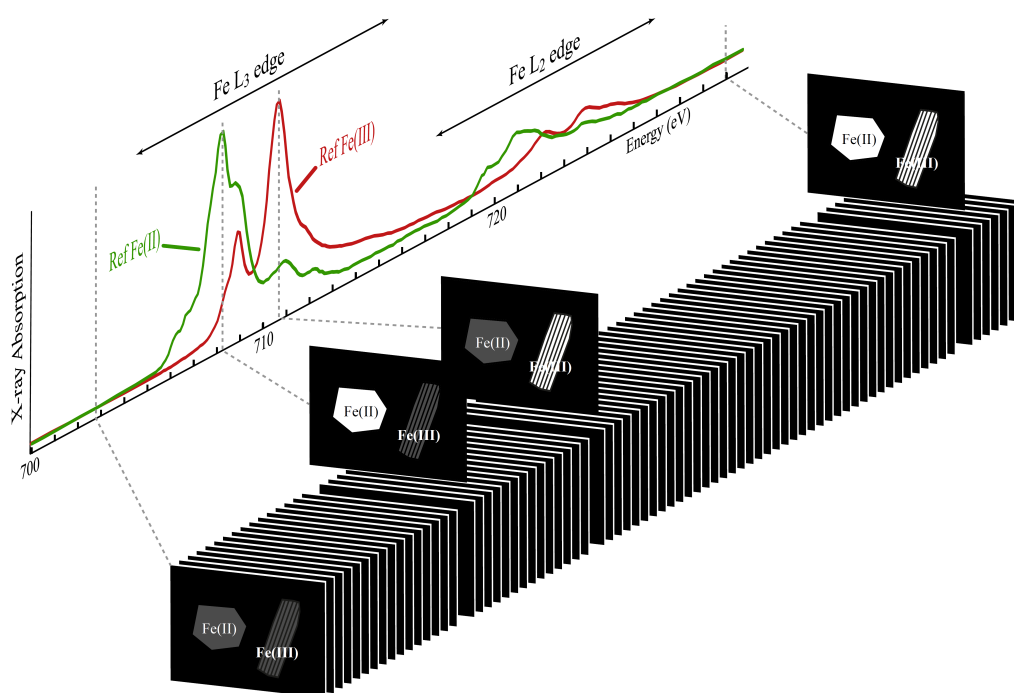


Figure 12: Schematic stacks of acquired images (STXM) and extracted average X-ray absorption spectra with peaks of the Fe L3 edge and the Fe L2 edge (XANES) (This image originates from a personal communication of S. Bernard).

II.iv.ii. Analytical conditions and post-processing of the data

STXM-XANES analyses were carried out on the IM9/Hermes line at the SOLEIL synchrotron (Paris-Saclay) during three beamtimes. These measurements were carried out at the synchrotron in order to have a sufficiently high acceleration voltage needed to study iron speciation and thus estimate the valency of this element and the quantity of oxidized iron likely to have produced H₂. The energy ranges covered by the STXM beamline go from 70 eV to 2.5 keV, and in the case of iron, the energy range used is 690-740 eV (Fe L_{2,3}-edge). XANES data were extracted from the acquired STXM stacks at energy increments of 0.1 eV for the whole

energy range (which is equivalent to the spectral resolution) with a dwell time (the scanning time) of 1 ms per pixel to prevent irradiation damages. The spatial resolution was around 25 nm. Then, the background was removed from the acquired spectra using standards (a synthetic fayalite and a pure Fe²⁺ glass developed by Le Guillou et al., 2015) to calibrate the acquired signal. The calibration consists of determining the start of the Fe³⁺ peak for the L₃ edge by comparing the acquired data to standards for which the maximum intensity of the Fe³⁺ peak is well known. Then, the calibration consists of measuring the ratio of the area of the Fe³⁺ peak over the total area of the peak (Fe²⁺ and Fe³⁺). The acquired ratio is linearly correlated to the known Fe³⁺/ Fe_{TOTAL} of the standards. All the calibration and data post-processing was determined following the method described by Bourdelle et al., (2013) and Le Guillou et al., (2015).

II.v. Transmitted electron microscopy (TEM)

II.v.i. Principles

In order to acquire higher-resolution images and chemical information, Transmitted Electron Microscopy (TEM) has been performed (McLaren, 1991). Conversely to SEM, TEM is used to study the electrons that pass through and interact with the sample. TEM analysis has already been used in order to look at nanometric scale H₂-generating mechanisms (Evans et al., 2017; Malvoisin et al., 2021).

In the case of transmission electron microscopy, the electrons in the beam are accelerated to higher voltages than in the SEM, around 200 keV, which improves spatial resolution. In microscopy, the wavelength of observation has to be similar to the size of the studied object. In the case of TEM, the spatial resolution is nanometric. To reach such spatial resolution, the wavelength has to be similar to the interatomic distance and, thus, generates diffraction phenomena. Consequently, TEM also enables the characterization of the crystal lattice of the minerals present. To achieve this, the configuration of the TEM differs from that of the SEM (Figure 13). The sample is positioned between the condenser and the objective, whereas in the SEM, the sample is positioned after the objective. Additional lenses are also added.

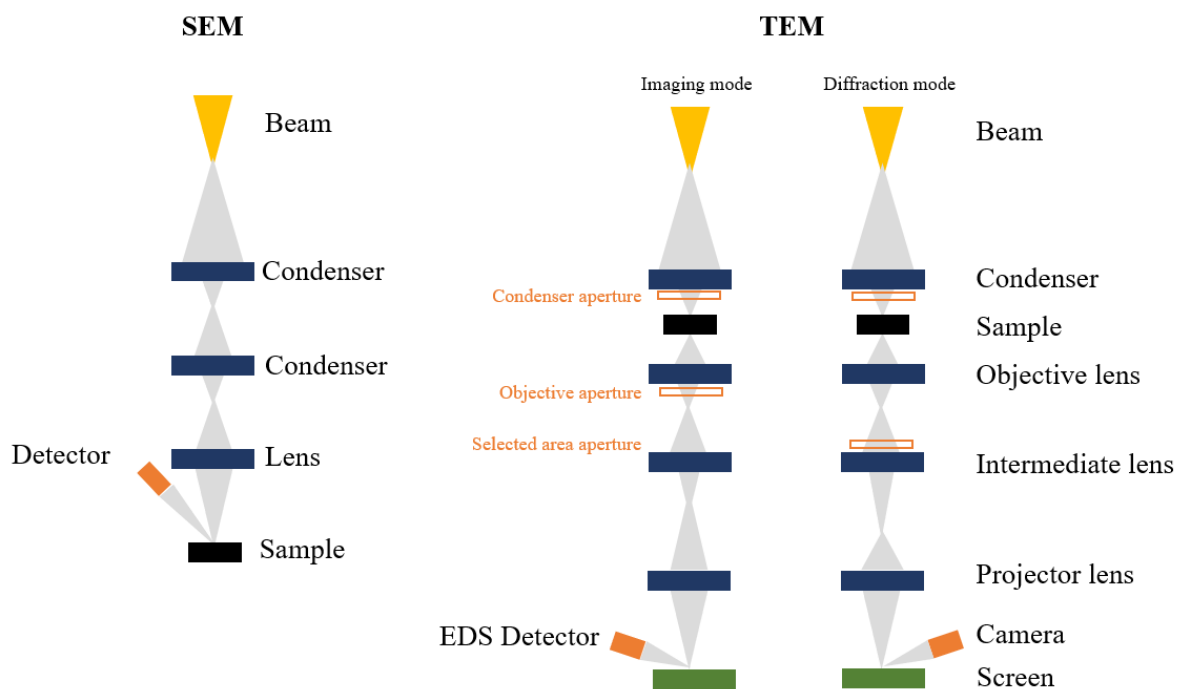


Figure 13: Schematic illustrations of the different architectures of the SEM and TEM (in imaging and diffraction modes).

There are two TEM operating modes: STEM (Scanning Transmission Electron Microscopy) or imaging mode and TEM or diffraction mode. In the first mode, the beam is focused and scans the sample's surface. The sample is studied in amplitude contrast mode, i.e., diffusion contrast. In the second mode, the focal plane and image plane are superimposed, enabling diffraction images to be acquired giving access to the sample's crystalline information. The sample is studied in phase contrast mode. Electrons are collected by an EDS detector in STEM mode, providing access to the chemical information characterizing the sample. A diaphragm is used to select the electrons collected and thus modify the resolution of the image obtained. In TEM mode, electrons are collected by a camera.

II.v.ii. Analytical conditions and post-processing of the data

Analyses were carried out using a TEM JEOL 2100F equipped with a field gun FEG operated at an accelerating voltage of 200 keV at *Institut de Minéralogie, de Physique des Matériaux et de Cosmochimie* (IMPMC, Paris, France), and a TITAN aberration-corrected TEM operated at 300kV at the IEMN (Lille, France). High-resolution images, electron diffraction, and chemical mapping were carried out on the first four FIB thin sections produced as part of this thesis and on a FIB thin section produced as part of earlier exploratory work. EDS maps data acquired with the TITAN MET were processed using the Hyperspy software, allowing for

quantitative mapping (de la Peña et al., 2017). Data from two FIB thin sections are presented in Chapter 5.

II.vi. Electron probe micro-analyzer (EPMA)

II.vi.i. Principles

EPMA analysis allows for the quantitative characterization of major, minor, and trace elements and for performing chemical mapping (Willich, 1992; Pownceby et al., 2007). It has been highly used in the past decades to provide a quantitative chemical composition of minerals in the context of serpentization and amphibolitization (Centrella et al., 2015; Evans et al., 2017; Tutolo et al., 2019; Lévy et al., 2022). This technique is based on interactions between an electron beam and matter. It is a non-destructive method that generates the emissions of new electrons and X-ray photons of different wavelengths characteristic of the matter. These are latter collected by a detector, analyzed by wavelength dispersive spectrometers (WDS, which analyze X-rays based on their wavelength), or by energy dispersive spectrometers (EDS), and converted to signals. The spectrometer signal has to be calibrated. In this study, dolomite is used for Mg, calcite is used for Ca, tephroide is used for Mn, and siderite is used for Fe.

II.vi.ii. Analytical conditions and post-processing of the data

An electron probe microanalyzer CAMECA SXFive with a spatial resolution of 1.2 μm was used to perform quantitative element mapping at the Centre Castaing (Toulouse, France). Si, Ti, Al, Fe, Mn, Mg, Ca, Na, K, and Ba were measured. EPMA data acquisition was performed at 48 nA and 15 keV for X-ray element mapping quantitative spot analysis. Internal standards were used to calibrate the acquired signal. Data processing was performed via XMapTools 4.1 (Lanari et al., 2014, 2019). A more detailed description of the data acquisition and calibration can be found in Chapter 6.

II.vii. X-ray microtomography (μCT)

II.vii.i. Principles

X-ray microtomography is a non-destructive, three-dimensional, micrometer-scale imaging technique (Landis and Keane., 2010). It has been used previously to perform phase characterization (Centrella et al., 2020; Saur et al., 2020) and was chosen over XRD in this study because it enables a higher resolution characterization of the sample as well as a 3D visualization of the minerals. The technique is based on the interactions between X-rays and matter. When the X-ray beam, with initial intensity I_0 , interacts with the sample under study,

the resulting interactions lead to a loss of photons in the initial signal according to Beer-Lambert's law:

(Equation 9): $I = I_0 \times \exp(-\mu d)$

The signal after interactions, with intensity I , is picked up by a detector that thus measures the attenuation of the X-ray beam. This attenuation depends on the medium studied, i.e., its thickness d , and its attenuation coefficient μ , which depends on its density and atomic number. A material with a low atomic number attenuates the signal very little, and vice versa. These variations in attenuation are reflected in the image, i.e., the 2D projection captured by the detector, by variations in shades of gray. By taking a number of projections at different angles, the corresponding 3D volume can be reconstructed by a mathematical algorithm (the standard algorithm being a filtered back projection algorithm (Kak and Slaney., 1988), enabling differentiation between the different minerals making up a natural sample.

In standard laboratory cone beam microtomographs, the sample rotates around its own central axis, and the detector and source are fixed. Several parameters define the acquisition:

- the desired voxel size of the reconstructed 3D image: $V = \frac{D}{M}$ with D the physical size of the detector pixels, and M the magnification (one voxel corresponds to one pixel in 3D)
- magnification, which can be geometric and/or optical, and defines the voxel size of the image:
 - for geometric magnification, magnification is determined by the distance between source and detector and source and object:
$$M = \frac{d_{source-detector}}{d_{source-object}}$$
 - for optical magnification, magnification is determined by the lens used
- the number of projections P to obtain a good reconstruction:
$$P \geq \frac{\pi}{2} \times \frac{T}{V}$$
 (T corresponds to the sample diameter and V to the desired voxel size)

Once the raw scans have been obtained and reconstructed, the data must be processed according to a precise methodology. The noise remaining in the reconstructed images can be smoothed out using specific filters. Once filtered, the images obtained can be segmented. This operation groups together pixels with the same grey-scale intensity, dividing the volume into sub-volumes that can be analyzed mathematically. Among other things, this enables obtaining the surfaces and volumes of phases of interest.

II.vii.ii. Analytical conditions and post-processing of the data

Three tomographs were used as part of this thesis project and are located at the DMEX imaging center at the Université de Pau et des Pays de l'Adour. The Bruker Skyscan 1172 is a medium-resolution scanner (Figure 14). The size of the samples studied is centimetric, and the corresponding voxel size is between 3 and 30 microns. Scans typically last a few hours. The second scanner is a Zeiss Xradia Versa 510. The samples studied are millimetric, and the minimum voxel size is 0.3 microns. These high-resolution scans last an average of ten hours. The third used scanner is a Tescan UniTOM XL Spectral to obtain a voxel size of 2.15 μm . Sample sizes can range from a few millimeters to several centimeters. Thanks to its more powerful source, this scanner can acquire good quality scans in a time span of tens of minutes. For scans in the order of 3 μm of resolution, the scanning time can reach up to one hour.

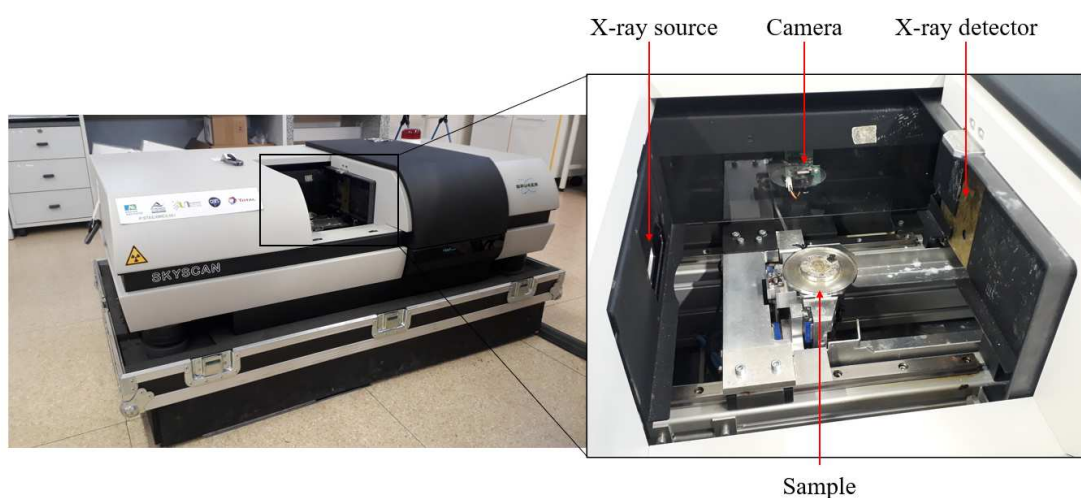


Figure 14: Bruker Skyscan 1172 and architecture of the source-object-detector. In this scanner, the sample is mobile.

II.viii. Synthesis: input and limitations

Several imaging techniques were used. Imaging resolution varies from millimeters to nanometers, and these techniques combined together provide key information such as chemical composition, speciation of certain elements, or crystal structure of the phases studied. These techniques are complementary as they give access to different scales of characterization. They are summarized in Table 5 below:

Method	Spatial resolution	Surface/ volume studied	Information acquired
OM	μm scale	$\text{cm}^2 - \mu\text{m}^2$	Images
SEM	1 μm to 2 nm	$\text{cm}^2 - \mu\text{m}^2$	Images and chemical information for elements > Li
TEM	nm scale	μm^2	Images and chemical information for elements > Li
STXM-XANES	25 nm	μm^2	Iron content and valence
EPMA	1.2 μm	$\text{cm}^2 - \mu\text{m}^2$	Maps of elements
XCT	μm	μm^3	Volume of phases

Table 5: Synthesis of the imaging techniques used during this thesis. (Abbreviation: OM=optical microscopy, SEM=Scanning Electron Microscopy, TEM=Transmitted Electron Microscopy, STXM-XANES=Scanning Transmitted X-ray Microscopy – X-ray Absorption Near Edges Structures, EPMA=Electron Probe Micro Analyzer, and XCT=X-ray Computed Tomography).

Optical microscopy allows for choosing samples of major interest before going deeper into the analysis. X-ray microtomography and SEM are performed on the selected samples. SEM analysis allows for performing a first-order characterization of the minerals constitutive of the sample and for identifying textural association and potential alteration features. SEM allows for spotting areas of interest while looking at mechanisms generating hydrogen. Once these areas are selected, FIB thin-sections can be performed and analyzed by STXM-XANES. If it appears that they are, indeed, mineral phases that could potentially generate H₂, they can then be analyzed by TEM to focus on the micro-to-nanometric characterization of the minerals and textures. Once these analyses have been performed, the suggested areas and mechanisms of H₂ generation are constrained. EPMA analysis and mapping are then performed to provide quantitative compositions of the minerals involved at the micrometric scale. Combined with X-ray microtomography scans, these data are used to provide a quantification of hydrogen production. This part of the methodology is described in the following section.

This methodology is highly resolute and allows for spotting interesting samples from the perspective of H₂ generation and, thus, potential H₂-generating rocks. It is an efficient first step in characterizing the hydrogen generation potential locally by looking at rock samples, even if it is time-consuming. One can easily say that to propose a quantitative model of hydrogen generation at the basement scale; this workflow must be applied to a multitude of samples, which is very time-consuming. To overcome this problem and improve this study's representativeness in the available time, we added new samples (gas and water) associated with similar basement rocks (Chapter 7). Rocks have also been sampled and will be the subject of further studies.

III. Hydrogen quantification workflow

Samples have been studied through diverse high-resolution techniques of microscopy. To improve the characterization of the hydrogen generation at the basement scale, a quantification of the amount of H₂ produced is done. In order to do so, a workflow including EPMA data, mass transfer calculation, and volumes extracted from the X-ray microtomography scans was developed.

This workflow can be divided into three parts (Figure 15): 1) the EPMA analysis and Gresens equations application (Gresens, 1967), 2) the X-ray micro-tomography volumes acquisition, and 3) the calculation of H₂ (mol)/ ton (host-rock).

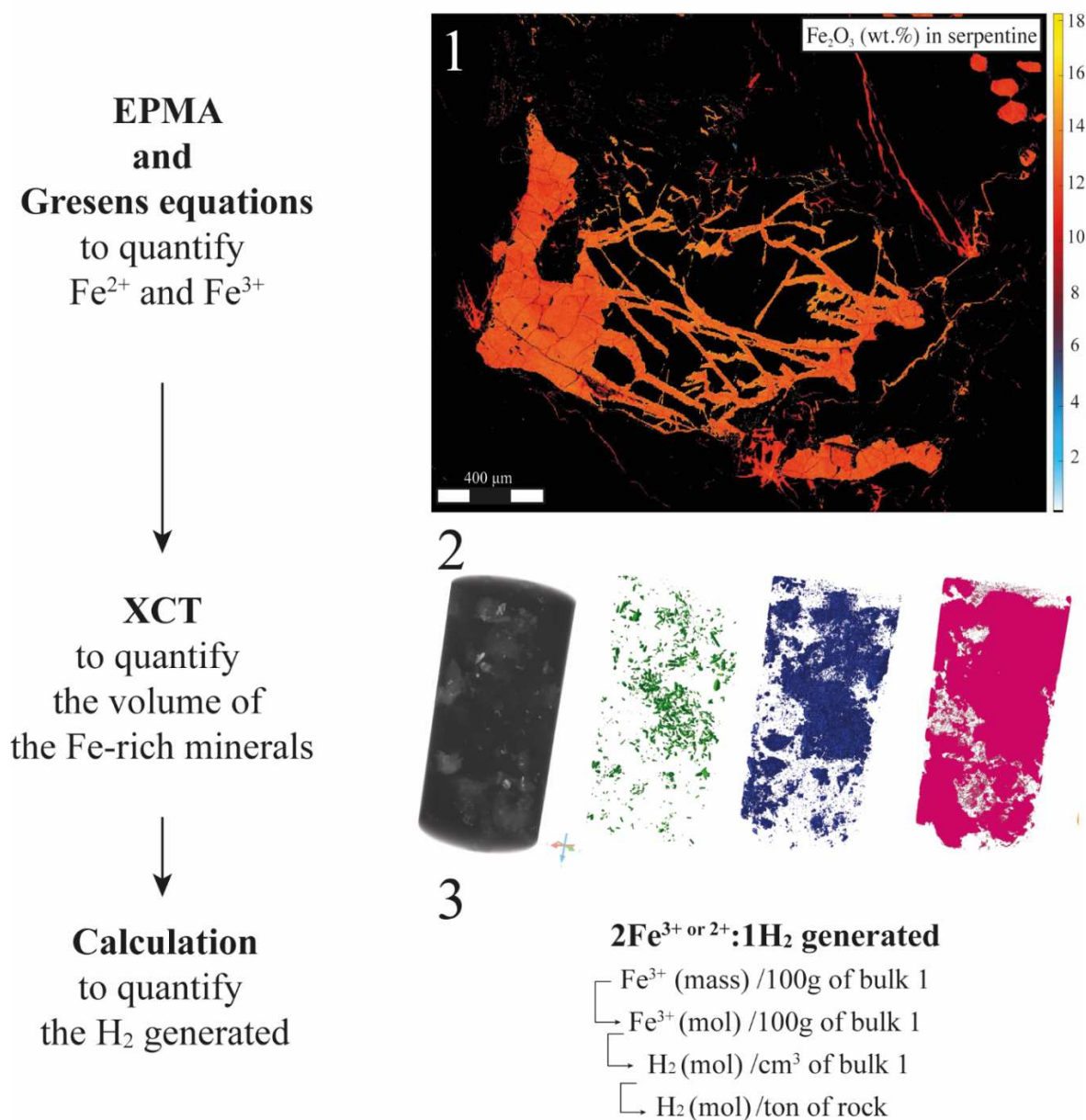


Figure 15: Hydrogen quantification workflow with 1- the Fe³⁺ map for a mineral of interest (here the serpentine), 2- the volume determination for each mineral by performing XCT (green is oxide, blue is for mafic minerals, and pink is for the felspathic matrix), and 3- the H₂ calculation applied for the whole rock.

The first part consists of performing EPMA on a chosen part of the sample to acquire quantitative compositions of the minerals of interest and elements maps (Fe, Si, Al, Mg, Mn, K, Ca, Na, P, Ti, Ba). EPMA does not allow for differentiating ferric and ferrous iron; it only

gives the amount of total iron. By coupling the total iron content obtained by EPMA with STXM data and the calculated density of minerals concerned, it is possible to interpolate the amount of Fe²⁺ and Fe³⁺ in the whole surface of the minerals of interest. Then, the Gresens mass transfer equation (Equation 10) is applied to estimate the gains and losses of elements during the previously identified fluid-mediated mineral replacements and thus to identify the potential reactions generating hydrogen.

$$\text{(Equation 10): } f_v \left(\frac{d_{\text{mineral}2}}{d_{\text{mineral}1}} \right) c_n^{\text{mineral}2} - c_n^{\text{mineral}1} = x_n$$

(x_n is the overall element gain/loss ratio during the replacement of 100g of mineral 1 by mineral 2 as a function of the solid volume variation, f_v is the volume factor (the volume variation), d_{mineral} is the density of the mineral, and c_n the weight fraction of the component in the specific mineral)

In addition, this equation allows us to determine if the chosen reactions induce density and/or volume variations. The masses of ferric and ferrous iron obtained can then be used to calculate the amount of H₂ generated.

The second part consists of using the X-ray microtomography data to determine the volume of the iron-bearing phase. The last part consists of applying the amount of hydrogen calculated to the volume in order to calculate the quantity of H₂ produced per unit mass of the iron-bearing minerals considered.

To obtain the quantity of H₂ generated by g_{rock} (unit mass of the total sample), the previous H₂ quantity determined has to be correlated with the total mass of the sample.

This workflow aims at giving a first-order quantification of the H₂ generated by the iron-oxidation reaction within the Kansas basement rocks. More detailed explanations can be found in Chapter 6.

Another quantification is possible and consists of quantifying the total capacity of the rock in terms of hydrogen generation by considering the amount of Fe²⁺ within the mafic minerals as the total amount of iron that could be oxidized and give H₂. This approach has been developed in a co-authored manuscript by Kularatne et al. (2023 in prep) and is accessible in the supplementary material of this thesis.

IV. Field sampling

To confirm the microscopy observations and the amount of H₂ calculated with the quantification workflow, but also to increase the representativeness of this study by adding new Mid-Rift System (MRS) samples, a field sampling campaign was done in the Northern part of the rift, where the basement rocks outcrop.

Indeed, gas sample analysis will allow for a better characterization of the gas emissions within the MRS, and rock sample characterization will allow for confirming observations made on the rocks from the Kansas part of the MRS, only accessible if wells are drilled. The rock samples will be the subject of future analyses and, thus, will not be presented in this manuscript.

IV.i. In-situ analysis of gas and water

The campaign was conducted in Minnesota in order to look for gas emissions within the Lake Superior part of the MRS. Eleven wells were sampled. Two of them belong to Talon Metals and are old exploration wells for ore deposits that presented flammable gas while drilling. The nine other wells are water wells located within private properties and are used for personal water consumption. A geological description of the sample sites and the Lake Superior part of the MRS is available in Chapter 7.

On the eleven wells sampled, only one free gas leakage was found. The gas was measured *in situ* by using a GA5000 instrument from Geotech. This one is able, thanks to H₂-sensitive electrochemical cells, to measure H₂ up to 1000 ppm. It also measures O₂, CO₂, CH₄, and NH₃. It gives qualitative measurements that can be subjected to atmospheric contamination, thus diluting the gas signal. The gas was flushed within the instrument when possible to avoid atmospheric contamination.

Unusual waters with bubbling gas were spotted within some of the nine water wells. The physicochemical properties of these waters were measured with a HI 98194 multiparameter from Hanna Instrument. This latter allows for measuring temperature, redox potential (Eh), conductivity, and pH. The results of these measurements are displayed in chapter 7 of this manuscript. In-situ gas and water analyses have been conducted numerous times while looking for new hydrogen emissions (Deville et al., 2016; Guélard., 2016; Pasquet et al., 2022), suggesting they are useful tools for identifying potential H₂ systems.

IV.ii. Sampling of gas and water

IV.ii.i. Gas sampling

On the two exploration wells belonging to Talon Metals, only one appeared to have been efficiently sealed from the atmosphere. A funnel with its end connected to a septum in order

to avoid atmospheric contamination was placed above both drilled holes. Gas was sampled within vacuumed exetenair[®] vials (6 mL and 12 mL) filled with a double needle. The pressure being slightly superior to the atmospheric pressure, the exetenairs were filled by the expansion of the gas within the empty volume. When gas was present as bubbles in the water, a tank continuously filled with the water from the well was used, and the gas was accumulated in a sealed funnel placed below the water surface. The gas was then sampled in the vials gas transfer. When a sufficient amount of gas was present, the gas was also sampled in steel containers that had been previously vacuumed. When the available volume made it possible, the gas was flushed before sampling in order to avoid contamination with air or accumulated and fractionated gas in the wellhead before opening. Multiple authors previously described and developed the gas sampling methodology (Vacquand., 2011; Guélard et al., 2017; Pasquet et al., 2022, amongst others).

IV.ii.ii. Water sampling

Water was sampled in exetenair[®] vials or falcon tubes. No headspace was left within the containers in order to avoid the re-equilibration of dissolved gas with air. Some containers were filled using a syringe with a micro-organisms filter ($\Phi = 0.2 \mu\text{m}$) to avoid biological contaminations. In addition, glass bottles, with higher volume than the exetainers and falcon tubes, were filled with water.

V. Geochemical analysis

Coupling gas and rock analyses is of prime interest in understanding and quantifying the mechanism at stake within the Precambrian basement of Kansas. Indeed, rock analysis testifies indirectly to potential hydrogen production. To quantify hydrogen production in a direct manner, it is possible to add natural gas analysis and quantification. It will also allow for cross-checking observations made by looking at the rock, leading to a better representation of the phenomenon.

V.i. Gas Chromatography (GC)

V.i.i.Principle

Gas chromatography is a technique used for identifying and quantifying gases (McNair et al., 2019). It aims to separate the different species and analyze the abundance of H_2 in our case. It is a technique based on the equilibrium between an injected gas phase and a stationary gas phase. Injected volatile molecules are transported by an inert carrier gas (helium or nitrogen). Depending on their affinity with the stationary phase, the molecules are released more or less

quickly and thus analyzed in a specific order by the detector (Figure 16). The analysis yields a chromatogram that can be compared with known standards. The position of the peaks provides information on the species analyzed and the intensity and width of their quantities.

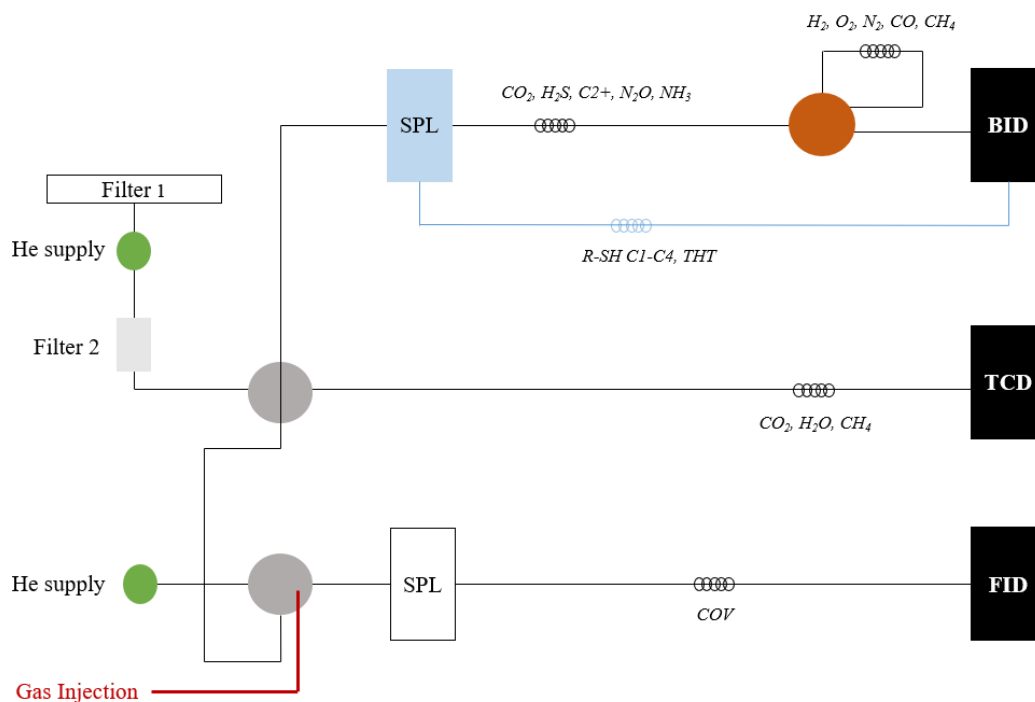


Figure 16: Schematic view of the gas chromatograph architecture (modified from Chemlys communication).

V.i.ii. Analytical conditions and post-processing of the data

A GC-BID 2030 from Shimadzu equipped with a Restek RT-Q-BOND 30m x 530 mmID column is used at IFPEN (Rueil-Malmaison, France). It is equipped with a highly sensitive barrier discharge ionization detector (BID), capable of identifying trace H_2 in gas mixtures to the ppm level. BID has a signal-to-noise ratio (S/N) 100 times higher than a thermal conductivity detector (TCD). A helium plasma that ionizes compounds is generated at low (near ambient) temperature to carry the analyzed the gas.

It also has a flame ionization detector (FID) and classical TCD columns. This GC is used for analyzing small quantities of H_2 (down to ppm). A vacuum injection system is coupled to this GC to control the injection of small quantities of gas, to avoid atmospheric contamination, and to facilitate quantification (Figure 17). A specific method was developed in order to analyze trace elements accurately. The injection line is vacuumed down to $2 \cdot 10^{-3}$ mbar; meanwhile, the right quantity of gas is sampled through a gas-tight syringe. The injection line is isolated from the pump, and the gas is injected into the line. The injection pressure is noted thanks to two pressure gauges; the first one is used to read pressure between 10^3 to 10^{-1} mbar, while the

second one is used to read pressure between 10^{-1} to 10^{-6} mbar. Ultimately, the analysis is launched with the control panel and lasts 17 to 8 minutes.

The C-bearing gases are identified at the beginning of the sequence, while the volatile gases are held in a molecular sieve. Finally, they are released and analyzed. The chromatographic response was calibrated with external standards being a mixture of the studied gas at different concentrations. The GC-BID 2030 can analyze from several dozen ppm to percent of hydrogen before reaching saturation. After calibration, a coefficient of deviation of the signal was calculated for each range of response of the analyzer.

The data were acquired with the software Chromeleon as a signal in millivolts and then converted into percentages by using the injected volume and injection pressure and applying the right coefficient of deviation.

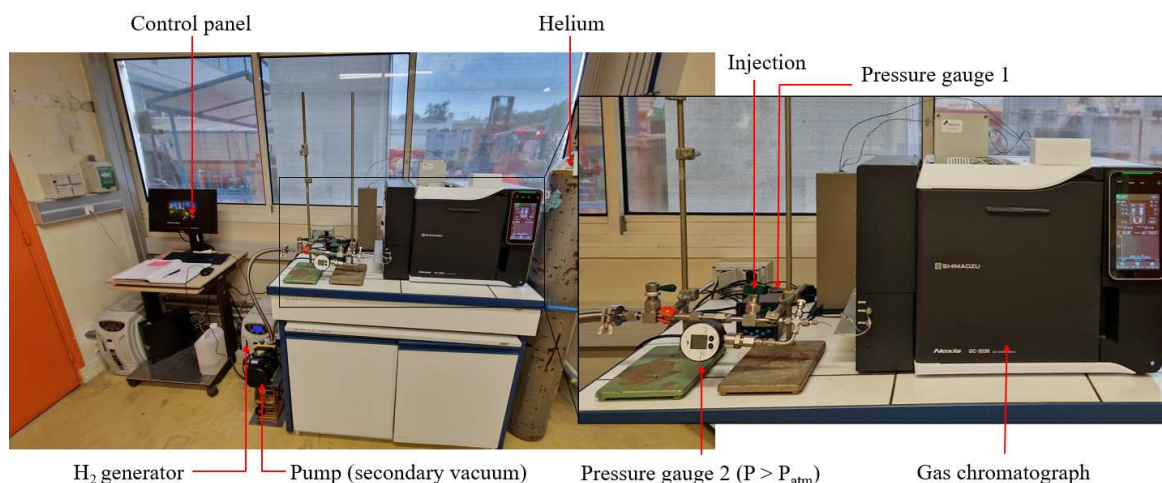


Figure 17: Injection setup coupled with the Gas chromatograph

A GC-7890B from Agilent equipped with a PoraPlotQ column and connected to a gas line was also used for this work. This GC is operated under an N_2 gas carrier to analyze He and H_2 . It is also operated under He as a gas carrier to analyze the other major species. This GC was used to analyze the major components of the gas (% to 300 ppm).

V.ii.Synthesis: input and limitations

Gas analyses are useful analytical techniques to characterize hydrogen emissions and their associated gases but have limitations. Indeed, gas chromatography does not allow quantifying traces and major components within a single analysis. Isotope Ratio Mass Spectrometer, which is used during this study and described in the supplementary material (Chapter 10, Supplementary 1), may provide answer as to the gas origin, but not necessarily a definitive

one, as the sample may be the result of gas mixing and thus have a mix of isotopic signatures. In addition, the gas may have fractionated during the sampling or degassing, modifying the isotopic signature and the final composition. It is mandatory to be careful when looking at such data and, when possible, to cross-check with analogs.

VI. Conclusion of the chapter

The multidisciplinary methodology used in this study aims to identify and describe, as closely as possible, the mechanisms within the basement rocks responsible for the generation of H₂. The goal was to cover multiple scales from the micrometric to the nanoscale. By combining optical microscopy and scanning electron microscopy (SEM), the mineralogical assemblage and the microtextures between phases were identified. Samples were then selected, and the composition, iron content, and crystallography of spotted H₂-generating minerals were characterized by combining STXM-XANES and transmitted electron microscopy (TEM). X-ray microtomography was used to cover the 3D evolution of iron oxidation within the spotted H₂-generated minerals and quantify the proportion of these latter within the rock. The goal was also to quantify the amount of H₂ the Kansas basement rocks generated. This latter was achieved by combining the quantitative and global chemical composition of the spotted minerals acquired by electron probe micro-analyzer (EPMA) with the mass transfer calculation and the volumes of spotted minerals acquired by X-ray microtomography (μ CT). Sampling and gas chromatography of gases from the northern part of the MRS were finally performed to cover the rift H₂ potential on a more regional scale.

This workflow is highly resolute, and some aspects are technical, such as discussed above, but it appears to be an efficient way to accurately identify and quantify, based on the iron oxidation hypothesis, the hydrogen potential of basement rocks in Kansas.

CHAPTER V. Mineralogy of the DR1-A well rock samples

The first part of this chapter aims to illustrate the samples of the studied well, the DR1-A well (Marshall County, Kansas, USA). Nine samples are located in the basement, and four samples are located in the sedimentary cover. The study of these latter is not in the scope of this thesis.

Optical microscopy has been used to give a first-order characterization of the mineralogical assemblage of the samples from the basement. Three samples (named K0, K1, and K2) are well preserved from alteration at this scale of observation. They comprise a feldspars matrix and clots of mafic minerals, including olivine, pyroxene, amphibole, and iddingsite, an iron-rich clay mineral. On the contrary, the six other samples show an increase in their alteration features when getting closer to the basement top. Primary minerals and iddingsite progressively disappear, and green clay minerals, oxides, and feldspars remain. In order to identify the potential source of the H₂ generation, the focus has been put on the K1 and K2 samples as the primary minerals, and the iddingsite identified within their mineralogical assemblage, are spatially the best distributed and the best preserved amongst the other samples.

The second part of this chapter corresponds to the first paper of this thesis and to the high-resolution microscopy study performed on K1 and K2 samples. Optical microscopy, Scanning Electron Microscopy (SEM), Scanning Transmission X-Ray Microscopy combined with X-ray Absorption Near Edges Structure (STXM-XANES) as well as Transmission Electron Microscopy (TEM) results are presented and discussed latter in this chapter in order to describe the Fe-rich minerals and the potential reaction generating hydrogen.

La première partie de ce chapitre a pour objectif de présenter les échantillons de roches du puits DR1-A (Comté de Marshall, Kansas, USA). Neuf échantillons sont localisés dans le socle et quatre échantillons appartiennent à la couverture sédimentaires sus-jacente. Ces derniers ne sont pas étudiés dans le cadre de cette thèse.

Dans un premier temps, une analyse par microscopie optique a été réalisée sur les neuf échantillons du socle avec pour objectif de caractériser les assemblages minéralogiques. Trois échantillons (nommés K0, K1, K2) semblent être (à l'échelle d'observation du microscope optique) préservés de l'altération. Ils sont composés d'une matrice de feldspaths et d'agrégats de minéraux mafiques : olivine, pyroxène, amphibole, et iddingsite, un silicate de fer. A l'inverse les six échantillons restants montrent une augmentation progressive de l'altération en remontant vers le toit du socle. Les minéraux mafiques primaires et l'iddingsite disparaissent progressivement et laissent la place à des veines de phyllosilicates, de carbonates ainsi que des oxydes qui parcourent la matrice feldspathique. L'objectif étant d'identifier la source potentielle d' H_2 dans ces roches, la suite de l'étude s'est portée sur les échantillons K1 et K2 qui présentent les minéraux primaires les mieux préservés ainsi que de l'iddingsite, potentiel marqueur de réaction.

La seconde partie de ce chapitre porte sur le premier article de cette thèse qui se concentre sur l'étude minéralogique haute-résolution effectuée sur les échantillons K1 et K2. Les résultats sont présentés et discutés dans la suite de ce chapitre, l'objectif étant de décrire les minéraux riches en fer et la réaction générant potentiellement de l' H_2 .

I. Introduction of the chapter

The DR1-A well (SE-SE-NW SEC. 1. T4S, R9E, KID: 1006461727) has been chosen regarding its specific location. Indeed, it is located near the H₂-emitting wells, several tens of kilometers east of the Mid-Rift System, near the Humboldt crustal fault, and thus above the Nemaha uplift. This latter allows the well to reach the basement easily, down to 458 meters. The drilling report (accessible on the KGS website) locates the transition between the sedimentary cover and the basement at 350 meters deep. The basement is described as a “weathered mafic-rich granite” with many “fracture zones”. Mafic minerals altered to green clay minerals are described within this so-called granite; levels of a red-feldspar-rich rock are also present within the basement. All rocks are described as fractured, with secondary minerals identified as calcite and quartz filling those fractures. Sulfides are also identified within some of them. When going deeper in the sequence, the same rocks are described as what seems to be “less oxidized” or at least less altered. The ferromagnesian content is high, and no quartz is visible within these basement rocks.

A sampling campaign was conducted during Julia Guélard’s Ph.D. thesis, allowing the study of the preserved core samples of the DR1-A well. This chapter presents a first-order characterization of these samples using optical microscopy to select representative samples. This selection is necessary to perform higher-resolution analysis to characterize the samples’ iron content and identify the potential source of H₂ in the basement rocks. The aim is also to identify the condition/ mechanism of formation of the Fe-rich minerals constitutive of the samples and, *in fine*, to identify the main potential mechanism responsible for hydrogen generation. The second part of this chapter is thus focused on the high-resolution microscopy study performed on K1 and K2 samples.

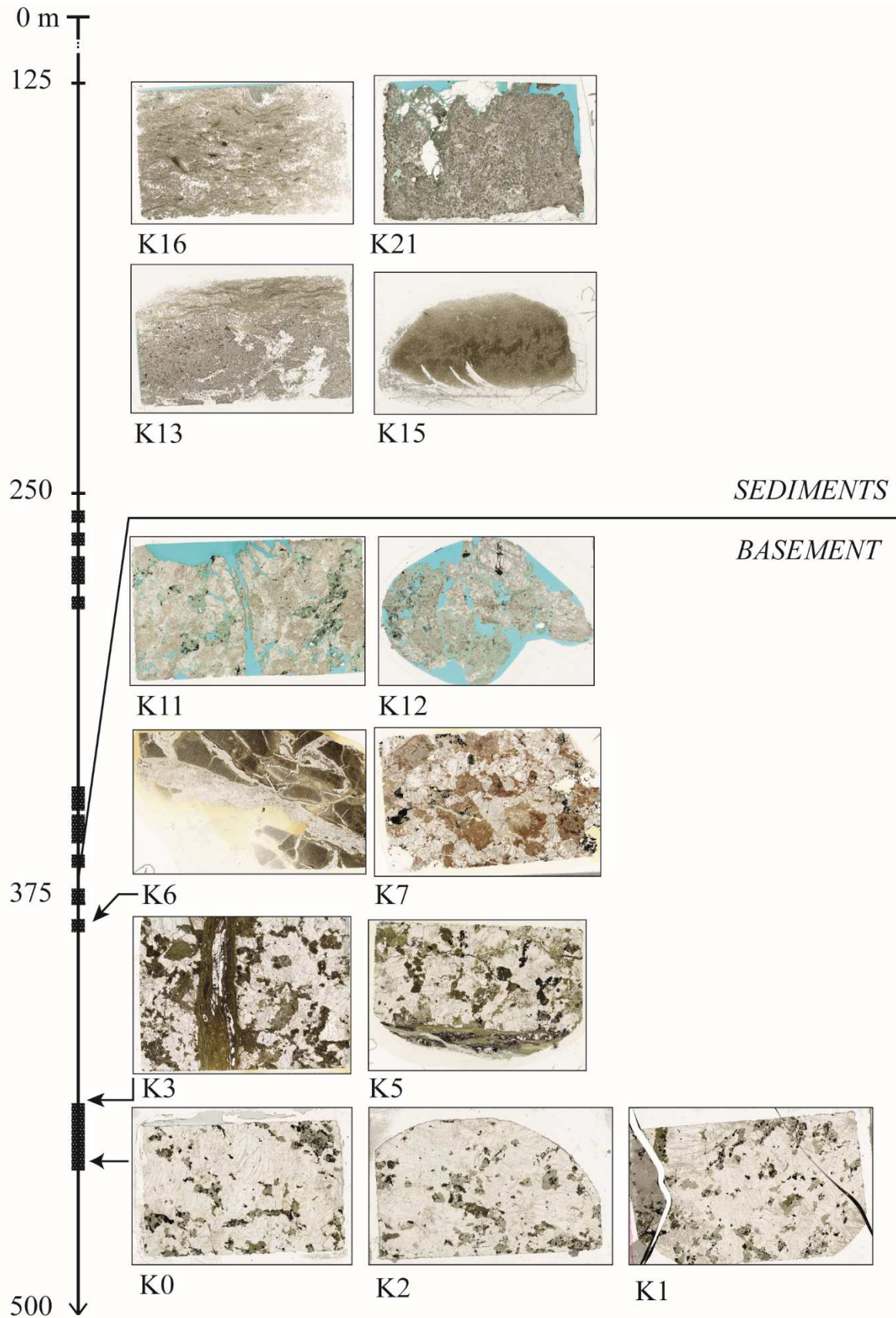


Figure 18: Thin sections of each sample of the DR1-A well in function of depth with the location of the top of the basement at 350 meters deep.

II. Mineralogy study

The preserved core samples of the DR1-A well belonging to the basement are magmatic rocks. They present similarities but also different degrees of alteration. The deepest core samples are K0, K2, and K1, which lie at respectively 454, 450, and 442 meters of depth (Figure 19). They are composed of a feldspathic matrix made of alkali feldspars and plagioclases. These feldspars are uncolored in natural light and grey in analyzed polarized light. Plagioclases present polysynthetic twinning, and alkali feldspars are associated with plagioclases as perthites. Clots of mafic minerals are identified within this feldspars matrix. They are identified as amphiboles, which are light brown in natural light and brown to green in analyzed polarized light. Amphiboles are present as rims around pyroxenes. These latter are uncolored to light green in natural light and have bright colors in analyzed polarized light. Clinopyroxenes are identified as perthites within orthopyroxenes. Pyroxenes and amphiboles are clustered around olivines, which are uncolored to slightly yellow in natural light and have bright colors in analyzed polarized light. A mineral yellow to dark brown in natural light, which we identify as iddingsite, is closely associated with olivine as they are in direct contact. Iddingsite has been previously described by previous studies as a pseudomorph hydrous silicate enriched in iron, being light yellow to dark brown in natural light (Ross., 1925; Edwards., 1938; Baker and Haggerty., 1967; Eggleton., 1984; Smith et al., 1987). At this scale, it is difficult to identify it elsewhere in the other minerals.

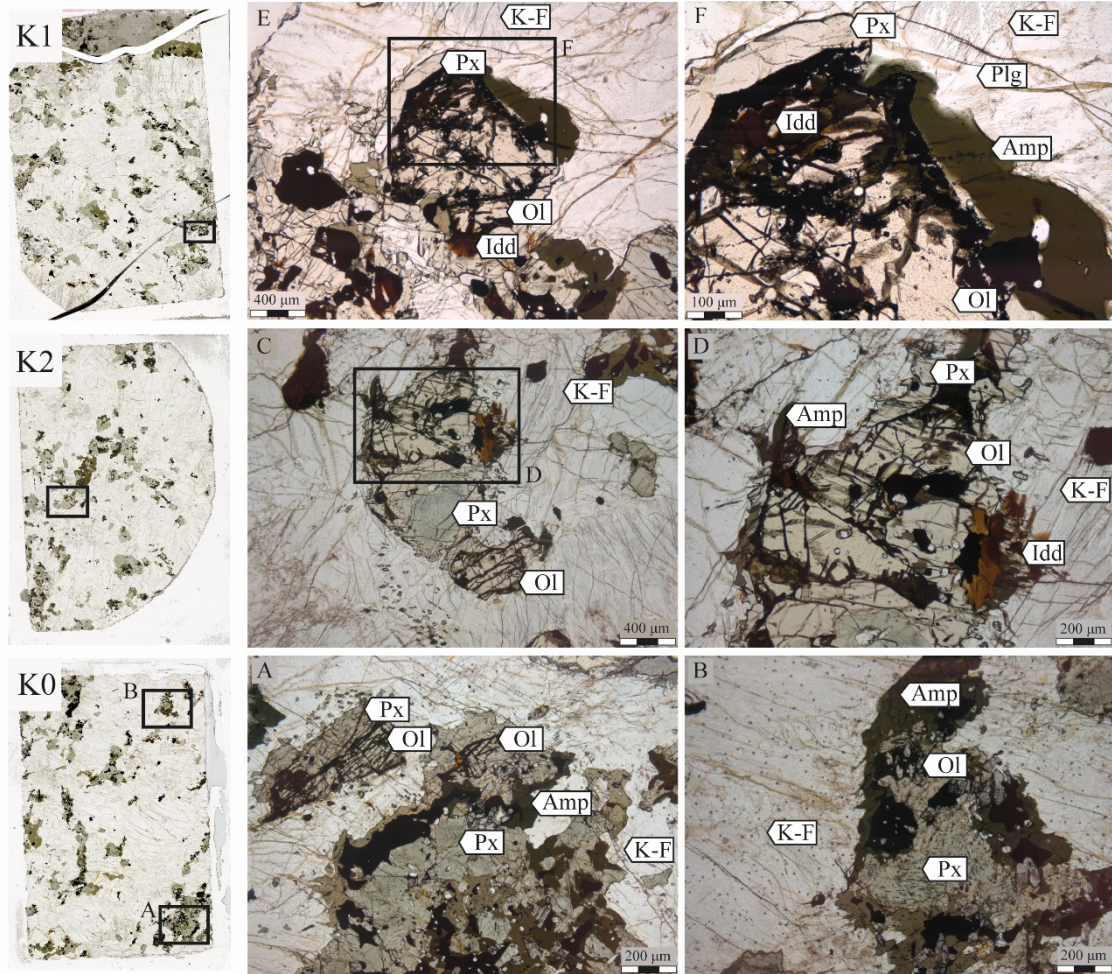


Figure 19: Scans of the thin sections of K0 (454m), K2(450m), and K1(442m) samples and associated optical micrographs in non-analyzed polarized light showing their mineralogical assemblages (K-F is for K-feldspar, Plg is for plagioclase, Ol is for olivine, Px is for pyroxene, Amp is for amphibole, and Idd is for iddingsite).

K3 and K5 preserved core samples are located at respectively 446 and 437 meters of depth. A similar mineralogical assemblage as K0, K2, and K1 is identified within these samples. It is made of alkali feldspar, plagioclase, olivine, pyroxene, amphibole, and iddingsite, with the same optical characteristics described above (Figure 20). However, some differences are present. Biotite grains are identified as associated with other mafic minerals (Figure 20. C). They are light brown in natural light and have medium bright colors in analyzed polarized light. No cleavages are identified. Mafic clots are associated, once again, with iddingsite, which is highly present within K3 and K5 samples. The difference with previous samples is that iddingsite seems to propagate through the feldspars matrix (Figure 20. G) and to completely replace some primary minerals (Figure 20. B. F).

K3 and K5 samples have visibly undergone a more advanced alteration and/ or mineral replacement than K0, K2, and K1. Veins of clay minerals are present and cross all the minerals constitutive of the samples (Figure 20. C. D. H). These clays are light yellow to dark green and brown in natural light (Figure 20). They have radial fibers (Figure 20. D.) and are associated with carbonates, quartz, and oxide (Figure 20. C. D. H). Of note, these veins of clay minerals, cross-cutting the whole sample, are the only alteration features identified.

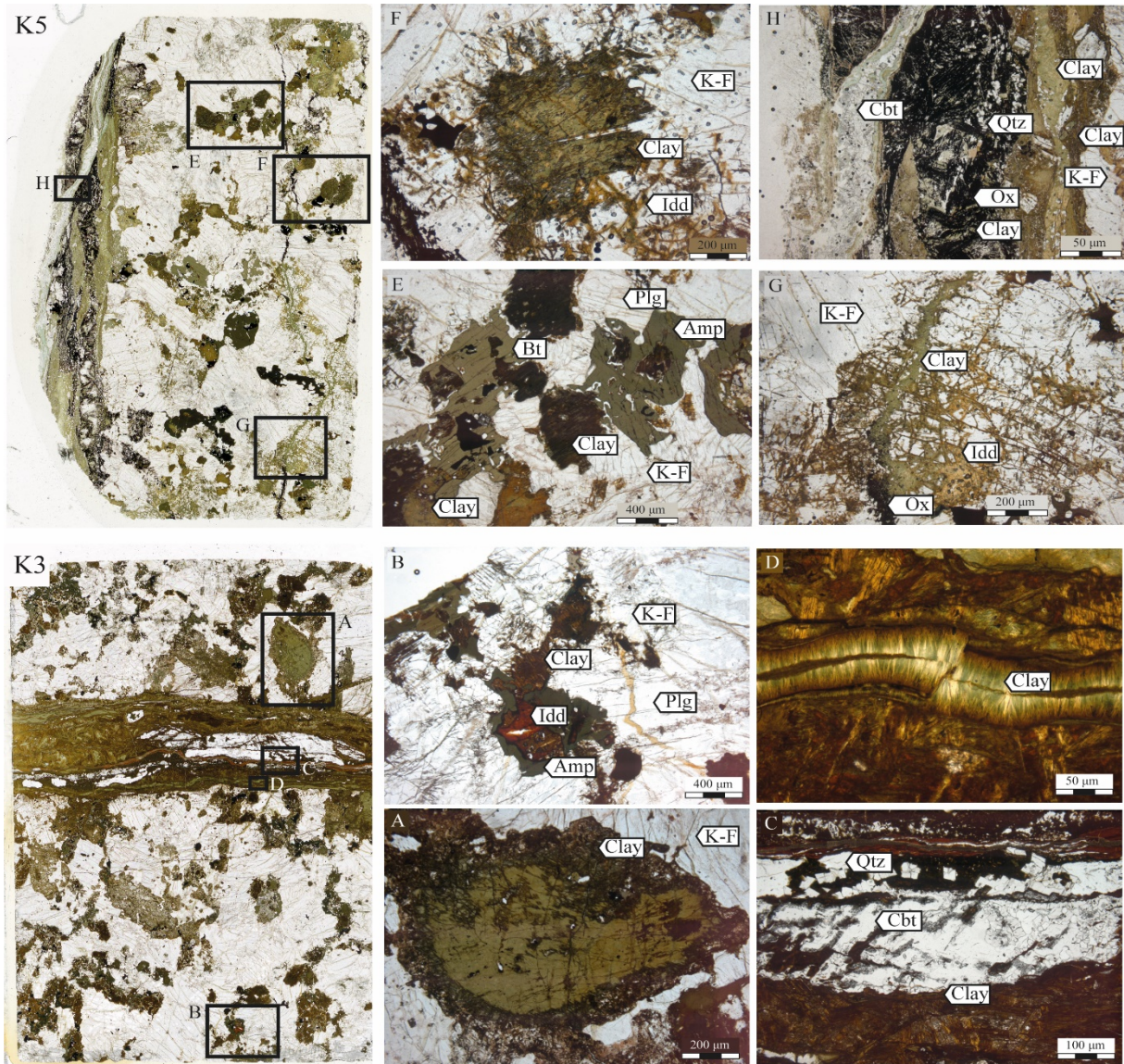


Figure 20: Scans of the thin sections of K3 (446m) and K5 (437m) samples and associated optical micrographs in non-analyzed polarized light showing their mineralogical assemblages (K-F is for K-feldspar, Plg is for plagioclase, Ol is for olivine, Px is for pyroxene, Amp is for amphibole, Idd is for iddingsite, Clay is for clay minerals, Bt is for biotite, Qtz is for quartz, and Cbt is for carbonates).

When going closer to the basement top, primary minerals (including olivine) completely disappear, and the samples are highly altered. Sample K6, at 381 meters of depth, comprises

clay minerals (Figure 21. A. B). These clay minerals are light yellow to green in natural light and are associated with sub-micron oxides, brown to red in natural light. The clay minerals are intersected by carbonates (Figure 21. A.)

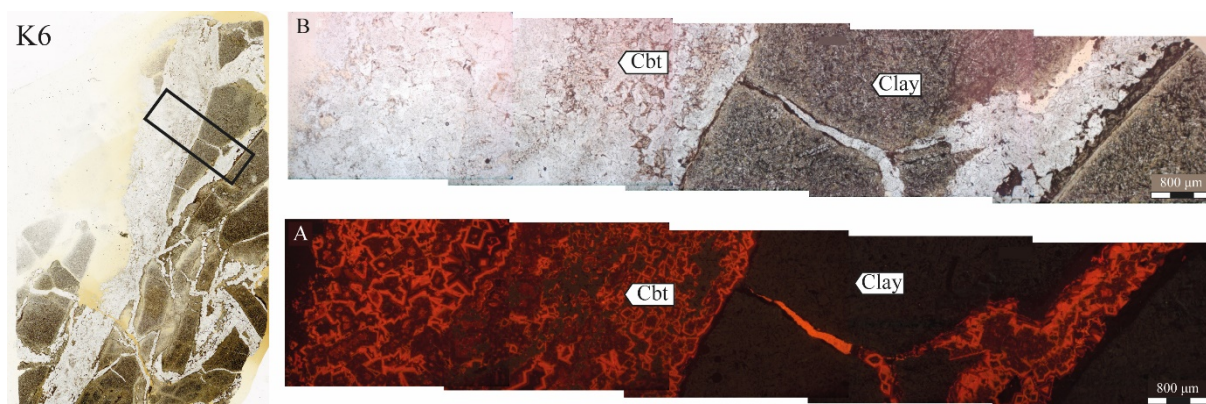


Figure 21: Scan of the thin section of K6 (381m); A- Cathodoluminescence showing the different generations of carbonates; B- associated optical micrograph in non-analyzed polarized light showing its mineralogical assemblages (Clay is for clay minerals and Cbt is for carbonates).

Sample K7 is located at 372 meters of depth, close to the basement top (Figure 22). Feldspars are identified and abundant. They present a pink coloration, showing they have undergone alteration. Indeed, carbonates are identified and, in some areas, clay minerals, and oxide are associated. No primary minerals (except feldspars) nor iddingsite are identified.

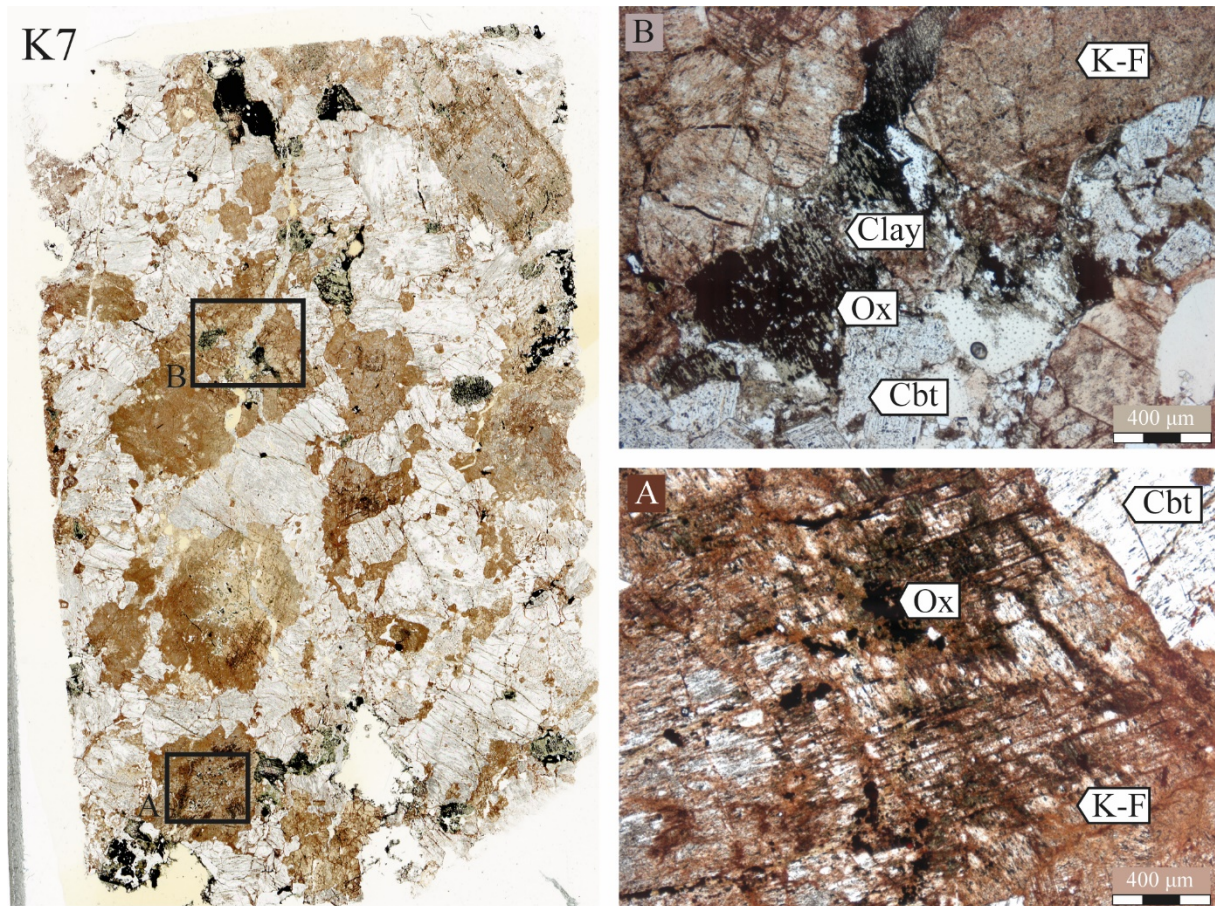


Figure 22: Scan of the thin section of K7 (372m) and associated optical micrographs in non-analyzed polarized light showing its mineralogical assemblages (K-F is for K-felspar, Clay is for clay minerals, Ox is for oxide, and Cbt is for carbonates).

Samples K11 and K12 represent the top of the basement and are highly altered and brittle. Feldspars are still identified, associated with clay minerals, green in natural light, and oxides (Figure 23). The initial mineral assemblage of these samples is hardly recognizable.

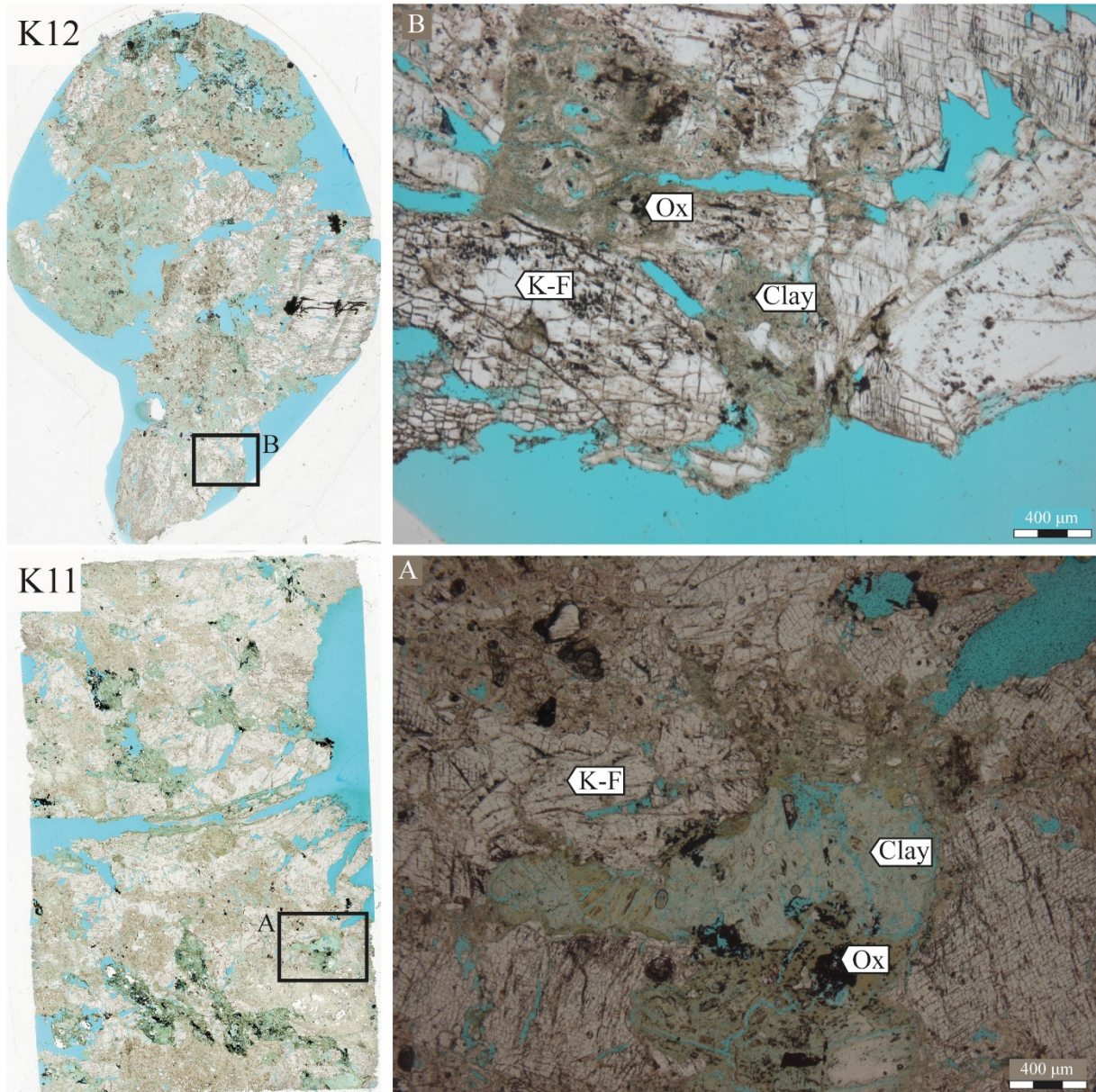


Figure 23: Scan of the thin sections of K11 (350m) and K12 (349.9m) and their associated optical micrographs in non-analyzed polarized light showing its mineralogical assemblages (K-F is for K-felspars, Clay is for clay minerals, Ox is for oxide).

III. Conclusion on the selection of K1 and K2 samples

This first-order characterization by optical microscopy of the samples from the DR1-A well highlights that the deeper samples, K0, K1, and K2, present the better-preserved primary mineralogical assemblages. Their constitutive minerals have a good potential for H₂ generation as they are iron-rich. The samples located closer to the top of the basement present similarities in terms of composition but have mineral evidence of alteration by the circulation of a potential external fluid.

Clay minerals, associated with oxides, carbonates, and quartz, are identified in veins or completely substitute the primary mineralogical assemblage. Samples K11 and K12 are characteristics of the top of the basement and are brittle and completely altered.

In order to clearly understand the source mineral of the potential H₂ generation by iron oxidation within the basement rock, we looked for mineralogical evidence of this oxidation on Fe(II)-rich minerals. Thus, we focused on K2 and K1 samples as they present primary minerals and iddingsite. Indeed, starting from sample K6, minerals are characterized by the formation of carbonates and quartz and by the disappearance of primary minerals and iddingsite, which are probably overprinted by the formation of the secondary minerals. Thus, other samples do not allow for studying primary minerals and finding the source of the potential H₂ generation through iron oxidation.

IV. Are Fe-rich-clay veins related to H₂ generation in the Kansas (USA) Precambrian crust?

Valentine Combaudon^{*1,2}, Olivier Sissmann¹, Sylvain Bernard³, Jean-Christophe Viennet³, Valentine Megevand^{3,4}, Corentin Le Guillou⁵, Julia Guélard¹, Isabelle Martinez⁶, François Guyot³, Hannelore Derluyn² and Eric Deville¹

1: IFPEN, Rueil-Malmaison, France ; 2: Université de Pau et des Pays de l'Adour, E2S UPPA, CNRS, TotalEnergies, LFCR, Pau, France; 3: Muséum National d'Histoire Naturelle, Sorbonne Université, CNRS UMR 7590, Institut de Minéralogie, Physique des Matériaux et Cosmochimie, 75005, Paris, France ; 4: Département des Sciences de la Terre, Ecole Normale Supérieure de Lyon, France ; 5: Université Lille, CNRS, INRA, ENSCL, UMR 8207, UMET, Unité Matériaux et Transformations, 59000 Lille, France 1 ; 6: Université de Paris Cité, Institut de Physique du Globe de Paris, CNRS, 75005, Paris, France

IV.i. Abstract

Natural hydrogen generation has long been considered to only occur at lithospheric boundaries by serpentinization of ultramafic rocks. Past studies have shown that natural H₂ was currently generated within the Kansas Precambrian crust along the Mid-Rift System (MRS), a 1.1 Ga aborted rift. To document the nature of the producing rocks, we conducted a multi-scale study of rock samples from the DR1-A well located in the same area as the H₂-producing wells in Kansas. We showed that this well reached an unmapped part of the MRS composed of fayalite-bearing monzo-gabbros in which we identified atypical veins of iddingsite, a complex mixing of Fe-rich phyllosilicates. Combining scanning and transmission electron microscopies (SEM and TEM) with scanning transmission X-ray microscopy (STXM) allowed us to differentiate at least two types of sub-micro-meters Fe-rich veins. A central reduced vein observed in the

fayalite and other mafic minerals as well as in the plagioclase contains a complex mixing of serpentine, chlorite, and mica, under the resolution of our analyses. On the contrary, a border vein, more oxidized, is found to be present only in direct contact with the fayalite. This external vein mainly contains iron and silicon, together with a few percent of potassium and calcium, and can be divided into two sub-veins composed of Fe³⁺-rich interstratified chlorite-smectite and Fe³⁺-rich serpentine in direct contact with the fayalite. Textures and microstructures of these phyllosilicates suggest that they crystallized from a late magmatic and differentiated fluid, which direct precipitation produced the central vein together with the exsolution of an H₂O-enriched fluid phase. This exsolved fluid, chemically far from equilibrium with the fayalite, was probably responsible for the deuteric alteration of the Fe-rich olivine, leading to the crystallization of the external veins enriched in ferric iron. Magmatic H₂ could have been trapped in the phyllosilicates whereas oxidative deuteric alteration might have produced H₂ as well.

Keywords: fayalite, iron-rich clays, Mid-Rift system, Precambrian, hydrogen

Highlights

- The K2 and K1 samples, from the DR1-A well, are fayalite-bearing monzo-gabbros.
- Mafic minerals such as iron-rich orthopyroxenes, and iron-rich amphiboles are also identified within these fayalite-bearing monzo-gabbros.
- Two generations of iron-rich clay minerals are described.
- One intergrowth of reduced-iron-rich clay minerals is made of serpentine, chlorite, and mica. It is found in all the minerals and was probably formed during a late magmatic event as it is associated with magmatic apatite, quartz, and mafic minerals.
- One oxidized iron-clay mineral has one part made of Fe³⁺-rich smectite, and one part made of Fe³⁺-rich serpentine in direct contact with the fayalite. It has not been identified within the other minerals. Its formation could be due to a late magmatic deuteric alteration.
- This late magmatic deuteric alteration could be prone to produce hydrogen by iron oxidation.

IV.ii. Introduction

Since the eighties, old petroleum wells in northeastern Kansas have been emitting gas with an average of 29-37 mol% of natural hydrogen (Coveney et al., 1986). Hydrogen is always associated with N₂ and He, and occasionally with CH₄. A more recent study from Guélard et

al., (2017) shows similar gas composition up to 92 mol% of H₂, highlighting a persistent regional flux. Analyses showed that the gas flux coming from the wells has a deep crustal origin associated with iron oxidation, coinciding with these wells reaching the basement. The latter, in Kansas, corresponds to the Mid-Rift System (MRS), a 1.1 Ga aborted rift composed of a km-scale accumulation of mafic rocks intruded in the Precambrian granitoid crust (Woelk et al., 1991). The emplacement of the rift was responsible for a major crustal reworking resulting in half grabens bounded by normal faults (Ojakangas et al., 2011). The last tectonic event occurred during the Pennsylvanian (300 million years ago) and was responsible for reactivating the normal Proterozoic faults in crustal faults and for uplifting major parts of the basement (Merriam., 1963; Coveney et al., 1987; Newell et al., 2007). The H₂-emitting wells are located above the Nemaha High and the Humboldt crustal fault, in northeastern Kansas, and are also located about tens of kilometers east of the Mid-Rift system (Figure 24). The origin of hydrogen has thus been attributed, thanks to previous gas analyses, to the Precambrian crust (Guélard et al., 2017).

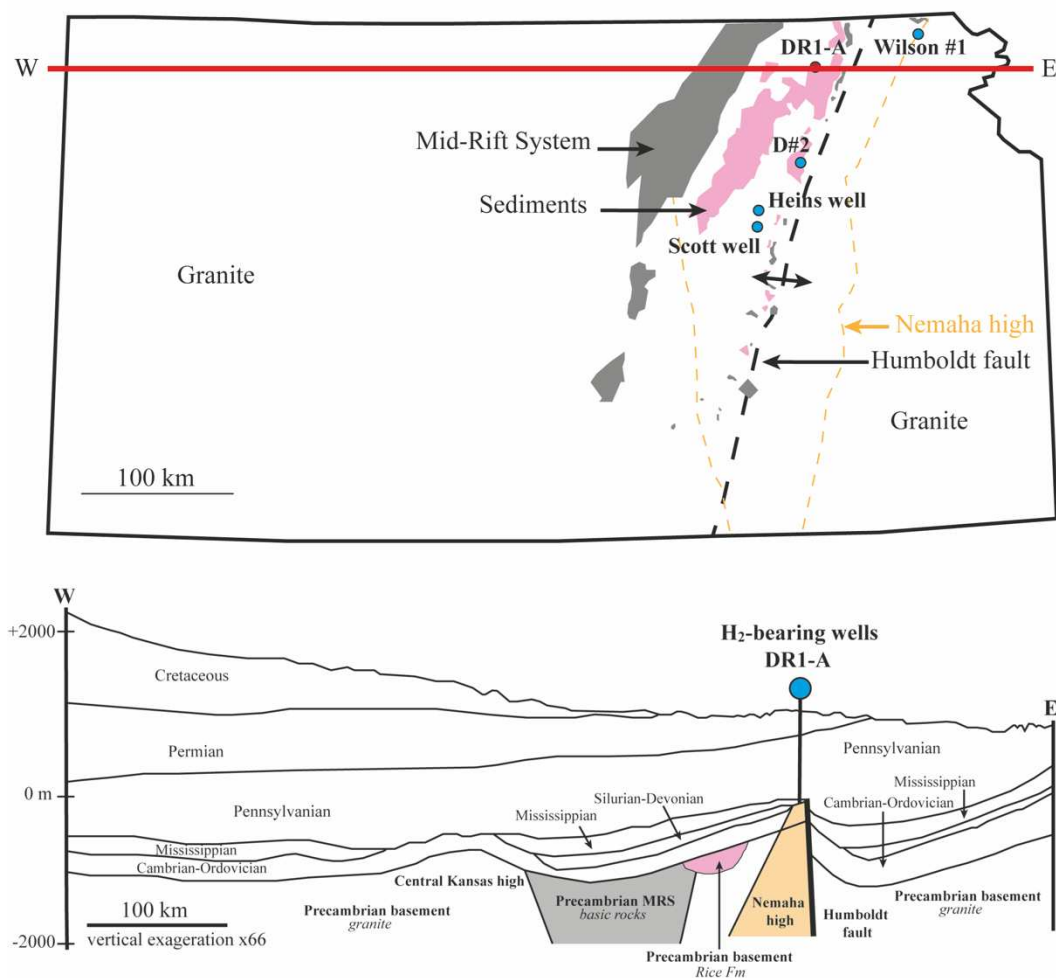


Figure 24: Simplified geological map of the basement top with the location of the H₂-bearing wells and DR1-A well (modified from Bickford et al., 1981, Coveney et al., 1987 and Guélard et al., 2017) and West-East cross-section of Kansas with the location of the H₂-bearing wells and the DR1-A well (modified from Bickford et al., 1981, Kansas Geological Survey (1984), Coveney et al., 1987, and Guélard et al., 2017).

Here, we report the characterization of preserved core samples coming from the DR1-A well located above the Nemaha High and the Humboldt fault and reaching the basement (Figure 24). The DR1-A well does not emit H₂ but reaches the same geological units as the ones reached by the H₂ emitting wells in Kansas. This latter cross 350 meters of Paleozoic sedimentary rocks and nearly 100 meters of Precambrian basement rocks. The study of these rocks is of prime importance because they could be the source and/ or the reservoir of H₂.

We report here the results of a multi-scale petrographic study including scanning electron microscopy (SEM), scanning transmission X-ray microscopy coupled to X-ray absorption near

edge structure spectroscopy (STXM-XANES), and transmission electron microscopy (TEM) on two samples K1 and K2 from the DR1-A well.

IV.iii. **Materials and methods**

IV.iii.i. **Samples**

The K1 and K2 samples belong to the DR1-A well. The depth of the well is 457 meters. K1 sample corresponds to a depth of 442 meters while K2 sample corresponds to a depth of 450 meters. The preserved core samples were provided by the Kansas Geological Survey.

IV.iii.ii. **Mineralogy**

Optical microscopy images have been acquired with a petrographic microscope at IFP Energies Nouvelles (Rueil-Malmaison, France) in transmitted and reflected light. Scanning Electron Microscopy (SEM) and Energy-dispersive X-ray spectroscopy (EDS) mapping were performed on thin sections of the K1 and K2 samples using a Zeiss Gemini SEM at IFP Energies Nouvelles (Rueil-Malmaison, France) and a Tescan VEGAIL LSU SEM at MNHN (Paris, France). International MAC standards for olivine, forsterite, diopside, albite and orthoclase were used to calibrate the acquired signal. Their SEM chemical compositions were also compared to their chemical compositions acquired with microprobe. Images and chemical analyses were performed at a 15 kV accelerating voltage using an 8 mm working distance in backscattered electron detection mode. Data were processed using the Hyperspy software (de la Peña et al. 2017).

IV.iii.iii. **FIB**

To be studied by STXM-XANES and TEM, the samples studied must be transparent to electrons, i.e., their thickness must be around 30 to 80 nm. To obtain electron-transparent sections, the samples were prepared using a SEM equipped with a FIB (Focused Ion Beam). This technique allows to prepare nanometric scale samples that will be studied to obtain high-resolution information (Ciobanu et al., 2011). FIB-ultrathin sections were extracted from the K1 and K2 samples using an FEI Strata DB 235 (IEMN, Lille, France) at low Ga-ion current to minimize local gallium implantation, amorphization, mixing of components, local compositional changes, or redeposition of the sputtered material on the sample surface (Bernard et al., 2009; Wirth, 2009).

IV.iii.iv. **Scanning transmission X-ray microscopy and X-ray absorption near edge structure spectroscopy**

Scanning transmission X-ray microscopy (STXM) and X-ray absorption near edge structure (XANES) data were collected on FIB sections using the HERMES STXM beamline at the synchrotron SOLEIL (Belkhou et al., 2015; Swaraj et al., 2017). XANES combined with STXM enables the speciation of a chemical element (iron in this work) to be obtained in the form of an absorption spectrum, and the element of interest to be quantified and located in the form of chemical mapping of the FIB- thin section (Bourdelle et al., 2013). XANES data were extracted from image stacks collected at energy increments of 0.1 eV over the iron (690–740 eV) absorption range with a dwell time of 1 ms per pixel to prevent irradiation damage (Wang et al., 2009). Data processing was done by fitting peaks of spectra from which the background was removed, and the concentration of Fe³⁺ was determined following the method described in Bourdelle et al. (2013) and Le Guillou et al. (2015).

IV.iii.v. **Transmission electron microscopy**

Transmission electron microscopy (TEM) was performed on one FIB-thin section of the K1 sample and two different FIB-thin sections of K2. The aim was to obtain images of the samples at the nanometric scale as well as diffraction images of the minerals constitutive of the samples. These later were investigated by STXM-XANES were studied by TEM, both in parallel beam with selected area electron diffraction (SAED) and scanning transmission electron (STEM) modes with a JEOL 2100 F equipped with a field emission gun (FEG) operating at 200 kV and with a TITAN Themis-300 aberration-corrected FEI TEM operating at 300 kV. EDS maps data were processed using the Hyperspy software (de la Peña et al. 2017).

IV.iv. **Results**

IV.iv.i. **Characterization at the micrometer-scale**

Optical micrographs of K2 and K1 samples from the DR1-A well are shown in Figure 25. Their mineralogical assemblage is typical of gabbroic rocks. They reveal feldspars, olivine, pyroxene, and amphibole as the main mineral phases. Alkali feldspars and plagioclase are uncolored in natural light and grey in analyzed polarized light. K-feldspars have perthitic textures composed of orthoclases. Polysynthetic twinning is observed in plagioclase. Amphibole is light brown in natural light and tend to appear brown to green in analyzed polarized light. Pyroxene is uncolored to light green in natural light and have bright colors in analyzed polarized light. Their orthogonal cleavages are visible. Pyroxene and amphibole are mostly clustered around the olivine throughout the rock (Figure 25A, C, D, E, and F). Olivine is uncolored to slightly yellow in natural light and have bright colors in analyzed polarized light (Figure 25A, B, C,

D, E, and F). They are cut by a thin and light yellow to dark brown mineral network forming veins (Figure 25B and D). The mineral forming the veins also mimic, in some places, the olivine shape and is associated with iron oxide (Figure 25F). The mineral forming the veins is present within the olivine as well as within minerals in contact with the olivine. At this scale, it does not appear in the felspathic matrix as clearly as in the olivine.

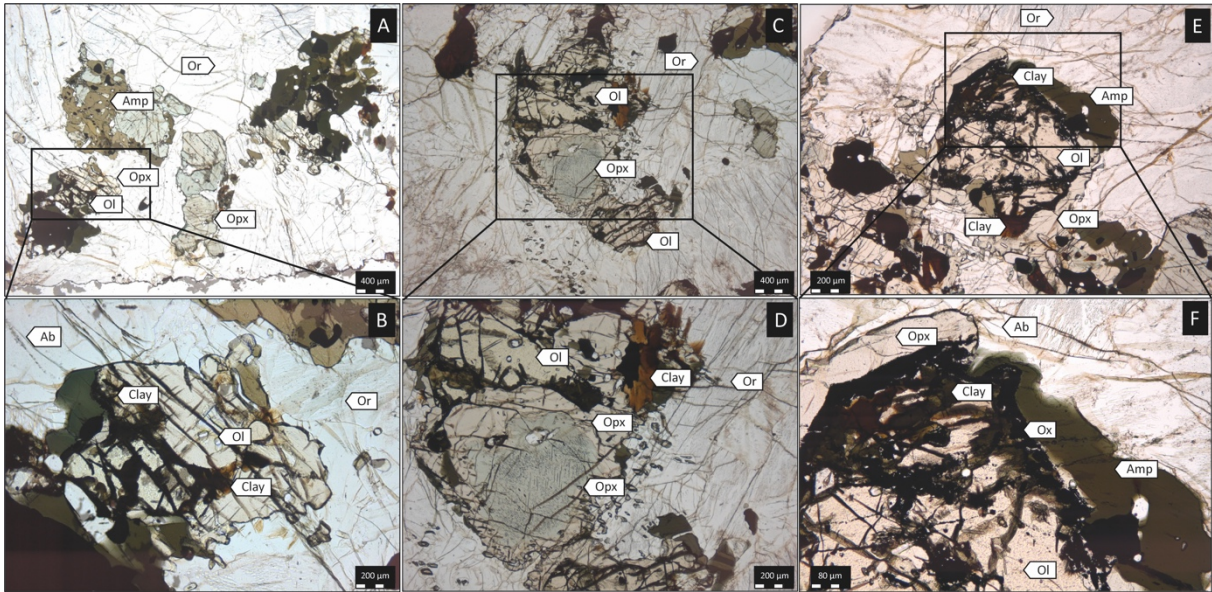


Figure 25: A- Optical micrographs in plane polarized light showing the K2 sample gabbroic mineralogical assemblage; B- Optical micrographs in plane polarized light zoomed on an olivine crystal and its associated aggregates of light yellow to dark brown colors clay mineral seen in A; C- Optical micrograph showing K2 olivine and associated mafic minerals inside the feldspar matrix; D- Optical micrographs in plane polarized light zoomed on the olivine – orthopyroxene association seen in C; E- Optical micrographs in plane polarized light showing the K1 sample gabbroic mineralogical assemblage; F- Optical micrographs in plane polarized light zoomed on the olivine and clays seen in E (Ab is for albite, Or is for orthoclase, Ol is for olivine, Opx is for orthopyroxene, Amp is for amphibole, Mag is for magnetite. Abbreviations have been defined by Whitney and Evans., 2010).

SEM data on K2 and K1 samples are shown in Figure 26. SEM-EDS provides semi-quantitative chemical compositions. All structural formulae given below have been recalculated from EDS data acquired with the SEM. K-feldspar is orthoclase with the following structural formula: $K_{0.8} Na_{0.2} AlSi_3O_8$. Plagioclase is albite with the following structural formula: $Na_{0.8} Ca_{0.2} Al_{1.2} Si_{2.8} O_8$. Rims of plagioclase are seen around the olivine, which is not the case for orthoclase. Both feldspars are closely associated and form perthitic textures.

Mafic minerals are seen as aggregates and can also form rims around olivine (Figure 26A and C). Note that plagioclase is also found at the border of these rims. These mafic rims are composed of amphibole identified as iron-rich pargasite: $\text{Ca}_{1.7} \text{Na}_{0.4} \text{Fe}_{3.5} \text{Mg}_{1.1} \text{K}_{0.2} \text{Al}_{1.9} \text{Si}_6\text{O}_{22}(\text{OH})_2$ and orthopyroxene as ferrosilite: $\text{Fe}_{1.6} \text{Mg}_{0.5} \text{Mn}_{0.1} \text{Si}_2\text{O}_6$ (Figure 26A, B, and C). In some areas, these ferrosilites are associated with clinopyroxene identified as augite: $\text{Ca}_{0.7} \text{Fe} \text{Mg}_{0.3} \text{Si}_2\text{O}_6$. Together they form large exsolution textures of several hundreds of microns in length. These iron-rich minerals have crystallized around more or less well-preserved olivine. They have been identified as fayalite, the iron-rich endmember of olivine: $\text{Fe}_{1.8} \text{Mn}_{0.1} \text{Mg}_{0.1} \text{SiO}_4$. They are being crosscut by veins of minerals rich in Fe and Si which seem to have developed along fractures (Figure 26B and D).

Veins crosscutting fayalite in the K2 and K1 samples exhibit different phases, symmetrically distributed along the vein axes. These later are made of an external part in direct contact with the fayalite. Note that veins only exhibit external parts within the fayalite. The contact between the external part of the veins and the hosting olivine is mostly characterized by scalloped patterns (Figure 27A). These veins are also made of a central part sometimes associated with iron oxide, apatite, and quartz (Figure 26B and D and Figure 27A). SEM investigations reveal that the central part of the vein is observed in the fayalite, the amphibole, the orthopyroxene, and the plagioclase. Narrower veins (under the micron) can also be seen within the K-feldspar mesostasis (Figure 26D and Figure 27). Except for the areas containing iron oxide, apatite, and quartz, these veins are mainly composed of Si and Fe, with the internal parts exhibiting higher Fe/Si values (Fe/Si of 1.2) than the external part of the veins (Fe/Si of 0.9).

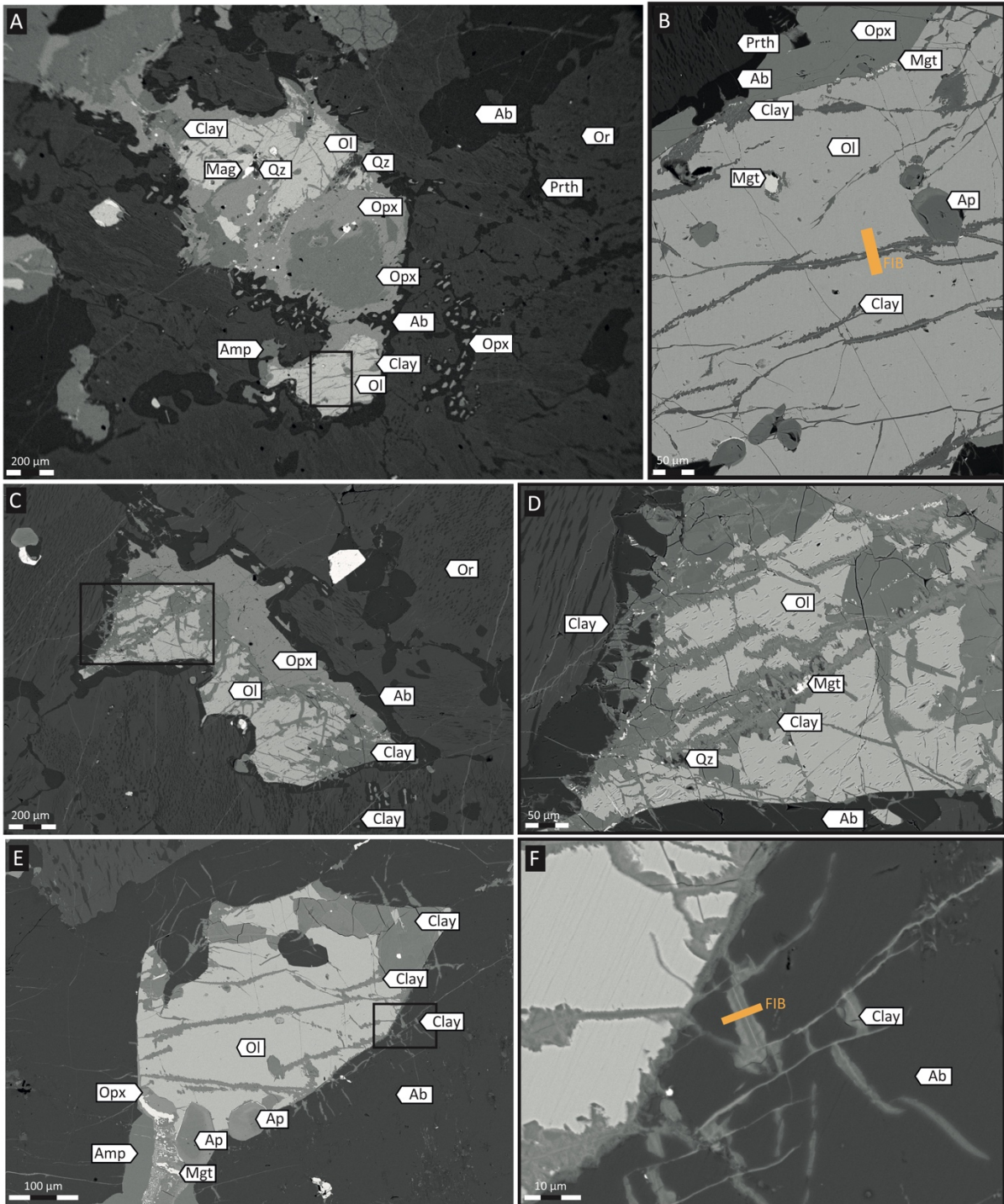


Figure 26: SEM images of A- The mineralogical assemblage of the K2 sample with an aggregate of mafic minerals; B- Veins of clay minerals going through an olivine grain, associated with apatite and iron oxide with the location of the FIB thin-section; C- The mineralogical assemblage of K1 sample with a rim of orthopyroxene and plagioclase in a feldspars mesostasis; D- Veins of clay minerals inside a fayalite crystal, clay minerals are associated to iron oxide and quartz; E- The mineralogical assemblage in K1 with the propagation of the veins in the plagioclase; F- Zoom on the veins within the plagioclase and localization of the K1 FIB thin-section (Or is for orthoclase, Ab is for albite, Ol is for olivine, Opx is for

orthopyroxene, Amp is for amphibole, Mag is for magnetite, Ap is for apatite, Qx is for quartz, Prth is for perthite).

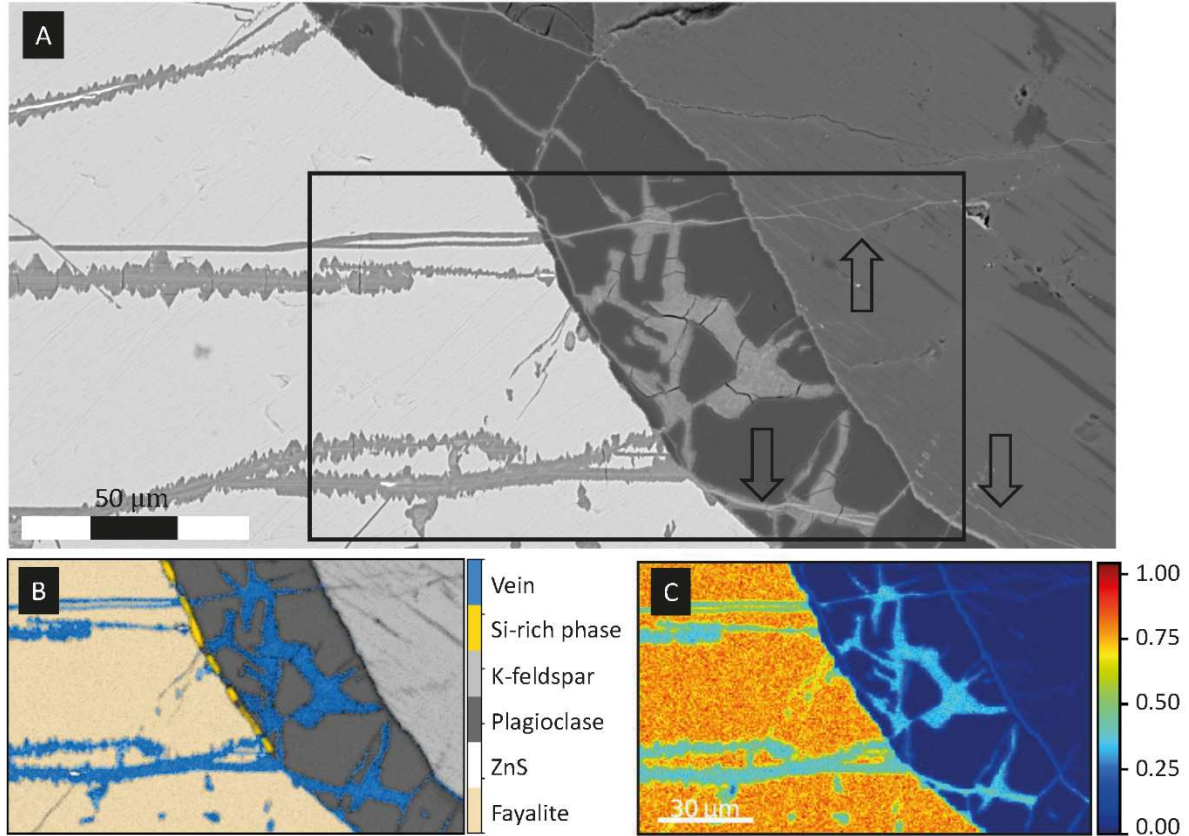


Figure 27: A- High-resolution SEM image of the olivine grain in the K2 sample and the propagation of the veins inside the rim and the mesostasis (see black arrows); B- Phase mapping (hyperspy) of the propagation of the veins; C- Mapping of the Fe/Si ratio signal, the color scale represents the ratio of the intensity of the X-ray signal, i.e., the number of counts.

Similar veins were observed in the K1 sample, showing orthopyroxenes and amphiboles in addition to quartz, iron oxides, and Fe – Si-rich minerals (Figure 28A and B). Due to the complex symplectic texture, it is difficult to assign these minerals to a specific part of the vein but what is striking is that these symplectites are limited to the fayalite and do not propagate to the other minerals. Some small iron oxides are also visible at the contact between fayalites and orthopyroxenes (Figure 28B).

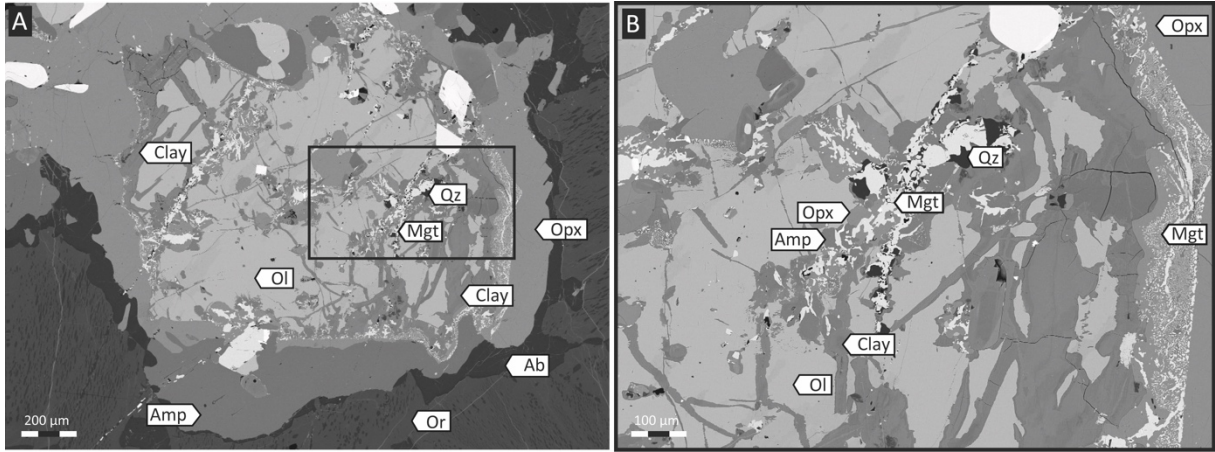


Figure 28: SEM images of the K1 sample, A- A fayalite crystal with its rim of mafic minerals (Opx and Amp) and plagioclase; B- A zoom on one vein inside the fayalite showing intergrowth of clay minerals, quartz, and iron oxide and mafic minerals such as amphibole and orthopyroxene, at the right of the image iron oxide can also be found at the border of the orthopyroxene.

Further investigations down to the nanoscale were conducted using STXM and TEM on FIB foils extracted from a vein hosted by a fayalite from the K2 sample and a vein hosted by a plagioclase from the K1 sample.

IV.iv.ii. Characterization at the sub-micrometer-scale

The spatially resolved STXM-XANES data collected over the FIB section extracted from a vein hosted by fayalite from the K2 sample (Figure 29A) reveal that the fayalite does not contain Fe^{3+} ($([\text{Fe}^{3+}]/\Sigma\text{Fe})=0.01\pm 0.02$) while the phases composing the veins contain more than 20% of Fe^{3+} , the external part of the vein in direct contact with the fayalite being richer in Fe^{3+} ($([\text{Fe}^{3+}]/\Sigma\text{Fe})=0.27\pm 0.02$) than the internal part ($([\text{Fe}^{3+}]/\Sigma\text{Fe})=0.19\pm 0.02$). Of note, the internal part of the vein is not homogeneous in terms of Fe^{3+} concentrations, with areas exhibiting $([\text{Fe}^{3+}]/\Sigma\text{Fe})$ values higher than 0.2 while other areas of the internal part only contain 15% of Fe^{3+} (Figure 29B and C).

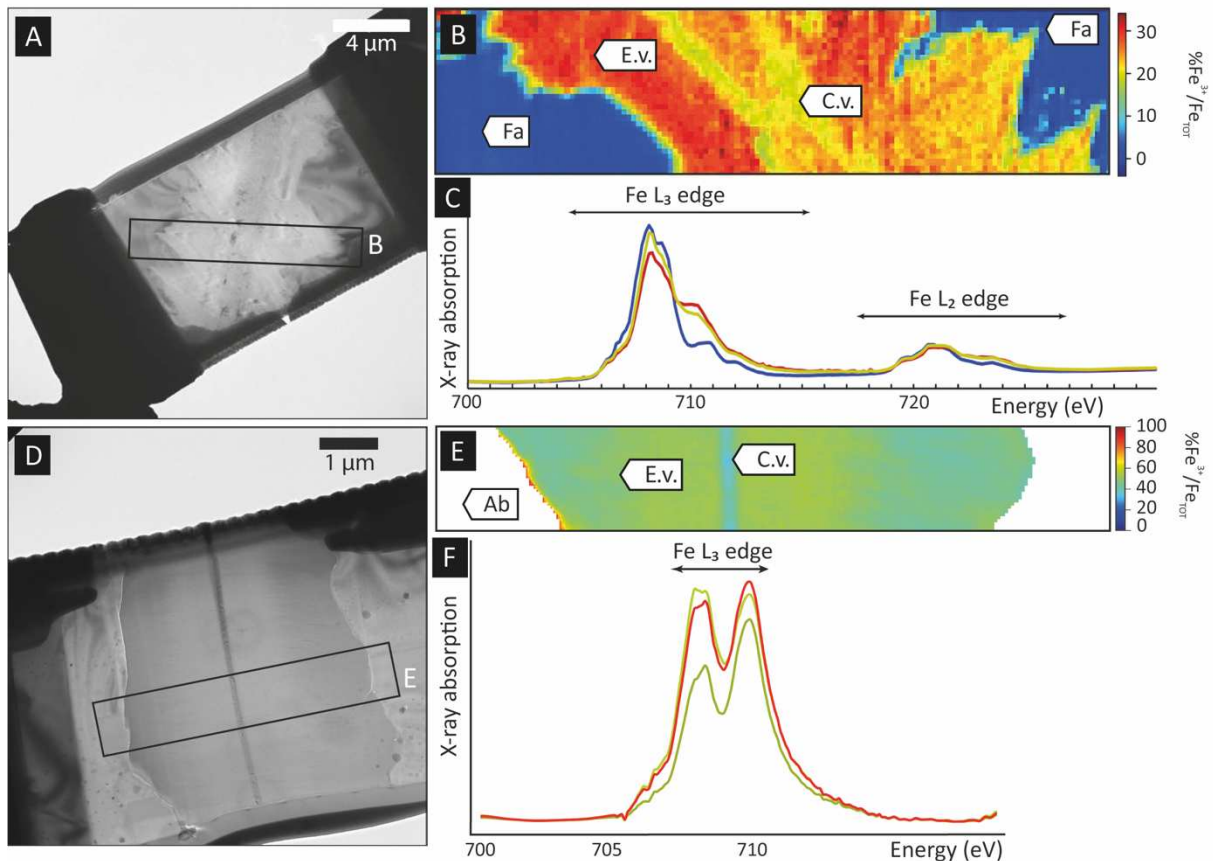


Figure 29: A- TEM image of the K2 FIB thin-section with the area mapped; B- Quantitative map of iron(III) in the K2 FIB thin section, each pixel corresponds to the percentage of iron(III) on total iron (Fa is for fayalite, E.v. is for external vein, C.v. is for central vein); C- Global X-ray absorption spectra for each part of the FIB thin section (blue spectra is for the fayalite, red spectra is for the external vein and green spectra is for the central vein), D- TEM image of the K1 FIB-thin section with the area mapped; E- Quantitative map of iron(III) in the K1 FIB thin-section (Ab is for albite, E.v. is for external vein, C.v. is for central vein); F- Global X-ray absorption spectra for each part of the area mapped (light green spectra is for the center of the vein, red spectra is for the border of the vein in direct contact with the plagioclase and dark green spectra is for the part between the border and the center mineral).

Spatially resolved STXM-XANES data were also collected on the FIB section extracted from a vein hosted by a plagioclase from the K1 sample (Figure 29D). The collected data reveal that the vein is not homogeneous in Fe^{3+} , with values of about 40% in the very central part (Figure 29E and F) while the remaining vein shows a gradient, with values close to 44% in the area in direct contact with the plagioclase and increasing up to 51% towards the center.

Further investigations were conducted using transmission electron microscopy (TEM), revealing that the veins are mostly made of phyllosilicates. Electron diffractions (SAED), high-resolution TEM and STEM images, as well as EDXS data, were collected to identify these

phases more precisely (Figure 30). The contact with the fayalite presents scalloped patterns typical of alteration fronts. The external part of the vein appears to be composed of two different parts displaying two distinct crystalline orientations (Figure 30A and Figure 30B). The clay minerals in direct contact with the fayalite were very unstable under the beam, but SAED patterns show d spacings of 7\AA , allowing their identification as serpentines sharing crystal orientations with the fayalite (Figure 30B b1). Conversely, the clay minerals composing the more internal part of the external vein appear well crystallized and exhibit d spacings of 14\AA , suggesting these are chlorites that also share crystal orientations with the fayalite (Figure 30B b2). These two parts of the external vein display similar Fe/Si values of 0.9 and exhibit 0.1 and 0.15 at% of potassium and calcium (Figure 30C), pinpointing the presence of interstratified chlorite/mica or chlorite/smectite, as also suggested by the ternary diagram shown on Figure 30D.

The internal part of the vein is heterogeneous but mostly composed of phyllosilicates which do not share crystal orientations with the fayalite (Figure 30B c). Some sheets are sub-circular and exhibit d spacings of 7\AA (Figure 30B c1). The SAED patterns correspond to a typical polycrystalline diffraction and show three well-distinguishable spots indicating d spacing of 2.5, 3.5, and 7\AA , and two more diffuse rings indicating d spacing of 2.5 and 4.5\AA , likely corresponding to the (001), (002), and $(2\bar{1}1)$ reflection of a serpentine, even though it could also correspond to chlorite. The internal part of the vein exhibits Fe/Si values of 1.2 and lower contents of Ca and K than the external part of the vein. As the external vein, the internal vein likely contains a mixture of possibly interstratified chlorite/smectite/mica and serpentine, as also suggested by the ternary diagram shown in Figure 30D. Unlike the contact between the external part of the vein and the fayalite, the contact between the internal and the external parts of the vein is sharp.

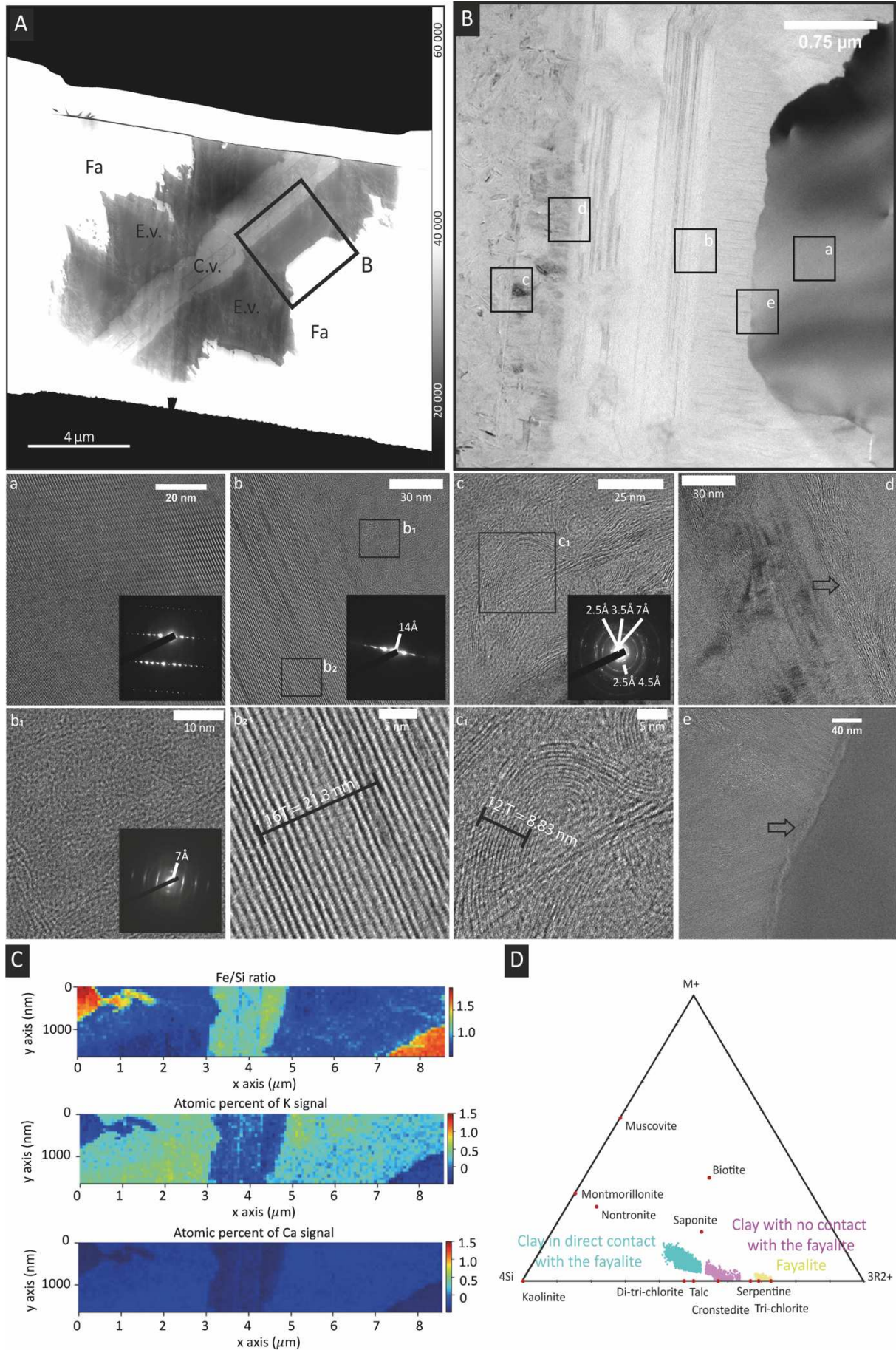


Figure 30: A- STEM image of the K2 FIB thin-section showing the multiple veins inside the fayalite. The black square is for the localization of the TEM image in B (Fa is for fayalite, C.v. is for central vein and E.v. is for external vein); B- TEM image of the filling of the vein with multiple zooms on areas of interest; a- TEM high-resolution image of the fayalite and its associated electron diffraction; b- TEM high-resolution image of the clay mineral in contact with the fayalite, its associated electron diffraction, and location of zooms b1 and b2 on the clay sheets; b1- Zoom on the clay mineral in direct contact with the fayalite; b2- Zoom on the well-crystallized sheets of the clay mineral in contact with the fayalite; c- TEM high-resolution image of the clay mineral with no direct contact with the fayalite and its associated electron diffraction and location of zoom c1; c1- Zoom on the sheets of the central clay mineral; d- TEM image of the contact between the two clay minerals; e- TEM image of the contact between the fayalite and the clay mineral; C- STEM-EDS maps of the Fe/Si ratio, atomic percent of K, and atomic percent of Ca of the clays going through the olivine (scale is in atomic percent); D- ($M+$; $4Si$; $3R2+$) ternary diagram representing the endmembers of clay minerals and the studied clay minerals in function of $M+$, the interlayer cationic charge, $3R2+$, the number of divalent cations in octahedral position and $4Si$, the amount of silica. It highlights the mixing of the phases between the chlorite, the smectite, and the serpentine endmembers.

TEM investigations reveal that the architecture of the vein varies between the ones hosted by the olivine and the one hosted by the plagioclase. The vein hosted by the plagioclase only exhibit the same central part as the one found in the olivine. The border part identified in direct contact with the olivine is not found in the plagioclase. Also the vein hosted by the feldspar does not show any alteration features at the contact with the host mineral (Figure 31). Figure 31B shows a TEM image of the straight contact between the clay mineral and the plagioclase with a typical SAED pattern for the plagioclase. The SAED pattern of the vein exhibits two sets of distinguishable hexagonal spots indicating distances of 2.6 and 4.6Å, matching with the $(\bar{1}11)$, $(1\bar{1}1)$, (020) and $(\bar{1}31)$, $(\bar{1}\bar{3}1)$, (200) reflexion of a clinocllore or a mica. Figure 31C C1 shows that crystallite expands over the very central part to the rest of the vein, highlighting that this very central part is made of the same phyllosilicates. These phyllosilicates exhibit variable orientations in the very central part of the vein (Figure 31C C1) but appear perpendicular to the contact with the plagioclase (Figure 31D). In addition, STEM-EDS maps reveal Fe/Si values from 1.0 for the main part of the vein to 1.2 for the very central part (Figure 31E). Gradients in potassium and calcium maps are visible from the border to the center, with high values at the border and in the very central part. The ternary diagram, is in Figure 31F, shows a gradual evolution of the composition of the clay minerals from the serpentine to the micas, passing by the chlorite endmembers. It highlights that this vein, within the plagioclase, is a complex mixing of phases.

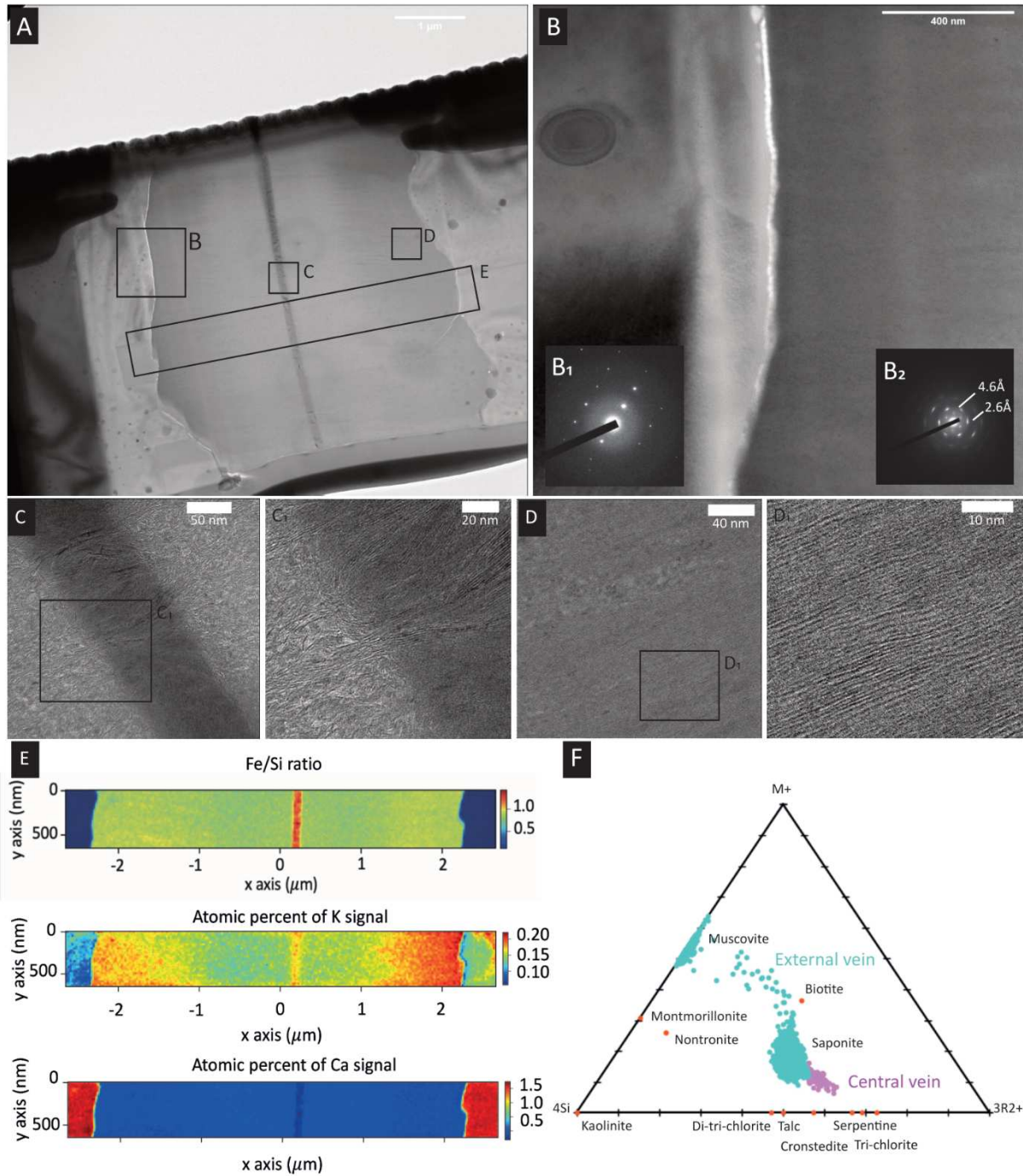


Figure 31: A- TEM image of K1 FIB thin-section; B- TEM image of the contact between the plagioclase and the vein; b1- the electron diffraction of the plagioclase; b2- The electron diffraction of the mineral filling the vein; C- HRTEM image of the center of the vein; C1- Zoom on the layers of the clay mineral filling the vein; D- HRTEM image of the border of the vein, D1- Zoom on the layers of the clay mineral that are in contact with the plagioclase; E- STEM-EDS maps of the Fe/Si ratio, the K and Ca contents (in atomic percent); F- ($M+$; $4Si$; $3R2+$) ternary diagram representing the endmembers of clay minerals and the studied clay minerals in function of $M+$, the interlayer cationic charge, $3R2+$, the number of divalent cations in octahedral position and $4Si$, the amount of silica. It highlights the mixing of the phases between the serpentine, the chlorite, and the micas endmembers.

IV.v. Discussion

IV.v.i. Mineralogy of K2 and K1 samples

Previous studies and drilling reports concluded that in Nemaha County, where the DR1-A well was drilled, the Precambrian basement was composed of granite, rhyolite, and metasediments (Bickford and al., 1981; Newell et al., 2007). The drilling report from 1999 described the part of the basement reached by the well as “*a mafic-rich and dark granite with little or no quartz*”. The present study concluded that the basement is closer to a monzo-gabbro. K1 and K2 samples contain mafic minerals such as fayalite, iron-rich pargasite, ferrosilite, and pigeonite dispersed within an albite and orthoclase mesostasis which does not contain any crystal of quartz. Mafic minerals have crystallized in aggregates and have a rim of albite. Pyroxene, located in contact with the fayalite, displays exsolution textures. The rest of the sample is composed of orthoclase with perthitic textures showing that orthoclase is set up in plagioclase. These textures indicate feldspars and pyroxenes have undergone a sub-solidus re-equilibration (Harlov et al., 1998, Putnis et al., 2007). This type of sub-solidus evolution is typical of plutonic rocks which undergo more or less slow cooling or have enough water, chlorine, and/or fluor to have a sufficiently low enough solidus. Indeed water, chlorine, and fluor induce changes in the properties of the magma (Filiberto and Treiman., 2009 a & b, Dalou et al., 2015). Altogether, the rock composing the Precambrian basement in that area has been produced following a classical sequence of crystallization with fayalite crystallizing first, followed by pyroxene, iron-rich pargasite, albite, and then orthoclase. The whole-rock analysis shown in the supplementary material (Supplementary table 1) confirms that this rock is a monzo-gabbro. Thus, the Precambrian basement reached by the DR1-A well at the depth of 442 and 450 meters is not a Precambrian granite as previously reported and although that well is located around 100 km east of the axis of the Mid-Rift System, we suggest that it reached an eastern and so-far unmapped extension of the rift.

IV.v.ii. Formation of the veins

Here we discuss the nature and origin of the veins crosscutting the olivines and the plagioclases in the samples investigated. The internal part of the veins hosted by the olivines is present within all the other minerals and is associated with iron oxides, apatites, and quartz, while the external part, in direct contact with the fayalite, was only observed within the olivines. While they present differences at the nanoscale, these veins have similarities with iddingsite, a mixture of hydrous silicates of iron(III) previously described in several publications (Ross, 1925; Edwards, 1938; Baker, 1967; Eggleton, 1984; Smith, 1987). Iddingsite mineralogical definition and conditions of formation have been highly debated over the last decades. It has been described as a light yellow to reddish brown mineral (Ross, 1925) and it is associated with both non-altered augites and feldspars (Ross, 1925 and Baker, 1967). The authors have shown that

iddingsite is found in fractures, inside the olivines, and that its formation allows for preserving the shape of olivine. Two hypotheses of formation have been formulated: 1) deuteric alteration of olivine by a residual magmatic liquid at high temperature; 2) post-deuteric (i.e., hydrothermal) alteration of olivine at intermediate to low-temperature conditions.

Deuteric alteration has been proposed by Ross (1925) and Edwards (1938) and described as the result of interactions between a residual magmatic liquid and previously formed minerals, resulting in the metasomatism replacement of olivine by iddingsite. Authors inferred that this process happened at the end of the cooling sequence, in the presence of a residual differentiated magma rich in water (and magmatic gas) responsible for iron oxidation (Edwards, 1938). In contrast, post-deuteric (e.g., hydrothermal) alteration was proposed as the source of iddingsite by Baker (1967), Eggleton (1984), and Smith (1987). Such intermediate to low-temperature alteration of olivine by an external oxidizing fluid circulating throughout the rock may lead to the formation of more or less interstratified chlorite, smectite, and goethite (Baker, 1967, Eggleton, 1984). Interstratification seems to be controlled by the temperature, with high to intermediate temperature giving chlorite and then decreasing temperature giving a mix of chlorite, smectite, and then goethite. The temperature of formation is easily constrained because goethite is only stable under 140°C (Eggleton et al., 1984). It seems more complicated to constrain chlorite formation as its range of formation goes from magmatic temperature (Viennet et al., 2020, 2021) to several hundred degrees (Baker, 1967). In this iddingsite definition, the system is marked by a loss of silica and magnesium, but iron, which is being oxidized, and manganese are preserved.

Here, the most likely scenario involves deuteric alteration (Figure 32). The veins have been produced via the direct precipitation of a late, differentiated magmatic fluid having been exsolved during the crystallization of the K-feldspars as perthites. In fact, in a scenario involving an external hydrothermal fluid having circulated within the rock, the K-feldspars would show some evidence of alteration, which is not the case here. Plus, the internal part of the veins is composed of interstratified chlorite/smectite/mica mixed with serpentine, iron-oxide, apatite, and quartz (Figure 32B), which are mineral phases typical of what could produce a residual, differentiated magma close to a granitic composition (Mas et al., 2008). Such residual magma, likely obtained during the crystallization of K-feldspars, has penetrated within the fractures of previously formed mafic minerals and plagioclases. This magmatic fluid being chemically far from equilibrium with the fayalite, was responsible for its deuteric alteration, producing the external parts of the veins (Figure 32C). The first phase replacing the fayalite must have been the interstratified chlorite-smectite. At some point, with the decreasing temperature, the alteration of the fayalite led to the production of serpentine intimately mixed with smectites (Figure 32D). Such production of Fe-rich clay minerals via the deuteric alteration of olivine is supported by the recent study of De Pasquale and Jenkins (2023), having

shown that a mixture of fayalite and more differentiated phases such as iron oxide, albite, quartz, and magnetite exposed to a decreasing temperature in the presence of water leads to the production of Fe-rich smectites.

Of note, the clay minerals composing the internal vein hosted by olivines and the veins hosted by plagioclases exhibit spatially variable Fe contents and ratios of $\text{Fe}^{2+}/\text{Fe}^{3+}$. Similar variations have been described by Meunier et al. (2008, 2012) for masses of magmatic Fe-rich saponites and chlorites found in basalts from the Mururoa Atoll (French Polynesia). These authors interpreted the Fe-zoning of these clay minerals, which crystallized at the end of the cooling stage of the basaltic bodies, as resulting from variations of iron availability in the residual magmatic fluid. Indeed, the authors propose that during the cooling state, the composition of the magma changes with increasing crystallization ratio so the composition of the residual magmatic liquid yielding the clay minerals varies. In addition, during the precipitation of the residual liquid, some elements are depleted because they are solubilized or because they are consumed by the crystallizing minerals, leading to the zoning observed. A similar explanation can be proposed here to explain the observed variations in Fe/Si values and Fe^{3+} concentrations.

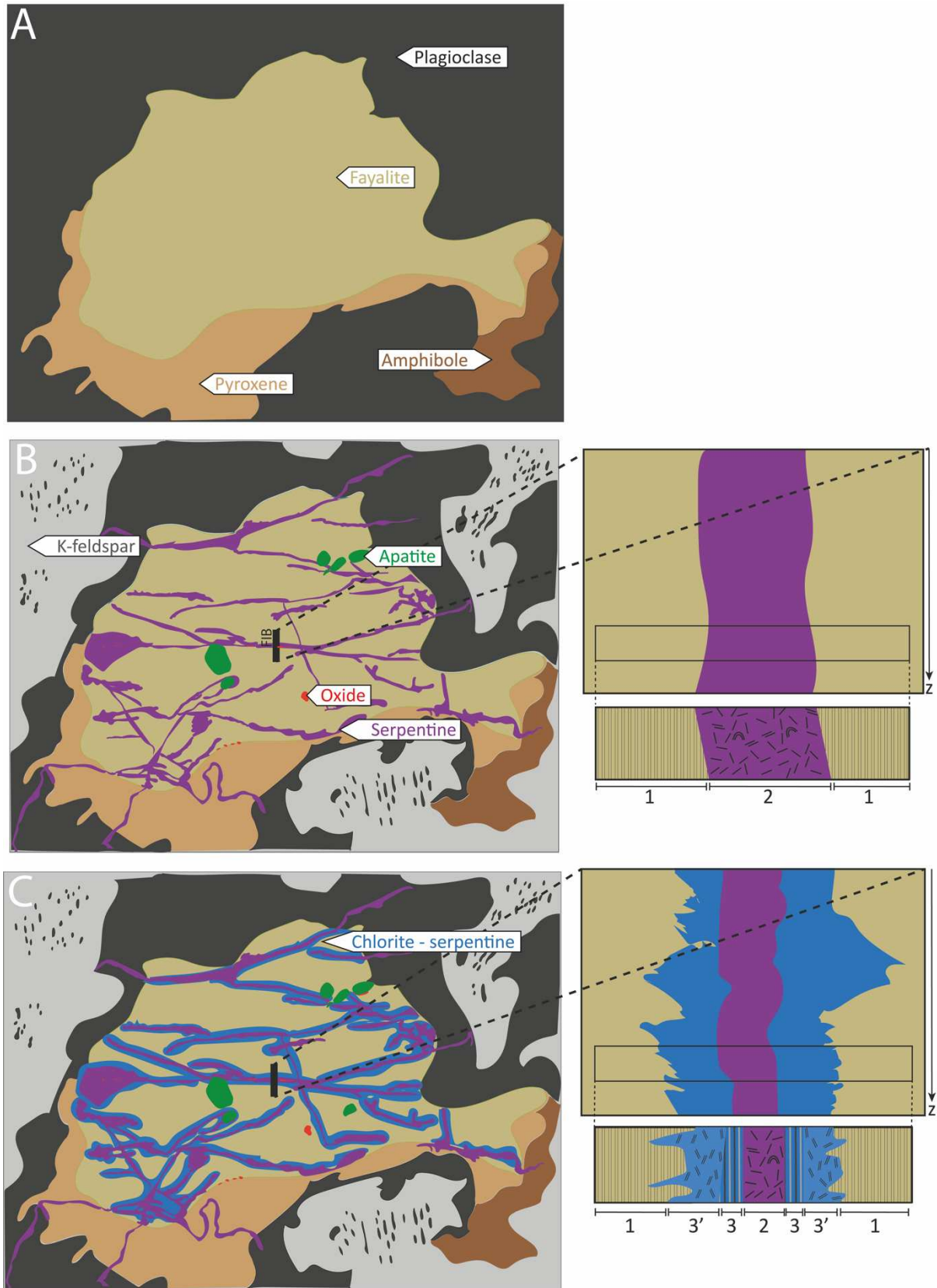


Figure 32: Synthesis sketches of the crystallization sequence in the K1 and K2 samples and zooms on veins formation; A- Fayalite, pyroxene, amphibole, and plagioclase in rims around the mafic minerals; B- Circulation of a differentiated residual liquid which give perthites of K-feldspars and leads to the

crystallization of the center serpentine and the exsolution of water. Apatite and iron oxides also crystallize at that time. The serpentine is cross cutting every previous mineral. Associated are zoom and sketches of the filling of the vein (1 is for fayalite crystallization and 2 for serpentine crystallization); C-Deuteric alteration of the fayalite by the exsolved water leading to the crystallization of the chlorite and then of the serpentine in direct contact with the fayalite while the temperature is decreasing. These two clay minerals are only found in fayalite. Associated are zoom and sketches of the filling of the vein (1 is for fayalite crystallization, 2 for serpentine crystallization, 3 for chlorite crystallization, and 3' for serpentine of the border vein crystallization).

IV.v.iii. **Generation of hydrogen**

Determining the chronology of crystallization of these iron-rich chlorite and serpentine is of prime importance in discussing the possible role that they played in the production of molecular hydrogen. It can be conceived that H₂ was originally present in the magma and that the residual magmatic liquid from which the veins have precipitated was thus enriched in H₂. Indeed, H₂ in magmatic system has been well described (Fischer and Chiodini., 2015). The crystallizing phyllosilicates should then be considered as an H₂ reservoir in these rocks.

Alternatively, or concurrently, it can be assumed that the deuteric alteration of olivine, responsible for the precipitation of the external part of the veins hosted by the olivines, has directly produced H₂, through a reaction similar to the following: $2\text{Fe}^{2+}\text{O} + \text{H}_2\text{O} \rightarrow \text{Fe}^{3+}_2\text{O}_3 + \text{H}_2$

Indeed, previous literature on deuteric alteration (Ross., 1925; Edwards., 1938) describe such event involving late magmatic fluids as oxidizing which and may allow to produce H₂. Igneous differentiation of iron-rich magma has been described in basalt-hawaiite bodies from the Mururoa Atoll (Mas et al., 2008) but also in nakhlites (Viennet et al., 2021). Although such systems present differences in their mineralogical compositions and origins, they are iron-rich, and their similar Fe-rich mineral phases resulting from alteration have been described to originate from oxidation due to late magmatic fluids.

Both hypotheses involve magmatic processes, implying that the generation of H₂ occurred during the formation of the rock, i.e., not recently (the basement of this intracratonic area does not exceed 60°C at present - Newell et al., 2007). Therefore, from the material studied here, H₂ could be considered partly as a “fossil” volatile. The measurements of H₂ during the last decades (Coveney et al., 1987; Newell et al., 2007; Guélard et al., 2017) suggest that H₂ has been stored in these rocks in some way, either as fluid inclusions or within the structure of clay minerals. Malaspina and co-authors (2023) have also recently demonstrated that molecular H₂ could be stored in inclusions within olivine under high pressure conditions. Truche et al. (2018)

have indeed demonstrated that H₂ could be stored in nanopores of chlorites thanks to adsorption mechanisms. This could also be the case here, potentially making the clay minerals studied here the reservoir of H₂ if not both the source and the reservoir of H₂. In this scenario, H₂ could have reached the well thanks to the concurrent presence of faults, fractures, and aquifers within the basement. The H₂ emitting wells are artesian wells so water is, indeed, circulating through these basement rocks and could have allowed for the mobilization of H₂.

However, H₂ production at the well head in Kansas was shown to be a regional trend and to be characterized by a continuous flux of gas by Guélard and co-authors (2017). We, therefore, do not exclude that other processes such as current and low-temperature oxidation of iron could take place in other rocks (not reached by available wells) of the Kansas basement making hydrogen generation and migration a contemporaneous and active process. Iron oxidation reactions occurring within the 350 meters of Paleozoic sedimentary rocks are also not to be excluded. We propose here a first scenario of H₂ generation linked to a late magmatic event but H₂ being currently produced at the surface and being characterized by a regional flux, we strongly recommend considering H₂ in Kansas the product of multiple reactions that still must be clearly established.

IV.vi. Conclusion

Part of the northeastern Kansas Precambrian basement is composed of iron-rich monzogabbros, such as the mafic rocks of the Mid-Rift System located further west. Iron in these rocks is present in the form of ferrous iron in fayalites, but also in iron-rich pargasites, ferrosilites, and pigeonites. These rocks contain veins of Fe-rich clay minerals, composed of a nanoscale mixture of chlorite, smectite, mica, and serpentine, likely produced via the direct precipitation of a late, differentiated magmatic fluid. Because this magmatic fluid was chemically far from equilibrium with the fayalite, it has been responsible for its deuteric alteration, producing the external parts of the veins and possibly generating H₂ which was, in turn, stored within the clay minerals composing the veins. Identifying the mineral environment in which H₂ was generated, as well as the lithology in which it is stored, provides key information for future natural hydrogen exploration, by allowing targeting specific areas. In this perspective, intracratonic settings rich in iron-rich phyllosilicates appear to be excellent candidates for hydrogen generation.

IV.vii. **Appendix A. Supplementary Material**

The supplementary material consists of the whole-rock chemistry data of the K2 sample (in weight percent).

		SiO ₂ %	Al ₂ O ₃ %	Fe ₂ O ₃ %	MnO %	MgO %	CaO %	Na ₂ O %	K ₂ O %	TiO ₂ %	P ₂ O ₅ %	Total %
ICP-OES iCap6500 (ox.%)	K2	56.32	16.38	9.90	0.30	0.90	4.01	4.09	5.44	1.33	0.43	98.82
Uncertainties (%) in the function of the concentration	>10 %	<2%	<2%	<2%			<2%		<5%	<5%	<5%	
	>5 %		<10%			<2%			<5%	<10%	<10%	<5%
	>1 %		<15%	<10%	<5%	<10%			<10%	<10%	<10%	<5%
	>0.5 %	<10%		<15%	<15%	<15%	<15%	<15%	<20%	<20%	<20%	<15%
	>0.1 %	<20%	<20%									**
	>0.05 %	**	**	<20%	<20%	<20%	<25%	<25%	<25%	<25%	<25%	
>0.01 %			**	**	**	**	**	**	**	**		
Detection limit	L.D. %	0.05	0.04	0.015	0.015	0.03	0.03	0.02	0.03	0.02	0.10	

Supplementary table 1: Whole-rock chemistry data of the K2 sample (in weight percent)

V. Conclusion of the chapter

The mineralogical study of the DR1-A well samples showed the basement rocks are iron-rich monzo-gabbros with fayalite, iron-rich orthopyroxene, and iron-rich amphibole, and present an increase in the alteration features when going closer to the basement top. The focus was made on the deepest samples K1 and K2 which show potential alteration features with the presence of iddingsite as veins within the iron-rich olivines and iron oxides but also show the initial mafic minerals still well preserved.

Indeed, these samples present a unique opportunity to look at, and understand, the link between the primary minerals and the iddingsite. A high-resolution microscopy workflow help to identify the iddingsite as two different phases: 1) the central vein being made of a nanometric mix of Fe²⁺-serpentine, chlorite, and mica; 2) the border vein being made of one part in contact with the central vein and made of Fe³⁺-smectite, and one part in direct contact with the fayalite and being made of Fe³⁺-serpentine.

We infer the central vein formed by precipitation of a late magmatic fluid enriched in ferrous iron resulting in a mixture of phyllosilicates and resulting in the exsolution of water thus in direct contact with the already crystallized fayalite. We believe this water induced a disequilibrium state and the deuteric alteration of the fayalite leading to iron oxidation, crystallization of the Fe³⁺-rich clay minerals phases, and potential H₂ generation. As such an event could have only happened at the end of a magmatic episode, in the late Precambrian times, we believe the H₂ potentially generated must have been trapped in the clay minerals structure or in fluid inclusions.

The following samples show veins of what seem to be different clay minerals as they have different characteristics in optical microscopy. They are also associated with veins of carbonates which attests to a new alteration event that we believe is posterior to the iddingsite formation

within the fayalite-bearing monzo-gabbros. At the basin or regional scale, it seems correct to imagine that fluids circulated within the monzo-gabbros and led to their alteration. A more complete discussion of all the samples and their implications in hydrogen generation will be presented in Chapter 8.

CHAPTER VI. Mass transfer study of a fayalite-bearing gabbro from the Kansas Precambrian basement (USA) and implications for natural hydrogen generation

This chapter is based on the multimodal and multiscale workflow used to quantify the amount of H_2 generated by iron oxidation within the fayalite-bearing monzo-gabbros of the Kansas Precambrian basement (USA). EPMA analysis on the K2 sample has been performed and data have been processed using the XMapTools 4.1 package. By using Gresen's equations, the masses of elements transferred during three potential mineral replacement reactions were calculated: 1) orthopyroxene replacements by amphibole, 2) olivine replacement by serpentine, 3) a simultaneous replacement of olivine and orthopyroxene by amphibole and serpentine. By assuming anoxic conditions and by coupling the amount of ferric iron or ferrous iron to the volumes of minerals acquired with μ CT, the amounts of hydrogen generated were determined for each reaction.

Ce chapitre est basé sur la méthodologie développée pour quantifier l'hydrogène généré lors de l'oxydation du fer présent dans les monzo-gabbros à fayalite du socle Précambrien du Kansas (USA). Des données de microsonde ont été acquises et traitées avec le logiciel XMapTools 4.1. Les équations de Gresens ont ensuite permis de calculer les masses d'éléments transférés lors de trois réactions de remplacement minéralogiques : 1) l'orthopyroxene remplacé par l'amphibole, 2) l'olivine remplacée par la serpentine, 3) un remplacement simultané de l'olivine et de l'orthopyroxene par l'amphibole et la serpentine. En assumant que les conditions étaient anoxiques, et en couplant les masses de fer ferrique et ferreux aux volumes de chaque minéral obtenu par μ CT, les quantités d' H_2 générées peuvent être calculées.

I. Introduction of the chapter

The K2 sample was previously studied by using high-resolution microscopy techniques. It allowed for characterizing, down to the nanometric scale, the fayalite, the other mafic minerals, and the iron-rich clay minerals, as well as their textural relationships and chemical compositions. This study allowed proposing a scenario of clay-minerals formation and potential hydrogen generation. The aim of this chapter and this second study on the K2 sample is to propose a quantification of the hydrogen generated. To perform such quantification, quantitative EPMA analysis was performed and coupled to a mass of element transfer calculation. μ CT data were acquired and give the volumes of the minerals considered for hydrogen generation. Coupled together such data give a first-order number of hydrogen generated.

II. Mass transfer study of a fayalite-bearing gabbro from the Kansas Precambrian basement (USA) and implications for natural hydrogen generation

Valentine Combaudon^{*1,2}, Stephen Centrella², Kanchana Kularatne^{2,3}, Olivier Sissmann¹, Pascale Sénéchal³, Eric Deville¹ and Hannelore Derluyn^{2,3}

1: IFPEN, Rueil-Malmaison, France ; 2: Université de Pau et des Pays de l'Adour, E2S UPPA, CNRS, TotalEnergies, LFCR, Pau, France ; 3 : Université de Pau et des Pays de l'Adour, E2S UPPA, CNRS, DMEX, Pau, France

II.i. Abstract

Natural H₂ has been discovered in wells drilled into the Precambrian basement of Kansas, USA, since the early 1980s. A significant amount of this natural H₂ is believed to be generated via fluid-rock interactions leading to the oxidation of Fe²⁺ in mafic minerals. However, petrological studies addressing the mechanisms and quantities of natural H₂ generation in intracratonic settings including Kansas are lacking. We estimated the natural H₂ that has been generated via Fe²⁺ oxidation within fayalite-bearing gabbros in the Precambrian basement of Kansas, using an electron microprobe micro-analyzer (EPMA) based quantitative petrological method. Three reactions were identified altering the original gabbro mineral assemblage: (1) Orthopyroxene + aqueous fluid → Amphibole + H₂; (2) Olivine + aqueous fluid → serpentine + H₂; (3) olivine + orthopyroxene + aqueous fluid → amphibole + serpentine + H₂. Assuming each reaction takes place in an open system (no mass preservation), we calculated the mass transfer associated with each specific reaction by coupling compositional maps to a mass balance equation (Gresens., 1967). The results show that each system loses Fe²⁺ while gaining Fe³⁺ and H₂O which is coherent with natural H₂ generation via the redox reaction between Fe²⁺ and water. These reactions proceed with an overall decrease in density (6 to 37.5%), and an

overall gain in volume (3.7 to 20.7 vol.%). For the reaction of orthopyroxene to amphibole, the reaction produces potentially 41.73 to 378.21 mol of H₂/ ton of rock; 11.18 to 130.36 mol of H₂/ ton of rock for olivine to serpentine, and 93.34 to 452.16 mol of H₂/ ton of rock for the Olivine + Orthopyroxene to amphibole + serpentine. Mass balance calculation shows that masses of elements behave the same way during reaction (1) and reaction (2) above. These results support a potential single fluid event with a reducing fluid. Natural H₂ exploration in intracratonic settings is currently at its early stages and this study brings new insights into understanding the mechanisms and quantities of natural H₂ generation in the intracratonic settings.

Keywords: hydrogen, mass transfer, fluid-mediated reaction, mineral replacement, redox conditions

Highlights:

- Mineral replacement reactions are identified within a fayalite-bearing monzo-gabbro of the Kansas Precambrian basement (USA).
- A mass balance calculation shows the system is losing Fe²⁺ and gaining Fe³⁺ and H₂O.
- The amount of hydrogen generated can be calculated, the values are one order below the values found in the literature.

II.ii. Introduction

In the scope of climate change, dihydrogen, also called natural hydrogen, if considered as an energy source could be a game changer as its consumption does not generate carbon dioxide. Natural hydrogen emissions have been studied for decades at plate boundaries, especially in the Mid Oceanic Ridges (MOR) (Moody., 1976, Campbell., 1988, Charlou et al., 1996 amongst others). The location of such emissions, at thousands of meters deep in the middle of the ocean, and hundreds of kilometers from the energy market, prevented the exploitation of this hydrogen. However, similar emissions have been recorded for decades in the middle of continents in Australia (Ward., 1933, Frery et al., 2021), Russia (Larin et al., 2014), or Mali (Prinzhofer et al., 2018) but as the research was mainly focused on serpentinization at the MOR, the origin(s) and quantification of this intracratonic gas are not well described.

Previous studies have shown that Kansas (USA) is the location of such natural hydrogen emissions (Coveney et al., 1987, Newell et al., 2007, Guélard et al., 2017). Guélard and co-authors (2017) showed this hydrogen has a deep-seated origin and is linked to iron oxidation.

Indeed, the Kansas Precambrian basement is rich in fayalite-bearing gabbros, which bear Fe³⁺ and Fe²⁺-rich clay minerals considered as potential H₂ generation markers (Combaudon et al., 2023, submitted in *Lithos*). Those minerals were differentiated into two generations: the first one was characterized as a Fe²⁺-rich mixing of serpentine, chlorite, and mica, and the second one as a Fe³⁺-rich interstratified chlorite-smectite and a Fe³⁺-rich serpentine in direct contact with the fayalite. Microtextures of the second iron-rich clay minerals assemblage suggested a mineral replacement by deuteric alteration of the fayalite. Fe-rich amphiboles were also identified in direct contact with Fe-rich orthopyroxenes, which are forming coronas around the fayalites, and thus testify for a fluid-mediated reaction potentially inducing compositional changes and potential H₂ generation.

In a more general aspect, fluid-mediated reaction (rock hydration) leading to mineral replacement is a major geochemical alteration process in the Earth's crust. When a fluid or an aqueous solution are circulating through the rock it can generate chemical disequilibrium conditions between the minerals of the rock and the fluid (Putnis et al., 2010). This can lead to mineral replacement in different ways: deuteric alteration, leaching, metasomatism, cation exchange, or pseudomorphism (Putnis et al., 2002). Mineral replacement always involves a fluid input and in every case, one mineral (or an assemblage of minerals) is replaced by one or more minerals to reach the thermodynamic stability. The mineral replacement is controlled by (i) a coupled dissolution-precipitation mechanism (Putnis et al., 2002) or (ii) by a pressure solution mechanism (Merino and Canals 2011). The reaction is associated with solid volume change and mass transfer in both cases. The dissolution of the parent mineral generates porosity, a key parameter in mineral replacement as this latter allows the fluid to access the reaction front. The interface between the dissolution of the parent mineral and the precipitation of the second mineral is also a key parameter to identify this kind of reaction. This interface is sharp, and it controls the mineral replacement as one part can be dissolved while another can be the location of precipitation. Thus, mineral replacement by dissolution-precipitation is a spatially heterogeneous process (Putnis et al., 2002). Mineral replacement often results in the preservation of the parent crystal shape i.e., pseudomorphism, because the dissolution rate is often the same as the precipitation rate (Maliva and Siever, 1988). In certain cases, even the crystal structure is preserved during mineral replacement, as it is the case during cation exchange (Putnis et al., 2002). In some cases, the shape of the parent structure is not preserved (Serpentinization, Plummer et al., 2012; soil weathering, Wilson., 2004). As a general concept, hydration reactions are often associated with a reduction of rock density (during sodium sulfate hydration, Flatt., 2002, during serpentinization, Toft et al., 1990). If the mass is preserved, then the solid has to expand. This expansion can be represented by the generation of stress in the system as a fracture (Plummer et al., 2012). If the mass is not preserved, then the previous model doesn't have to be applied. Using the example of the reaction of periclase (MgO) to

brucite ($\text{Mg}(\text{OH})_2$), (Carmichael, 1987) attested that even if the solid density decreases, the overall volume of the solid is maintained. This implies that the stress generated by the density reduction has to be compensated. Conclusions were that the induced stress would be dissipated by mass transfer to maintain the overall volume of the solid and minimize the stress fields.

As mineral replacement reactions are driven by the circulation of a fluid or an aqueous solution, it implies that the system, at least at the grain scale, is open and that mass transfer of material from the reaction area can happen (Putnis et al., 2010). It raises two important questions: what is happening within the system in terms of element transfer? What are the mechanisms driving the reaction? Is it a change in pressure and temperature inducing a change in the mineralogy or is it the infiltration of a fluid inducing a disequilibrium state?

An easy way to provide an answer is to look at microstructural textures and interfaces between minerals of interest. Several studies have shown that replacement reactions driven by a fluid-induced compositional change lead to coronas of new minerals forming around the parent mineral (Putnis et al., 2010). The other questions can be resolved by performing a mass balance evaluation at the thin-section scale, in order to better constrain the element mass redistribution within the sample and to better characterize specific reactions using element mass behavior to estimate the associated fluid redox conditions and the behavior of the solid (compaction or expansion).

In the specific case of hydrogen generation, looking at mineral replacement driven by a fluid-induced compositional change allows for studying and quantifying potential iron oxidation. Thus, performing a mass balance evaluation is a way to quantify the evolution of elements and redox conditions. If we associate this evaluation with the quantification of volumes of minerals done by micro-computed X-ray tomography (μCT), we can *in fine* determine the element transfer in 3D, at the rock scale, and estimate the generation of H_2 per unit volume of rock.

In this paper, we used the approach of Centrella and co-authors (2015) by coupling compositional maps to a mass balance equation (Gresens 1967) to get a better insight into the hydration reaction of the fayalite-bearing monzo-gabbro from the Kansas Precambrian basement. The aim of this study is to show that mineral replacement within this sample induces a density change, an input of water, and significant transfers of elements within the system. We also aim to show that when volumes are considered, these reactions induce much lower solid volume variations as previously described in the literature considering mass preservation. Finally, we discuss the potential of these fluid-mediated reactions for natural hydrogen generation by quantifying the amount of gas generated.

II.i. Geological context

Our study focused on the Precambrian basement of Kansas (USA), near the Mid-Rift System. The basement is mostly composed of granitic rocks. Authors distinguish the North and the South terranes. U-Pb on zircons and Rb-Sr dating performed on granitic samples belonging to the South terranes gave an age of 1.626 Ga. They are described as deformed granite composed of quartz, plagioclase, microcline, and biotite with secondary minerals such as zircon, apatite, and magnetite, originating from igneous rocks (Bickford et al., 1981). Van Schmus et al. (1993) also described the northern Kansas basement as granitic terranes whose ages ranged from 1.579 to 1.649 Ga, but some younger granite bodies intruded into this basement have also been described in north-eastern Kansas and have been dated around 1.34 Ga. The origin of these Precambrian granitic terranes is still being discussed but they could have originated from accreting arc-crustal elements or could be the results of extensional tectonics and crustal block remodeling. Conversely to the granitic basement, the Mid-Rift system is well known and is considered to be an aborted Precambrian continental rift whose formation started more than 1.1 Ga ago within the North American craton and is extended along more than 1000 km from Kansas to Lake Superior province (Woelk et al., 1991). Based on the work of Ojakangas et al., (2001), we know the rift-related rocks are composed of a lower volcanic syn-rift sequence in which 90% of the rocks are known to be flood basalt and 10% to be rhyolite. On top of this syn-rift sequence, is the post-rift subsidence phase characterized by a clastic sedimentary sequence (Ojakangas et al., 2011). A recent study shows that rocks belonging to the Mid-Rift system can be found east of the well-planned portion of the rift, above the Nemaha High (Combaudon et al., 2023, submitted in *Lithos*).

Wells in this area have been emitting gas and the first studies measured an average of 29-35 mol% of natural hydrogen (Coveney et al., 1986), highlighting a persistent regional flux. The gas is always associated with N₂ and He, and occasionally with CH₄. A more recent study has shown similar gas composition up to 92 mol% of H₂ (Guélard et al., 2017). Associated noble gas and water analyses showed that the gas has a deep crustal origin associated with water reduction and iron oxidation. H₂ emitting wells are located above the Nemaha high and are aligned along the Humboldt crustal fault, about ten kilometers east of the well-planned portion of the MRS (**Erreur ! Source du renvoi introuvable.**). The last tectonic event is a compressional one from the Pennsylvanian (300 Ma) making Kansas a relatively inactive geological area. Only microseismicity has been recorded along the Humboldt crustal fault (Steeple et al., 1979).

II.ii. Material and methods

II.ii.i. Petrology

The K2 sample belongs to the DR1-A well and is located at a depth of 450 meters within the Kansas (USA) Precambrian basement. The sample has been described as a fayalite-bearing gabbro, it contains fayalite, iron-rich pyroxenes, amphiboles, orthoclases, and albites. Iddingsite has been described as associated with the mafic minerals. Quartz, iron oxide, and apatite are described as veins and are also associated with these iddingsite and mafic minerals (Combaudon et al., 2023, submitted in *Lithos*). The volume of each mineral has been quantified by image processing of X-ray micro-tomographic scans as described in Kularatne et al (2023, *in prep*). They worked on a cylinder with a diameter of 8.75 mm and a height of 16.76 mm that was drilled in a representative zone of the K2 sample. The volume of the cylinder is approximately 1.00 cm³. Volume fractions of 81.51, 11.38, 5.31, 1.30, and 0.50 vol.% were found respectively for feldspars, pyroxene, amphibole, fayalite, and oxide.

II.ii.ii. Electron probe microanalyzer (EPMA)

Based on the X-ray scan of the full cylinder, the cylinder was cut along the shortest length to expose a surface containing all characteristic minerals of the K2 sample. This surface was subsequently polished using a diamond polishing paste of decreasing grit sizes 1 µm, 0.25 µm, and 0.03 µm. The polished surface of the cylinder was first studied by scanning electron microscopy (SEM) using a MEBFEG JEOL JSM 7100F instrument operated at an accelerating voltage of 15 keV and an accelerating voltage of 48 nA, at the Centre Castaing (Toulouse, France). SEM-BSE analysis and SEM-EDS element distribution maps allowed choosing an area of interest (4 mm²) with typical mineral assemblage present in the gabbro sample for further study using EPMA. Data acquisition was performed using a CAMECA SXFive instrument operated at 15 keV and 48 nA. Ten elements were analyzed for standardization: Na, Mg, Al, Si, K, Ca, Ti, Fe, Mn, and Ba using a beam size of 2 nm and 0.125 dwell time. Six profiles were obtained so that the profiles intersect every mineral phase in the chosen area. Each profile approximately contained ~ 50 spots. This measurement served as the internal standard to generate compositional maps. External standards were used: dolomite for magnesium, calcite for calcium, tephroide for manganese, and siderite for iron. The quantitative data processing was performed using the XMapTools 4.1 package (Lanari et al., 2014, 2019). The spatial and chemical resolution of the quantitative maps and the detailed internal standardization procedures are given by Lanari et al. (2018). As an electron probe microanalyzer does not allow for differentiating the ferric and ferrous iron contents, the estimation of the FeO and Fe₂O₃ contents of amphibole was performed based on Leake (1997).

II.ii.iii. Method of mass transfer calculation

The mass balance equation used, from Gresens (1967), allows to estimate element mobility, particularly to quantify gains and losses of elements of interest, during a fluid-mediated rock transformation with a homogeneous fluid phase.

(Equation 12 is used for the case of two minerals and n components, but it can also be used for a more complex assemblage of minerals:

$$\text{(Equation 11): } f_v \left(\frac{d_{\text{mineral 2}}}{d_{\text{mineral 1}}} \right) c_n^{\text{mineral 2}} - c_n^{\text{mineral 1}} = x_n$$

f_v is the volume factor, which can be related to the solid volume variation ($f_v = 1$ means no volume variation, $f_v < 1$ means the volume is decreasing, $f_v > 1$ means the volume is increasing), d_{mineral} is the density of the mineral considered, $c_n^{\text{mineral 1}}$ is the weight fraction of component n in the mineral of interest, and x_n is the gain or the loss for each component in gram per 100g of the initial mineral. Positive values correspond to a gain of mass while negative values correspond to a loss of mass through the fluid phase.

Mineral densities (d) were calculated on the basis of a linear combination of end members assuming an ideal solid solution between each end-member of a mineral (Equation 12, mineral n, with density d_n and weight fractions x_n) (Centrella et al. 2018).

$$\text{(Equation 12): } d = \sum_{i=1}^n [(d_1 \times x_1) + \dots + (d_n \times x_n)]$$

Olivine density has been estimated based on a linear combination between fayalite [Fe_2SiO_4], forsterite [Mg_2SiO_4], and tephroite [Mn_2SiO_4] with respective densities of 4.39, 3.27, and 4.25 g.cm^{-3} (Birle et al., 1968). Based on compositional maps, olivine density is estimated at around 4.32 g.cm^{-3} . Orthopyroxene density has been estimated based on a linear combination between enstatite ($[\text{Mg}_2\text{Si}_2\text{O}_6]$ – Carlson et al., 1988) and ferrosilite ($[\text{Fe}_2\text{Si}_2\text{O}_6]$ – Burnham et al., 1971), with respective densities of 3.20 and 3.95 g.cm^{-3} . Based on the acquired compositional maps, orthopyroxene density is estimated to be around 3.81 g.cm^{-3} . Amphibole solid solutions are more complex, and it can be difficult to estimate their correct density. Based on compositional maps, amphibole density is estimated at around 3.58 g.cm^{-3} based on the nomenclature of Leake 1978. Amphibole is defined as a hastingsite thanks to Deer et al., 2013. Serpentine density has been estimated based on a linear combination between lizardite ($[\text{Mg}_3\text{Si}_2\text{O}_5(\text{OH})_4]$, 2.57 g.cm^{-3} – Mellini et al., 1982), greenalite ($[\text{Fe}^{3+}, \text{Fe}^{2+}]_{2-3}\text{Si}_2\text{O}_5(\text{OH})_4]$, 3 g.cm^{-3} – Shirozu et al., 1965), and cronstedtite ($[\text{Fe}^{2+}_2 \text{Fe}^{3+}_2\text{Si}_2\text{O}_5(\text{OH})_4]$, 3.59 g.cm^{-3} – Hendricks et al., 1939). $\text{Fe}^{3+}/\text{Fe}^{2+}$ were estimated by Combaudon et al. 2023, submitted in *Lithos*. Based on compositional maps, serpentine density is estimated at around 2.70 g.cm^{-3} . K-feldspar and plagioclase densities have been estimated based on a linear combination between albite [$\text{NaAlSi}_3\text{O}_8$], anorthite

[CaAl₂Si₂O₈], and orthoclase [KAlSi₃O₈] with respective densities of 2.62 (Prewitt et al., 1976), 2.73 (Foit et al., 1973), and 2.52 g.cm⁻³ (Colville et al., 1968). Based on compositional maps, their values are estimated at around 2.53 g.cm⁻³ and 2.64 g.cm⁻³ respectively. Biotite density has been estimated based on a linear combination between annite [KFe²⁺₃AlSi₃O₁₀(OH, F)₂], phlogopite [KMg₃(AlSi₃)O₁₀(OH, F)₂], and siderophilite [KFe²⁺₂Al(Si₂Al₂)O₁₀(OH, F)₂] with respective densities of 3.34 (Hazen et al., 1973), 2.83 (Hendrick et al., 1939), and 3.00 g.cm⁻³ (Brigatti et al., 2000). Based on compositional maps, biotite density is estimated at around 3.2 g.cm⁻³. For magnetite, a pure end-member is selected based on Cornell et al (2003) and gives a density of 5.15 g.cm⁻³.

As (Equation 12 uses a volume factor, it can be converted into solid volume variation as the following equation from Gresens., 1967.

(Equation 13): Solid volume variation (%) = $(-1 + f_v) \times 100$

Assuming an open system, the volume change can be determined by making two assumptions: 1) by considering an element immobile, and 2) by minimizing the total mass transfer associated with the reaction considered (Hermann et al., 2013). We choose to focus on the second assumption as immobile elements are not well described in our system. As first described by Centrella et al. 2020, to minimize the total mass transfer (Equation 12 has to be solved for each element measured and for a defined range of volume factors (f_v)). Then, for each volume factor considered, the total mass transfer is calculated by summing up the mass changes (x_n) for all elements, allowing to find the volume variation that corresponds to the minimum mass transfer (Centrella et al., 2020, Centrella et al. 2023a). Results obtained from the Gresens analysis are plotted in a mass transfer diagram using a scaling approach i.e., an approach allowing to enlarge the representation of the data without changing their signification and relation to each other (Grant., 1986, Grant., 2005, Centrella et al. 2023a).

The approach used in our study relies on coupling local bulk compositions from compositional maps with the mass balance equation (Centrella et al., 2015, 2016, Centrella et al., 2018, Centrella et al., 2023a, Centrella et al. 2023b). The calculation assumes that only one fluid is responsible for the reaction and that its chemical composition remains constant during the reaction. Here, the calculation is made assuming an open system meaning that mass will not be preserved.

II.ii.iv. Method of H₂ generation estimation

Results from the mass balance calculation allow to quantify the mass behavior for each individual element during the fluid-mediated mineral/rock transformation. Regarding H₂ production, we consider that H₂ is formed by iron oxidation following (Equation 14) and that the ratio between the ferric iron produced and the ferrous iron consumed is of 2Fe²⁺ or 2Fe³⁺: 1H₂.

(Equation 14): $\text{Fe}^{2+} + \text{H}_2\text{O} \rightarrow \frac{1}{2} \text{H}_2 + \text{iron oxides}$

We thus used the mass of Fe²⁺ or Fe³⁺ obtained with the mass balance calculation, to determine the amount of H₂ produced by a unit volume of the primary mineral, knowing the density of that mineral. Then we used the volume of the minerals obtained with μCT to obtain the quantity of H₂ generated by a mass unit of bulk 1 within the K2 sample. The μCT scans performed with the Bruker scanner gave the following volumes: 0.02 vol% of oxides, 2.7 vol% of olivine, 15.2 vol% of orthopyroxene and amphibole (no distinction possible), and 81.9 vol% for the feldspars matrix. The μCT scans performed with the Tescan scanner gave the following volumes: 0.11 vol% of oxides, 0.77 vol% of olivine, 3.14 vol% of amphibole, 6.74 vol% of orthopyroxene, and 89.05 vol% of feldspars matrix. Then we considered the quantity of H₂ produced per kilogram of rock by correlating the previous calculation with the total mass of the K2 sample analyzed. The calculation was made by considering reactions with a pseudomorphic replacement ($dV=0$ and $f_v=1$) and a volume variation by minimizing the mass transfer (MMT).

Note that we choose not to consider a reaction with iron oxides as they were identified and quantified with μCT but too close to the resolution of the EPMA beam which did not allow to obtain quantitative measurements. We, thus, choose to neglect iron oxides for the rest of the study.

II.iii. Results

II.iii.i. Quantitative petrological mapping of the fayalite-bearing gabbro from the Kansas Precambrian basement

The BSE-SEM image of the studied area of the K2 sample is shown in Figure 33. A. K2 sample mineralogical assemblages, textures, and microtextures have already been described by Combaudon and co-authors (2023, submitted in *Lithos*). In particular, phyllosilicates repartition within all the minerals have been imaged and described at the nanometric scale. Here, the focus is on a larger scope in order to establish a global characterization of iron partitioning in the sample.

Following the results of the previous study, the sample is composed of fayalite, the iron-rich endmember of olivine, orthopyroxene, amphibole, serpentine, feldspars, iron oxide, quartz, and apatite (Figure 33 B). Veins of clay minerals run mainly through the fayalite. They are a complex mixture of serpentine, smectite, mica, and chlorite which can be divided into two generations (Combaudon et al., 2023, submitted in *Lithos*). At the EPMA resolution, only serpentine is detected.

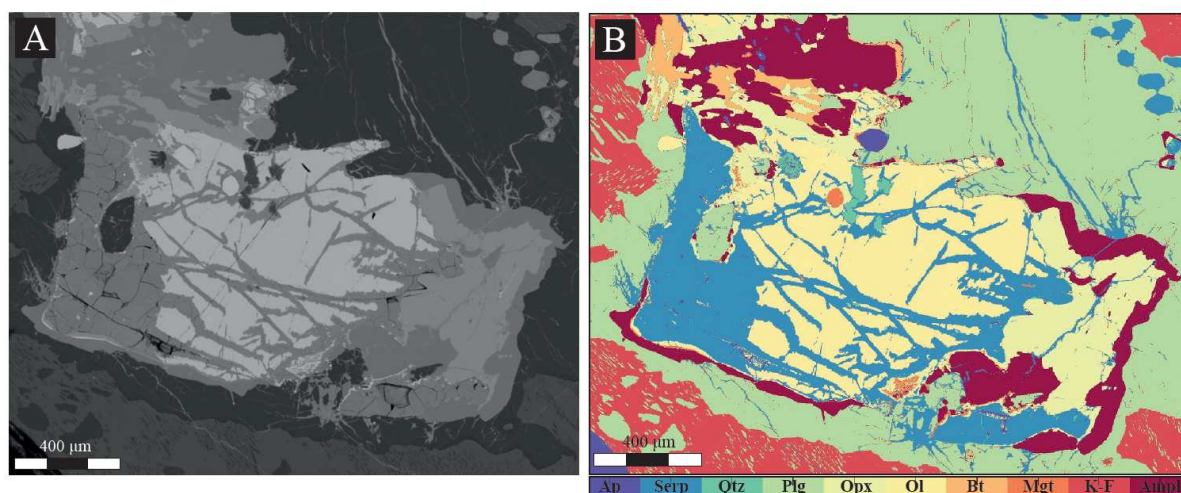


Figure 33: A- BSE-SEM image of the area studied; B- Phases map of the studied area obtained from WDS element maps using the software XMapTools 4.1. (Lanari et al., (2014, 2019). (Ap is for apatite, Serp is for serpentine, Qtz is for quartz, Plg is for plagioclase, Opx is for orthopyroxene, Ol is for olivine, Bt is for biotite, Mgt is for magnetite, K-F is for K-feldspar, Amph is for amphibole).

The average chemical composition of each individual phase is presented in Table 6. It is obtained from an average compositional map. Olivine has been identified as the iron-rich endmember fayalite [Fa_{0.91}]. Orthopyroxene, with 43.8 ox.wt.% of FeO and only 5.3 ox.wt.% of MgO, has been identified as ferrosilite [Fs_{0.81}]. Biotite is identified within the K2 sample and is closely associated with orthopyroxene and amphibole. Biotite, with 28.1 ox.wt.% of FeO, 6.45 ox.wt.% of MgO, and 4.52 ox.wt.% of TiO₂ corresponds to a siderophilite [Sid_{0.55}]. Plagioclase has been identified as albite [Ab_{0.74}] and K-feldspar has been identified as orthoclase [Or_{0.87}]. Iron oxide has been identified as magnetite Fe₃O₄. Amphibole is iron, calcium, and aluminum-rich with 28.05 ox.wt.% of FeO_{Total} and 10 ox.wt.% of CaO and Na₂O. The estimation of ferric iron in amphibole was made following the calculation described by Leake (1997). Thus, amphibole is identified as hastingsite and is composed of respectively 23.51 ox.wt.% and 4.54 ox.wt.% of FeO and Fe₂O₃. H₂O has been calculated by calculating the LOI (loss on ignition) and assuming it corresponds to the water content. (LOI = 100 – Σcations (wt.%)). It reaches 1.93 wt.%. Serpentine is iron-rich with 42.09 wt% of FeO_{Total}, associated with 2.85 ox.wt.% of Al₂O₃, 1.44 ox.wt.% of MgO, 1.28 ox.wt.% of MnO, and 1.09 ox.wt.% of Na₂O. H₂O has been

and reached 10.1 ox.wt.%. The ferric iron content calculated with STXM data ($[\text{Fe}^{3+}]/\Sigma\text{Fe}=0.27\pm 0.02$) in Combaudon et al., 2023 was used to estimate ferric iron content in serpentine. FeO (total) is about 42.39 wt% and was converted in element weight percent by multiplying with the molar weight ($\text{Fe}_{\text{total}} = 32.95 \text{ wt}\%$). Based on STXM, this mass is composed of 27% of Fe^{3+} and 73% of Fe^{2+} . The specific Fe^{2+} and Fe^{3+} were then converted into FeO and Fe_2O_3 respectively. FeO and Fe_2O_3 mineral maps are presented in Figure 34.

	Fayalite	Orthopyroxene	Amphibole	Serpentine	Biotite	K-feldspar	Plagioclase	Magnetite	Fa + Opx	Serp + Amph
SiO ₂	29.90	47.51	41.52	39.99	36.19	65.96	64.45	0.00	36.88	40.78
TiO ₂	0.00	0.02	0.64	0.03	4.52	0.03	0.02	0.00	0.03	0.45
Al ₂ O ₃	0.04	0.31	10.04	2.85	16.11	18.39	22.73	0.00	0.19	5.75
FeO	64.79	43.80	28.05	42.39	28.10	0.18	0.96	100.00	56.85	36.45
MnO	2.64	1.96	0.63	1.28	0.10	0.02	0.11	0.00	2.32	1.11
MgO	2.10	5.30	4.45	1.44	6.45	0.06	0.07	0.00	3.33	2.66
CaO	0.06	0.60	10.45	0.62	0.01	0.80	4.63	0.00	0.36	4.83
Na ₂ O	0.02	0.05	1.67	1.09	0.02	2.10	9.10	0.00	0.03	1.28
K ₂ O	0.03	0.06	1.67	0.18	8.92	12.90	0.52	0.00	0.04	0.72
BaO	0.01	0.02	1.26	0.02	0.76	1.09	0.03	0.00	0.01	0.08
H ₂ O			1.93	10.10						5.85
Total	99.61	99.62	102.31	99.99	101.20	101.52	102.63	100.00	100.06	100.00
FeO	64.79	43.8	23.51	30.04	28.10	0.18	0.96	31.00	56.85	26.52
Fe ₂ O ₃	0.00	0.00	4.54	12.35	0.00	0.00	0.00	69.00	0.00	9.92
FeO/(Fe ₂ O ₃ + FeO)	1.00		0.84	0.71	1.00	1.00	1.00	0.31	1.00	0.73
Normalized to:	4Ox	3Ox	23Ox	14Ox	11Ox	8Ox	8Ox			
Si	1.000	1.012	6.491	4.486	2.740	3.009	2.777			
Al	-	0.005	1.850	0.221	1.402	0.991	1.198			
Ti	0.001	0.000	0.075	-	0.231	-	-			
Cr	0.001	-	0.000	0.009	-	-	-			
Fe	1.813	0.746	3.601	4.218	1.440	-	-			
Mn	0.075	0.036	0.083	0.131	0.025	-	-			
Mg	0.105	0.171	1.037	0.240	1.091	-	-			
Ca	-	0.016	1.750	-	0.040	0.006	0.234			
Na	-	0.000	0.506	-	-	0.125	0.763			
K	-	-	0.251	-	0.842	0.847	0.030			
Ni	0.001	-	0.000	0.009	-	-	-			
Ba	-	-	0.004	-	-	-	-			
Sum	2.996	1.986	15.649	9.312	7.811	4.978	5.003			
End-members										
	Xfo	0.053 Xen	0.190	XGln	Xchry	0.050 Xan	0.283 Xab	0.128 Xab	0.743	
	Xfa	0.910 Xfs	0.810	XTr	Xgreen	0.946 Xphl	0.214 Xan	0.006 Xan	0.228	
	Xtep	0.038		XFtr		Xsid	0.557 Xorth	0.867 Xorth	0.029	
				XTs						
				XPrG						
Density (g.cm-3)	4.32	3.81	3.58	2.70	3.20	2.53	2.64	5.15	4.07	3.31

Table 6: Average microprobe analyses of minerals constitutive of the sample studied (in ox.wt.%). Olivine, orthopyroxene, amphibole, serpentine, and biotite density were calculated on the basis of a linear combination of end members assuming an ideal solid solution. FeO* is iron total. Estimation of Fe_2O_3 in amphibole was made following Leake's work (1997). Fe_2O_3 in serpentine was obtained with STXM-XANES in Combaudon et al., 2023. Xfo = XForsterite, Xfa = XFayalite, Xtep = XTephroide, XEs = XEnstatite, Xfs = XFerrosilite, Xchry = Xchrysotile, Xgreen = XGreenalite, Xan = XAnnite, Xphl = XPhlogopite, Xsid = XSiderophyllite, Xab = XAlbite, Xan = XAnorthite, and XOrth = XOrthose.

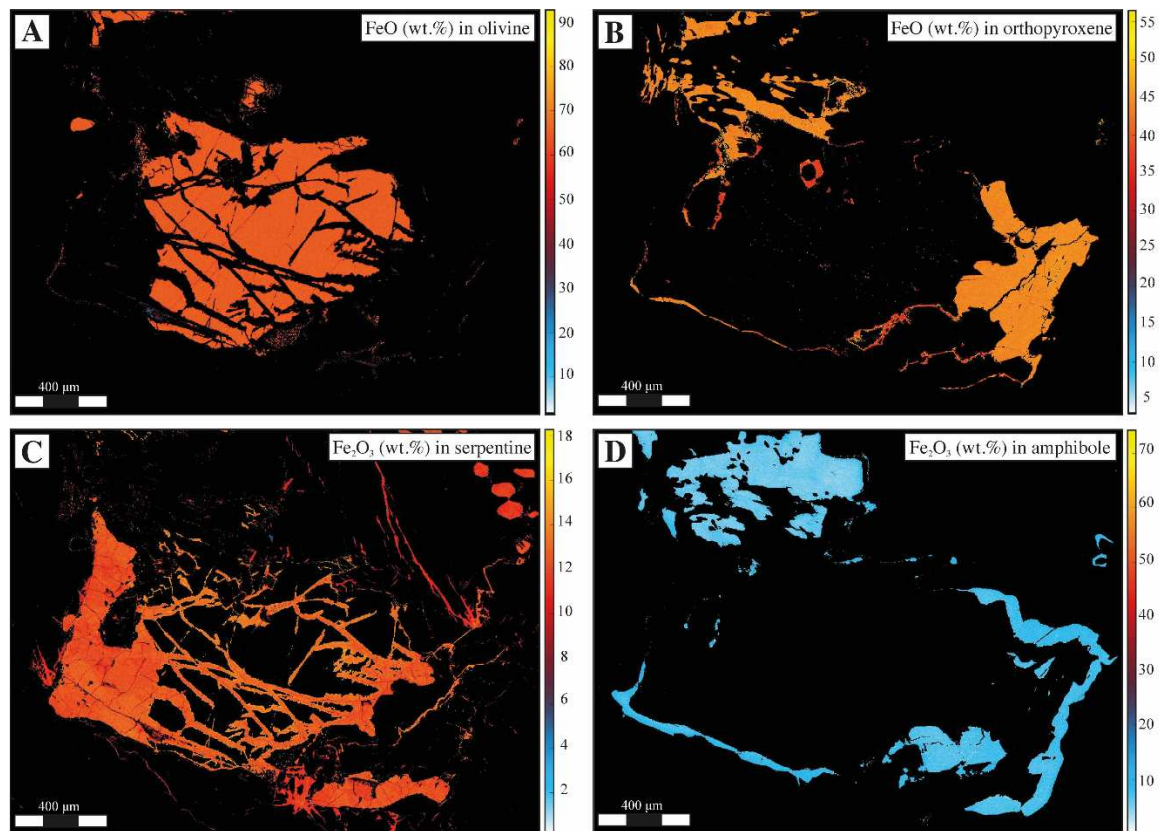


Figure 34: A- Compositional map of FeO in olivine (in oxide weight percent); B- Compositional map of FeO in orthopyroxene (in ox.wt.%); C- Compositional map of Fe₂O₃ in serpentine (in ox.wt.%), and D- Compositional map of Fe₂O₃ in amphibole (in ox.wt.%). The phase map is presented in Figure 1.

II.iii.ii. Hypothesis on metamorphic reactions potentially leading to Fe²⁺ oxidation within the fayalite-bearing gabbro of the Kansas Precambrian basement

In order to better characterize mass transfer within the minerals constitutive of the K2 sample and in particular in order to better characterize iron evolution, we focused on three potential metamorphic reactions: 1) orthopyroxene being replaced by amphibole; 2) olivine being replaced by serpentine; and 3) olivine and orthopyroxene being simultaneously replaced by serpentine and amphibole as a unique product.

We choose to focus on these three reactions because of the unique textural association of these minerals. Indeed, the serpentines are numerous inside olivine. They also cross-cut orthopyroxene, amphibole, and plagioclase but their size, and iron content seem to decrease when moving away from the iron-rich olivine. It could also be explained by a topographic effect due to the density contrast between phases. A more complete description of their textural association with other minerals is proposed in Combaudon et al., 2023.

The serpentine can be differentiated into two sub-serpentines, one that can be found in the other mafic minerals and plagioclase, and which might have directly precipitated from the

residual magmatic liquid, and a second only found in the olivine which might have been formed by deuteric alteration. This latter is the reason why we chose to consider this reaction. Also, it is important to say that magnetite was identified by BSE-SEM imaging as associated with serpentine, but its grain size was under the resolution of the EPMA beam, thus, it was not possible to take it into account during our mass balance calculation. Orthopyroxene and amphibole are also closely associated with sharp contacts typical of mineral replacement.

While they both appear as a rim around the olivine and the serpentine their interaction could have happened during a different reaction than reaction 1, such as reaction 2. It is also possible to imagine olivine and orthopyroxene to have reacted together to form serpentine and amphibole such as in reaction 3. Finally, the interface between these minerals is always sharp.

Note that even if orthopyroxene replacement by serpentine (commonly called bastite) is common in such rock (Wicks and Whittaker., 1977, Mevel., 2003, Dungan., 2009) we did not find any textural evidence of such reaction within this sample; therefore, we choose to not consider this mineral replacement reaction in this study.

II.iii.iii. Mass transfer calculation

Results for such calculation are presented in Figure 34 and Figure 35. The first one represents the sum of the mass transfer for each specific reaction in the function of the solid volume variation. The second one represents the mass transfer diagram resulting from compositional maps, density, and solid volume variations.

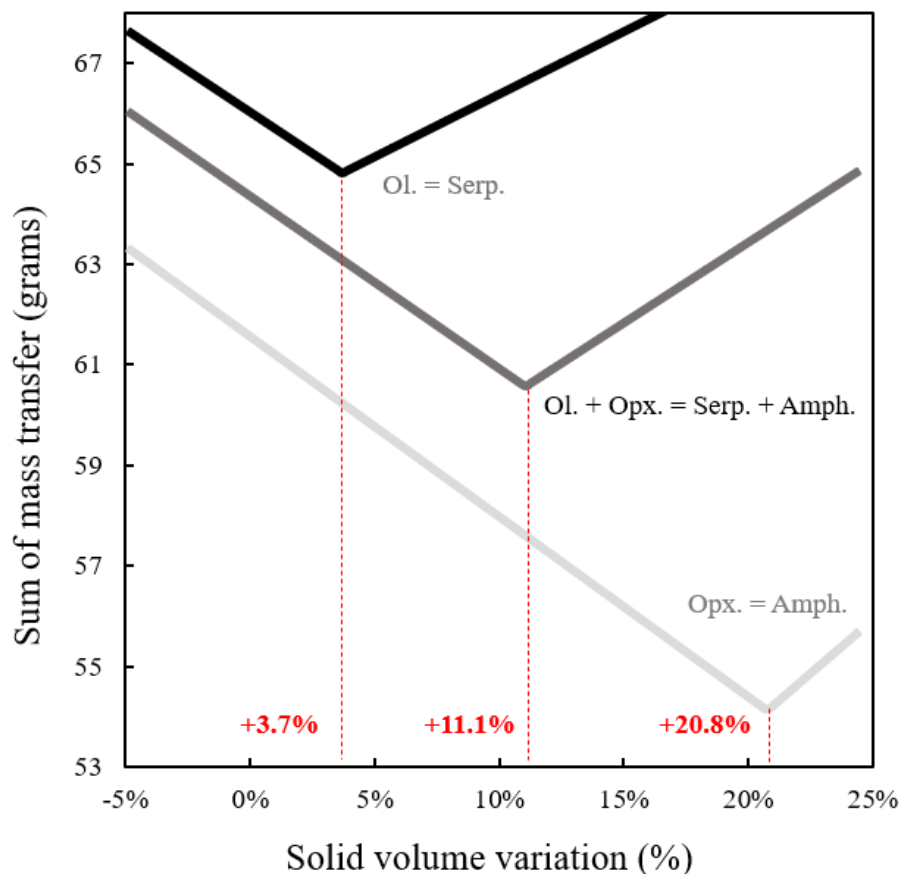


Figure 35: Sum of gains and losses of elements as a function of the volume change during the three reactions. When minimizing the mass transfer, reaction 1 of orthopyroxene being replaced by amphibole induces a volume change of +20.8%. When minimizing the mass transfer, reaction 2 of olivine being replaced by serpentine induces a volume change of +3.7%. When minimizing the mass transfer, reaction 3 of (olivine + orthopyroxene) being replaced by (amphibole + serpentine) induces a volume change of +11.1%. These volume variations represent the optimal solid volume variation accompanying the density change induced by the mineral replacement considered.

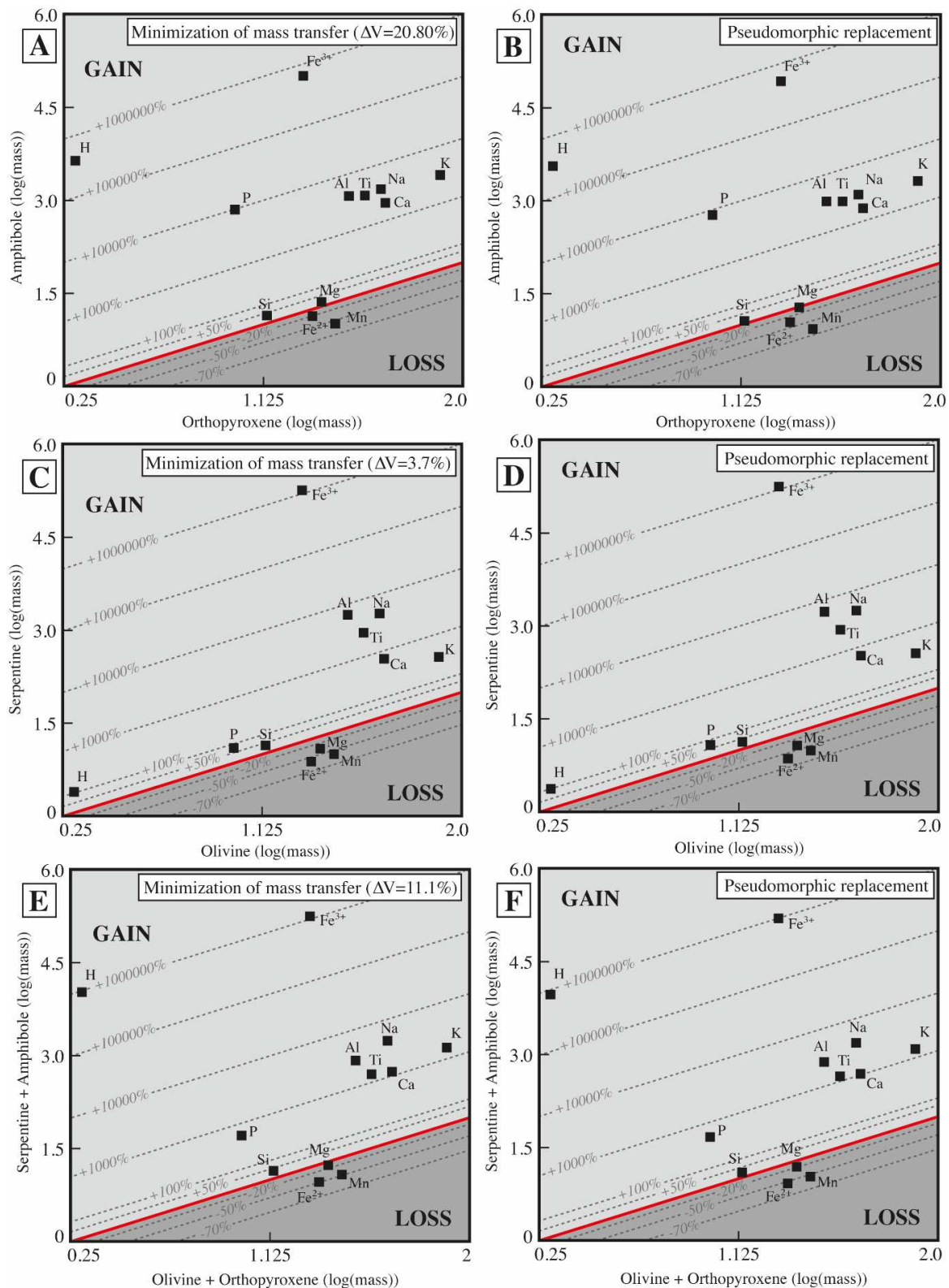


Figure 36: A- Mass transfer diagram for the three possible reactions with the assumptions of minimizing the mass transfer and with no volume variation. These diagrams compare the element composition of the product with its original parent. A and B are for reaction 1, amphibole replaces orthopyroxene. C and D are for reaction 2, serpentine replaces olivine. E and F are for reaction 3, serpentine and amphibole replace olivine and orthopyroxene. Red line indicates the 0% of mass change, and the dashed line the % of mass change.

II.iii.iii.i. *Replacement of orthopyroxene by amphibole*

Mass transfer calculation demonstrated that, by minimizing the mass transfer (Equation 15), 100g of orthopyroxene gives 108.32g of amphibole (+ 8.32 % of mass gained). This reaction corresponds to a volume factor of 1.208 (Figure 35), which is equivalent to a solid volume variation of +20.8% with 22.53g of mass added to the system and 14.21g of mass lost from the system (Equation 15). On the opposite of closed system and stoichiometric equations with mass preservation, the following equations show products associated with bulk 1 at the left and reactants lost at the right with bulk 2. Thus, elements at the left are gained and elements at the right are lost. By considering a pseudomorphic reaction (Equation 16), 100g of orthopyroxene gives 96.27g of amphibole (3.7 % of mass loss) with 18.53g of mass added to the system and 22.26g of mass lost from the system. In both cases, amphibole replacing orthopyroxene induces an overall loss of Fe²⁺, Mn, and Mg and a gain of Fe³⁺, Ti, Al, Ca, Na, K, P and H₂O (Figure 36 A. and B.).

(Equation 15, $\Delta V = 20.8\%$): **100g of orthopyroxene** + 0.002g Si + 0.43g Ti + 5.92g Al + 3.63g Fe³⁺ + 8.12g Ca + 1.38g Na + 1.54g K + 1.27g P + 0.25g H = **108.32 g of amphibole** + 13.13g Fe²⁺ + 0.96g Mn + 0.12g Mg

(Equation 16, $\Delta V = 0\%$): **100g of orthopyroxene** + 0.35g Ti + 4.87g Al + 3.01g Fe³⁺ + 6.65g Ca + 1.13g Na + 1.26g K + 1.05g P + 0.2g H = **96.27g of amphibole** + 3.82g Si + 16.73g Fe²⁺ + 1.06g Mn + 0.65g Mg

Mass transfer diagrams for reaction 1 show there is little change in mass for most of the elements except for Fe³⁺, Fe²⁺ and H₂O.

II.iii.iii.ii. *Replacement of olivine by serpentine*

Mass transfer calculation demonstrated that, by minimizing the mass transfer (Equation 17), 100g of olivine gives 74.51g of serpentine (~ 26% of mass loss). This reaction corresponds to a volume factor of 1.307, which is equivalent to a solid volume variation of + 3.7% (Figure 35) with 9.34 g of mass added to the system and 34.83 g of mass lost from the system (Equation 17). By considering a pseudomorphic reaction, 100 g of olivine gives 72.88 g of serpentine (~ 27% of mass loss) with 9g of mass added to the system and 36 g of mass subtracted from the system (Equation 18). In both cases, serpentine replacing olivine induces an overall loss of Fe²⁺, Mn, and Mg and a gain of Fe³⁺, Ti, Al, Ca, Na and H₂O (Figure 36 C. and D.).

(Equation 17, $\Delta V = 3.7\%$): **100g of olivine** + 0.01g Ti + 1.11g Al + 6.46g Fe³⁺ + 0.29g Ca + 0.59g Na + 0.09g K + 0.003g P + 0.79g H = **74.51g of serpentine** + 0.001g Si + 32.90g Fe²⁺ + 1.31g Mn + 0.61g Mg

(Equation 18, $\Delta V = 0\%$): **100g of olivine** + 0.01g Ti + 1.07g Al + 6.23g Fe³⁺ + 0.28g Ca + 0.57g Na + 0.08g K + 0.003g P + 0.64g H = **72.88g of serpentine** + 0.50g Si + 33.53g Fe²⁺ + 1.33g Mn + 0.64g Mg

Mass transfer diagrams for reaction 2 show there is little change in mass for most of the elements except for Fe³⁺ and Fe²⁺. The system loses 32.90 to 33.53g of Fe²⁺ while gaining 6.46 to 6.23 g of Fe³⁺.

II.iii.iii.iii. *Replacement of (olivine + orthopyroxene) by (amphibole + serpentine)*

Mass transfer calculation demonstrated that, by minimizing the mass transfer, 100g of olivine and orthopyroxene give 86.90g of serpentine and amphibole (Equation 19, ~ 13% of mass loss). This reaction corresponds to a volume factor of 1.111, which is equivalent to a solid volume variation of + 11.1% (Figure 35) with 14.02g of mass added to the system and 27.12g of mass lost from the system (Equation 19). By considering a pseudomorphic reaction, 100g of olivine and orthopyroxene give 81.65g of serpentine and amphibole (~ 18% of mass loss) with 12.57g of mass added to the system and 30.92g of mass subtracted from the system (Equation 20). In both cases, serpentine and amphibole replacing olivine and orthopyroxene induce an overall loss of Fe²⁺, Mn, and Mg and a gain of Fe³⁺, Ti, Al, Ca, Na, K and H₂O (Figure 36 E. and F.).

(Equation 19, $\Delta V = 11.1\%$): **100g of olivine and orthopyroxene** + 0.01g of Si + 0.23g Ti + 2.65g Al + 6.28g Fe³⁺ + 2.87g Ca + 0.84g Na + 0.51g K + 0.05g P + 0.59g H = **86.90g of serpentine and amphibole** + 25.54g Fe²⁺ + 1.03g Mn + 0.56g Mg

(Equation 20, $\Delta V = 0\%$): **100g of olivine and orthopyroxene** + 0.21g Ti + 2.37g Al + 5.65g Fe³⁺ + 2.56g Ca + 0.75g Na + 0.46g K + 0.05g P + 0.53g H = **81.65g of serpentine and amphibole** + 1.72g of Si + 27.40g Fe²⁺ + 1.10g Mn + 0.70g Mg

Mass transfer diagrams for reaction 3 show there is little change in composition for Ti, Na, K, P, and Mg. Conversely, the mass of Fe, Al, Ca, and Mn are evolving. The system loses 25.54 to 27.40g of Fe²⁺ while gaining 6.28 to 5.65 g of Fe³⁺. It also gains 2.37 to 2.65g of Al and 2.56 to 2.87g of Ca. Of note, in the case of a pseudomorphic replacement, 1.72g of Si is lost in the fluid, which is not the case if considering a volume variation of +11.1%.

Even though all three reactions have different mineralogical assemblages, densities, and solid volume variation, they all have similar mass behavior regarding Fe²⁺, Fe³⁺, Al, Mg, Na, Si, and H₂O. All solid volume variations are positives and reactions induce a mass loss.

II.iv. Discussion

II.iv.i. Density decreases and solid volume variation during mineral replacement reaction

Density has to be considered when looking at mineral replacement reactions because it is a good marker of the evolution of the amount of element for a given volume of rock/mineral (Gresens., 1967, Ague., 1991).

In this study, during orthopyroxene replacement by amphibole, the density of the initial orthopyroxene is 3.81 while the density of the amphibole is 3.58, thus, 6% of the density of the primary silicate is lost during the reaction. In our sample olivine density has been calculated to be 4.32 while serpentine density has been calculated to be 2.7, thus, 37.5% of the initial density of the primary olivine is lost during the reaction. Finally, for the third reaction, the density of the primary reactants (olivine + orthopyroxene) is 4.07 while the products of the reaction (serpentine + amphibole) have a density of 3.31, thus, 18.7% of the density of the primary minerals is lost during the reaction.

A density decrease induced by a mineral replacement is accompanied by a solid volume variation and/ or by a mass loss (if the volume is constant). We determined the solid volume variation for each reaction by minimizing the mass transfer (i.e., gains and losses of mass). For reaction 1, the solid volume variation is +20.8%. For reaction 2, the solid volume variation is +3.7%. For reaction 3, the solid volume variation is +11.1% (Figure 35). Reactions inducing a density decrease have already been described in the literature. During the amphibolitization reaction, depending on the density of the primary mineral the final density will evolve. Centrella (2015) showed that during the transition of granulite to amphibolite the density goes from 3 g.cm⁻³ to 2.84 g.cm⁻³. This change in density is attributed to the hydration and metamorphism of the protolith leading to amphibolitization. In the same way, due to the addition of water to the system, olivine replacement by serpentine induces a decrease in the density because olivine is replaced by a hydrous phase whose density is lower than the primary silicate, as previously described by Mevel (2003).

Every reaction induces a positive solid volume variation (+3.7 to +20.8%). They are less important than the ones found in the literature which reach an increase of 50 to 60% for serpentinization (Shervais et al., 2005). Orthogonal fractures are observed at both micro and macro-scales but as a difference with Wicks et al., 1997, the fractures are not pervasive. In consequence not all the stress generated by hydration reactions due to local density change

was accommodated by the fracturation. A component of the stress was thus accommodated by the release of mass through the fluid phase as described by Carmichael (1987). Carmichael, 1987 attested that even if the solid density decreases, the overall volume of the solid can be maintained during a reaction. This implies that the stress generated by the density reduction must be compensated. Conclusions were that the induced stress would be dissipated by mass transfer to maintain the overall volume of the solid and minimize the stress fields. Since both serpentine and amphibole are loss of mass reactions, stress can easily be compensated by the release of mass through the fluid phase (Centrella et al. 2015, 2016).

II.iv.ii. Mineral replacement by considering a mass transfer

While the K2 sample shows textural evidence of replacement reactions it appears mandatory to better constrain the elements transfers within the system. Carmichael (1969) proposed an empirical method to do so by considering a unique thin section as part of a more global open system that is the studied rock. His approach consists in dividing the global reaction as sub-reactions happening at a lower scale. He showed that textural characteristics of metamorphic rocks can be used to understand these sub-reactions within the thin section closed system i.e., local and coupled dissolution-precipitation reactions. Understanding these sub-reactions allows to better understand elements transfer induced by changes in composition within one larger global and open system.

In general, most of the literature associated with olivine and orthopyroxene replacements consider both reactions as a closed system meaning that mass is preserved (Shervais et al., 2005, Andreani et al., 2013). It is also commonly assumed that iron is immobile during such reactions (Mevel., 2003, Godard et al., 2008). For example, the iron redox evolution from MOR to subduction zones was studied by bulk rock analyses, microprobe analyses, magnetic measurements, SEM, and μ XANES spectroscopy (Debret et al., 2014). The study showed that the iron content does not vary during the reaction (authors looked at the bulk rock $\text{Fe}_2\text{O}_3^{\text{TOT}}$ at different stages) and that in consequence no iron is released in the remaining fluid but rather partitioned in the secondary phases. Authors infer that the fluid composition, and so the iron budget, is controlled by the redox of the reaction (Debret et al., 2014). The small evolutions in total iron content (a few percent) are due to the evolution of the modal abundances of the protolith mineral from MOR to subduction zones as it has been shown that the primary mineralogy controls the chemical composition of secondary phases (Toft et al., 1990, Godard et al., 2008). The open character of the system is not taken into account, neither the evolution of density, nor volume.

A mass balance study of serpentinized harzburgite and dunite shows that serpentinization leads to a slight enrichment in Mg, in Fe, and a depletion in Si, Ca, and Al which are lost (Shervais

et al., 2005). Thus, the total mass of the system decreases during serpentinization (Shervais et al., 2005). Shervais and co-authors run mass balance calculation using the GENMIX program (LeMaitre, 1981) on two reactions and by normalizing their data to 100% anhydrous phases in order to eliminate volume or mass changes caused by hydration and to focus on mass transfer: 1) Mg-rich olivine being replaced by Mg-serpentine, brucite, and magnetite, 2) Mg-orthopyroxene being replaced by Mg-serpentine. For 80 to 84g of Mg-rich olivine, reaction 1 produces a similar mass of serpentine, 12 to 16g of brucite (MgOH_2), and 3 to 4g of magnetite (Fe_3O_4). For 87g of Mg-rich orthopyroxene, reaction 2 produces 85g of serpentine and 14g of SiO_2 . They also run similar models with Fe-rich olivine; they have similar results except that magnetite production is suppressed as more iron goes into serpentine. Our system loses Si, Mg, and Fe^{2+} , and gains Ca and Fe^{3+} so once again, major differences are observed from the previous study and may be due to a different parent mineral.

A more recent study performed mass balance calculation on peridotite samples from ODP Leg 153 (MARK region, 23°N) by considering iron partitioning thanks to μ -XANES analysis at the Fe K-edge (Andreani et al., 2013). They examined how serpentine formation contributes to the iron budget and thus influences H_2 generation. As indicated above, previous studies showed that the iron budget is controlled by primary mineralogy. In this study, calculation indicated that there was no obvious gain or loss of iron in the whole rock during the reaction, proving that iron must have been redistributed in the secondary phases (Toft et al., 1990, Godard et al., 2008). Thus, Andreani and co-authors used iron as an immobile element to perform mass balance calculations within their samples to focus on redox evolution. The bulk Fe^{3+} content increases linearly with the advance of the reaction and ferric iron is partitioned within serpentine and magnetite (Andreani et al., 2013).

Lécuyer and co-authors (1990) described the transition from greenschist to amphibolitic facies during a hydrothermal alteration in the Trinity ophiolite (California, USA). Authors applied Gresens equations in order to characterize the mass transfer of major elements during the water-rock interactions (Lécuyer et al., 1990). In gabbros, no clinopyroxene relics are found but occurrences of Mg-hornblendes are described. In mafic cumulates, clinopyroxenes are replaced by actinolite (and plagioclase by epidote). The authors estimate the volume factor to be 1.07. In ultramafic cumulates, olivines are replaced by serpentine and magnetite, and clinopyroxenes and orthopyroxenes are replaced by hornblende, talc, and chlorite. The authors estimate the volume factor to be respectively 1.15 and 1.1. They showed that chemical fluxes are linked to the water-rock ratio and thus to the penetration of water within the rock. Ca-rich amphiboles are described as forming under 300 to 500°C while Mg-rich amphiboles as forming under 500 to 700°C. Mineral equilibria indicate temperatures of formation to be around 500°C. Thus, authors infer that the amphibolitization of pyroxenes happens under high-temperature conditions, probably at the top of the magmatic chamber (Lécuyer et al., 1990).

Their formation lowers the pH of the fluid and consumes H⁺ (Bischoff et al., 1975). Mass transfer calculation shows that extensive pyroxene replacement by amphibole induces Mg and Fe gains, and Ca loss. We did observe a Fe³⁺ gain but no Mg gain, nor Ca loss. These differences may result from a different chemical composition of the original orthopyroxene.

In the ultramafic cumulates described in the Trinity ophiolites, serpentinization is dominant (over amphibolitization) with a loss on ignition (L.O.I), ranging between 5 to 12%, with significant losses of Si, Ca, Fe, and Mg (Lécuyer et al., 1990). We did observe Si, Mg, and Fe²⁺ losses but Ca and Fe³⁺ were added to the system. The L.O.I. calculated for reaction 2 is in the same order as the one calculated by Lécuyer and co-authors (1990).

Here, differences with the above examples are: 1) the primary mineralogy, and 2) the detailed investigation of the sample from Kansas relies on mass balance calculation in an open system in order to properly characterized how behaves the solid and the mass during a fluid-mediated rock transformation, which is not the case for the first three studies. We considered the ferrous and ferric iron budget at the sample scale and thus established the elements transfer for what we are convinced are the three main reactions.

The first reaction considered here is the orthopyroxene replacement by amphibole. Both by considering a pseudomorphic replacement or by minimizing the mass transfer, this reaction induces a loss of Fe²⁺ and Mg in the fluid and a gain of Fe³⁺ and Ca. If considering a pseudomorphic reaction, the system loses 3.73g of elements. If considering the mass transfer, the system loses 14.21 g of elements. The calculated loss on ignition (L.O.I), which is the volatile content that we assume is here the H₂O content, is positive with a value of 1.93g. Water is then left in excess after the reaction.

The second reaction considered here is the olivine replacement by serpentine. Again, both by considering a pseudomorphic replacement or by minimizing the mass transfer, this reaction induces a loss of Fe²⁺, Si, and Mg in the fluid and a gain of Fe³⁺ and Ca. If considering a pseudomorphic reaction, the system loses 27g of elements. If considering the mass transfer, the system loses 34.83 g of elements. The calculated L.O.I is positive with a value of 10.10g showing this replacement reaction generates water in excess. It shows a fluid-mediated reaction within a Fe-rich monzogabbro can lead to Fe-rich olivine replacement by a Fe-rich serpentine by iron oxidation.

Finally, the third reaction considered olivine and orthopyroxene reacting together to the fluid circulation to give serpentine and amphibole. Both by considering a pseudomorphic replacement and by minimizing the mass transfer, this reaction induces a loss of Fe²⁺ and a gain of Fe³⁺. If considering a pseudomorphic reaction, the system loses 18.33g of elements. If

considering the mass transfer, the system loses 27.12 g of elements. The calculated L.O.I is positive with a value of 5.85g, showing this reaction generates water in excess.

II.iv.iii. Comparison between olivine replacement by serpentine and orthopyroxene replacement by amphibole

Olivine replacement by serpentine and orthopyroxene replacement by amphibole lead to density decrease and volume increase. Olivine is replaced more easily than orthopyroxene due to its relative instability during hydration events because of its high kinetic of dissolution (Daval et al., 2011, Sissmann et al., 2014). Orthopyroxene dissolution at temperature above 300°C (and $P > 50$ MPa), and without aluminium in the system, is faster than olivine dissolution, which seems to not be the case in our sample (Allen and Seyfried., 2003, Pens et al., 2016). Thus, replacement happens faster, and the proportion of hydrated minerals is more important during olivine replacement rather than during the orthopyroxene one, which can explain the difference in the density changes. In addition, these mineral replacements induce similar element behaviors. Indeed, to cause a density change, elements have to be transferred into secondary phases and into the circulating fluid and leave the system if the amount lost is superior to the amount gained. As some exit the system, some are also gained. This study showed that in every hypothesis (by minimizing the mass transfer or by considering no solid volume variation) and for each reaction, Fe^{3+} , H_2O , Si, Al, Ti, Na, Ca, K, and P are gained, and Mg, Mn, and Fe^{2+} are lost. The difference comes mainly with the proportion of Fe^{3+} gained. For example, if minimizing the mass transfer, the orthopyroxene replacement by amphibole leads to a gain of 3.63g of Fe^{3+} while the olivine replacement by serpentine leads to a gain of 6.46g of Fe^{3+} .

The third reaction tested is showing similar results with density changes, solid volume increase, and element transfer numbers being slightly higher than the ones for orthopyroxene replacement by amphibole.

II.iv.iv. What about redox evolution?

Thus, the mass transfer resulting from these three fluid-mediated replacement reactions leads to a Fe^{2+} lost and a Fe^{3+} gain. If the fluid is anoxic the reaction can lead to a potential H_2 production by iron oxidation. Thus, under oxidizing and anoxic conditions, olivine replacement by serpentine and orthopyroxene replacement by amphibole induce the oxidation of iron and possibly H_2 generation following. As for the two other reactions, the third one could generate H_2 by iron oxidation.

All three reactions do not generate the same amount of ferric iron. Knowing that densities have been calculated on the assumption of an ideal solid solution and that analytical uncertainties on local bulk composition do exist, it is reasonable to consider these values as good insights into what happened in the sample. It gives a good idea of the mobility of the elements during a fluid-mediated mineral replacement and allows us to determine redox conditions during this replacement. The fact that the masses behave the same way during orthopyroxene and olivine respective replacements supports a potential single fluid event. The redox conditions must have been similar in order to produce Fe^{3+} and H_2O . Using redox-sensitive element such as iron, it appears that both reactions support a generally reduced fluid condition leading to iron oxidation within the minerals.

II.iv.v. What about hydrogen?

II.iv.v.i. Estimation of hydrogen generation associated with each reaction

The volumes of minerals obtained with μCT were used to estimate the hydrogen production of the three reactions. Due to technical difficulties, mainly the resolution of the scans being higher than the smallest grains in the sample and the iron-rich minerals having close attenuation coefficients, a certain number of assumptions had to be done for the Bruker μCT scans: 1) orthopyroxenes and amphiboles are considered as one volume, 2) the volume of fayalite was used to do the calculation of reaction 2 thus giving a quantity of H_2 higher than the real one. We are well aware that the numbers we give are high estimates of the production of H_2 . However, we consider that regarding the technical difficulties of imaging heterogeneous samples in 3D thanks to μCT , it remains interesting to perform this kind of calculation even with high uncertainties.

In addition, hydrogen quantification by rock study is usually done by considering balanced equations, or by using the multimodal workflow like the one developed in Kularatne et al., (2023, *in prep*). Here, we are able to estimate the amount of H_2 generated for each reaction specifically and not just for the whole rock and the equations do not need to be balanced as we consider the mass transferred only (Table 7, Figure 37).

With the Bruker scans							
Reaction		masse (g) of Fe(III)/100 g of bulk 1	mol of Fe(III)/ 100g of bulk 1	mol of H ₂ / cm ³ of bulk 1	mol of H ₂ / t of rock		
2Fe(III):1H ₂	MMT		3.63	0.07	1.24E-3	69.16	
	ΔV=0	1	3.01	0.05	1.03E-3	378.21	
	MMT		6.46	0.12	2.50E-3	25.12	
	ΔV=0	2	6.23	0.11	2.41E-3	24.22	
	MMT	3	This calculation is not possible because this segmentation does not differentiate opx and amph				
	ΔV=0						
Reaction		masse (g) of Fe(II)/100 g of bulk 1	mol of Fe(II)/ 100g of bulk 1	mol of H ₂ / cm ³ of bulk 1	mol of H ₂ / t of rock		
2Fe(II):1H ₂	MMT		13.13	0.24	4.48E-3	250.13	
	ΔV=0	1	16.73	0.30	5.71E-3	318.71	
	MMT		32.90	0.59	1.27E-2	127.90	
	ΔV=0	2	33.53	0.60	1.30E-2	130.36	
	MMT	3	This calculation is not possible because this segmentation does not differentiate opx and amph				
	ΔV=0						
With the Tescan scans							
Reaction		masse (g) of Fe(III)/100 g of bulk 1	mol of Fe(III)/ 100g of bulk 1	mol of H ₂ / cm ³ of bulk 1	mol of H ₂ / t of rock		
2Fe(III):1H ₂	MMT		3.63	0.07	1.24E-3	50.33	
	ΔV=0	1	3.01	0.05	1.03E-3	41.73	
	MMT		6.46	0.12	2.50E-3	11.61	
	ΔV=0	2	6.23	0.11	2.41E-3	11.18	
	MMT	3	6.28	0.11	1.86E-3	103.63	
	ΔV=0		5.65	0.10	1.67E-3	93.34	
Reaction		masse (g) of Fe(II)/100 g of bulk 1	mol of Fe(II)/ 100g of bulk 1	mol of H ₂ / cm ³ of bulk 1	mol of H ₂ / t of rock		
2Fe(II):1H ₂	MMT		13.13	0.24	4.48E-3	182.04	
	ΔV=0	1	16.73	0.30	5.71E-3	231.95	
	MMT		32.90	0.59	1.27E-2	59.08	
	ΔV=0	2	33.53	0.60	1.37E-2	60.21	
	MMT	3	25.54	0.46	9.31E-3	421.47	
	ΔV=0		27.40	0.49	9.98E-3	452.16	

Table 7: H₂ production calculation for each reaction by considering the Bruker and the Tescan μCT scans and their associated volume characterization

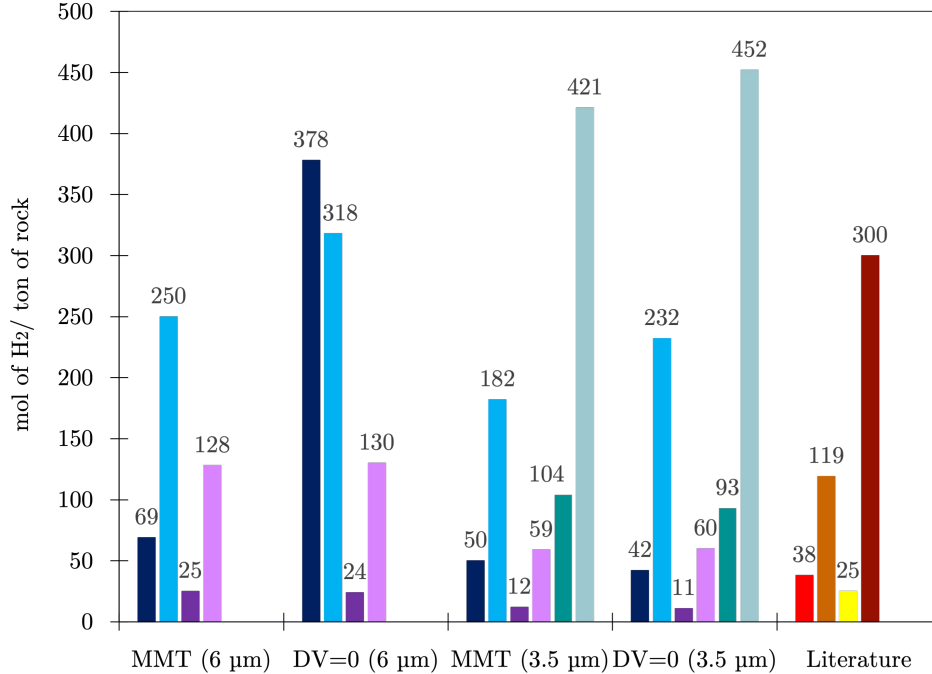


Figure 37: Graphical representation of the amount of H₂ produced (by mol of H₂/ ton of rock) in the function of the different scenarios (in dark blue Opx → Amp by considering the amount of Fe³⁺ gained and in light blue Opx → Amp by considering the amount of Fe²⁺ lost ; in dark purple Ol → Serp (Fe³⁺) and in light purple Ol → Serp (Fe²⁺) ; in dark green Ol + Opx → Amp + Serp (Fe³⁺) and in light green Ol + Opx → Amp + Serp (Fe²⁺) ; in red data is from Geymond et al., 2023, in orange data is from

Groveza et al., 2017, in yellow data is from McCollom et al., 2016, and in brown data is from Leong et al., 2023.

Indeed, by considering the ferric iron generated for each reaction and (Equation 14, the calculation gives a range of H₂ of 24.22 to 378.21 mol of H₂ per ton of K2 sample (Table 7, Figure 37). The first reaction gives a higher quantity of H₂ per ton of rocks. By considering the ferrous iron consumed by each reaction, the calculation gives a range of H₂ produced of 59.08 to 452.16 mol of H₂ per ton of K2 sample (Table 7, Figure 37). These results depend on the phase volumes acquired with the Bruker μ CT and thus are upper limits values.

When considering the replacement of orthopyroxene by amphibole H₂ values are always higher than the ones obtained for the replacement of olivine by serpentine (Table 7, Figure 37). If considering reaction 3 of both replacements happening simultaneously the amount of H₂ generated is significantly higher.

These results can be compared with previous studies (Figure 37). The serpentinization of harzburgite powder (300°C, 350 bar, WR ratio of 2, from 0 to 14569 hours) gave a generation of hydrogen between 3.13 to 119.19 mmol of H₂/ kg of rock (Groveza et al., 2017). Experimental alteration of crushed San Carlos olivine at temperature between 200 and 320°C (35 MPa, WR ratio of 1.8 to 2.6, from 43 to 8183 hours) led to a hydrogen generation up to 25 mmol of H₂ /kg of olivine (McCollom et al., 2016). The alteration of pure magnetite at 80°C (100 bars with a water rock ratio of 2, for 4 months gave) 38 mmol of H₂/ kg of rock. At 200° (200 bars, same water-rock ratio, for 2 months), the alteration of pure magnetite gave 10 mmol of H₂/ kg of rock (Geymond et al., 2023). Calculations of serpentinization rates by considering ferric and ferrous iron incorporation in the reactions products yield an amount of 0.3 mol of H₂/ kg of ultramafic rocks or 300 mol of H₂/ ton of rock (Leong et al., 2023). Thus, the calculated amounts of hydrogen generated by the reactions tested in this paper are in the same order of magnitude of the amount proposed by previous studies.

II.iv.v.ii. *Implication for hydrogen generation within intracratonic areas*

While being subject to many uncertainties due to the volume extraction by μ CT, these calculations give a good image of the availability of iron to be oxidized and thus to produce H₂ within intracratonic rocks. They show that if amphibolitization is happening in oxidizing and anoxic conditions, it can be an efficient way to generate hydrogen. What has to be kept in mind is that amphibolitization produces water available to allow for the oxidation of ferric iron to ferrous iron. The fluid must be oxidizing and anoxic in order to produce H₂. Olivine replacement by serpentine is once again characterized as an H₂-producing reaction no matter

the volume of the primary olivine or the amount of Fe^{2+} or Fe^{3+} but we show it is less efficient than the two other reactions. Finally, reaction three shows that fayalite and orthopyroxene replacement can happen simultaneously and produce substantial amounts of H_2 . All three reactions are producing water in excess, which can enable them to be self-sustaining.

One of the main differences between our study and the previous ones is that our mineralogical assemblage is enriched in iron. We are considering iron-rich endmembers or iron-rich solid solutions. As we know that the iron budget of rocks, having undergone mineralogical replacement, is controlled by the composition of the primary minerals (Toft et al., 1990), it seems correct to quantify this amount of iron being transferred within the K2 sample. What is striking is that contrary to previous studies, there are quantitative gains and losses of iron. The reactions we tested are not isochemical if considering iron because the mass of iron within the system varies. Ferrous iron is lost to the system because it oxidizes in ferric iron. This latter is, then, incorporated into the amphibole and serpentine. What we don't know is the role of magnetite which we were not able to include in these calculations, as it was under the resolution of the beam and not abundant enough in the sample. We also don't know the proportion of potential Fe^{2+} lost in the fluid compared to the Fe^{2+} oxidized and incorporated in the Fe^{3+} -bearing minerals. We only know the balance is negative as more Fe^{2+} is lost than Fe^{3+} is gained. We could probably imagine that a fraction of the total Fe^{2+} lost is solubilized and extracted from the system. If this latter meets the temperature, pH, and redox conditions favorable for its oxidation and for simultaneous water reduction, it could be a source of H_2 once again.

II.v. Conclusion

The fayalite-bearing gabbro from the Kansas (USA) Precambrian basement shows evidence of mineral replacement of Fe^{2+} -rich phases that could generate natural H_2 . 1) iron-rich orthopyroxene being replaced by iron-rich amphibole; 2) iron-rich olivine being replaced by iron-rich serpentine; 3) iron-rich olivine and orthopyroxene being replaced by iron-rich serpentine and amphibole. The mass transfer calculation shows that each reaction implies a decrease in the density for each mineral replaced (6 to 37.5% decrease from the initial parent density) and an increase in volume (3.7 to 20.7%). All three reactions show, in different proportions, a loss of Fe^{2+} to the circulating fluid, and a gain in Fe^{3+} and H_2O in the newly formed minerals. Thus, if no oxygen was present in the fluid, it implies that mineral replacement could have generated iron oxidation and its associated H_2 generation. Mass balance calculation coupled with μCT volume estimation of each mineral allowed us to estimate the H_2 generation within the K2 sample following the three reactions described above. H_2 values range from 11.18 to 452.16 mol of H_2 per ton of rock. While being suggested to analytical uncertainties

these data give a highlight of the potential generation of hydrogen by mineral replacement within intracratonic areas such as the Kansas Precambrian basement.

II.vi. Acknowledgments

This research was funded under the framework of E2S UPPA supported by the Nouvelle-Aquitaine Region and by the “France 2030” Investment Program managed by the French National Research Agency (ANR-16-IDEX-0002). H. Derluyn acknowledges the support from the European Research Council (ERC) under the European Union’s Horizon 2020 research and innovation program (grant agreement No 850853)”. The authors thank Arnaud Proietti and Philippe De Parseval for conducting SEM and EMPA analysis at the Centre de Microcaractérisation Raimond Castaing, Université de Toulouse. The authors wish to acknowledge the Kansas Geological Survey and K.D. Newell for their help through sampling. Special thanks to Pascale Sénéchal for assisting in sample preparation and tomography of the K2 sample at DMEX, Université de Pau et des pays de l’Adour.

II.vii. Authors contributions

H.D., O.S., and E.D. designed the project. K.K. and S.C. conducted the EPMA analysis. V.C., S.C., and K.K. processed the acquired data. V.C. and K.K. did the H₂ calculation. V.C., S.C., K.K., H.D., O.S., and E.D., contributed to the final interpretations. V.C. wrote the manuscript and all authors contributed to its revision.

II.viii. Declaration of interest

The authors declare that they have no known competing financial interests or personal relationships that could have appeared to influence the work reported in this paper.

CHAPTER VII. Composition and origin of gases associated with high pH waters within the Mid-Rift System in Minnesota (USA)

This chapter aims at characterizing gas and water samples from northeastern Minnesota acquired during a sampling field trip in October 2023. The study was conducted in the northern part of the Mid-Rift System, where magmatic and volcanic complexes are outcropping. Wells with bubbling water were sampled for gas composition and isotopic analyses. Physico-chemical properties of the water were measured. Five wells show reduced water (negative Eh) with basic pH. The other wells show positive Eh and neutral to slightly basic pH. Gas analysis showed that gas from these five wells is dominated by CH₄ (up to 58%). The carbon and deuterium isotopic (¹³C-D) values of CH₄ display a mix of potential abiotic, biotic, and thermogenic origins. ⁴He in significant content is associated with this methane. Its isotopic signature shows a trend between atmospheric and crustal origin. In addition, two wells reaching the Tamarack intrusion, a dozen kilometers south of the other wells, were sampled for free gas. These wells present gases mainly composed of CH₄ (up to 68%), high contents of He (up to 1.3%), and no water. The ¹³C-D isotopic composition of methane and the C1/C2+ ratio suggests a complex origin, and as it stands, it is difficult to differentiate a thermogenic signature from a microbial signature. ⁴He isotopic signature is crustal. Traces of hydrogen were detected at the hundredth ppm level, suggesting a potential active generation in the subsurface overprinted by current consumption mechanisms. Those observations are complemented by the detection of volatile fatty acids (VFAs) such as formate and acetate at the hundredth μmolar level. The presence of those short-chain organic compounds suggests potential hydrogen consumption through abiotic carbon and hydrogen interaction or through microbial acetogenesis.

L'objectif de ce chapitre est de caractériser les échantillons de gaz et d'eau provenant du nord-est du Minnesota acquis pendant une mission de terrain réalisée en octobre 2023. L'échantillonnage a eu lieu dans la partie nord du Mid-Rift System là où les roches volcaniques et magmatiques du rift affleurent le mieux. Des puits d'eau servant à la consommation d'eau (potable ou non), présentant des eaux avec des bulles de gaz, ont été échantillonnés afin de déterminer la composition des gaz et leur signature isotopique. Les paramètres physicochimiques des eaux ont été mesurés sur le terrain en tête de puits. Cinq d'entre elles présentent des eaux réduites aux pH basiques. Les analyses de gaz ont montré que la majorité des échantillons sont constitués de CH_4 dont l'origine pourrait être en partie abiotique, biotique ou thermogénique. Des quantités significatives d'hélium sont associées à ce méthane. La signature isotopique de cet hélium est complexe à déterminer car celui-ci semble être caractérisé par une composante crustale ainsi que par une composante atmosphérique. Du gaz libre a été échantillonné dans deux autres puits (sans eaux associées) à l'aplomb de l'intrusion de Tamarack, appartenant elle aussi au MRS. Les gaz sont enrichis en CH_4 et 4He . Les signatures isotopiques de ces gaz semblent thermogéniques et microbiennes. Des traces d' H_2 ont été détectés dans certains de ces puits à des valeurs oscillant dans les centaines de ppm. Par ailleurs, des acides gras volatiles (VFAs) tels que le formate et l'acétate ont été quantifiés dans les eaux à des valeurs comprises entre 100 et 750 μ mol/l. La présence de ces composés organiques à chaînes courtes suggère une consommation potentielle d'hydrogène à travers des interactions abiotiques entre du carbone et l'hydrogène, ou un processus microbien d'acétogénèse.

I. Introduction of the chapter

Northeastern Minnesota is known for its Precambrian rocks. In that region, the Lake Superior part of the Mid-Rift System (MRS) intruded Paleoproterozoic and Archean rocks during the Mesoproterozoic. The basement is outcropping, as no Paleozoic, Mesozoic, or Cenozoic rocks are recorded in the area. In addition, the last glaciations preserved the basement rock from alteration for a very long time, so the outcrops are well preserved. The rocks have been highly mined, but Minnesota has a specific conservation policy for preserved core samples; many of them are accessible for academics to study, and the literature on rock type and mineralogy is extensive. The state also has many water wells directly drilled in the basement rocks, making associated waters easily accessible. In conclusion, this region allows for directly studying the Precambrian rocks of the rift that are deeply buried in Kansas, and the policy of data conservation allows for the collection of qualitative additional data that helps to find interesting spots.

With this in mind, we conducted a sampling mission in October 2023 in order to explore potential hydrogen and/or methane emissions. Gases and associated waters were sampled in northeastern Minnesota, where magmatic and volcanic rocks of the MRS are outcropping. This chapter aims to synthesize Minnesota geology and potential H₂-generating rocks, sampling conditions, and techniques used to characterize such gases. The results of gas chromatography (GC), gas chromatography combustion isotope ratio mass spectrometry (GC-C-IRMS), noble gases spectroscopy analyses, and high-performance liquid chromatography (HPLC) are displayed in the following chapter and discussed in order to identify the composition and origin of the sampled gases.

II. Article 3: Composition and origin of gases associated with high pH waters within the Mid-Rift System in Minnesota (USA)

Valentine Combaudon*^{1,2}, Olivier Sissmann¹, Julia Guélard¹, Don McKeever², Sonia Noirez¹, Hannelore Derluyn², and Eric Deville¹

1: IFPEN, Rueil-Malmaison, France ; 2 McKeever Drilling, Minnesota, USA ; 3: Université de Pau et des Pays de l'Adour, E2S UPPA, CNRS, TotalEnergies, LFCR, Pau, France

II.i. Abstract

H₂ emissions have long been studied at plate boundaries, in contexts where serpentinization of ultramafic to mafic rocks is believed to be dominant. Several studies have shown that occurrences of H₂ emissions are also recorded within intracratonic areas where the origin of the gas has yet to be determined.

The Mid-Continent Rift extends from Kansas to the Lake Superior region. It is a Precambrian aborted rift from 1.1 Ga composed of a multi-kilometric scale accumulation of mafic rocks. The southernmost part of the rift has been studied in Kansas because of occurrences of H₂ emissions in old wells. Water and gas associated with this H₂ have been analyzed and show that pH is almost neutral (7.4), the Fe content in the fluid is high (1.1mM), and He from crustal origin is present up to 2.9% (Guélard et al., 2017). The northernmost part of the rift, in Minnesota, is outcropping, and no gas wells have been studied so far. Only a few public water wells have been analyzed, showing the pH was highly basic. Such pH is known to be typical of H₂ production by serpentinization of mafic rocks and is a key parameter in hydrogen exploration.

Following a field sampling survey within the mafic rocks of Minnesota, wells presenting free gas or water with dissolved gas were sampled. Characterizing natural gas associated with intracratonic areas and being able to identify the origin of these gases are of major importance in providing key information for future natural gas exploration. The gases collected and analyzed by gas chromatography (GC) comprise He, CH₄, CO₂, and heavier hydrocarbons. H₂, up to 500 ppm, is recorded in several tested wells. Carbon and deuterium isotopic compositions of CH₄ were characterized by combustion isotope ratio mass spectrometry (GC-C-IRMS). Noble gas analyses were also conducted on these CH₄-rich gases. High-performance liquid chromatography (HPLC) was conducted on the associated waters to characterize their content of volatile fatty acids (VFA).

The results display three types of gases. Gas 1 is of thermogenic origin with depleted ¹³C-D isotopic values. Gas 2 seems abiotic as its ¹³C-D isotopic signature is heavy with significant hydrogen content. Gas 3 is potentially the result of a mix between a thermogenic and an abiotic gas as the ¹³C-D isotopic values are typical of thermogenic gases, but VFA contents seem to indicate an abiotic mechanism occurs in the subsurface. In addition, high pH (up to 11.4) and very low Eh (down to -300 mV) suggest redox reactions may have occurred in most of the wells sampled.

Keywords: abiotic methane, natural hydrogen, helium, Mid-Rift System, Precambrian

Highlights:

- CH₄ is the main component in the sampled gases, and its ¹³C and ²D isotopic signatures are complex. The Tamarack wells display free gas with isotopic values typical of a thermogenic origin. The DMK and BC wells have dissolved gases with isotopic values, which advocate for a potential mix of carbon sources.

- All gases are enriched in ^4He . Noble gas isotopy shows helium associated with the thermogenic CH_4 has a crustal origin. Helium associated with CH_4 having a more complex origin displays a crustal origin with atmospheric contamination.
- H_2 reaches nearly 500 ppm in DMK well#3, 100 ppm in DMK well#1, and 400 ppm in Tamarack well#2. The waters associated with DMK well#3 and the other DMK and BC wells are reduced and highly basic. In addition, all these gases (except those of DMK well#2) are associated with the iron-rich rocks of the Precambrian crust of Minnesota.
- Formate and acetate contents in waters of DMK well#1, DMK well#2, and BC well#1 are significant and testify to H_2 being consumed at the subsurface, potentially to produce CH_4 .

II.ii. Introduction

For a long time, natural hydrogen was only studied at the Mid-Oceanic Ridges (Welhan and Craig., 1979; Campbell., 1988) in lithospheric plate boundary areas where studies of the emissions were complex and their exploitation impossible. Methane was observed with this abiotic hydrogen, but in the continental domain, methane and heavier hydrocarbons were mostly considered biotic gases originating from microbial methanogenesis or thermogenic maturation of organic matter.

However, sub-surface fluids in the continental crust, rich in methane and natural hydrogen, are now intensively studied (Schoell., 1988; Sherwood-Lollar et al., 1988; Potter et al., 2004; Etiope and Sherwood-Lollar., 2013; Guélard., 2016, amongst many others). CH_4 and H_2 -rich fluids are now considered a major “fuel” for microorganism development within the crust (Nelson et al., 2005), but also, when found in significant amounts, as a reliable energy source (Truche et al., 2020). Methane origins are also studied to better constrain CH_4 variations within Mars’s atmosphere (Etiope et al., 2013).

As Precambrian rocks represent nearly 70% of the surface area of the continental crust (Goodwin., 1996) and are often not prone to thermogenic reactions, other production pathways of hydrogen and hydrocarbons have to be considered. For more than a decade, the scientific community has carried out a significant effort to better constrain abiotic reactions susceptible to produce hydrogen, methane, and other hydrocarbons within the Precambrian rocks of the continental crust.

These gases have been found and characterized in the Canadian Shield, the Fennoscandian Shield, or the Kansas Precambrian basement (Sherwood-Lollar et al., 1988, 1993, 2006, 2014; Guélard et al., 2017; Warr et al., 2019). Studies have shown that the gas content, the isotopic

values, as well as the physicochemical parameters of associated waters have similarities with gases of volcanic and geothermal origins, such as gases recorded at the Mid-Oceanic ridges (Welhan and Craig., 1979; Campbell., 1988) or in ophiolitic contexts (Deville et al., 2016). This led authors to suggest that abiotic reactions such as metamorphism of carbonate-graphite-bearing rocks or gas-water-rock interactions (GWRI) like iron carbonates decomposition (McCullom., 2003), or serpentinization (Moody., 1976) could produce significant amounts of H₂, CH₄, and other hydrocarbons within the Precambrian basement rocks. However, in such contexts, gases are often the results of mixing or postgenetic alteration, and their final content and isotopic values do not reflect their origin, making the study of such gases complicated. By coupling geology, major gases composition, and isotopy, as well as noble gases composition and isotopy, it is possible to constrain the origin and mechanisms responsible for such gas generation.

Northeastern Minnesota rocks have been described as part of the North American craton. Mesoproterozoic mafic and ultramafic rocks belonging to the Lake Superior part of the Mid-Rift System (MRS) have intruded Paleoproterozoic and Archean rocks (Miller et al., 2002; Jirsa et al., 2011) (Figure 38). We spotted these rocks for abiotic hydrogen and methane potential generation as they present similarities with the Canadian and Fennoscandian shields rocks as well as the H₂-CH₄-generating rocks of the Mid-Oceanic Ridges (MOR), and the Kansas Precambrian rocks. In this study, we present in-situ physicochemical parameters of waters associated with rocks from the MRS, as well as gas chromatography (GC), gas chromatography combustion isotope ratio mass spectrometry (GC-C-IRMS), noble gases spectroscopy, and high-performance liquid chromatography (HPLC) analyses performed on associated gases. This study aims to show that the Precambrian rocks of Minnesota are prone to produce abiotic hydrogen and short-chain organic compounds such as methane or volatile fatty acids (VFAs) and represent a unique opportunity to better constrain abiotic gas synthesis and to better understand the unique role of Precambrian rocks in hydrogen generation.

II.iii. Geological context

Minnesota rocks belong to the Canadian Shield and include rocks from the Archean to Cretaceous ages. A large majority of these rocks are Archean rocks divided into several sub-provinces, Paleoproterozoic rocks form the Penokean orogen and the Animikie basin, and Mesoproterozoic magmatic and volcanic rocks form the northern part of the Mid-Rift System (Figure 38).

This study was conducted within the northeastern Mesoproterozoic rocks of the MRS. This latter was formed between 1115 and 1086 Ma during 4 main rifting episodes (Miller et al., 2002). The first stage (1115 - 1107 Ma) is mainly outcropping near Lake Nipigon (Ontario,

Canada - Heaman et al., 2007) and corresponds to the earliest magmatism recorded with mafic to ultramafic rocks being formed. The latent stage (1107 - 1100 Ma) corresponds to a hiatus in the mafic magmatism due to extensive underplating of the crust by mantle melt, which causes partial melting of the crust and thus allows for crystallization of felsic rocks (Miller and Vervoort, 1996). The main stage (1110 - 1094 Ma) is characterized by magma with a tholeiitic composition (Miller, 2002). Finally, the late stage (1094 - 1086 Ma) of the rifting is characterized by the interbedding of lavas and detrital sedimentary rocks, marked by subsidence, and by the Grenville orogeny east of the rift (Cannon, 1994).

The rocks of the studied area are divided into several volcanic and magmatic complexes and into subsequent intrusions. The Tamarack intrusion, 80 km south of Duluth, is an ultramafic cumulate intruded in the Paleoproterozoic Animikie basin. The intrusion belongs to the first rifting stage and is not outcropping (Joslin., 2004; Goldner., 2011; Taranovic et al., 2015). A recent study (Taranovic et al., 2015) divided it into two major ultramafic intrusive sequences: the Bowl intrusion in the south and the Dike area intrusion in the north (which host most mineralizations). The Dike area is divided into the CGO for the coarse-grained olivine-bearing intrusion (Fo₈₉₋₈₂) and the FGO for the fine-grained olivine-bearing intrusion (Fo₈₄₋₈₂). They are made of peridotite, feldspathic peridotite, feldspathic pyroxenite, melatroctolite, and melagabbro. The Bowl peridotites comprise serpentine, magnetite, and chlorite as secondary minerals, traducing hydrothermal alteration and serpentinization.

Then, from the north of Duluth, the rocks forming the rift are divided into three complexes. The North Shore Volcanic Group (NSVG) is a co-magmatic volcanic and interflow sedimentary edifice of 7 to 10 km of thickness. The emplacement of this edifice was dated between 1108 and 1107 Ma by U-Pb on zircons (Green, 2002). The Duluth Complex was then emplaced into the base of the NSVG between 1108 and 1098 Ma. It is the main magmatic edifice of the rift with semi-continuous ultramafic to felsic rocks that cover nearly 5000 km² (Miller and Severson, 2002). The Duluth complex covers the pre-rift Paleozoic sedimentary rocks (Virginia Formation and Biwabik Iron Formation) and Archean granites and greenstone terranes (Giants range batholith). The complex is divided into 4 main syn-rift series: the layered series, the anorthositic series, the felsic series, and the early gabbroic series, which is divided into intrusions. Peridotites from the Duluth Complex have been studied and show evidence of altered olivine (Fa₃₆₋₄₄), fayalite (Fa₅₃₋₈₀), magnetite, and iron-rich clay minerals (Evans et al., 2017, see Chapter 7 - Supplementary figure 1). The Duluth Complex is covered the syn-rift Beaver Bay Complex, the younger and last magmatic complex of the area, emplaced between 1098 and 1095 Ma and divided into at least 13 intrusions of mafic and ultramafic rocks (Miller and Chandler, 1997). One of them is the Sonju Lake intrusion, which is composed of mafic and ultramafic rocks, especially oxidized olivine-bearing gabbros and serpentinized oxide dunites (Joslin, 2004). Isolated miscellaneous intrusions, made of mafic to felsic rocks, are also part of

the rift and are located at Canada's border. They are grouped with none of the complexes cited above because of uncertainties regarding the chronology of their formation (Miller et al., 2002). No post-rift Paleozoic or Mesozoic rocks are present in the studied area (Jirsa et al., 2011).

The studied wells reach intrusions of the Tamarack Complex, the Duluth Complex, the Beaver Bay Complex, the NSVG, and the Miscellaneous intrusions.

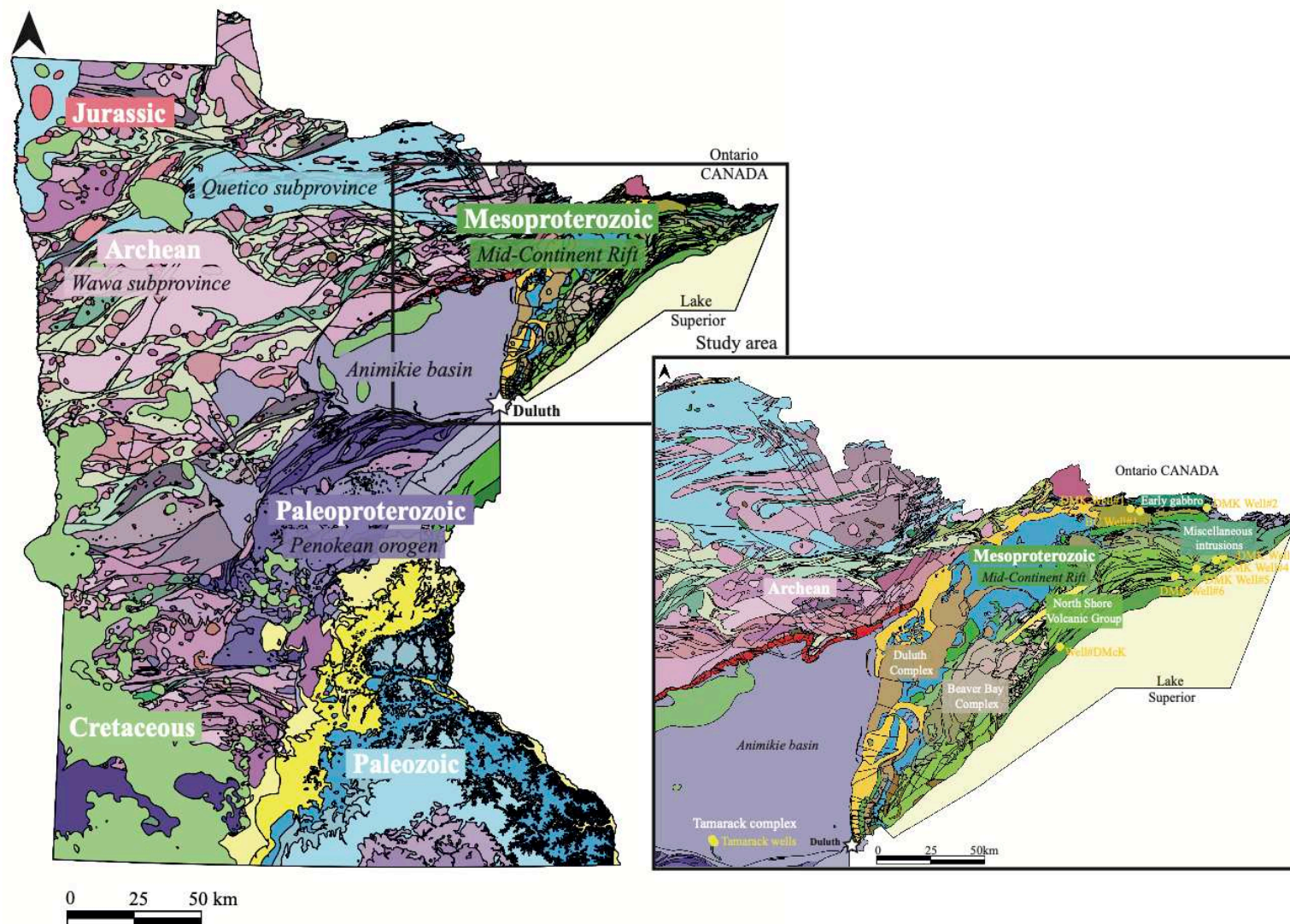


Figure 38: Simplified geological map of Minnesota with the location and zoom on our study zone with the major geological complexes and the location of the studied wells (gis data are from the Minnesota Geological Survey, see the complete description of the geological map in Jirsa et al., 2011).

II.iv. Materials and methods

II.iv.i. Surface measurements

Gas samples were collected on non-artesian wells. Thus, the water was flushed for over a minute in order to yield a representative chemical composition and not to measure old accumulated and re-equilibrated water in the wellhead. Temperature, redox potential (Eh), conductivity, and pH were measured for each water using a HI 98194 multiparameter from Hanna Instrument. Gas composition was measured for each well of the Tamarack intrusion using a GA5000 instrument. Two measures of the gas flux were performed for each gas well.

II.iv.ii. Gas sampling and well conditions

Tamarack Well #1 was not sealed and exposed to atmospheric contamination; we believe no gas flux was present. Tamarack Well#2 was correctly sealed, and at the opening of the well, a gas accumulation, as well as a small gas flux, were present. The gases were sampled at the opening of the well, in exetainers® (Labco©) and in steel containers that had been previously vacuumed. The gases were above the atmospheric pressure; thus, the steel containers were flushed with the gases before sampling. The expansion of the gases in the pre-vacuumed containers filled the exetainers.

DMK Wells and BC Well #1 are drinking water wells. DMK well#1 and DMK#1-2 are the same well sampled at two different times. Gas was present as bubbles within most of the wells we sampled. Thus, water was pumped from the aquifer, accumulated within a tank, and a sealed funnel was placed below the water surface to let the gas accumulate and to prevent any atmospheric contamination. Gas was sampled using a double-sided needle to connect a septum placed on the top of the funnel to vacuumed exetainers vials.

II.iv.iii. Gas analysis

II.iv.iii.i. Gas chromatography

Gas compositions of H₂, CH₄, CO₂, C₂H₆, O₂, and N₂ as trace components were determined by using a GC-BID 2030 from Shimadzu equipped with a Restek RT-Q-BOND 30m x 530 mmID column at IFPEN (Rueil-Malmaison, France). This GC is also equipped with an FID and a TCD column and is operated under a He gas carrier. These analyses were performed on gases sampled in exetainers. H₂, CH₄, CO₂, and C₂H₆ were quantified by a dedicated method implemented for this purpose. The chromatographic response was calibrated with external standards being a mixture of the studied gas at different concentrations. Uncertainties were determined by calculating standard deviations from gas standards and are displayed in the result section. Each analysis was bracketed with blanks.

A second GC connected to a gas line was used for pressurized gas samples stored in steel containers. Gas compositions of H₂, CH₄, CO₂, C₂H₆, O₂, and N₂ as main components were determined by using a GC-7890B from Agilent equipped with a PoraPlotQ column at IFPEN and operated under an N₂ gas carrier for He and H₂, and He for the rest of the species (Rueil-Malmaison, France). This GC is used to measure larger gas quantities than the GC-BID 2030 previously used. The chromatographic response was calibrated with external standards being a mixture of the studied gas at different concentrations. Uncertainties were determined by calculating standard deviations from gas standards and are displayed in the result section. Each analysis was bracketed with blanks.

II.iv.iii.ii. Noble gas spectrometry

Relative abundance of noble gases (⁴He, ²⁰Ne, ³⁶Ar, ⁸⁴Kr, ¹²⁹Xe, and ⁴⁰Ar/³⁶Ar) are determined using quadrupolar mass spectrometry. ³⁸Ar/³⁶Ar, ³He/⁴He, ²⁰Ne/²²Ne, ²¹Ne/²²Ne, and ²⁰Ne/⁴He ratios were determined using a VG spectrometry with a magnetic sector for higher resolute analysis. Noble gas spectrometry was performed at IFPEN (Rueil-Malmaison, France). Analytical uncertainties for each gas and ratios are displayed in the results section.

II.iv.iii.iii. GC-C-IRMS

The carbon isotopes of CO₂, CH₄, and C₂H₆ and the deuterium isotopes of CH₄ were measured using a MAT253 (Finnigan Mat-Thermo Fisher) triple collection mass spectrometer coupled to a gas chromatograph, operating with He as a carrier gas, at IFPEN (Rueil-Malmaison, France). Isotopes were calibrated using international standards. The analysis uncertainties are displayed in the results section. Each analysis was bracketed with blanks.

II.iv.iii.iv. High-performance liquid chromatography

Volatile fatty acids formate and acetate were quantified on an Agilent HPLC equipped with an Aminex HPX-87H from Biorad, and a spectra system RI 150 refractometer detector, which measures the refractive index of an analyte relative to the solvent. The solvent phase was deionized water with 0.01M sulfuric acid with an output of 0.6 mL.min⁻¹. The column was maintained at 60°C during the analysis. The apparatus also has a second detector, a Waters 2487 dual UV detector at 210 nm. As linear response and standard reproducibility were better on the RI detector, those results were considered over the UV. However, they can be found in Supplementary Table 1.

II.iv.iv. Summary of the analyses performed

Analysis done\Well	DMK well#1	DMK well#1-2	DMK well#2	DMK well#3	DMK well#4	DMK well#5	DMK well#6	DMcK well#1	BC well#1	Tamarack well#1	Tamarack well#2
Surface measurements	X	X	X	X	X	X	X	X	X		
GA 5000										X	X
GC (traces)	X	X	X	X		X	X			X	X
GC (majors)		X	X	X							X
Noble gases		X	X	X						X	X
GC-C-IRMS	X	X	X	X		X	X		X	X	X
HPLC	X	X	X	X	X	X	X	X	X		

Table 8: Summary of the analyses performed for each sample (X is for samples analyzed twice).

II.v. Results

II.v.i. Surface measurements

Water from DMK well#1, DMK well#1-2, DMK well#2, DMK well#3, and BC well#1 is reduced (Eh as low as -298.4 meV) and basic (pH ranges from 10.57 to 11.4). Water from DMK well#4, DMK well#5, and DMK well#6 is slightly reduced (Eh ranges from -20.8 to -32.3 meV) and neutral to slightly basic (pH ranges from 8.3 to 9.42). The water of the DMcK well is oxidized and basic (Table 9). In addition, measured temperatures are ranging from 5.64 to 11.82 °C.

	DMK Well#1	DMK Well#1-2	DMK Well#2	DMK Well#3	DMK Well#4	DMK Well#5	DMK Well#6	BC Well#1	DMcK Well	
Latitude	48.054779	48.054779	48.047316	47.841494	47.828946	47.796196	47.768139	48.042927	47.488058	
Longitude	-90.530676	-90.530676	-90.057707	-89.968807	-90.014867	-90.136688	-90.268604	-90.472453	-90.989913	
pH	11.4	10.57	10.57	10.64	9.42	9.23	8.30	10.71	10.40	10.55
Eh (mV)	-16	-241.8	-316.9	-219	-32.3	-25.9	-20.8	-298.4	134	129.5
Cond (mS/cm)	5952	6827	71	2594	9975	1927	2305	2566	167	102
T (°C)	5.64	6.52	9.4	10.4	8.09	5.72	9.40	6.72	11.82	7.99
Gas (Y/N)	Y	Y	Y	Y	N	N	Y	Y	N	N

Table 9: Physico-chemical parameters of water at the wellhead.

Tamarack well#1 was not correctly sealed from the atmosphere and did not present any gas flux or accumulation. Therefore, the GA500 analysis showed the detectable gas was mostly O₂ (with the balance being N₂). Conversely, Tamarack well#2 presented a gas accumulation at the opening and then a small gas flux. Measurements showed the gas was made of more than 90% CH₄ associated with 4.9 to 6.3% of O₂, 2000 to 1000 ppm of CO₂, and 14 to 15 ppm of H₂.

II.v.ii. Gas analysis

II.v.ii.i. Trace composition by Gas Chromatography

Tamarack Well#1 and Tamarack Well#2, DMK Well#1, DMK Well#1-2, DMK Well#2, DMK Well#3, DMK Well#5, and DMK Well#6, and BC Well#1 presented enough gas to be sampled. The gas was sampled at atmospheric pressure in exetainers and analyzed by gas chromatography to characterize their trace compositions (Figure 39) and their C1/C2 ratio (Table 10). CH₄ is the main compound and ranges from 2500 ppm to 18.83%, except for DMK wells#3, DMK well#5, and DMK well#6, where CH₄ ranges from 12.2 to 60.5 ppm (Figure 39). All samples are composed of CO₂, the Tamarack well#2 being the most enriched one in CO₂, with 8608.7 ppm (Figure 39). C₂H₆ has been detected, especially in gas where CH₄ concentration is high and ranges from 39.8 to 1484.2 ppm. Finally, H₂ has been detected in Tamarack Well #1, Tamarack Well #2, BC Well #1, and DMK Well #1-2, but never exceeded 10 ppm (± 3 ppm) (Figure 39).

Well name	Number of the sample	Injected volume mL	H ₂ ppm	σ ppm	CH ₄ ppm	σ ppm	CH ₄ %	CO ₂ ppm	σ ppm	C ₂ H ₆ ppm	σ ppm	C1/C2
Tamarack well 1	1	0.5			2498.3	8	0.25	130.8	24	46.2	2	54
Tamarack well 1	2	2	3.0	3	3229.1	85	0.32	141.0	24	39.8	2	81
Tamarack well 2	2	3.1	1.4	3	46203.3	25	4.62	62.6	24	467.4	4	99
Tamarack well 2	2	2			174223.8	25	17.42	297.2	24	1193.4	4	146
Tamarack well 2	1	0.5			188306.9	25	18.83	8608.7	24	1484.2	4	127
BC well#1	1	0.5	9.7	3	130622.4	25	13.06	45.9	24	681.3	4	192
DMK well#1	2	0.5			19889.8	25	1.99	48.2	24	410.8	2	48
DMK well#1	3	1			85776.1	25	8.58	30.1	24	467.0	4	184
DMK well#1	3	2			27651.1	25	2.76	17.3	24	187.8	4	147
DMK well#1-2	2	0.5	3.7	3	37904.7	25	3.79	5.5	24	1221.1	4	31
DMK well#2	1	0.5			50312.7	25	5.03	60.7	24	114.1	2	441
DMK well#2	2	2			35312.5	25	3.53	37.9	24	94.1	2	375
DMK well#3	1	0.5			12.2	8		382.5	24			
DMK well#3	3	2			18.8	8		679.7	24			
DMK well#5	1	0.5						735.4	24			
DMK well#6	1	0.5			60.5	8		246.3	24			

Table 10: Gas composition in H₂, CH₄, CO₂, and C₂H₆ analyzed as trace components, C1/C2 ratio. Blank spaces indicate no values were recorded.

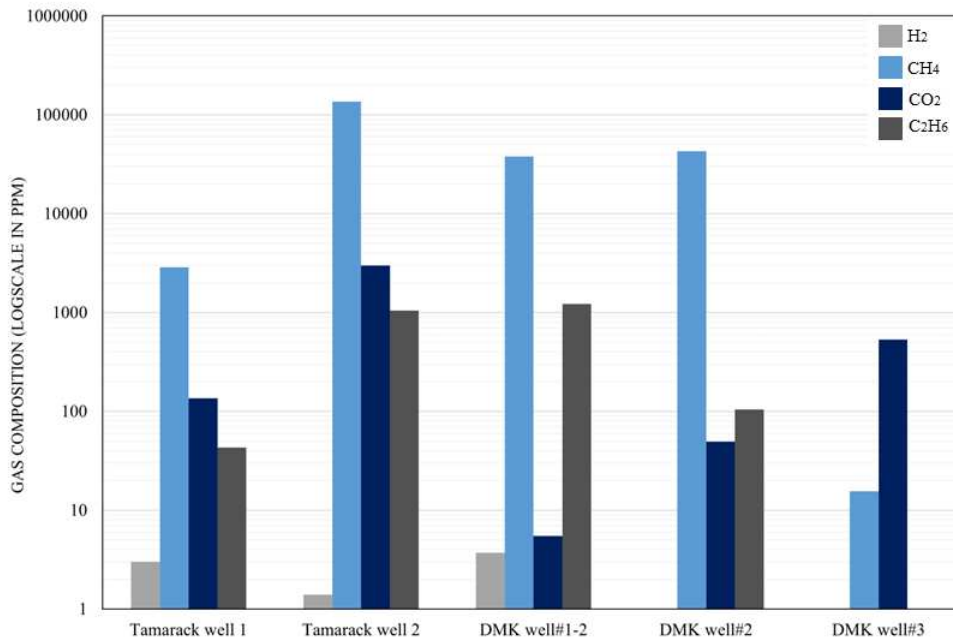


Figure 39: Gas composition in H₂, CH₄, CO₂, and C₂H₆ acquired by gas chromatography for Tamarack wells and DMK wells# 1-2, 2, and 3.

II.v.ii.ii. Major composition by Gas Chromatography

The gases were also sampled at atmospheric pressure in inox tubes and analyzed by gas chromatography to characterize their major gas compositions (Figure 40) and their C1/C2 ratio (Table 11). CH₄ is the main compound, ranging from 4 to 59.6%, except for DMK wells#3, where CH₄ reaches 400 ppm (Table 11). All samples are composed of CO₂, the Tamarack well#2 being the most enriched one, with 2158 ppm (Table 11). C₂H₆ has been recorded in DMK well#2-2 and DMK well#1 and ranges from 5420 ppm to 1.5% respectively. Finally, H₂ is recorded in DMK well#1-2, DMK well#3, and Tamarack well#2-1, with respective values of 53, 468, and 433 ppm.

Well name	DMK Well#1-2	DMK well#2	DMK Well# 2-2	DMK well#3	Tamarack well#2-1	Tamarack well#2-2
Corrected pressure	1198,3	1138,31	660,48	1164,57	1167,82	356,36
Normalized compositions (%)						
He	0,094	0,235	1,109	0,004	1,220	1,335
H ₂	0,005	0,000	0,000	0,047	0,043	0,000
CH ₄	52,326	4,272	59,486	0,004	58,714	59,619
CO ₂	0,167	0,016	0,186	0,047	0,105	0,216
Ar	0,000	0,000	0,000	0,000	0,000	0,000
O ₂	8,667	13,727	6,006	20,211	6,418	5,647
N ₂	37,591	82,085	32,607	79,691	33,315	33,160
C ₂ H ₆	1,552	0,020	0,548	0,000	0,541	0,550
C ₃ H ₈	0,034	0,007	0,011	0,000	0,010	0,011
i-C ₄ H ₁₀	0,008	0,001	0,005	0,000	0,004	0,005
n-C ₄ H ₁₀	0,029	0,006	0,002	0,000	0,000	0,001
Total	100	100	100	100	100	100
C₁/C₂+	34	210	109	131	109	108

Table 11: Gas composition in He, H₂, CH₄, CO₂, Ar, O₂, N₂, and C₂+ acquired by gas chromatography with a TCD and FID columns for Tamarack wells and DMK wells# 1-2, 2, 2-2, and 3.

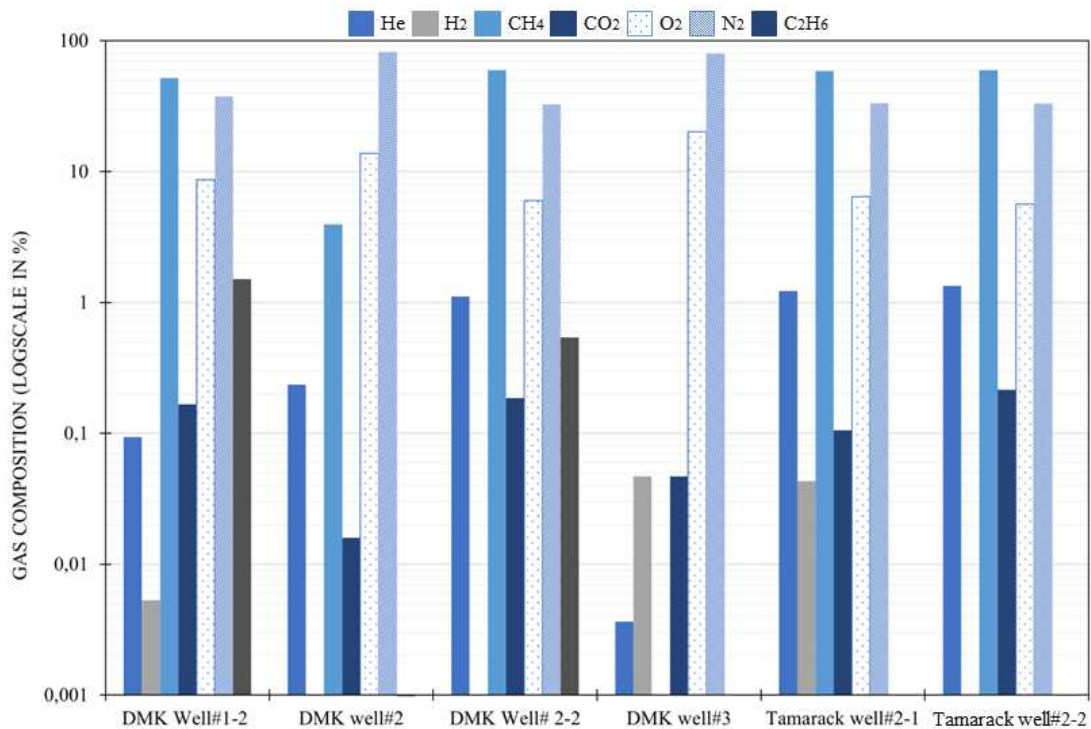


Figure 40: Gas composition in He, H₂, CH₄, CO₂, Ar, O₂, N₂, and C₂+ acquired by gas chromatography for Tamarack wells and DMK wells# 1-2, 2, and 3.

II.v.ii.iii. *Noble gas analysis by mass spectrometry*

Noble gas analysis was performed on gas samples from Tamarack well#1, Tamarack well#2 (two samples), DMK well#1-2, DMK well#2 (two samples), and DMK well#3. Such analyses were not performed on DMK well#1, DMK well#4, DMK well#5, DMK well#6, BC well#1, and DMcK well#1 which did not allow good gas sampling and thus gas analysis.

Atmospheric Derived Noble Gases (ADNG) of the Tamarack well#1, with values displayed in Table 12, have a typical atmospheric signature (Stute and Schlosser., 2000) (Figure 41). The $^{40}\text{Ar}/^{36}\text{Ar}$ ratio is 295.5 (air value, Nier., 1950). It is coherent with our field observations because the well was not sealed properly, and no gas flow was detected, which can explain the large atmospheric contamination of the sample.

ADNG contents of Tamarack well#2, Tamarack well#2-2, DMK well#1, DMK well#2, DMK well#2-2, and DMK well#3 show an atmospheric component with a small depletion in these gases (Table 12). ADNG patterns for DMK well#1-2 sample do not show a degree of depletion correlated with the elemental mass of the noble gases ($\text{Kr} > \text{Ar} > \text{Ne}$) as ^{84}Kr is less depleted than ^{20}Ne and ^{36}Ar , which is not the case for the other samples. The $^{40}\text{Ar}/^{36}\text{Ar}$ ratio of each sample is close to the air value of 295.5 (Nier., 1950).

Tamarack well#2 and Tamarack well#2-2 show a surprising enrichment in ^4He of $1.28 (\pm 0.09)$ and $1.32 (\pm 0.09) \%$ (Figure 41) in comparison with the atmospheric value of ^4He of 5.2 ppm (Glückauf and Paneth., 1946). DMK well#1-2, DMK well#2, DMK well#2-2, and DMK well#3 show lower but still significant enrichment in ^4He , with values of $2371.2 (\pm 164)$, $2594.1 (\pm 180)$, and $81.4 (\pm 6)$ ppm.

Helium of Tamarack well#2 has a crustal signature in each case with a $^3\text{He}/^4\text{He}$ ratio of $3.16 \cdot 10^{-8}$ and $2.74 \cdot 10^{-8}$ compared to the typical crustal $^3\text{He}/^4\text{He}$ ratio of $1.3 \cdot 10^{-8} \pm 0.009$ (Gerling et al., 1971). DMK well#1-2, DMK well#2, DMK well#2-2 values show a slightly crustal signature with $^3\text{He}/^4\text{He}$ ratio of $9.84 \cdot 10^{-8}$, $1.23 \cdot 10^{-7}$, and $1.20 \cdot 10^{-7}$. DMK well#3 $^3\text{He}/^4\text{He}$ ratio is $1.82 \cdot 10^{-7}$.

The $^4\text{He}/^{40}\text{Ar}$ ratios of Tamarack well#2 are respectively 4.15 and 4.48, which is coherent with the calculated ratio of the continental crust being 4.9 (Ballentine et al., 1991). DMK well#1-2, DMK well#2, DMK well#2-2, and DMK well#3 $^4\text{He}/^{40}\text{Ar}$ ratios are significantly lower than the calculated ratio of the continental crust.

The $^{40}\text{Ar}/^{36}\text{Ar}$ ratios of Tamarack well#2 associated with the ^4He enrichment do not show a crustal isotopic signature as they are similar to the atmospheric value which is coherent with the atmospheric component of the samples. DMK well#1-2, DMK well#2, DMK well#2-2, and DMK well#3 $^{40}\text{Ar}/^{36}\text{Ar}$ ratio associated with the ^4He enrichment traduce the atmospheric component of the samples.

Noble gas analyses reveal that all the gas sampled in Tamarack well have a crustal component (^4He enrichment) with a more or less important atmospheric contribution (Figure 42). DMK well#1-2, DMK well#2, DMK well#2-2, and DMK well#3, have a less pronounced crustal isotopic signature overprinted by the atmospheric component of the gases.

Sample	Tamarack well 1	Tamarack well 2-1	Tamarack well 2-2	DMK Well#1-2	DMK Well#2	DMK Well#2 (2)	DMK Well#3
Pressure (bar)	64	63,0	63,8	61,6	61,6	4,1	5
Date of analysis	22/3/23	8/3/23	9/3/23	12/4/23	3/5/23	3/5/23	4/5/23
Noble gases	ppm	ppm	ppm	ppm	ppm	ppm	ppm
^4He	9,7	12858,0	13258,7	1440,4	2371,2	2594,1	81,4
^{20}Ne	16,252	5,446	5,247	6,046	13,206	14,264	17,408
^{36}Ar	27,788	10,485	10,022	11,655	25,591	29,763	31,669
$^{40}\text{Ar}^*$	8211,48	3098,35	2961,59	3528,20	7562,23	8894,39	9358,28
^{84}Kr	5,84E-01	2,19E-01	1,91E-01	2,63E-01	4,19E-01	6,39E-01	6,11E-01
^{129}Xe	2,42E-02	1,17E-02	3,53E-03	1,05E-02	1,03E-02	3,10E-02	1,76E-02
$^{40}\text{Ar}/^{36}\text{Ar}$	295,5	295,5	295,5	302,7	295,5	298,8	295,5
$^{38}\text{Ar}/^{36}\text{Ar}$	0,018	0,019	0,019	0,019	0,019	0,019	0,019
$^3\text{He}/^4\text{He}$	1,00E-06	3,16E-08	2,74E-08	9,84E-08	1,23E-07	1,20E-07	1,82E-07
$^{20}\text{Ne}/^4\text{He}$	1,6786	0,0004	0,0004	0,0042	0,0056	0,0055	0,2139
$^4\text{He}/^{20}\text{Ne}$	0,596	2361,091	2526,710	238,222	179,552	181,865	4,676
$^4\text{He}/^{40}\text{Ar}$	0,00	4,15	4,48	0,41	0,31	0,29	0,01
NG uncert.	+/-	+/-	+/-	+/-	+/-	+/-	+/-
^4He	0,7	891,7	919,1	99,8	164,3	179,7	5,6
^{20}Ne	1,007	0,338	0,325	0,375	0,818	0,884	1,079
^{36}Ar	0,398	0,151	0,143	0,167	0,366	0,426	0,463
^{84}Kr	2,71E-02	1,02E-02	8,85E-03	1,22E-02	1,94E-02	2,97E-02	2,85E-02
^{129}Xe	2,24E-03	1,09E-03	3,12E-04	9,48E-04	9,59E-04	2,99E-03	1,65E-03
$^{40}\text{Ar}/^{36}\text{Ar}$	2,8	2,9	2,9	3,0	2,8	1,4	2,8
$^{38}\text{Ar}/^{36}\text{Ar}$	0,0	0,0	0,0	0,0	0,0	0,0	0,0
$^3\text{He}/^4\text{He}$	6,31E-08	8,40E-09	1,44E-08	1,46E-08	2,15E-08	1,22E-08	4,01E-08
Normalized to Air values	ppm	ppm	ppm	ppm	ppm	ppm	ppm
^4He	1,8	2453,8	2530,3	274,9	452,5	495,0	15,5
$^3\text{He}^*$	1,3	56,0	50,2	19,5	40,3	42,8	2,0
^{20}Ne	0,988	0,331	0,319	0,368	0,803	0,867	1,058
^{36}Ar	0,880	0,332	0,317	0,369	0,811	0,943	1,003
^{84}Kr	0,898	0,337	0,293	0,405	0,645	0,983	0,940
$^{40}\text{Ar}/^{36}\text{Ar}$	1,000	1,000	1,000	1,024	1,000	1,011	1,000
$^3\text{He}/^4\text{He}$	0,723	0,023	0,020	0,071	0,089	0,087	0,132

Table 12: Relative abundance of noble gases and isotopic ratios (^4He , calculated ^3He , ^{20}Ne , ^{36}Ar , calculated ^{40}Ar , ^{84}Kr , ^{129}Xe , $^{40}\text{Ar}/^{36}\text{Ar}$, $^{38}\text{Ar}/^{36}\text{Ar}$, $^3\text{He}/^4\text{He}$, $^{20}\text{Ne}/^4\text{He}$,) for each well, air normalized values and uncertainties.

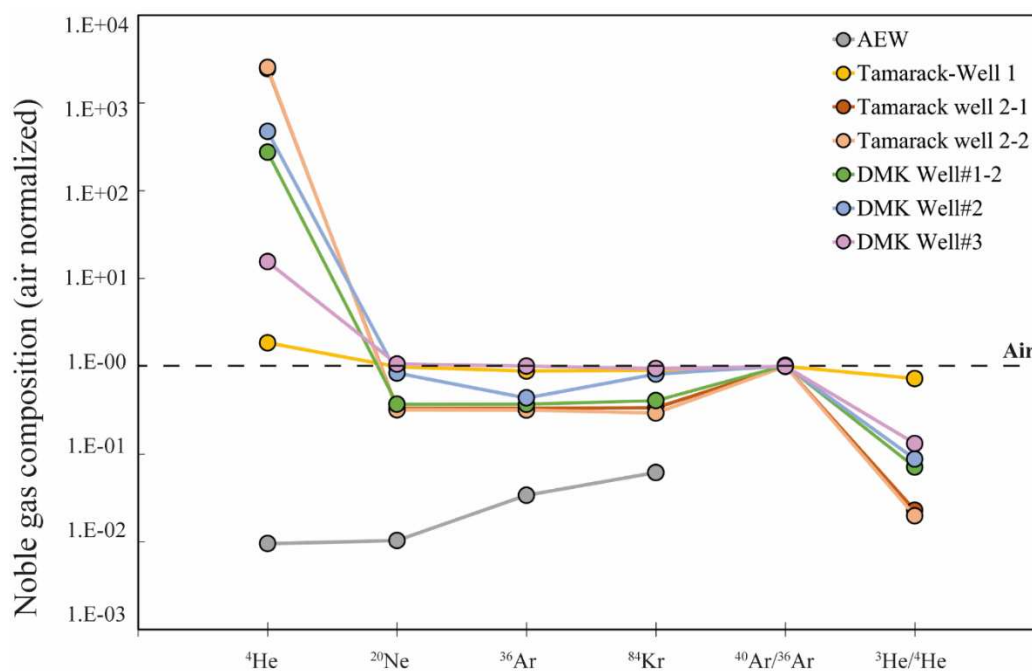


Figure 41: Relative abundance of the air-normalized isotope composition of noble gases (^4He , ^{20}Ne , ^{36}Ar , ^{84}Kr , $^{40}\text{Ar}/^{36}\text{Ar}$, and $^3\text{He}/^4\text{He}$) for each studied well. Also plotted is the relative abundance isotope composition of noble gas for the air-equilibrated water. Noble gases above the air average composition (black dashed line) are enriched compared to air, while all noble gases below the air average composition are depleted compared to air.

II.v.ii.iv. Methane isotopic composition analysis by GC-C-IRMS

Gas composition and associated carbon and deuterium content of the previously analyzed gas were acquired by GC-C-IRMS and are displayed in Table 13. Besides N_2 and O_2 , methane is the dominant compound in most wells, followed by CO_2 and C_2H_6 .

In the free gas wells, Tamarack well#1 displays significant CH_4 concentrations despite atmospheric contamination (up to 3424 ppm), with 131 to 172 ppm of CO_2 , and 43 to 50 ppm of C_2H_6 . Tamarack well#2 reaches 13% of CH_4 , 7051 ppm of CO_2 , and 1487 ppm of C_2H_6 . The second set of analysis performed on the gas sampled in inox tubes displays CH_4 concentrations up to 59.62%, with 5500 ppm of C_2H_6 , 110 ppm of C_3H_8 , and 50 ppm of i- C_4 .

In the water-bubbling wells, DMK well#1 methane concentrations range from 1.4 to 6.1%, with up to 59 ppm of CO_2 , and 467 ppm of C_2H_6 . DMK well#1-2 reaches 2.7% of CH_4 , 7 ppm of CO_2 , and 1224 ppm of C_2H_6 . The second set of analysis displays CH_4 concentrations up to 52.33%, with 1.6% of C_2H_6 and a few ppm of C_3H_8 , i- C_4 , and n- C_4 for DMK well#1-2. DMK well#2 displays 3.6% of CH_4 , 74 ppm of CO_2 , and 122 ppm of C_2H_6 . The second set of analysis displays CH_4 concentrations up to 4.3%, with 200 ppm of C_2H_6 and a few ppm of C_3H_8 , i- C_4 , and n- C_4 for DMK well#2. BC well#1 reaches 9.3% of CH_4 , 56 ppm of CO_2 , and 683 ppm of C_2H_6 . For DMK wells #3, 5, and 6, CO_2 is the dominant gas with up to 829 ppm, 897 ppm, and 300 ppm, respectively. Only DMK well#3 and 5 display CH_4 with up to 24 and 76 ppm.

In addition, most wells display trace amounts of H_2 , with values up to 500 ppm in DMK well#3.

Isotopic values displayed in this paragraph are average values from Table 14. Triplicate analyses were performed when possible on the sample. Tamarack well#1 is characterized by a deuterium value of -277‰ and a carbon isotopic value of -57‰. Tamarack well#2 has a deuterium isotopic value of -336‰ and a carbon isotopic value of -45‰, and a second set of values of -327 to -330‰ and -47 to -47.4‰. These two wells have the more ^{13}C and D-depleted methane values in this study.

The more enriched gases sampled are from DMK well#1-2, which has a deuterium isotopic value of -155 to -145‰ and a carbon isotopic value of -19‰ and DMK well#1 which has a deuterium isotopic value of -159‰ and a carbon isotopic value of -19‰. Thus, variations of the carbon

and deuterium isotopic content of CH₄ are recorded from one site to another. DMK well#2 has a deuterium isotopic value ranging from -279 to -274‰ and a carbon isotopic value of -31‰.

BC well#1 has a deuterium isotopic value of -274‰ and a carbon isotopic value of -30‰. These two wells have slightly ¹³C and ²H-enriched methane compared to Tamarack wells.

The carbon and deuterium isotopic signatures of CH₄ of the studied wells displayed a large range of values with ¹³C and D-depleted methane in Tamarack wells and ¹³C and D-enriched methane in DMK well#1, 1-2, 2, and BC well#1 compared to the Tamarack ones. These data show that it is complex to apprehend CH₄ origins in intracratonic settings and raise questions on:

- the geological source of carbon (Whiticar et al., 1986).
- the mechanisms of the generation (Lancet and Anders., 1970; Sherwood-Lollar et al., 1988, 1993, 2006).

Well name	H ₂ (ppm)	CH ₄ (ppm)	σ (±)	CO ₂ (ppm)	σ (±)	C ₂ H ₆ (ppm)	σ (±)	C ₁ /C ₂	δD CH ₄ per mil vs SMOW	σ (±)	δ ¹³ C CH ₄ per mil vs. VPDB	σ (±)
DMK well#1		31700,59	36327	38,92	27	365,51	218	87	-159,049	3,944	-18,892	0,737
DMK well#1-2	3,74	27039,36		6,67		1223,54		22	-155,060	0,678	-18,928	0,342
DMK well#2		30540,43	7566	60,18	20	111,57	15	274	-278,615	5,677	-30,955	0,518
DMK well#3		17,89	8	648,38	257							
DMK well#5				897,82								
DMK well#6		76,20		300,66								
Tamarack well 1	3,61	3015,71	577	151,47	29	46,11	5	65	-277,216	0,886	-58,678	0,125
Tamarack well 2	1,62	97190,22	78987	2496,84	5582	1050,45	742	93	-335,975	3,575	-45,345	7,533
BC well#1	9,73	93179,60		56,03		682,67		136	-274,079	1,472	-30,028	0,128

Table 13: Gas composition and isotopic ratios of δ¹³C of CH₄ per mil versus SMOW and δD of CH₄ per mil versus VPDB, with calculated standard deviation, for the first set of analysis (gas from exetenaurs). Blank spaces indicate no values were recorded.

Well name	H ₂ (ppm)	CH ₄ (%)	C ₂ H ₆ (ppm)	C ₃ H ₈ (ppm)	i-C ₄ (ppm)	n-C ₄ (ppm)	C ₁ /C ₂ +	δD CH ₄ per mil vs SMOW	δ ¹³ C CH ₄ per mil vs. VPDB
DMK well#1-2	100,00	52,33	15500,00	340,00	80,00	290,00	34	-144,91	-18,75
DMK well#2		4,27	200,00	70,00	10,00	60,00	214	-273,81	-31,13
DMK well#3	500,00								
Tamarack well 2-1	400,00	58,71	5400,00	100,00	50,00		109	-327,78	-47,4
Tamarack well 2-2	0,00	59,62	5500,00	110,00	40,00	10,00	108	-330,88	-47

Table 14: Gas composition and isotopic ratios of δ¹³C of CH₄ per mil versus SMOW and δD of CH₄ per mil versus VPDB for the second set of analysis (gas from inox tubes). No standard deviation is calculated for these results as only one injection and analysis were done for each sample. Blank spaces indicate no values were recorded.

II.v.ii.v. Volatile Fatty acids analysis

HPLC analysis of the sampled fluids shows that some of the samples contain high concentrations of formate and acetate (see Table 15). Four of the samples collected at private water wells (DMK well#1, DMK well#2, D.MCK well#1-4, and BC well#1-4) show acetate

values between 178 and 191 $\mu\text{mol/L}$. Formate concentration in those samples exhibits higher values, varying between 629 and 756 $\mu\text{mol/L}$. Those values are given with a 10% uncertainty obtained on an external standard. The absence of VFAs' detection in the remaining five water samples may result from improper sampling or sample conservation.

Lake Superior (this study, Precambrian Canadian shield)		
#Well_Sample	Acetate ($\mu\text{mol/L}$)	Formate ($\mu\text{mol/L}$)
DMK well#1.1	181	756
DMK well#2	178	629
DMK well#1-2.4		
DMK well#3.4		
DMK well#4.1		
DMK well#5.4		
DMK well#6.4		
D.MCK well#1	191	643
BC well#1.4	183	635

Table 15: Acetate and formate concentrations in sampled fluids. Blank space indicates compounds were below the detection limit.

II.vi. Discussion

II.vi.i. Helium origin

Such helium content, up to 1.3% in the Tamarack well#2 gas, raises questions about its origin. $^3\text{He}/^4\text{He}$ and $^4\text{He}/^{40}\text{Ar}$ ratios of Tamarack well#2 and DMK well#1-2 are favorable for a crustal origin of helium (Figure 42). Similar helium content and $^3\text{He}/^4\text{He}$ ratios have been measured for gases from the Canadian Shield (Sherwood-Lollar et al., 1988, 1993). For DMK well#1-2, DMK well#2, and DMK well#3, the crustal isotopic origin of ^4He is mixed with the isotopic signature of atmospheric helium. The U, Th, and K content of the rocks and the Li content of the fluids are not known yet; thus, the proportion of such crustal helium in the measured gases can't be determined yet.

All three gases have similar ratios to those obtained for Kansas samples attributed to a crustal origin (Guélard et al., 2017).

A mantle origin for helium seems not convincing as the typical magmatic $^3\text{He}/^4\text{He}$ ratio ranges from $8.42 \cdot 10^{-6}$ to $1.40 \cdot 10^{-5}$ (O'Nions and Oxburg., 1983). The $\text{CO}_2/^3\text{He}$ ratio of the MORB ranges from $1 \cdot 10^9$ to $10 \cdot 10^9$ (Marty and Jambon., 1987), while the $\text{CO}_2/^3\text{He}$ ratio calculated from the noble gas composition in Table 12 displays values between 18 and 234 for the five studied wells (Chapter 7, Supplementary table 3). This excludes a mantellic origin of helium. In addition, the $^4\text{He}/^{40}\text{Ar}$ ratios are lower than the average mantellic ratio of 1.7 (Ballentine et

al., 2002) or much higher in the case of the Tamarack wells, which correspond to the average crustal ratio of 4.9 (Ballentine et al., 1991).

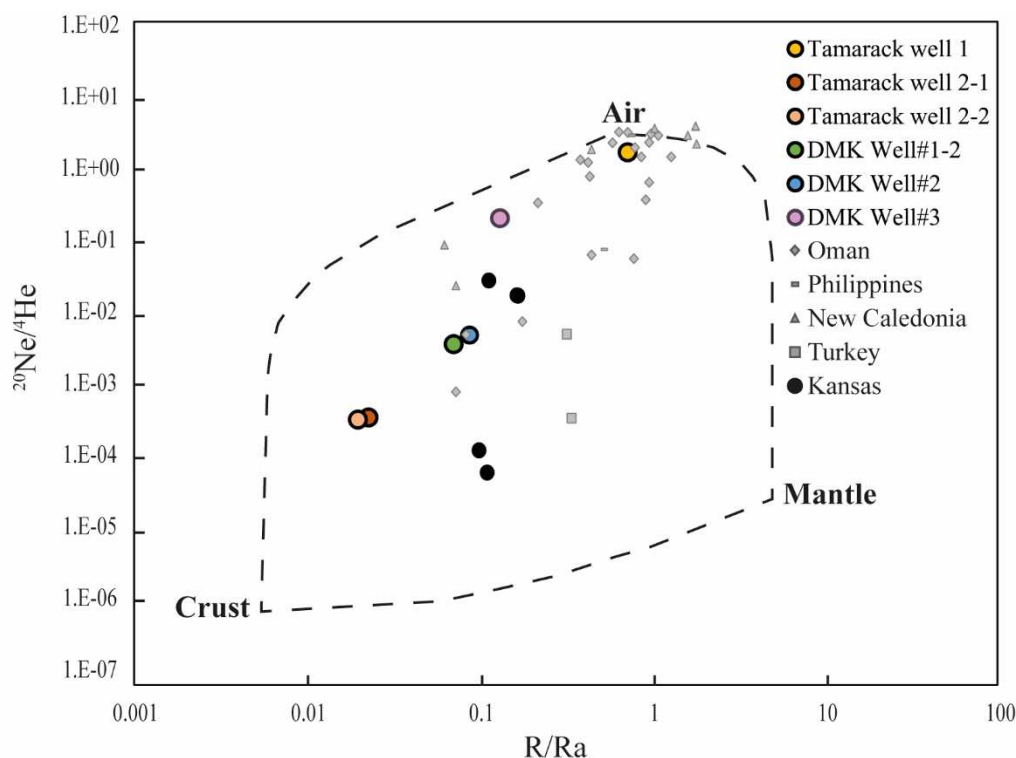


Figure 42: $^{20}\text{Ne}/^4\text{He}$ in the function of R/Ra ($^3\text{He}/^4\text{He}$ air normalized) for each well with air, crustal, and mantle endmembers (Additional points in grey and black are from Christel Vacquand's Ph.D. dissertation (2011), Julia Guélard's Ph.D. dissertation (2016), and Vacquand et al., 2018).

With our current data, it is also complex to determine the closed or open nature of the system from which helium originates, and thus the potential mixing of gases of different origins, which may result in the isotopic signature of DMK well# 1-2, DMK well#2, and DMK well#3. U, Th, K, and Li contents of rocks and fluids will be determined in a further study and might give information on the residence time of ^4He and ^{40}Ar within the system. Such data should help to estimate the origin and the potential mixing of the gases studied.

II.vi.ii. What are the different pools of methane?

Methane is typically distinguished by the origin of its carbon atoms and by its producing reaction (Etiope and Sherwood-Lollar., 2013). It can form through the thermogenic degradation of organic matter (Equation 21) (Welhan., 1988; Seewald., 2003).

(Equation 21): $\text{RCH}_2\text{CH}_2\text{CH}_3 + 4\text{H}_2\text{O} \rightarrow \text{R} + 2\text{CO}_2 + \text{CH}_4 + 5\text{H}_2$ (Seewald., 2003)

It can also be from microbial methanogenesis pathways conducted by hydrogenotrophic, formatotrophic, or acetotrophic methanogens (Woltemate et al., 1984; Whiticar et al., 1986; Miller et al., 2018). Microbial methane is typically ^{13}C -depleted and covers a wide range of deuterium values (Whiticar et al., 1986; Giunta et al., 2019). In that scenario, the methane isotopic signature is influenced by the different biological metabolisms, i.e., the carbon source and the genetic processes.

In fine it is also influenced by the availability of the carbon resource at the sampling time, i.e., by the post-genetic processes such as mixing, migration, or biodegradation. Lighter carbon is more easily consumed by living organisms, which only leave heavier carbon available in the gas. Such consumption directly influences the carbon isotopic signature. Thermogenic methane is, therefore both ^{13}C and D-enriched compared to biogenic methane (Schoell, 1988; Sherwood-Lollar., 1993). The isotopic signature of thermogenic methane is highly dependent on temperature and pressure conditions, migration processes, and post-generation interactions with microbial activity (Schoell., 1988).

On the other hand, abiotic methane can be produced by several reactions, which are divided into magmatic or mantle-derived CH_4 (Equation 22) and gas-water-rock interactions (GWRI). The main abiotic reactions considered in this study are uncatalyzed aqueous CO_2 reduction (Equation 23), methanation (or Sabatier reaction) (Equation 24), and carbonate methanation (Equation 25). Two types of isotopic signature are described for abiotic methane: 1) ^{13}C -D-enriched values or “heavy abiotic CH_4 ” characteristic of volcanic-hydrothermal systems, and 2) ^{13}C -D-depleted values or “light abiotic CH_4 ” characteristic of Precambrian crystalline igneous rocks (Etiopie and Sherwood-Lollar., 2013).

(Equation 22): $\text{CO}_2 + 2\text{H}_2\text{O} = \text{CH}_4 + 2\text{O}_2$ i.e., late magmatic despeciation of C-O-H fluids during magma cooling (Etiopie and Sherwood-Lollar., 2013).

(Equation 23): $\text{CO}_2 + \text{H}_2 \rightarrow \text{HCOOH}$ (formic acid), $\text{HCOOH} + \text{H}_2 - \text{H}_2\text{O} \rightarrow \text{CH}_2\text{O}$ (formaldehyde), $\text{CH}_2\text{O} + \text{H}_2 \rightarrow \text{CH}_3\text{OH}$ (methanol), $\text{CH}_3\text{OH} + \text{H}_2 - \text{H}_2\text{O} \rightarrow \text{CH}_4$ i.e., *uncatalyzed aqueous CO_2 reduction* (Seewald et al., 2006)

(Equation 24): $\text{CO}_2 + 4\text{H}_2 = \text{CH}_4 + 2\text{H}_2\text{O}$ i.e., *methanation*

(Equation 25): $\text{CaCO}_3 + 4\text{H}_2 = \text{CH}_4 + \text{Ca}(\text{OH})_2 + \text{H}_2\text{O}$ i.e., carbonate methanation (Reller et al., 1987)

Abiotic methane is, at the current state of knowledge, defined by a dozen of potential reactions and covers a wide range of carbon and deuterium isotopic signatures. During the reaction, multiple carbon sources can be recorded and impact the origin of the final carbon isotopic

signature. In addition, experimental studies have shown that experimental abiotic ^{13}C values of CH_4 can overlap thermogenic values of CH_4 (McCollom., 2013). Thus, abiotic methane is hardly uniquely distinguishable by its isotopic signature as it often overlaps thermogenic and biogenic isotopic signatures.

Other geochemical and geological tools can be used in order to better constrain methane origins, such as noble gases and associated species composition and isotopy, regional geology, and hydrogeology, and the identification of potential postgenetic alteration processes that may change the final isotopic signature, such as mixing, oxidation, or even fractionation (Etiope and Sherwood-Lollar., 2013).

II.vi.iii. The Northeastern Minnesota methane

II.vi.iii.i. Similarities with other Precambrian shield isotopic values of methane

In the case of northeastern Minnesota gases, the carbon and deuterium isotopic signatures cover a wide range of values. Tamarack well#2 has the most ^{13}C and ^2H -depleted CH_4 with values similar to values of the Witwatersrand Basin (Driefontein mines, South Africa). Indeed, the Driefontein gases display carbon isotopic values of CH_4 between -40.2 to -55.5‰ and deuterium isotopic values of CH_4 between -218 to -403‰. The rocks of the Driefontein mines are volcano-sedimentary rocks overlaying 3.0 Ga granitic rocks. The methane analyzed was characterized as abiogenic at the time of the study (Sherwood-Lollar et al., 2006). It should, however, be mentioned that an increased amount of literature since then would suggest such signatures to be characteristic of thermogenic gases.

BC well#1 and DMK well#2 follow the same isotopic trend with slightly less depleted carbon and deuterium isotopic values. Their ^{13}C and D contents are similar to the ones of the Fennoscandian shield (Juuka region, Finland). Indeed, the Juuka gases display carbon isotopic values of CH_4 between -22.4 and -29.3‰ and deuterium isotopic values of CH_4 between -200 and -281‰. The rocks bearing the Juuka gas accumulation are composed of serpentinized and altered ultramafic rocks, and the methane of the Juuka region has been characterized as abiotic (Sherwood-Lollar et al., 1993).

DMK well#1 and DMK well#1-2, which are two different samples of the same well, have more ^{13}C and D-enriched values similar to the ones found in volcanic-hydrothermal systems little affected by organic matter in sediments (Etiope and Sherwood-Lollar., 2013). This origin does not seem coherent with the intracratonic context of the sampling area, and such deuterium and carbon isotopic signatures may represent mixing processes with an abiotic trend.

II.vi.iii.ii. *The northeastern Minnesota methane origins from ^{13}C -D isotopic values*

Figure 43 displays the deuterium values in function of the carbon values of CH_4 for each studied well. The Tamarack well#1 is subject to important atmospheric contamination, thus, its carbon and deuterium isotopic signatures are difficult to interpret but seem to be the result of a mix between a thermogenic and a microbial origin.

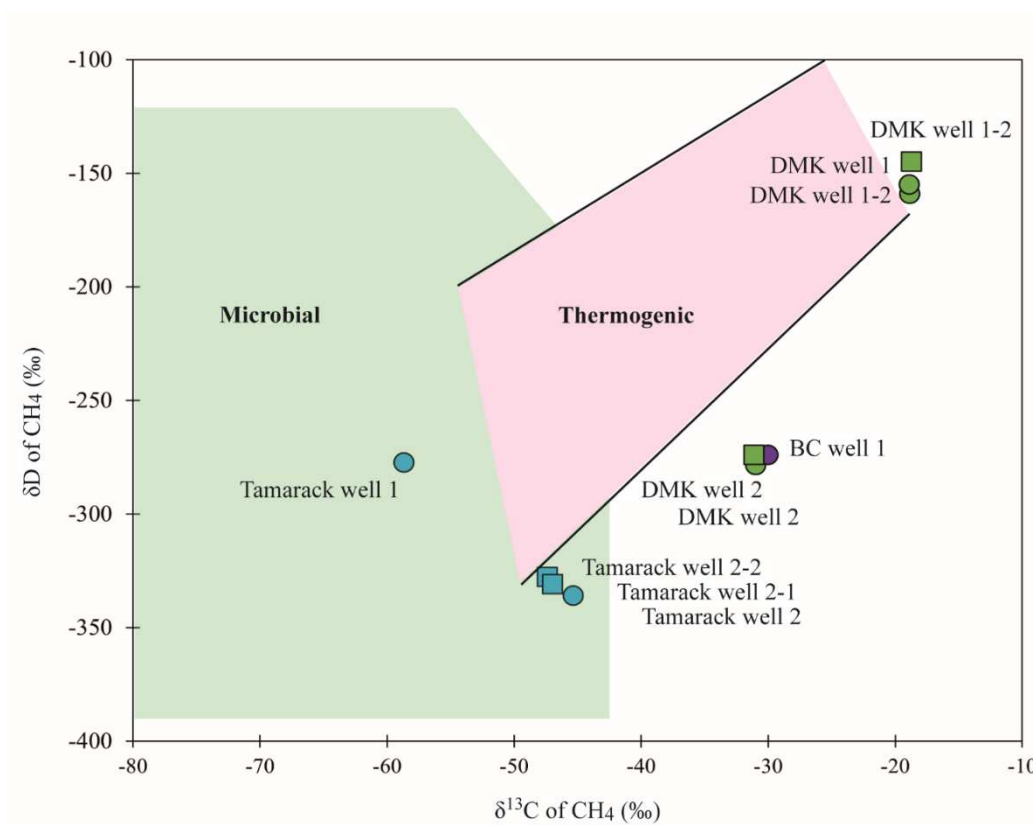


Figure 43: Schoell diagram of deuterium isotopic values of methane versus carbon isotopic values of methane for the Tamarack wells, the DMK wells# 1, 1-2, 2, and 3, as well as BC well#1. The dots are for the first set of analyses. The squares are for the second set of analyses (modified from Giunta et al., 2019).

Tamarack wells#2 values, while being outside of the current delimitations of thermogenic values, are ^{13}C -D depleted and could be considered thermogenic. It is, however, impossible to rule out a microbial component for such gases. DMK well#2 and BC well#1 values are outside the thermogenic delimitations in Figure 43 but their ^{13}C -D depleted values could be thermogenic as well as microbial. For DMK well#1 and DMK well#1-2 the isotopic values display a different trend with ^{13}C -D enriched values which could potentially be abiotic.

Figure 44 displays the ^{13}C isotopic values of CH_4 in function of the $\text{C}1/\text{C}2+$ ratio. Tamarack gases are once again outside of the described values of thermogenic and microbial methane.

Their isotopic values are depleted, and their C1/C2+ ratios are around 100. They could have originated from thermogenic processes as well as biological ones. DMK well#2 and BC well#1 have C1/C2+ values between 100 and 1000 and might reflect the mixing of gases of different origins with a major thermogenic trend. DMK well#1 and DMK well#1-2 have C1/C2+ values below 100 but with a ¹³C enriched methane and could correspond to abiotic gases. Their origin is complex to establish.

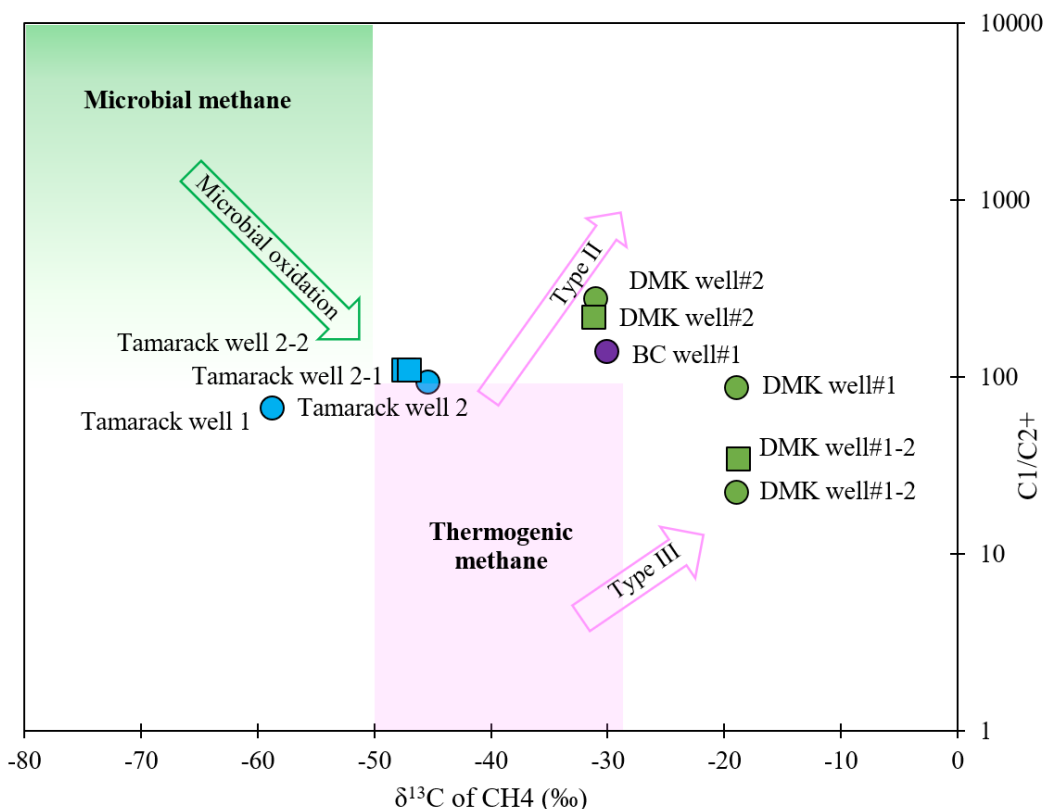


Figure 44: Bernard diagram of carbon isotopic values of methane versus C1/C2+ ratios for the Tamarack wells, the DMK wells# 1, 1-2, 2, and 3, as well as BC well#1. The dots are for the first set of analyses. The squares are for the second set of analyses.

II.vi.iii.iii. Geology as a tool to help identify methane origins

To support the potential origin of the methane recorded in the Tamarack well#2, DMK well#1, DMK well#1-2, DMK# well 2, and BC well#1, one can look at the rocks reached by those wells.

DMK well#1 (and so DMK well#1-2) reaches gabbroic cumulates of the Duluth Complex from the Mid-Rift System (all rock types and well depths are reported by the Minnesota Department of Natural Resources). One could imagine that such rocks have been the location of GWRI like serpentinization which could explain the complex isotopic signature of the gas. We infer that methane could have been produced by equation 24 or 25. Our current state of knowledge does

not allow us to be more specific. The presence of traces of hydrogen in the gas phase and associated reduced and basic pH waters are good indicators for a hydrogen-producing reaction to actually happen in these iron-rich rocks and thus to provide H₂ for equations 24 and 25. It is also impossible to eliminate or confirm reaction 26 as we do not know any occurrence of carbonates-bearing rocks in the studied area, and we do not have access yet to water chemistry.

DMK well#2 reaches Paleoproterozoic metamorphic rocks derived from shale-rich sedimentary rocks (all rock types and well depths are from the Minnesota Department of Natural Resources). DMK well#2 ¹³C and ²H-depleted isotopic values fit well with a thermogenic origin, which could be explained by the shale-rich rocks prone to producing hydrocarbons.

BC well#1 reaches gabbroic cumulates of the Duluth Complex (all rock types and well depths are from the Minnesota Department of Natural Resources). This latter has already been described as serpentinized in some parts (Evans et al., 2017).

The Tamarack well#2 reaches, at 613 meters, the olivine cumulates of the Tamarack intrusion, previously described as serpentinized (Goldner et al., 2011). However, the intrusion lies on the Animikie Paleoproterozoic rocks, where metasedimentary black shales have been described (Taranovic et al., 2015) and could induce a thermogenic production of methane.

II.vi.iii.iv. Formate and acetate synthesis as a tool to distinguish thermogenic, microbial, and abiotic gases

The presence of VFAs in significant amounts strongly indicates that H₂ is being consumed in the subsurface, either by abiotic synthesis or microbial activity. As demonstrated experimentally by various authors (McCollom and Seewald, 2007), Fischer-Tropsch-Type (FTT) reactions (such as the Sabatier reaction) occurring in water do not directly produce methane from H₂ and CO₂ (or CO) interactions, but rather intermediate organic compounds, with varying degrees of oxidation (Figure 45). Such species have also been described in natural sites where H₂ is emitted (Lang et al., 2020), and are believed to form on the reaction pathway to methane, with decreasing redox conditions.

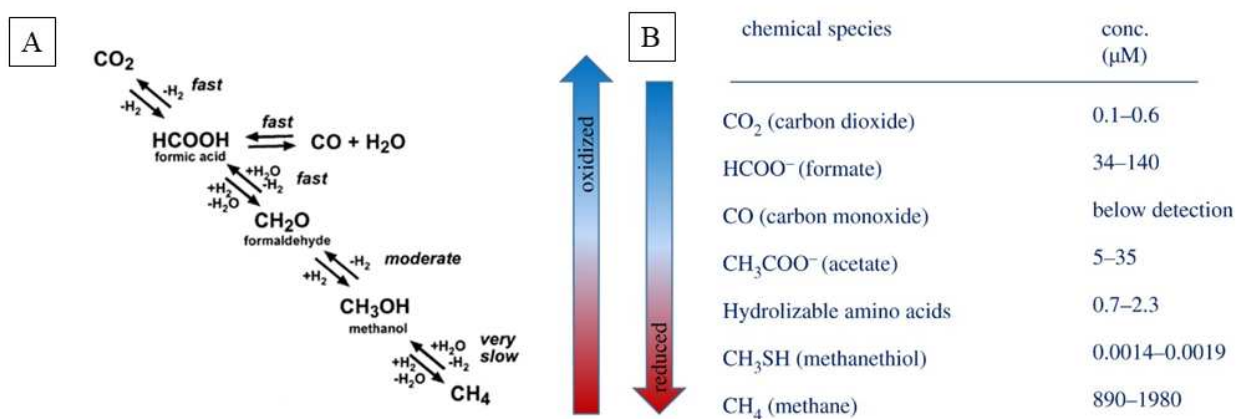


Figure 45: A- Intermediate species forming experimentally during CO_2 and H_2 interactions in water, along the reaction pathways to CH_4 (McCollom and Seewald, 2007); B- Chemical compounds detected within the lost city hydrothermal fluids, listed with decreasing redox potential (from Lang et al., 2020)

Amongst those intermediate species, commonly known as the “building blocks of life” (Proskurowski et al. 2008), literature studies of natural sites have mostly focused on short-chain organic acids formate and acetate, as they appear to be the organic compounds with the highest concentrations, and thus the easiest to detect and quantify. Whether they are formed in high pH environments (Lost City hydrothermal vent, Lang et al., 2018; Marianas mud volcanoes, Eickenbusch et al., 2019; The Cedars ophiolitic complex, Kohl et al., 2016) or near-neutral pH brines (Kidd Creek Precambrian shield, Sherwood-Lollar et al., 2021), the current consensus on their formation mechanisms lies in abiotic synthesis through interaction of H_2 and carbonate radicals. Figure 46 compares the concentrations of those species between Lake Superior water wells (this study), Kidd Creek, The Cedars, the Marianas mud volcanoes, and Lost City hydrothermal fields.

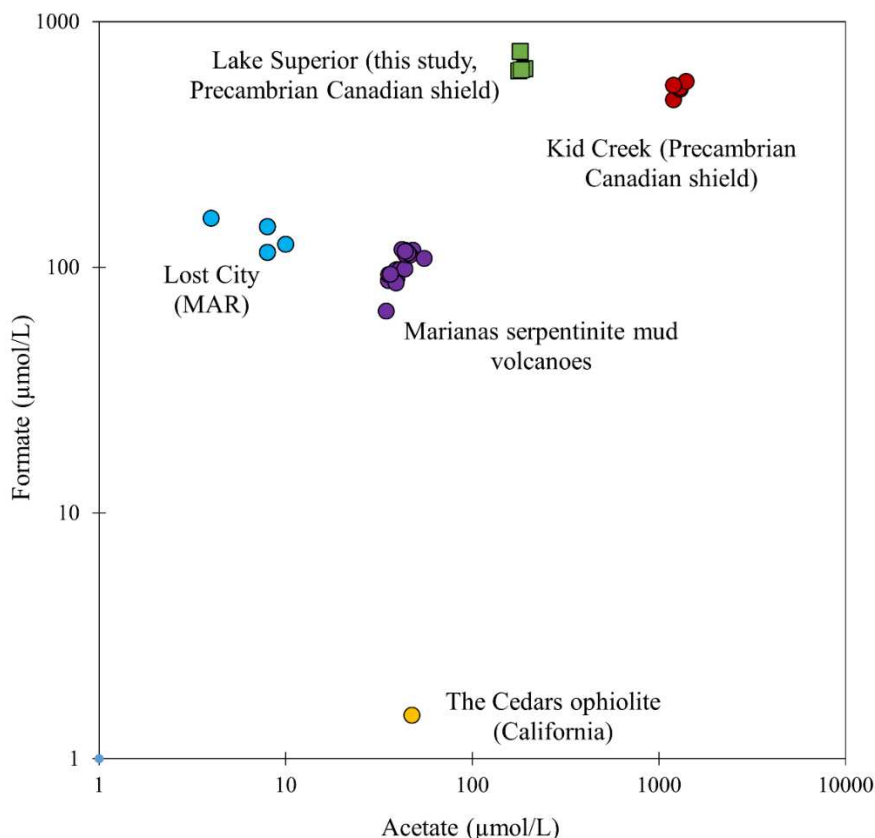


Figure 46 : Formate and acetate concentrations in brines collected at H_2 and CH_4 producing sites. High concentrations suggest abiotic synthesis. Data from this study, Sherwood-Lollar et al., 2021, Kohl et al., 2016, Eickenbusch et al., 2019 and Lang et al., 2018.

In most sites, formate is in greater concentration than acetate. It could be explained by the fact that the shortest organic compounds form first from dissolved carbonate radicals by consuming H_2 , before transforming to less oxidized molecules. Kidd Creek brines, however, exhibit remarkably high levels of acetate (over 1000 μM), higher than formate (up to 600 μM). Furthermore, the heavy isotope values of those compounds (up to -6.9‰ for acetate; Sherwood-Lollar et al., 2021) strongly suggests they could not have been produced by acetogens microbial community, or derived from the isotopically light TOC within the host rocks.

The samples collected in the Canadian Precambrian shield along Lake Superior in private water wells have high concentrations of formate, just like the ones reported for Kidd Creek brines. Those high values, up to 756 $\mu mol/L$, raise the possibility of abiotic synthesis reactions to occur. Combined with hundreds of ppm of H_2 and a “heavy” isotopic composition of CH_4 (-30‰ to -18‰), these values sit on the border between abiotic and thermogenic signatures. The presence of those VFAs suggests that H_2 is being produced in those brines and consumed as it circulates through the subsurface up to the surface. Isotope data on the fluids would provide additional insight into the formation mechanisms of those compounds. Whether it’s 100%

abiotic or not, a partly microbial production of those volatiles, through acetogenesis, for instance, would still be consuming hydrogen, suggesting its presence in the subsurface.

II.vi.iv. Global Picture

It is well known that it is difficult to accurately isolate methane origin because 1) the source of carbon can be multiple and 2) sub-surface interactions with microbial activity or other postgenetic alterations processes can influence the final isotopic signal. However, the gases studied seem to differentiate into three gases: gas 1) the lighter gases from Tamarack with a potential thermogenic or microbial origin, gas 2) the heavier gases from DMK well#1 and 1-2 with a potential abiotic origin, and gas 3) right in the middle, the gases from DMK well#2 and BC well#1 which isotopic signatures support mixing of different origins, especially a thermogenic and a microbial one.

Gas 1: Tamarack well#2 has significant CH₄ concentrations associated with CO₂, H₂, and heavier hydrocarbons. The ¹³C-D isotopic values of CH₄ are the most depleted of all the gases analyzed. Tamarack well#2 reaches 1.3% of ⁴He, its isotopic signatures, ⁴He/³He, and ⁴He/⁴⁰Ar ratios, are similar to crustal ones. The well reaches the ultramafic Tamarack intrusion, which underlies black-shale-rich rocks of the Paleoproterozoic part of the basement. These gas and rock characteristics support the idea of a mix of different processes at the origin of gas 1.

Gas 2: DMK well#1 (and well#1-2) has heavy ¹³C-D isotopic values of CH₄ and displays significant values of VFA with higher contents of formate than acetate. ⁴He content is still high (>1000 ppm), and its isotopic signature shows a crustal component. Both wells display formate and acetate concentrations above 150 μM/L. VFAs suggest hydrogen production could have happened in the subsurface and be consumed to produce methane by abiotic or biotic processes. Associated waters are reduced and basic, similar to those found in serpentinization contexts (Kelley et al., 2005; Vacquand., 2011; Deville et al., 2016, amongst others). The wells reach the mafic and ultramafic rocks of the MRS, which make a significant part of the basement. All these gas and water characteristics support the idea of an abiotic reaction being at the origin of gas 2.

Gas 3: BC well#1 and DMK well#2 have more depleted ¹³C-D isotopic values of CH₄ but present VFA with concentrations in the same order as DMK well#1. ⁴He content is high (>2000 ppm) and its isotopic signature shows a crustal component. Both wells display formate

and acetate concentrations in waters above 150 $\mu\text{M/L}$, coherent with a subsurface H_2 production. The associated waters are reduced and basic. What is striking is DMK well#2 reaches metasedimentary Paleoproterozoic rocks, and BC well#1 reaches mafic rocks of the MRS. All these gas and water characteristics support the idea of a mix of different processes being at the origin of gas 3.

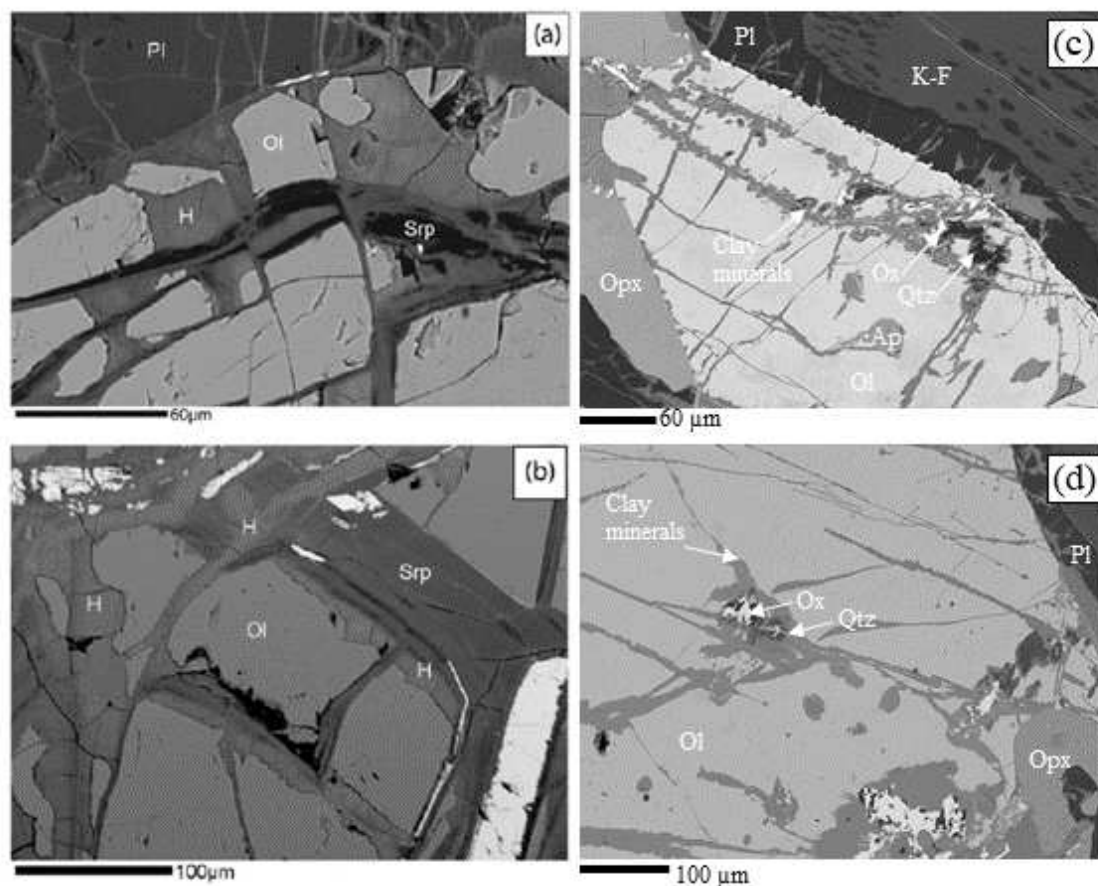
DMK well#3 isotopic values were not determined, but the gas shows significant amounts of CH_4 associated with variable proportions of H_2 , CO_2 , C_2H_6 , C_3H_8 , *i*- C_4 , and *n*- C_4 . It has H_2 concentrations up to 500 ppm with traces of CO_2 and CH_4 and a significant VFA content. All the elements prone to significant hydrogen generation are present and highlight the need for a more exhaustive study of such Precambrian shield gases.

II.vii. Conclusion

Significant methane and crustal helium concentrations are associated with basic and reduced waters. These gas occurrences are found in northeast Minnesota, where Precambrian iron-rich rocks outcrops and where serpentized and altered rocks have already been described. In addition, helium and methane contents and carbon and deuterium signatures of these gases are similar to gases of the Canadian and Fennoscandian Precambrian shields identified as crustal helium and thermogenic to abiogenic methane, which leads us to believe that Minnesota gases could have a similar origin. Still, uncertainties such as accurate identification of CH_4 production mechanisms, carbon origin, and processes of potential mixing of the gases in the sub-surface are still unknown. The role of potential H_2 in methanogenesis is under investigation, but as rocks and high pH and negative Eh brines typical of serpentization environments are present in the area, it seems plausible to believe that redox reactions through water-rock interactions are the major mechanism driving H_2 generation in the Minnesota Precambrian basement. The high amounts of short-chain organic acids present in those fluids suggest a consumption of the H_2 , still detected as trace amounts.

Further fluid and gas analyses are currently being performed to help constrain the carbon cycle in the area and the extent of hydrogen consumption. Doubly substituted isotopologues measurements of methane could allow us to determine a potential equilibrium temperature and to clearly identify the conditions under which it formed. The elemental composition of the brines will provide insight into the rocks and minerals encountered during the circulation of water. Isotope analysis on H_2O and dissolved organic matter will provide data on the type of water encountered (meteoric or ancient) and the mechanisms consuming hydrogen, allowing us to establish a more robust gas formation and circulation model within the rocks.

III. Supplementary



Supplementary figure 1: A and B – Back-scattered electron images of sample MD444 from Evans et al., 2017, C and D- SEM images of K2 sample with Ol for olivine, Ox for oxide, Qtz for quartz, Pl for plagioclase, Ap for apatite, Opx for orthopyroxene, K-F for K-feldspar, and Clay minerals for the several generations of clay minerals identified in K2.

Lake Superior (this study, Precambrian Canadian shield)		
	UV detector	
	Acetate ($\mu\text{mol/L}$)	Formate ($\mu\text{mol/L}$)
DMK well#1.1	285	538
DMK well#2	239	451
DMK well#1-2.4		
DMK well#3.4		
DMK well#4.1		
DMK well#5.4		
DMK well#6.4		
D.MCK well#1	312	578
BC well#1.4	232	413

Supplementary table 2: Acetate and formate concentrations in sampled fluids obtained with the UV detector. n.d. is for not determined and indicates compounds were below the detection limit.

	CO ₂	³ He	CO ₂ / ³ He
	%	ppm	
DMK Well#1-2	0,167	19,5	86
DMK Well# 2-2	0,186	40,3	46
DMK well#3	0,047	2	234
Tamarack well#2-2	0,216	50,2	43
Tamarack well#2-1	0,105	56	19

Supplementary table 3: CO₂ concentrations (%) from Table 3, calculated ³He concentrations (ppm), and CO₂/³He ratio for each studied well.

CHAPTER VIII

CHAPTER VIII. Synthesis and discussion on the H₂-potential of the Mid-Rift System

This chapter synthesizes the main results of this thesis work i.e., the mineralogy of the DR1-A well samples, the potential H₂-generating reactions, the quantification of gas generated, as well as the gases sampled in the Lake Superior part of the Mid-Rift System (MRS), their compositions, and isotopic values. It highlights the remaining questions and the perspectives of this study. The H₂ potential of the Lake Superior part of the MRS, which has similar mineralogies to the ones found in Kansas, as previous studies have already highlighted, is discussed. The H₂ potential of the whole rift is also addressed.

L'objectif de ce chapitre est de synthétiser les principaux résultats de ce travail de thèse i.e., la minéralogie des échantillons du puits DR1-A, les potentielles réactions ayant pu produire cet hydrogène, la quantité de gaz générée, ainsi que les gaz du Minnesota, leur composition et leurs valeurs isotopiques. Les questions soulevées par ce travail sont synthétisées et des perspectives de travail sont avancées. Le potentiel de génération d'H₂ de la partie supérieure du rift est discuté, en effet des études ont déjà mis en avant des assemblages minéralogiques semblables à ceux décrits dans ces travaux. Le potentiel de génération d'H₂ de l'ensemble du rift est aussi abordé.

I. Introduction

Based on previous studies on gas samples, this work allowed for characterizing the basement rocks associated with H₂-emissions in Kansas. The mineralogy of the samples from the DR1-A well was determined. A high-resolution microscopy workflow was conducted on the deepest samples to clearly identify the minerals and reactions involved in hydrogen generation. The results of such a study are synthesized in this chapter. The minerals found in the highest samples give additional pieces of information that are discussed here, as well as prime order quantification of the overall H₂ generation. The remaining questions regarding this hydrogen are presented and discussed.

In addition, a sampling trip was conducted in the northern part of the rift to improve the representativeness of this work. The results are presented and yield similarities between the two study cases. To demonstrate that our results are significant, similarities found in the literature between the Kansas case and the Minnesota case are displayed and allow for showing the Mid-Rift System has a huge hydrogen potential.

II. Synthesis of the thesis results

II.i. Previous gas study: why did we choose to study the Kansas Precambrian basement?

The work conducted during this thesis was made possible thanks to the previous studies conducted on the natural hydrogen emissions in Kansas (Coveney et al., 1987; Newell et al., 2007; Guélard et al., 2017). Guélard and co-authors (2017) showed that hydrogen was associated with metamorphic N₂, crustal He, and in minor proportions with CH₄. Waters were also studied and displayed reduced and neutral to basic values, highlighting a potentially abiotic origin (Guélard et al., 2017). This natural hydrogen, identified as a continuous flux thanks to numerous samples, was characterized as originating from the Precambrian basement (Guélard et al., 2017). Julia Guélard's doctoral work (2016) laid the foundations for a mineralogical study on the Kansas Precambrian basement rocks associated with these H₂ emissions to confirm the abiotic and crustal origin of the gas.

In addition, the Precambrian basement in Kansas has been described for decades now as intruded by the Mid-Rift System, one of the major geological features of the Mid-American continent (Van Schmus and Hinze, 1985; Hinze and Braile, 1988; Dickas and Mudrey, 1997; Ojakangas et al., 2001, amongst many others). This rift makes the Kansas Precambrian basement a good candidate for hydrogen generation as it is a kilometeric-scale accumulation of iron-rich rocks (Ojakangas et al., 2001).

II.ii. Sample material

Hydrogen emissions are aligned along the Nemaha High, a Paleozoic compressional feature of east Kansas, and the Humboldt crustal fault inherited from the Precambrian (Steeple et al., 1979). In this work, we accessed rocks from the DR1-A well, which is located near the H₂-bearing wells and is one of the few wells in Kansas reaching the basement. Rocks were sampled, and nine thin sections of basement rocks (from 349 to 454 meters of depth) were made and studied during this study.

II.iii. Microscopy: mineralogy of the deepest samples of the DR1-A well

Our focus was quickly put on the deepest samples, K1 and K2, of respective depths of 442 and 450 meters, as they present the best-preserved primary minerals identified as olivine, pyroxene, and amphibole. They are good candidates for hydrogen generation by water-rock interactions (WRI) as we observe closely associated with them what we inferred (at the optical microscopy scale) to be secondary minerals. These latter were identified by the mean of optical microscopy as potential iddingsite, a hydrous iron-rich silicate formed by deuteric alteration (Ross, 1925; Edwards, 1938; Baker, 1967; Eggleton, 1984; Smith, 1987), oxides, and apatite. These observations were confirmed by SEM analysis, which shows all primary minerals are iron-rich and that iddingsite is closely linked to fayalite, the iron-rich endmember of olivine, and divided into two different iron-rich phyllosilicates.

A complete and high-resolution study of K1 and K2 samples with STXM-XANES and TEM was conducted. Both samples were described as fayalite-bearing monzo-gabbros. The study highlighted that the two different iron-rich phyllosilicates within the fayalite can be characterized as 1) a central Fe²⁺-rich complex mix of serpentine, chlorite, and mica also present in the other mafic minerals and in the feldspathic matrix and 2) a border Fe³⁺-rich zone subdivided into a Fe³⁺-rich chlorite-smectite and a Fe³⁺-rich serpentine. This latter is in direct contact with the fayalite. The central phyllosilicate was potentially formed by the precipitation of a residual magmatic liquid, as they are in some places cut by magmatic apatite and also associated with quartz and iron oxides. Their formation also led to the exsolution of an H₂O-enriched fluid phase. The border phyllosilicates are only found in the fayalite and were potentially formed from the deuteric alteration of the fayalite due to the disequilibrium state induced by the precipitation of the center phyllosilicate and the exsolution of the fluid phase. This scenario could fit with establishing the Mesoproterozoic Mid-Rift System (MRS), allowing for late magmatic conditions to happen. Hydrogen could have been produced during the oxidative event of deuteric alteration or produced as a residual gas of the magmatic activity. This implies that hydrogen was generated 1.1 Giga years ago, and then stored over a long period of time. This trapped hydrogen could easily be released today thanks to microseismicity (Steeple et al., 1979) and water circulation within the basement (Macfarlane., 2000).

II.iv. Other samples from the DR1-A well and their H₂ potential

Other samples belonging to the DR1-A well were accessible and studied by the mean of optical microscopy. When going closer to the basement top, the samples show primary minerals, iddingsite, and new alteration features. K3 and K5 samples are located at respectively depths of 446 and 437 and display the same mineralogical assemblage as K0, K1, and K2. Iddingsite, in these samples, seems to completely replace some primary minerals. In addition, clay minerals are also present as multi-micrometric veins within the whole thin section and are associated with carbonates and quartz. These new veins are good indicators of a secondary alteration event, potentially covering the first deuteritic alteration event. K6 and K7 samples, located at 381 and 372 meters depths, seem to have undergone a more advanced alteration as K6 is completely made of clay minerals intersected by carbonates. K7 is made of altered feldspaths, clay minerals, oxides, and carbonates. Finally, K11 and K12 samples are located at the interface between the basement and the sedimentary cover. They are completely altered and brittle. Thus, the basement samples of the DR1-A well seem to present a gradient in the alteration (Figure 47). To our knowledge, the first episode of deuteritic alteration is visible up to K5 and 437 meters, and then is overprinted by at least two secondary alteration events with clay minerals and then carbonates formation, which happened probably at lower temperatures and more recently. Such associations between clay minerals and carbonates have already been studied, especially in ophiolitic contexts (Noel et al., 2018; Lévy et al., 2022).

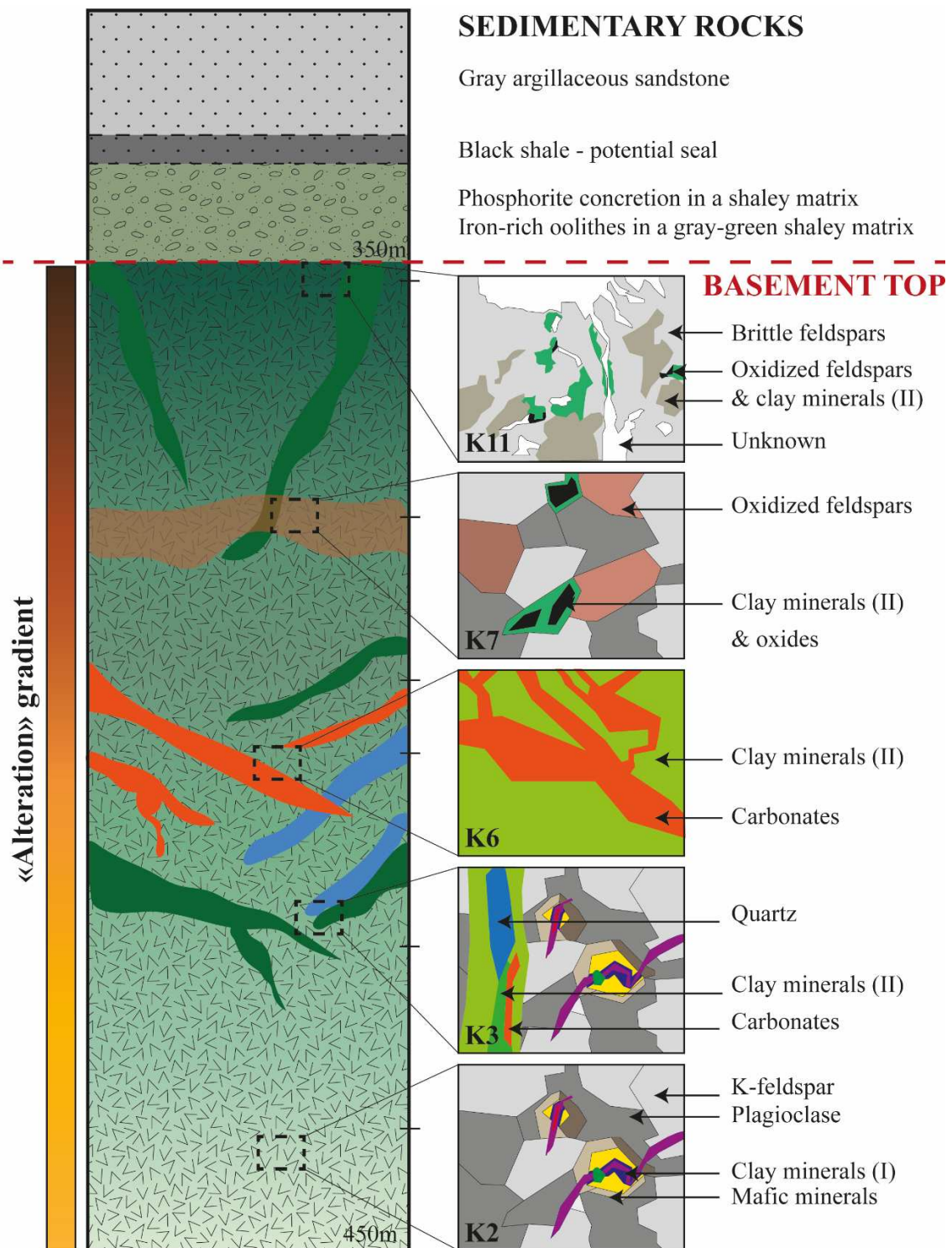


Figure 47: Schematic vertical profile of the DR1-A well. The K2, K3, K6, K7, and K11 are schematized (at the micrometric scale) and localized in the profile as they are characteristic of the basement at their respective depths. They clearly display an alteration gradient increasing up to the basement top. Of note, different clay minerals are represented in these schemes as we have identified several generations of them (I. is the late magmatic event, II. is the second and posterior potential event of fluid circulation). In the K11 schema, the unknown part represents the mineral(s) lost during the thin-section realization as the sample is very brittle. We infer that the clay mineral is missing in these parts. The first sedimentary rocks, in direct contact with the basement, are also schematized as they could represent potential seals for the hydrogen generated in the basement.

II.v. Estimation of quantities of hydrogen generated by the Kansas Precambrian rocks

The fayalite-bearing monzo-gabbros identified with the deepest samples, K1 and K2, could be the location of hydrogen generation during the oxidative deuteric alteration of the fayalite. The formation of the iron-rich phyllosilicates during a late magmatic event could also have been the opportunity to store magmatic hydrogen within the clay minerals structures. To confirm the hypothesis of hydrogen generation, we performed a quantitative EPMA and X-ray microtomography study on the K2 sample. By applying the Gresens equations (1967), a mass transfer evaluation at the sample scale was done. It was coupled to the volume of minerals extracted from μ CT. The amount of potential H₂ generated by 1) orthopyroxene replacement by amphibole, 2) olivine replacement by serpentine, and 3) a simultaneous replacement of orthopyroxene and olivine was then estimated. The mass transfer calculation shows that all three reactions behave similarly, leading to Fe²⁺ loss, Fe³⁺, and H₂O gains with density decrease and solid volume variation. This leads us to believe H₂ could have been generated during a single fluid oxidation event. Hydrogen generation calculation displayed values between 41.73 to 378.21 mol of H₂/ ton of rock for orthopyroxene replacement, 11.18 to 130.36 mol of H₂/ ton of rock for olivine replacement, and 93.34 to 452.16 mol of H₂/ ton of rock for a simultaneous replacement of both mafic minerals. These numbers are one order of magnitude below the numbers currently discussed in the scope of intracratonic H₂-generating rocks (Groveza et al., 2017; McCollom et al., 2016; Geymond et al., 2023), but they have the merit of showing that hydrogen generation by oxidation of iron-rich rocks within intracratonic rocks is possible. However, it raises more general questions about the “H₂-system”, i.e., the reservoir, the potentially associated seal, and the migration pathways.

In addition to this potential hydrogen generation during a late magmatic event and related to olivine or orthopyroxene replacements, the upper samples show the markers of additional events of alteration with an increase of the alteration minerals proportion when going closer to the basement top. We infer that the basement rocks have undergone at least two alteration events with potential H₂ generation during these water-rock interactions. As only optical microscopy has been performed on these samples, such minerals' chemical composition and iron content are unknown. We currently do not have any pieces of evidence attesting to this hypothesis, but such events have already been described in the literature as prone to H₂ and CH₄ generation (Noel et al., 2018; Lévy et al., 2022). Indeed, in mafic and ultramafic environments, when reactions of serpentinization happen, they lead to hydrogen production and reduce water. Carbon dioxide can be reduced, even carbonate minerals, and thus produce methane following Fischer-Tropsch reactions (Charlou et al., 2002). If enough CO₂ is present in the fluid and interacts with Ca-Mg-Fe-rich primary minerals, it can lead in addition to carbonate precipitation (Noel., 2018). The carbonatation reaction depends on the amount of dissolved CO₂, temperature, pressure, and fluid composition. It can happen under a wide range

of temperatures lower than 235°C (in the oceanic domain, Alt and Shanks., 2003) down to a dozen degrees in ophiolitic contexts (Kelemen et al., 2011). When clay minerals are found to be associated with carbonates in mafic environments, they constitute a good marker of low-temperature WRI.

We conclude that the Kansas Precambrian basement rocks can be defined as H₂-generating rocks through a late magmatic event and probably lower-temperature water-rock interactions. We clearly identify iron oxidation of primary minerals of magmatic rocks probably belonging to the MRS as a major component of this H₂ flux. We cannot rule out the hypothesis of hydrogen generation by other mechanisms, such as radiolysis within the Precambrian granitoid crust or by potential late maturation of organic matter within the sedimentary cover. We cannot rule out iron oxidation within the sedimentary rocks. In fact, if we consider a regional hydrogen system, it seems more reasonable to believe the flux is due to several mechanisms rather than one unique reaction.

II.vi. Minnesota: Synthesis of the gas study

In this work, hydrogen emissions occurring in Kansas were studied through the prism of rock samples and microscopy techniques. A high-resolution characterization was done on a few samples as such work is time-consuming. One can criticize the representativeness of such a study as this latter was performed on only two samples. It is worth notifying, however, that only a few samples of the basement rock are accessible in Kansas. Most of the wells in this state were drilled in the scope of oil and gas discovery, and thus, drilling was stopped when encountering basement rocks.

To deal with this representativeness problem, a sampling field trip was conducted in Minnesota, where the Lake Superior part of the MRS outcrop. Rocks were sampled and will soon be studied according to the methodology developed in Chapter 7. Gas and water were also sampled, and gas analyses were conducted during the last year of this thesis. Thanks to gas chromatography (GC) and gas chromatography combustion isotope ratio mass spectrometry (GC-C-IRMS), sampled gases were identified as mostly composed of potentially abiotic CH₄, He with a major crustal origin, CO₂, and C₂H₆. Associated waters are reduced and have a basic pH typical of the context of serpentinization (Kelley et al., 2005; Vacquand., 2011; Deville et al., 2016, amongst others). These results, with the presence of the iron-rich rocks of the MRS, support the hypothesis of hydrogen generation by WRI, such as serpentinization. This event could have been followed by a potential hydrogen and carbon dioxide consumption, leading to abiotic methane formation.

III. Take home messages

- The **DR1-A well**, located near the H₂-emitting wells, the **Nemaha topographic high**, and the **Humboldt crustal fault**, reaches the **Precambrian basement**.
- The basement is there characterized as a **fayalite-bearing monzo-gabbro**. This latter is composed of iron-rich olivine (**fayalite**), iron-rich orthopyroxene (**ferrosilite**, **pigeonite**), clinopyroxene, iron-rich amphibole (**hastingsite**, **Fe-rich pargasite**), a feldspathic matrix of plagioclase (albite) and K-feldspath (orthoclase). Several generations of **Fe-rich clay minerals**, apatite, and quartz are associated with the mafic minerals, especially fayalite.
- The clay minerals might have formed during a **late magmatic event** inducing: 1) the precipitation of the residual magmatic liquid enriched in iron within all the minerals already formed, 2) the **deuteric alteration of the fayalite** leading to **iron oxidation** and a potential **hydrogen generation**.
- When going up to the basement top, the samples show **an increase in the overall alteration** with the appearance of **new clay minerals, carbonates, and quartz veins**. This suggests a **second event of alteration**. This event could be posterior as these minerals cross all the primary minerals. It could have induced a **second episode of hydrogen generation**.
- An EPMA analysis coupled with μ CT scans allows for quantifying the amount of hydrogen generated within the deepest samples of the DR1-A well: between **41.73 to 378.21 mol of H₂/ ton of rock for orthopyroxene replacement**, **11.18 to 130.36 mol of H₂/ ton of rock for olivine replacement**, and **93.34 to 452.16 mol of H₂/ ton of rock for a simultaneous replacement** of both mafic minerals.
- This fayalite-bearing monzo-gabbro may be part of the Precambrian Mid-Rift System.
- Waters sampled in the Lake Superior part of the MRS are reduced and are highly basic.
- **Gases** are mainly composed of **CH₄** with variable amounts of **CO₂**, **C₂H₆**, and, on some occasions, **H₂**. **Helium** is present in significant amounts (up to 1.3 vol% in Tamarack well#2) and has a **potential crustal origin**.
- The carbon and deuterium isotopic origin of **CH₄** is variable, with 1) a trend of **¹³C-²H depleted gases** and 2) a trend of **¹³C-²H enriched gases**.
- The **abiotic origin of such gases is not completely confirmed** as the source of the carbon can be multiple and sub-surface interactions might have altered the isotopic signal.

IV. Remaining questions and perspectives

This study raises several questions:

- *Question 1:* What is the accurate origin of the gases recorded in Minnesota?

- *Question 2:* Did the secondary alteration events in the Kansas Precambrian rocks really generate hydrogen?
- *Question 3:* If question 2 is positively answered, when does it happen?
- *Question 4:* What are the proportions of “deuteric hydrogen/ magmatic hydrogen stored” and “secondary hydrogen” in the total flux?
- *Question 5:* Can hydrogen be adsorbed within the clay minerals structure during long geological periods of time?
- If question 5 is positively answered, *question 6:* How much hydrogen can be stored?
- This leads to *question 7:* Can hydrogen be stored in reservoirs like those in the oil and gas industry?
- And *question 8:* Is this hydrogen economically interesting?

To answer question 1, water associated with these gases is under analysis. Cations and anions compositions will give additional information on rock encountered during water migration by calculating the saturation of the fluid with respect to various mineral phases and give clues on the generating mechanisms. Dissolved organic carbon isotope compositions, specifically those of volatile fatty acids, will also help resolve the questions of H_2 consumption mechanism and methane origin, as they may indicate microbial or abiotic consumption of H_2 . (Seewald et al., 2006). Water isotope analysis is also under consideration as it greatly helps to characterize the type of water (meteoric or ancient) (Sherwood-Lollar et al., 2007). Doubly-substituted isotopologues (or “clumped”) analysis of methane is also being considered and should help to constrain the formation mechanism, and possibly formation temperature, of methane (Douglas et al., 2017).

To address question 2, the iron content and partitioning of the clay minerals associated with these alteration events must be characterized. An easy way to do so is to do inductively coupled plasma optical emission spectroscopy (ICP-OES) to access the global composition of the minerals and their total iron content, as has been done during Julia Guélard’s thesis on the Kansas waters. Then ^{57}Fe Mössbauer spectroscopy can be done on the most interesting samples to access the iron valency and the quantity of Fe^{3+} as it has been done recently in the scope of an H_2 -generating study by Geymond and co-authors (2022). Coupling these two types of chemical information makes it easy to identify if the spotted minerals are prone to generate hydrogen.

Identifying the moment of hydrogen generation (question 3) is more complicated as datations have to be performed, which are easily constrained by the size of the minerals. To do so, secondary ions mass spectrometry (SIMS) can be performed to access ^{18}O isotopic values of the minerals and *in fine* to provide the age of formation as it has been done recently by Lévy and co-authors (2022). U/Pb datations can also be performed on carbonate minerals to help

constrain the age of the last alteration events, as it has been proposed by (Rasbury and Cole., 2009).

Determining the proportions of all types of hydrogen within the global flux is way more complicated as their proportions in the gas mix can vary with time and space. Thanks to carbon and deuterium isotopy of the associated species, or thanks to noble gases, it is possible to isolate the origin of each gas as it is already done to constrain methane origins (Etiope and Sherwood-Lollar., 2013).

As to questions 5 and 6, hydrogen storage within the structure of the clay minerals is probably to be regarded under the scope of adsorption mechanisms, which have been mentioned by Truche and co-authors (2018). This mechanism has been described in hydrogen storage studies (Edge., 2015) but has still to be clearly demonstrated in geological contexts.

Questions 7 and 8 will be addressed in the more general context of intracratonic areas in section V of this chapter.

V. Discussion on the MRS potential for hydrogen generation

Minnesota gases are mostly CH₄ and CO₂, while the Kansas ones are mostly H₂ and N₂. In each case, the gases are associated with crustal He and reduced waters. Similarities between both study cases are identified and justify studying Minnesota gases and rocks to better understand what is happening in this part of the rift.

Some explanations of the differences between both cases can be drawn easily: 1) the basement is outcropping, subject to atmospheric contaminations and meteoric water circulation; 2) it is also subject to microbial activities susceptible to consume H₂ and/or to generate CH₄; 3) some metasedimentary rocks with potential significative graphite contents are reached by the CH₄-bearing wells; thus, an unknown proportion of methane could be due to thermogenic reactions which is not the case in Kansas.

However, previous studies (Chapter 8, Section V.i) have highlighted rocks with similar mineralogies to those found in the Kansas Precambrian rocks, which have proven hydrogen emissions. The following part of this chapter aims to show that the Mid-Rift System, especially the Lake Superior part, is a good candidate for natural hydrogen generation.

V.i. Previous studies on the Lake Superior part of the MRS (Minnesota, USA) and links with potential H_2 generation

V.i.i. The lake superior part of the MRS synthetic geological context

As it has been previously described in this work, Minnesota is home to the northern part of the Mid-Rift System (Figure 48). In this area, the MRS intruded Archean and Paleoproterozoic rocks, and the four stages of rifting were recorded. A lot of similarities can be drawn between the Kansas and the Minnesota parts of the rift.

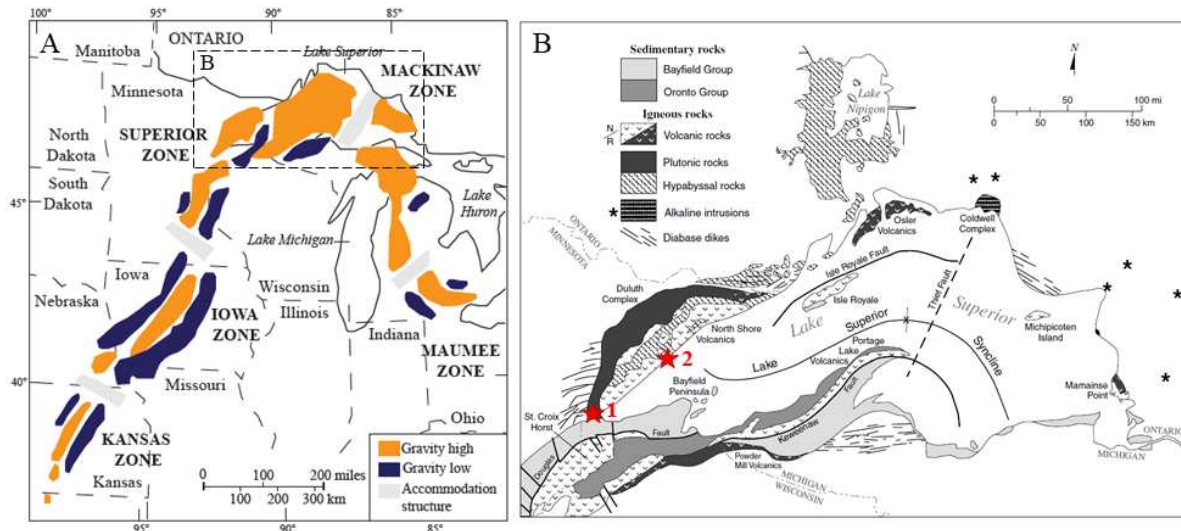


Figure 48: A- Simplified geological map of the gravimetric anomalies of the MRS (modified from Ojakangas et al., 2001 after Dickas and Mudrey., 1997) with the location of B- Geological map of the northern part of the Mid-Rift System with 1) the location of Evans et al., 2016; Tutolo et al., 2019; and 2) Joslin, 2004 studies (modified from Ojakangas et al., 2001 after Hinze et al., 1997).

Like in Kansas, a post-rifting compressional event responsible for the failure of the rifting episode is probably responsible for the reactivation of normal faults in reverse faults. It allows for uplifting volcanic rocks and syn-rift sediments above more recent sediments (Cannon et al., 1989; Green et al., 1989) (Figure 49).

The St. Croix horst, a major geological feature of the southern part of the MRS in Minnesota, is bounded by these reverse faults and is one of the expressions of this compressional event (Figure 48). As uplift proceeded, the rocks of the St. Croix horst have undergone erosion and metamorphism.

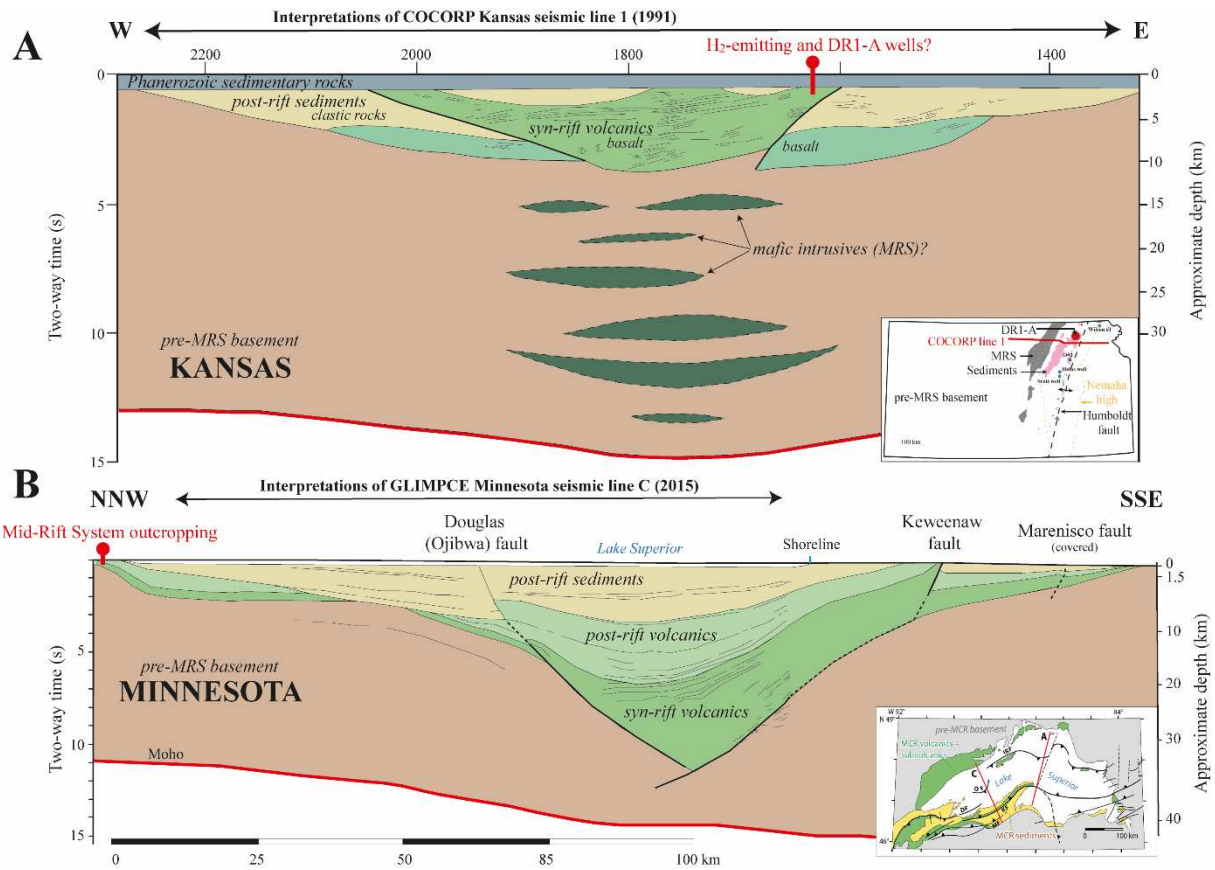


Figure 49: A- Geologic interpretation of the seismic profile COCORP Kansas Line 1 acquired during the eighties (modified from Woelk and Hinze., 1991), B- Geologic interpretation of the seismic profile GLIMPCE line C acquired at the end of the eighties in Minnesota (modified from Stein et al., 2015 after Green et al., 1989). Locations of both seismic lines can be found in the two smaller maps at the bottom right. Of note, both seismic profile are dated from nineties and their geological interpretation must be treated with caution.)

The Lake Superior province of the MRS can, however, be differentiated from the Kansas zone by its unique intrusive rocks, which are divided into the North Shore Volcanic Group (NSVG), the Duluth, and the Beaver Bay complexes, and ultimately unclassified miscellaneous intrusions (Figure 50) (for more details, please refer to chapter 7 – Section II.iii).

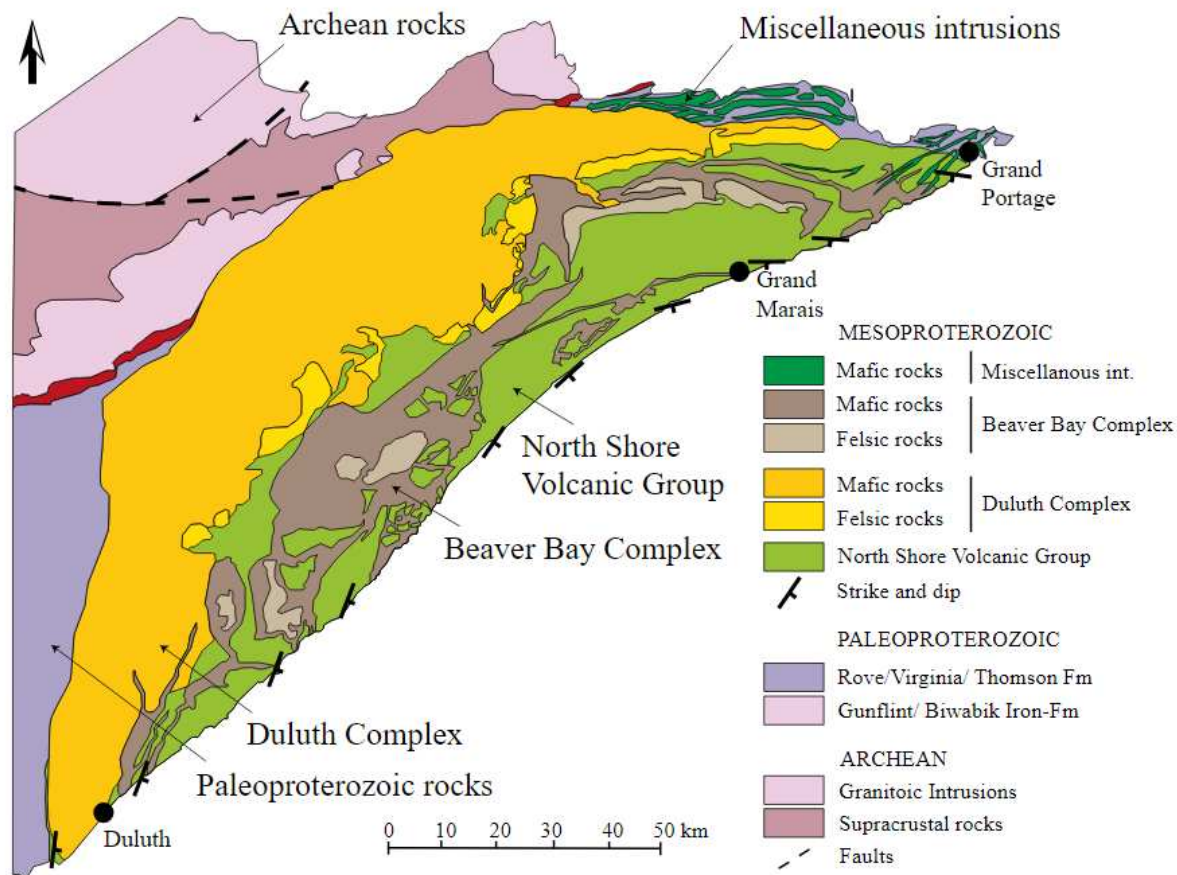


Figure 50: Simplified regional map of the Precambrian rocks of the Northeastern part of Minnesota with the North Shore Volcanic Group, the Duluth Complex, the Beaver Bay Complex, and the Miscellaneous intrusions of the MRS, intruded into the Paleoproterozoic rocks of the Rove, Virginia and Thomson formations, the BIF of Gunflint and Biwabik, and the Archean granitoid intrusions, and supracrustal rocks (modified from Miller et al., 2002).

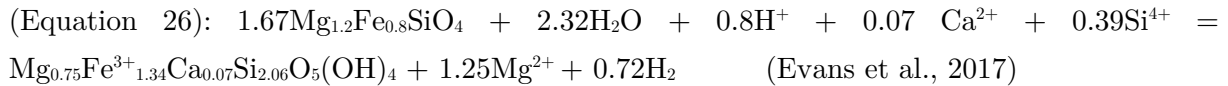
Because these intrusive rocks outcrop and have remarkable similarities with the few samples accessible of the Kansas basement, they represent a unique opportunity to better understand the links between H₂ emissions and the Precambrian basement rocks of the Mid-Continent. Previous studies have looked deeper into the mineralogy of these different units and rocks (Figure 49).

V.i.ii. Similarities between the Duluth Complex and the Kansas Precambrian basement

Evans and co-authors studied peridotites from the Duluth complex's Layered Series. They described serpentine (lizardite, chrysotile, and clinochlore) enriched in iron being associated at the nanoscale with chlorite (Mg-hisingerite, low-Al ferrosaponite, and chamosite), magnetite, and metamorphic fayalite (Fa₅₃₋₈₀) as micro-veins being formed within iron-rich igneous

forsterite (Fe_{38-43}). In addition, they described hisingerite as being replaced by a Fe^{2+} -rich ferrosaponite and pores of chrysotile being filled with a Si-rich ferrosaponite, forming a second generation of iron-rich phyllosilicates. These two species have up to 1 wt% of sodium and potassium.

The authors described a complex chain of mineral replacement leading to an increase in the iron ratio (XFe) and a depletion of Mg (probably being leached) compared to the protolith. They infer it could have happened during a fluid-mediated late event of alteration, under oxidizing conditions and temperatures around 300°C progressively decreasing to 100°C. The chemistry of the fluid seems to be a major control of the composition of the alteration products. They infer that the unusual Mg-depletion and associated increase in the iron ratio seem to be controlled by the fluid (pH, undersaturation of Mg, redox) and not by the initial iron content of the primary minerals (Evans et al., 2017). It is of particular interest as the formation of iron-rich hisingerite from olivine made possible the release of H_2 with the following reaction:



A complementary study by Tutolo and co-authors (2019) on ferroan peridotites and gabbros from the Duluth Complex, the Laramie Complex (Wyoming, USA), ores, Banded Iron Formation, and Nakhla meteorites, containing Mg- Fe^{2+} -serpentine and Fe^{3+} -hisingerite, showed that intermediate compositions of serpentine and chlorite can co-exist in a stable state as solid-solution rather than end-members. Once again, they demonstrated that serpentinization of Fe-rich peridotites can increase the Fe ratio of the alteration products compared to the protolith with associated depletion of Mg and relative enrichment of Fe^{2+} , Fe^{3+} , Si, and Mn. They infer that such mineral replacement happens under high α SiO_2 , low α H_2 , and below 200°C, allowing for hydrogen production.

The primary and secondary minerals described by these authors are similar to those identified within Kansas's fayalite-bearing monzo-gabbros (Chapter 5). They describe a nanometric-scale mixing of serpentine, smectite, chlorite, and magnetite. The major difference is the presence of forsterite (absent in our samples) and the occurrence of secondary fayalite (which is primary in our samples). No quartz or mica within the clay minerals is described. While the authors diverge from our hypothesis of the formation of such minerals, we all believe that such mineralogical assemblages have been formed under conditions favorable for H_2 generation (Chapter 6).

V.i.iii. Similarities between the Beaver Bay Complex and the Kansas Precambrian basement

North of the Duluth Complex, part of the Beaver Bay Complex, Joslin (2004) studied the mineralogy and mineralization of the Sonju Lake intrusion (SLI). The SLI is made of mafic cumulates described as dunite, troctolite, gabbro, oxide gabbro, and apatite olivine ferrodiorite. These rocks display weak deuteric alteration consisting of the uralitization of pyroxene and the replacement of olivine by serpentine, talc, and magnetite. Once again, similar mineralogical assemblages to the ones found in Kansas (Chapter 5) are described in this part of the rift. Processes leading to the olivine and orthopyroxene replacements are not discussed, but such mineralogical assemblages are good evidence for potential hydrogen production, as we infer in Chapter 5 and Chapter 6.

V.i.iv. Similarities between the Tamarack intrusion and the Kansas Precambrian basement

Approximately 80 km south of Duluth, the Tamarack intrusion is an unexposed ultramafic intrusion and has been highly explored for its Cu-Ni-PGE sulfide deposits (Rio Tinto). It was emplaced 1105.6 ± 1.2 million years ago in the Paleoproterozoic Animikie Basin, composed of black shales (Figure 51-A) (Goldner., 2011). The intrusion is divided into two major ultramafic intrusive sequences (Figure 51-B and C): the Bowl intrusion in the south and the Dike area intrusions in the north (which host most of the mineralizations), made of peridotite, feldspathic peridotite, feldspathic pyroxenite, melatroctolite, and melagabbro. The Bowl peridotites are composed of serpentine, magnetite, and chlorite as secondary minerals, traducing hydrothermal alteration and serpentinization (Taranovic et al., 2015)

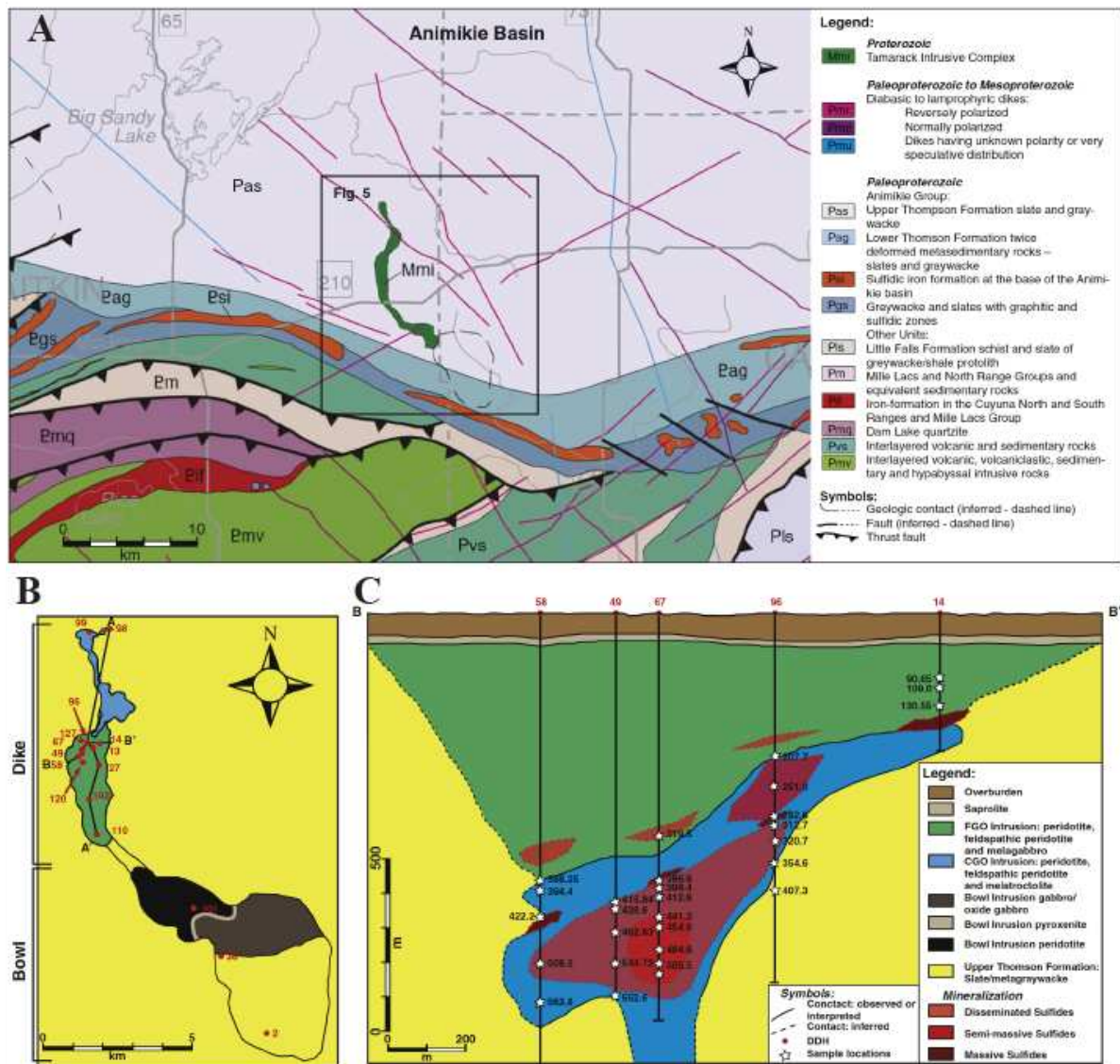


Figure 51: A- Regional geological map with the location of Tamarack intrusion (from Taranovic et al., 2015, after the Geological Map of Minnesota from Jirsa et al., 2011), B- Geological map of the intrusion (from Taranovic et al., 2015, after an unpublished Rio Tinto Exploration map), C- W-E cross-section of the Dike (from Taranovic et al., 2015).

Regarding the mineralogical composition of the different units of the intrusion and the identified serpentinization and hydrothermalism events, it seems highly plausible that hydrogen is or has been generated. This coincides with the gas measurements performed and displayed in Chapter 7, which show significant amounts of hydrogen. The literature and data presented in this work show that more research is needed.

V.ii. The H₂ potential of the MRS

Why is the MRS, as a whole geological object, an interesting study case in order to understand a more global H₂ system? The rift extends over more than 2000 km from Kansas to Minnesota and goes down to south-eastern Michigan (Ojakangas et al., 2001). Its extension is around 100km, which means iron-rich rocks potentially generating hydrogen, and yet not discovered, could be numerous.

To understand an H₂ system from the large-scale/ regional point of view, i.e., from the H₂-generating rock to the reservoir, the seal, and the migration pathways, the Mid-Rift System is, in our opinion, the best study case. Several areas in the Superior zone (Figure 47-A) show basement rocks enriched in primary and secondary minerals typical of iron oxidation. It demonstrates that this part of the rift is a good candidate for H₂ generation. In the four remaining zones, especially in Kansas, Nebraska, and Iowa, the rocks are covered by Paleozoic sedimentary rocks to Quaternary glaciogenic deposits (Anderson., 1992; Ojakangas et al., 2001). They have been studied for their oil & gas accumulations; thus, the data are numerous. The occurrence of sedimentary rocks, but also topographic highs, and major faults are good features for potential hydrogen reservoirs, stratigraphic seals, and major fluid pathways. Global characterization of each feature should be conducted in one of the five parts of the MRS.

A quick calculation can be done to accentuate the importance of the MRS. Applying the amount of Fe³⁺ generated by the olivine replacement into serpentine (33.53g/ 100g of olivine), determined in Chapter 6, to the total volume of the Duluth Complex, an estimation of the hydrogen potential can be determined. Several assumptions have been made, such as 1) the whole complex is composed of the same fayalite-bearing monzo-gabbros found in Kansas, 2) only the olivine is replaced, and 3) only the iron oxidation reaction is considered. The volume of the Duluth Complex is calculated with the surface (5000 km²) found by Miller et al., 2010, and the maximum depth (13 km) found by Allen et al., 1997. We make the assumption that this depth is constant in order to simplify the calculation. In these conditions, the olivine replacement reaction within the Duluth Complex could generate 1.22.10¹² tons of H₂. This number should be considered with extreme caution and as an unrealistic upper limit. If considering only one thousand of this latter, the amount of hydrogen generated drops to 1.22.10⁸ tons, which is equivalent to 1% of the actual world consumption (Global Hydrogen Review 2022, IAE). This number is still an upper limit, but it shows that mafic and ultramafic intrusions of the MRS could potentially produce significant amounts of H₂.

VI. Conclusion of the chapter

The Kansas basement rocks associated with H₂ emissions are fayalite-bearing monzo-gabbros. H₂ might have been generated during several different events: 1) a late magmatic event by deuteric alteration of the fayalite, thus, by iron oxidation, 2) by a late event of water circulation

with the iron-rich monzo-gabbros leading to a potential new event of iron oxidation at lower temperatures. A radiolytic hydrogen generation cannot be ruled out. We infer, however, that, due to the occurrences of large amounts of iron-rich rocks linked to the MRS, the major component in the overall H₂ generation is iron oxidation.

The Minnesota part of the MRS yields gas mainly composed of CH₄, CO₂, and, in places, a few hundred ppm of H₂. Helium is associated with these gases in significant contents (up to 1.3%), and its isotopic signature, while being not completely uniform, yields a crustal origin. The CH₄ could be formed from a microbial or abiogenic consumption of H₂, but further studies are mandatory to better constrain this origin. What is clearly significant is that potentially abiogenic gases are associated with the Precambrian iron-rich rocks of northeastern Minnesota, some of which have been described as serpentinized. This is coherent with our observations and the reduced and highly basic waters sampled with the gases.

The Kansas and Minnesota cases show the Mid-Rift System has a significant hydrogen generation potential. Iron-rich rocks, with mineralogical assemblages already described as prone to generate H₂, are numerous in the MRS. In Kansas, for example, these H₂-generating rocks have undergone late magmatic events and more recent tectonic events. They both provide favorable conditions to generate hydrogen as they ensure the right temperature and water circulation for H₂-generating reactions to occur. They are now covered by Paleozoic sedimentary rocks, which could provide efficient seals, allowing H₂ to accumulate. These rocks are also the location of major aquifers with water circulating down to the basement thanks to anterior faults and fractures, which should be considered good migration pathways. This water may help to maintain a contemporaneous hydrogen generation. It could also provide a natural reservoir for hydrogen, regarding the state of constraints of the system.

While a major part of this work was focused on the Kansas part of the rift, it does not seem unreasonable to believe the four other zones have similar features. The Mid-Rift System, which extends over more than 2000 km, appears as a good candidate for hydrogen generation and for more global H₂ systems with H₂-generating rocks, efficient seals, and migration pathways.

CHAPTER IX. Conclusions and perspectives

In this last chapter, the potential of global intracratonic areas in generating hydrogen is discussed by showing that rocks such as the ones of the MRS can also be found elsewhere. The main characteristics of a good “H₂ system” (similar to a good petroleum system) within intracratonic rocks are then synthesized. It shows that although studying these systems deserves further investigations, such geological context has good potential for natural hydrogen generation.

Dans ce chapitre final, le potentiel H₂ des zones intracratoniques de manière générale est discuté. Cette discussion est appuyée sur des études ayant identifiées des roches à la minéralogie similaire au MRS ou des roches précambriennes à la composition minéralogique différente mais ayant des émissions d’H₂ bien caractérisées. Pour terminer, et afin de démontrer que les zones intracratoniques sont particulièrement intéressantes dans la prospection en H₂ naturel, les grandes caractéristiques d’un système H₂ intracratonique sont présentées et démontrent que l’étude de ces systèmes mérite d’être approfondie.

I. Potential of natural hydrogen generation within intracratonic areas and perspectives

When looking at areas with similar features of the Mid-Rift System, geological systems prone to generate H₂ seem to exist worldwide. The following section of this chapter aims to show that, even in different geological contexts, similarities with what we found in Kansas and Minnesota can lead to potential or proven hydrogen generation. In complement, a synthesis of the H₂-generating rocks and the associated geological contexts is proposed by Lévy et al. (2023) (Chapter 10, Supplementary 3).

I.i. Other studies with similarities but in different geological contexts

I.i.i. Occurrence of intrusive mafic clots within the Younger Granites of Nigeria

Even if the iron-rich mineralogical assemblages studied in this work are uncommon, other areas with different ages and geological contexts are also characterized by such iron enrichment.

Fe-rich silicates have been identified as associated with clay minerals within the Younger Granites of Nigeria by Mücke. (2003). Anorogenic ring complexes of the Younger Granites intruded the Precambrian basement between the end of the Trias and the beginning of the Cretaceous because of the opening of the South Atlantic.

These granites are characterized by fayalite clots of two types: type 1) irregularly formed, made of fayalite replaced by Fe-amphibole, magnetite on the grains boundaries; the rim is also composed of grunerite, calcic amphibole, Fe-Ca pyroxene, and mica as the external part of the clot; 2) relics of fayalite, ilmenite, and magnetite, rimmed by calcic-amphibole, they are made of ferrosaponite, and characterized by shrinkage cracks. Pyroxene clots are also described within these rocks, even if they are less numerous than the fayalite ones. They are intergrown with saponitized fayalite and a mixture of grunerite and magnetite. They have a rim of calcic-amphibole and/ or an unknown alteration product. In addition, amphibole clots are present and composed of only iron-rich amphiboles (ferro-edenite, hastingsite, ferro-hornblende, and ferro-actinolite). These minerals, particularly enriched in iron, bear a lot of similarities with what was shown previously in Chapter 5 and Chapter 6.

The author proposes that during the cooling of the magma, a decrease in the temperature and input of water could have allowed for fayalite decomposition and alteration into Fe-amphibole, magnetite, and Fe-saponite. The author gives the following order of crystallization: fayalite and pyroxene as early crystallization products between 850 and 750°C, followed by the formation of amphibole and mica between 750 and 600°C during the cooling of the melt. Once late conditions (<600°C) are reached, and water is added, the primary silicates become unstable and decompose into a complex solid solution of Fe-rich amphiboles, ferrosaponites, and greenalites.

This atypical iron enrichment of this granite, as mafic clots, is probably due to the presence of iron formations within the Nigerian basement, which was molten and mixed with the ascending magma during the crustal extension (Eborall and Wright., 1974, Mücke., 2003). Mücke. (2003) infers the water content and the fO_2 were low enough to allow the iron to dissolve within the magmatic liquid and then be partitioned within silicates and not magmatic oxides. Even if no measurement nor H_2 subsurface mapping is associated with this mineralogy study (yet), the “decomposition” and alteration of these iron-silicates is a good indicator of potential H_2 generation during these mafic clots formation, as it has been shown in Chapter 5 and Chapter 6.

I.i.ii. Hydrogen generation associated with per-alkaline granite alteration as an analog for the origin of intracratonic hydrogen

The per-alkaline igneous intrusions of Strange Lake (Canada), Lovozero and Khibiny (Russia), and Ilimaussag (Greenland) differ from the MRS rock lithologies but are associated with up to 40 mol% of H_2 within fluid inclusions and fracture networks (Krumrei et al., 2007, Salvi and Williams-Jones., 1992, Nivin., 2019, 2020). They represent a unique example of intracratonic hydrogen and a good example for our study.

Previous studies (Vasyukova and Williams-Jones., 2019) proposed this gas was generated during a late subsolidus hydrothermal alteration of ferrous minerals, resulting in the pseudomorphic replacement of Fe^{2+} -bearing amphibole (arfvedsonite) by Fe^{3+} -bearing pyroxene (aegirine) and magnetite. The hydrothermal alteration could be due, at Strange Lake, to the exsolution of brine from the melt with a CH_4 -dominated vapor phase. This brine would have altered the silicates and evolved during the system's cooling to become a mixture of CH_4 , H_2 , and other hydrocarbons.

Truche and co-authors., (2021) conducted high-temperature and fluid-controlled (pH, salinity) batch reactor experiments in order to demonstrate that amphibole alteration leads to H_2 generation. They tested unreacted quartz, Strange Lake samples (whole rock), and monomineralic arfvedsonite under a temperature range between 280 and 400°C and for 650 hours. These experiments showed that dissolution features on arfvedsonite are associated with secondary zircons and Fe^{3+} -bearing phases as magnetite and phyllosilicates. Contrary to what is observed in natural samples, no aegirine is formed. H_2 is generated by the hydrothermal alteration of the Fe-rich amphibole with a neutral to alkaline fluid, with temperatures above 280°C. This H_2 generation by iron oxidation during amphibole alteration is more efficient than a similar alteration of olivine within a harzburgite. Two factors seem to favor H_2 : 1) the fluid being alkaline, with a low salinity, and 2) the presence of the whole granitic rock during the experiment. Indeed, per-alkaline granite alteration produces alkaline fluid, favoring hydrogen generation (Truche et al., 2021).

Truche and co-authors' study is of prime interest as it demonstrates clearly that H₂ can be generated within intracratonic areas. While being performed on a different lithology and geological context, it provides keys to understanding what is happening within intracratonic rocks. It also shows that in intracratonic contexts, not only olivine-bearing rocks have to be considered when looking at H₂-generating rocks.

I.i.iii. Synthesis

A key point in these two intracratonic rocks is their iron enrichment, their mineralogical assemblages made of mafic minerals, the mineral replacement reactions identified, and thus the conditions of formation of the minerals and hydrogen. They are associated with younger rocks or rocks with different chemical compositions, but they still present huge similarities with the MRS rocks. They are, indeed, a good glimpse of the actual potential of intracratonic rocks in the scope of hydrogen generation by iron oxidation. They show that MRS is no exception in the wide world of potential hydrogen-generating intracratonic areas.

I.ii. Other reactions occurring in intracratonic rocks with potential hydrogen generation

When speaking about the hydrogen potential of intracratonic areas, it is impossible to avoid considering other potential H₂-generating reactions. These reactions can be divided into three main categories: 1) redox reactions, the main reactions considered in this work; 2) radiolysis; and 3) late maturation of organic matter. This latter has been proposed recently by Horsfield et al., (2022) and Mahlstedt et al., (2022) and will not be discussed here. It is in the scope of H₂-generating continental rocks, but such a reaction has yet to be identified within intracratonic rocks.

Radiolysis could be considered as a major component of intracratonic hydrogen. It has been intensively studied (Lin et al., 2005; Sherwood-Lollar et al., 2007). While we choose to focus on the iron oxidation reaction, we do not ignore that a part of the hydrogen emitted in Kansas is probably due to radiolysis. The Mid-Rift system is intruded into complex Precambrian rocks, some of which are granitoids with significant radiogenic content (Bickford et al., 1981 for the granitic basement of Kansas; Miller et al., 2002 for the Archean granite of the Giants range batholith which is the footwall of the Duluth Complex in Minnesota). Consequently, we know that radiolysis cannot be completely ruled out. However, the vicinity of kilometric-scale amounts of mafic and ultramafic rocks tips the scale towards a redox origin, as it has already been the case in some parts of the Canadian and the Fennoscandian shields (Sherwood-Lollar et al., 2007). The major point of such information is to show that hydrogen intracratonic systems are complex systems with multiple potential sources.

I.iii. The required characteristics of an H₂ system

When talking about an “H₂ system” or “H₂ deposit” (in the sense of an exploitable hydrocarbon system), four main characteristics should be considered: 1) the H₂-generating rock, 2) the dynamic state or steady state of the system (which can lead to the concept of the reservoir), 3) the migration pathway, and 4) the seal/ the cap rock (Figure 52).

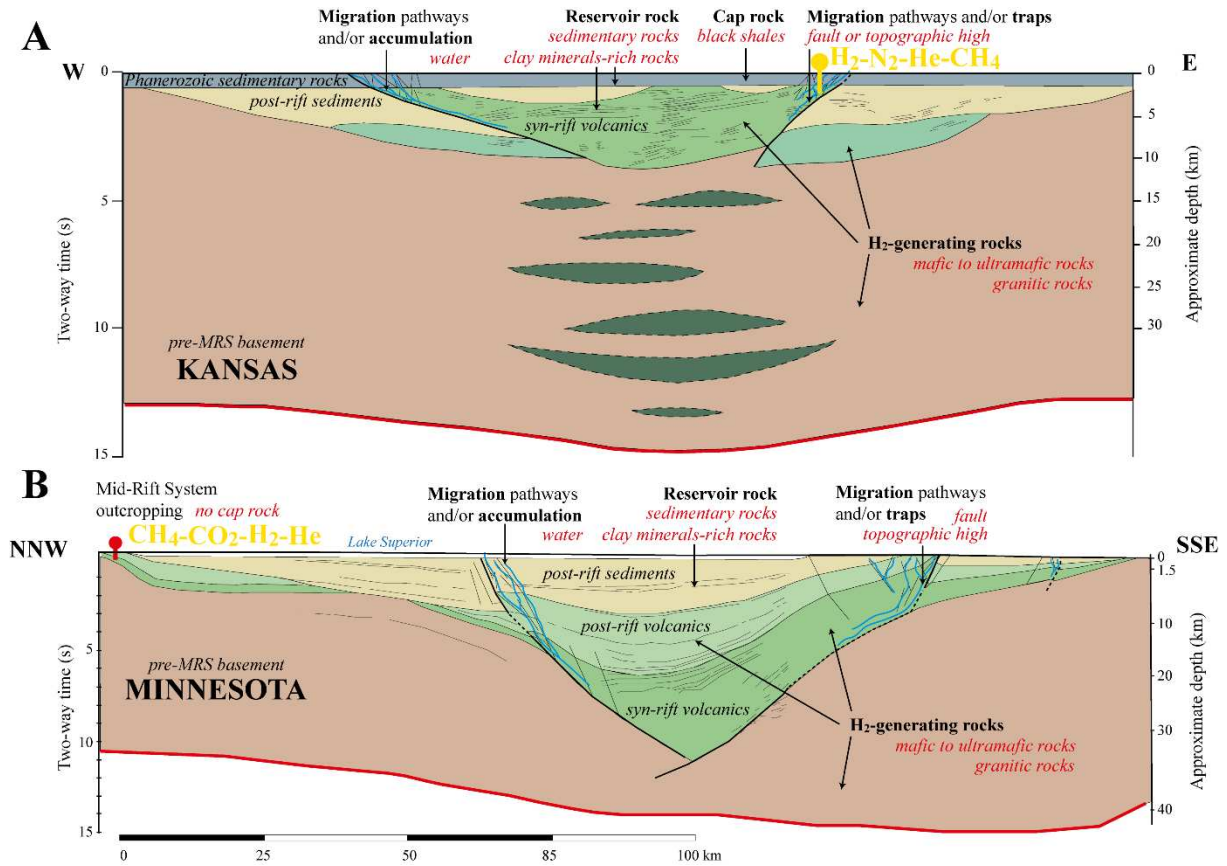


Figure 52: A- Geologic interpretation of the seismic profile COCORP Kansas Line 1 acquired during the eighties (modified from Woelk and Hinze., 1991) in addition, the main characteristics of the H₂ system are represented, B- Geologic interpretation of the seismic profile GLIMPCE line C acquired at the end of the eighties in Minnesota (modified from Stein et al., 2015 after Green et al., 1989) in addition, the main characteristics of the H₂ system are represented. Locations of both seismic lines can be found in the two smaller maps at the bottom right.

The first point has been exhaustively studied in the previous chapters of this thesis and will not be further considered here.

The second point is of prime interest to the scientific community as it is a key factor in determining the renewable character of natural hydrogen. There is, nowadays, no general consensus on this topic, but one can synthesize this topic into two concepts: 1) a present-day generation with no accumulation, i.e., a constant self-maintained flux of hydrogen, or 2) an actual or fossil generation with gas accumulation in potential reservoirs.

The present-day generation with a dynamic state is characterized by an H₂ flux with no accumulation. It has been described at the mid-oceanic ridges (MOR) where hydrothermalism, and thus hydrogen generation, are maintained by the continuous input of seawater and by the exothermic features of serpentinization (Kelley et al., 2005, 2007; Macdonald et Fyfe., 1985). In continental systems, such generation has been proposed in ophiolitic context (Lévy et al., 2022), but the contemporaneous generation of H₂ is still under consideration by the authors as it implies low-temperature serpentinization. In intracratonic systems, such a dynamic generation state with no accumulation has yet to be demonstrated.

The fossil generation implies an accumulation of gas over short to long periods of time. For example, in Mali, hydrogen has been described by Maïga and co-authors (2023) as a flux, as no decrease in the production of the gas has been identified. Hydrogen potentially originates from the basement and migrates as a dissolved gas in deep sandstone reservoirs and as a shallower free-gas phase in karstic carbonates. The authors also believe hydrogen could be generated in the reservoir, which superimposes the concept of current generation, fossil generation, and accumulation. In Kansas, Guélard and co-authors (2017) suggested hydrogen is emitted as a flux because decades of sampling have always shown significant hydrogen values. In addition, we showed that hydrogen had been potentially generated in the basement during a late magmatic event, making hydrogen a fossil gas. We also believe that a current, or at least a more recent hydrogen generation, happened within the basement during a late fluid circulation. The Kansas and Mali cases both support the concept of fossil and actual hydrogen accumulation.

The potential accumulation of hydrogen raises the question of this latter's residence time and behavior within the subsurface. Hydrogen is, indeed, a reactive and mobile gas. Its accumulation is counter-intuitive. However, Sherwood-Lollar and co-authors (2007) demonstrated that deep Precambrian shield fractures can be the location of water with dissolved H₂ accumulations in closed systems. In that case, the deep and ancient waters act as “small-scale reservoirs” of hydrogen previously produced during GWRI. It would also appear that minerals, especially clay minerals, are prone to hydrogen adsorption (Truche et al., 2018). If demonstrated in natural systems, such mechanisms could allow to store of large amounts of hydrogen.

To accumulate, the gas has to migrate from the H₂-generating rock to the potential reservoir rock (unless one rock is doing both jobs). Sherwood-Lollar and co-authors (2007) demonstrated that H₂ migration can be hydrology-controlled. Water with dissolved hydrogen can accumulate in deep fractures, which, under T/P conditions, are sealed by mineral crystallization. When a new and modern fluid circulates, the fractures are reopened, and the H₂-bearing waters can migrate. In the case of Kansas, microseismicity is recorded, especially along the Humboldt crustal fault (Steeple et al., 1979). We can imagine that even a small-scale tectonic event

could generate sufficient constraints to release the basement-related hydrogen trapped in minerals or deep fluids.

In the oil and gas sector, it is currently admitted that a good seal is needed for gas accumulation. Due to the specific characteristics of the hydrogen molecule, sedimentary seals such as shale levels (Guélard et al., 2017), dolerites (Maïga et al., 2023), or salt layers (Leila et al., 2022) should be considered. Stratigraphic traps such as faults and topographic highs (such as the ones in Kansas) should also be considered.

Is it economically realistic to consider exploiting intracratonic hydrogen? When considering that the Precambrian crust represents 70% of the total continental crust and intracratonic radiolytic and iron-related H₂, Sherwood-Lollar and co-authors (2014) estimate the global H₂ production to be around 0.36 to 2.27·10¹¹ moles/ year. These numbers are in the same order of magnitude as the ones for marine systems, but there is still a considerable lack of understanding of H₂ deposit features. Such numbers are probably underestimations and may be revised to higher amounts as exploration projects start around the globe.

CHAPTER X. Supplementary 1: Methodology

The aim of this supplementary is to introduce the analytical geochemical analyses performed in complement to gas chromatography (GC). Gas chromatography combustion isotope mass spectrometry (GC-C-IRMS) and noble gases spectroscopy (NGS) were not detailed in the main part of this manuscript as they were used routinely and did not require any particular development.

L'objectif de ce chapitre annexe est d'introduire les analyses géochimiques effectuées en complément de la chromatographie gazeuse (GC). Le fonctionnement du GC combiné à un spectromètre de masse isotopique (GC-C-IRMS) et du spectromètre permettant d'analyser les gaz rares n'ont pas été détaillés dans la partie principale du manuscrit car ceux-ci ont été utilisés en routine et n'ont pas nécessités de développement spécifique.

I. GC-C-Isotope Ratio Mass Spectrometry

I.i. Principle

Isotopes of the same element differ by their mass; this difference induces isotopic fractionation during the evolution of the fluids within the different reservoirs of the crust. In other words, isotopes of the same element are distributed in the crust as a function of an assigned process, thus allowing for determining the origin of the gas by studying its isotopic content and ratios. The technique is based on the measurements of the relative abundance of isotopes in a sample thanks to combustion and pyrolysis of the sample. The used GC-C-IRMS can analyze and quantify gaseous species (H_2 , CH_4 , CO_2 , C_2^+) but also measure the isotopic ratios of carbon and hydrogen ($\delta^{13}\text{C}$ and δD), enabling us to better constrain the origin (biotic, abiotic, and thermogenic) and formation temperature of these gases (Bernard et al., 1976; Whiticar, 1999). Isotopic ratios have been highly used in the past decades, especially in the scope of hydrogen and methane generation (Sherwood-Lollar et al., 1993; Etiope et al., 2016; Guélard., 2016). In this context, a GC-C-IRMS, which is a magnetic sector mass spectrometer coupled to a GC, is used during this thesis (Figure 53). Carbon-bearing components are analyzed by combustion of the gas, which allows for oxidation of the compounds, then sent to the spectrometers where they are ionized and analyzed in function of their mass. CH_4 and H_2 are analyzed by pyrolyzing the gas to convert methane into hydrogen and carbon. The signal has to be calibrated using international standards as isotopes are identified by comparison with these standards.

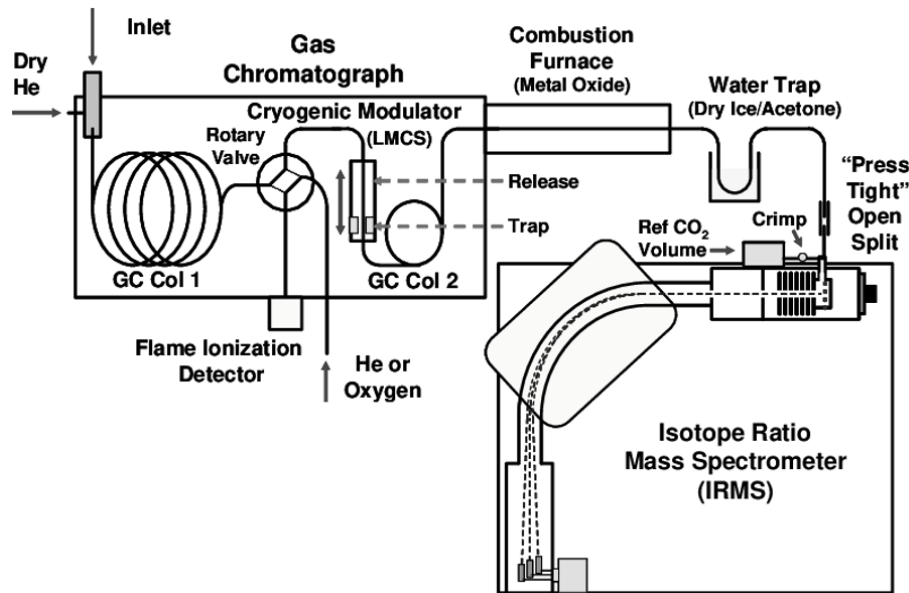


Figure 53: Schematic view of a GC-C-IRMS (Tobias et al., 2009)

I.i. Analytical conditions and post-processing of the data

A MAT253 (Finnigan Mat-Thermo Fisher) triple collection mass spectrometer coupled to a gas chromatograph, operating with He as a carrier gas, is used at IFPEN (Rueil-Malmaison,

France). Results are reported in ‰ units relative to Pee Dee Belemnite (PDB) for carbon and Standard Mean Ocean Water (SMOW) for hydrogen, with respective analytical uncertainties of 0.5‰ and 5‰.

II. Noble gas spectroscopy

II.i. Principle

Noble gases (He, Ne, Ar, Kr, Xe, and Rn) are stable and inert species. They cannot fractionate, which makes their absolute content and their ratio useful tracers of processes (accumulation and migration) happening on Earth (Ballentine and Sherwood-Lollar, 2002; Sherwood-Lollar et al., 1993; Battani et al., 2000; Guélard., 2016). They have two main origins: 1) the nucleosynthesis during Earth accretion, these noble gases are called “primordial gases”; 2) the decay of radioactive elements within the crust, these noble gases are called “radiogenic gases” (Ozima and Podosek, 2002). The origin of radiogenic gases within the crust can be determined by their proportions (mantle, continental crust, atmosphere). The analysis of the gases is made with a vacuumed purification system in order to concentrate, isolate, and quantify each gas, and two spectrometers, one with a magnetic sector and one with a quadrupolar mass sector, in order to determine their isotopic values (Figure 54).

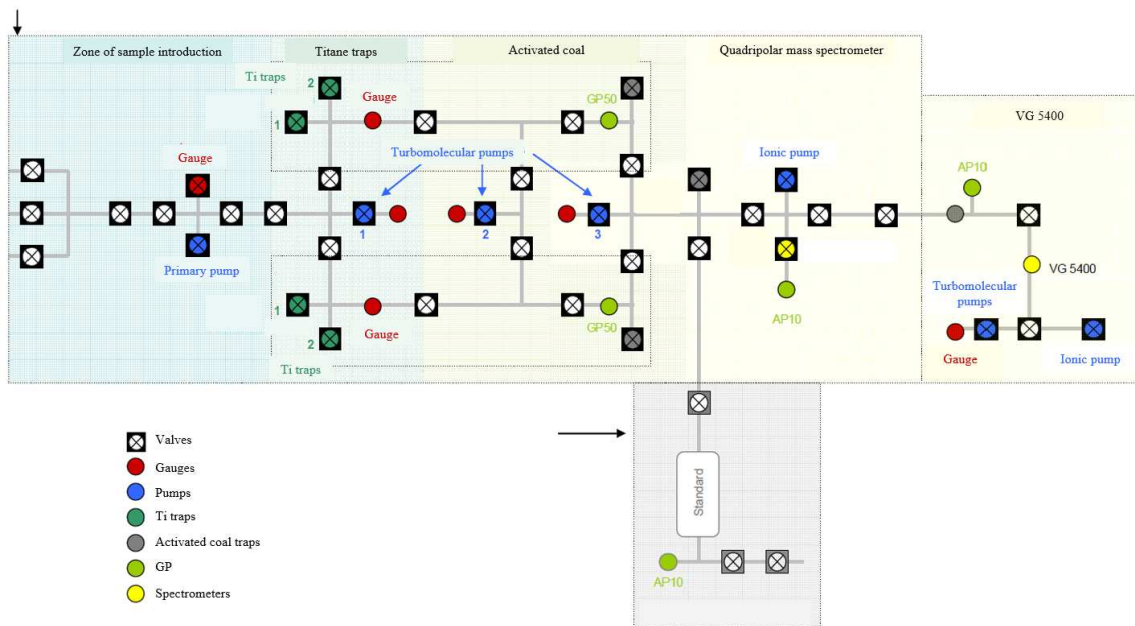


Figure 54: Schematic architecture of the noble gases analyzer (modified from Julia Guélard 2026 doctoral dissertation)

II.ii. Analytical conditions and post-processing of the data

The elemental compositions of the noble gases were determined by a HiQuad quadrupole mass spectrometer (Pfeiffer Vacuum), and a QUADRAR line was used to determine the contents of

^4He , ^{20}Ne , ^{36}Ar , and ^{84}Kr . The uncertainties for the quantification of noble gases with this method are in the following range: He: $\pm 7\%$; Ne: $\pm 7\%$; Ar: $\pm 2\%$; Kr: $\pm 5\%$. Isotope ratios were determined with a Micromass GV5400 high-resolution magnetic sector mass spectrometer. The uncertainties of the $^3\text{He}/^4\text{He}$ ratio are 10%.

CHAPTER XI: Supplementary 2: Supplementary works

The aim of this supplementary is to display the four side projects conducted during this thesis:

L'objectif de ce chapitre annexe est de mettre en avant les quatre projets annexes réalisés en parallèle de cette thèse :

- **Combaudon, V.**, Moretti, I., Kleine, B. I., & Stefánsson, A. (2022). Hydrogen emissions from hydrothermal fields in Iceland and comparison with the Mid-Atlantic Ridge. *International Journal of Hydrogen Energy*, 47(18), 10217-10227.
- Geymond, U., Briole, T., **Combaudon, V.**, Sissmann, O., Martinez, I., Duttine, M., & Moretti, I. (2023). Reassessing the role of magnetite during natural hydrogen generation. *Frontiers in Earth Science*, 11, 1169356.
- Lévy, D., Roche, V., Pasquet, G., **Combaudon, V.**, Geymond, U., Loiseau, K., & Moretti, I. (2023). Natural H₂ exploration: tools and workflows to characterize a play. *Science and Technology for Energy Transition (in publication)*
- Kularatne, K., Senechal, P., **Combaudon, V.**, Darouich, O., Subirana, M.A., Proietti, A., Delhaye, C., Schaumlöffel, D., Sissmann, O., Deville, E., & Derluyn, H. (in prep). X-ray micro-computed tomography-based approach to quantify natural H₂ generation by Fe(II) oxidation in the intracratonic lithologies.

- I. Combaudon, V., Moretti, I., Kleine, B. I., & Stefánsson, A. (2022). Hydrogen emissions from hydrothermal fields in Iceland and comparison with the Mid-Atlantic Ridge. *International Journal of Hydrogen Energy*, 47(18), 10217-10227.

Abstract: Hydrogen emissions from geothermal systems are well known, for example associated with mafic and ultramafic rock formations along mid-ocean ridges (MOR). Here we report concentrations and emissions for H₂ from geothermal fields in Iceland that provides the only MOR on Earth that exposes a largely submarine rift on land and compare them with submarine vent systems along the mid-Atlantic Ridge (MAR). The concentrations of H₂ in Icelandic hydrothermal fluids are 0.022-20.5 mmol/kg comparable to H₂ concentrations in MAR hydrothermal fluids of 0.07- 26.5 mmol/kg. According to geochemical modeling, the H₂ is considered to form in these settings associated with chemical reactions of primary mineral leaching, Fe^{+II} to Fe^{+III} oxidation and secondary mineral precipitation and reduction of water to hydrogen. The main factors influencing these reactions are rock type and source water composition. Geothermal power plants in Iceland emit in total ~1.2 kt H₂ per year (2019-20) or on average ~0.7 g/MWh. The H₂ is today emitted to the atmosphere but could in principle be utilized given technical aspects of such extraction are implemented.

Keywords: Natural Hydrogen; hydrothermal; Iceland; mid-Atlantic ridge

II. Geymond, U., Briole, T., Combaudon, V., Sissmann, O., Martinez, I., Duttine, M., & Moretti, I. (2023). Reassessing the role of magnetite during natural hydrogen generation. *Frontiers in Earth Science*, *11*, 1169356.

Abstract: Interactions between water and ferrous rocks are known to generate natural H₂ in oceanic and continental domains via the oxidation of iron. Such generation has been mainly investigated through the alteration of Fe²⁺-silicate and some Fe²⁺-carbonates. So far, magnetite (α -Fe₃O₄) has never been considered as a potential source mineral for natural H₂ since it is considered as a by-product of every known chemical reaction leading to the formation of H₂, despite it bears 1/3 of Fe²⁺ in its mineral lattice. This iron oxide is rather seen as a good catalyst for the formation of H₂. Recently, hydrogen emissions were observed in the surroundings of banded iron formations (BIF) that are constituted of, among other minerals, magnetite. Thus, this work is an attempt to constrain the true potential of magnetite by means of batch reactor experiments and additional thermodynamic calculations. It explores theoretical and experimental reaction pathways of magnetite during water-rock interactions, focusing on low temperatures (T < 200°C). For the purpose of the experiments, gold capsules filled with magnetite powders were run at 80°C and 200°C. Gas products were analyzed using gas chromatography (GC) while solid products were characterized by X-ray diffraction (XRD), Mössbauer spectroscopy, and scanning electron microscopy (SEM). After experimental alteration, high amounts of H₂ were quantified while mineralogical transitions were observed by SEM. It showed self-reorganization of the primary iron oxide resulting in sharp-edge and better crystalized secondary minerals. In parallel, XRD analyses showed tiny changes between the patterns of the initial powder and the solid products of the reaction. Finally, Mössbauer spectroscopy revealed that the starting magnetite was partly converted to maghemite (γ -Fe₂O₃), a metastable Fe-oxide only containing Fe³⁺. Major implications arise from these results. Concerning H₂ exploration, this work provides evidence that natural hydrogen can be generated at near-ambient temperatures. It also infers that magnetite-rich lithologies such as BIF should be targeted while looking for H₂ source rocks. In addition, these outcomes could be of major interest to mining companies as they provide key elements to understanding the formation of BIF-hosted iron ores.

Keywords: natural hydrogen, magnetite, maghemite, water-rock interactions, Mössbauer, spectroscopy

III. Lévy, D., Roche, V., Pasquet, G., Combaudon, V., Geymond, U., Loiseau, K., & Moretti, I. (2023). Natural H₂ exploration: tools and workflows to characterize a play. *Science and Technology for Energy Transition (in press)*

Abstract: Natural dihydrogen (H₂) exploration is now active in various countries, but tools and workflows that help to characterize prospective zones are still poorly defined. This review paper is dedicated to sharing our experience in characterizing H₂ plays based on exploration efforts carried out in many countries in Europe, North and South America, Africa and Oceania between 2017 and 2023. We decided to focus on onshore exploration where three main reactions are generating H₂: (i) redox reactions between Fe²⁺ and H₂O, (ii) radiolysis of water and (iii) organic late maturation where H₂ comes from hydrocarbons. This leads to classifying the H₂ generating rocks (H₂_GR) into four types that seem us the more likely to be of economic interest: basic and ultrabasic rocks of oceanic/mantellic affinity (H₂_GR1), iron-rich bearing sedimentary and intrusive rocks, (H₂_GR2), radioactive continental rocks (H₂_GR3) and organic matter-rich rocks (H₂_GR4).

For the pre-fieldwork, the workflow aims to target new promising areas for H₂ exploration. Cross-referencing the presence of H₂_GR in the basement, classical geological-hydrodynamic features (fault, water source) and already-known H₂ occurrences at the surface remain essential, but should be accompanied by remote sensing analyses to detect possible H₂ occurrences. For the fieldwork, the focus is on gas and rocks. A discussion is led concerning the importance of punctual measurements and long-term monitoring of gas seepages, which allows to conclude on the dynamics of H₂ leakage from depth through space and time. For the post-fieldwork, we present the most useful analytical tools to characterize H₂ gas seepages and the suspected H₂_GR. The critical parameters to estimate the H₂ potential of a rock are the content in Fe²⁺/Fetot (H₂_GR1 & H₂_GR2), the content of radioactive element U, Th, K (H₂_GR3), and the total organic content (H₂_GR4).

The hydrogen exploration is in its infancy and all the profession is attempting to define an automated and fast workflow. We are still far away from it due to lack of data, yet this review presents a practical guide based on the current knowledge.

Keywords : Natural H₂, exploration, H₂ generating rocks, H₂ play

IV. Kularatne, K., Senechal, P., Combaudon, V., Darouich, O., Subirana, M.A., Proietti, A., Delhaye, C., Schaumlöffel, D., Sissmann, O., Deville, E., & Derluyn, H. (*in prep*). X-ray micro-computed tomography-based approach to quantify natural H₂ generation by Fe(II) oxidation in the intracratonic lithologies.

Abstract: We present an X-ray micro-computed tomography (micro-CT) based method to estimate the potential of H₂ generation in the Fe(II)-rich source rocks in the intracratonic settings. This method combines 3D micro-CT with chemical information obtained from SEM EDS, micro-Raman spectroscopy and NanoSIMS. To obtain a first order estimation of H₂ generation, this method assumes that H₂ is generated via the complete oxidation of Fe(II) in the Fe-rich minerals within the host-rock. This method neither considers the actual geochemical reaction/s that could yield different Fe(II):H₂ ratios nor the reaction kinetics.

Micro-CT imaging combined with energy dispersive scanning electron microscopy (SEM EDS) and μ Raman analysis is used to identify the Fe(II)-rich minerals represented by greyscale values on 2D micro-CT slices of the imaged sample. However, one can also use quantitative electron microprobe (EMPA) analysis or automated mineralogical analysis to replace the 2D chemical imaging techniques, depending on the size of the sample to be analyzed. Once the Fe(II)-rich minerals are identified on the 2D micro-CT slice, the chemical and mineralogical information can be propagated within the imaged 3D micro-CT volume to obtain the volumes of Fe(II)-rich phases. Then, using the mineral density and theoretical or actual Fe(II) content in each phase, potential H₂ production in the host-rock can be obtained in mol (H₂)/ ton (rock). Alternatively, this number can be calculated by obtaining the volumes using X-Ray powder diffraction (XRD) of the sample, but the advantage here is the ability of analyzing a large sample such as a whole drill-core of the host-rock, to obtain the most representative values, non-destructively.

We developed this method using a fayalite-gabbro obtained from a natural H₂ emitting well in Kansas, USA. The results show that the rock is enriched in pyroxene and fayalite which contain abundant Fe(II). Assuming complete oxidation of Fe(II), our estimate reaches 1217.08 ± 67.34 mol (H₂)/ ton (rock). Furthermore, the rock is highly veined and consists of two fracture networks that account for $\sim 1.03 \pm 0.57$ vol.% of the rock. These fractures are filled with Fe(III)-rich minerals reflecting early Fe(II) oxidation.

Micro-CT allows imaging samples ranging from 1 m to a few micro-meters allowing to image the large-scale and small-scale heterogeneities in rocks. We believe that the proposed method could be useful in characterization of Fe(II)-rich source rocks and estimation of their natural H₂ generation potential in the early stages of natural H₂ exploration in the intracratonic settings.

Key words: correlative, imaging, fluid-rock interactions, igneous rock, gabbro, Kansas, SEM-EDS, micro-Raman, NanoSIMS

CHAPTER XII: Bibliography

I. Chapter 1

Campbell, A. C., Palmer, M. R., Klinkhammer, G. P., Bowers, T. S., Edmond, J. M., Lawrence, J. R., Casey, J. F., Thompson, G., Humphris, S., Rona, P., & Karson, J. A. (1988). Chemistry of hot springs on the Mid-Atlantic Ridge. *Nature*, 335(6190), 514–519. <https://doi.org/10.1038/335514a0>

Charlou, J.-L., Donval, J.-P., Jean-Baptiste, P., Dapoigny, A., & Rona, P. A. (1996). Gases and helium isotopes in high temperature solutions sampled before and after ODP Leg 158 drilling at TAG Hydrothermal Field (26°N, MAR). *Geophysical Research Letter*, 23(23), 3491–3494. <https://doi.org/10.1029/96gl02141>

Guélard, J. (2016). Caractérisation des émanations de dihydrogène naturel en contexte intracratonique.

International Energy Agency. (2022). *Global Hydrogen Review 2022 – Analysis*. IEA. <https://www.iea.org/reports/global-hydrogen-review-2022>

Malvoisin, B., Brunet, F., Carlut, J., Rouméjon, S., & Cannat, M. (2012). Serpentinization of oceanic peridotites: 2. Kinetics and processes of San Carlos olivine hydrothermal alteration. *Journal of Geophysical Research: Solid Earth*, 117(B4), n/a-n/a. <https://doi.org/10.1029/2011jb008842>

Marcaillou, C. (2011). Serpentinisation et production d'hydrogène en contexte de dorsale lente : approche expérimentale et numérique. In *theses.hal.science*. <https://theses.hal.science/tel-00676948/>

McCollom, T. M., & Bach, W. (2009). Thermodynamic constraints on hydrogen generation during serpentinization of ultramafic rocks. *Geochimica et Cosmochimica Acta*, 73(3), 856–875. <https://doi.org/10.1016/j.gca.2008.10.032>

Moody, J. B. (1976). Serpentinization: a review. *Lithos*, 9(2), 125–138. [https://doi.org/10.1016/0024-4937\(76\)90030-x](https://doi.org/10.1016/0024-4937(76)90030-x)

II. Chapter 2

Barbarin, B. (1999). A review of the relationships between granitoid types, their origins and their geodynamic environments. *Lithos*, 46(3), 605–626. [https://doi.org/10.1016/s0024-4937\(98\)00085-1](https://doi.org/10.1016/s0024-4937(98)00085-1)

Campbell, A. C., Palmer, M. R., Klinkhammer, G. P., Bowers, T. S., Edmond, J. M., Lawrence, J. R., Casey, J. F., Thompson, G., Humphris, S., Rona, P., & Karson, J. A. (1988). Chemistry of hot springs on the Mid-Atlantic Ridge. *Nature*, 335(6190), 514–519. <https://doi.org/10.1038/335514a0>

Carlin, W., Malvoisin, B., Lanson, B., Brunet, F., Findling, N., Lanson, M., Magnin, V., Fargetton, T., Jeannin, L., & Lhote, O. (2023). FeIII-substituted brucite: Hydrothermal synthesis from (Mg_{0.8}Fe_{II}0.2)-brucite, crystal chemistry and relevance to the alteration of ultramafic rocks. *Applied Clay Science*, 234, 106845. <https://doi.org/10.1016/j.clay.2023.106845>

Charlou, J. L., Donval, J. P., Fouquet, Y., Jean-Baptiste, P., & Holm, N. (2002). Geochemistry of high H₂ and CH₄ vent fluids issuing from ultramafic rocks at the Rainbow hydrothermal field (36°14'N, MAR). *Chemical Geology*, 191(4), 345–359. [https://doi.org/10.1016/s0009-2541\(02\)00134-1](https://doi.org/10.1016/s0009-2541(02)00134-1)

Charlou, J.-L., Donval, J.-P., Jean-Baptiste, P., Dapoigny, A., & Rona, P. A. (1996). Gases and helium isotopes in high temperature solutions sampled before and after ODP Leg 158 drilling at TAG Hydrothermal Field (26°N, MAR). *Geophysical Research Letter*, 23(23), 3491–3494. <https://doi.org/10.1029/96gl02141>

Coveney, J., Goebel, E. D., Zeller, E. J., Dreschhoff, G. a. M., & Angino, E. E. (1987). Serpentinization and the origin of hydrogen gas in Kansas. *Am. Assoc. Pet. Geol., Bull.; (United States)*, 71:1(71). <https://www.osti.gov/biblio/6532504>

Cox, G. M., Halverson, G. P., Minarik, W. G., Le Heron, D. P., Macdonald, F. A., Bellefroid, E. J., & Strauss, J. V. (2013). Neoproterozoic iron formation: An evaluation of its temporal, environmental and tectonic significance. *Chemical Geology*, 362, 232–249. <https://doi.org/10.1016/j.chemgeo.2013.08.002>

Frery, E., Langhi, L., Maison, M., & Moretti, I. (2021). Natural hydrogen seeps identified in the North Perth Basin, Western Australia. *International Journal of Hydrogen Energy*, 46(61), 31158–31173. <https://doi.org/10.1016/j.ijhydene.2021.07.023>

Geymond, U., Briolet, T., Combaudon, V., Sissmann, O., Martinez, I., Duttine, M., & Moretti, I. (2023). Reassessing the role of magnetite during natural hydrogen generation. *Frontiers in Earth Science*, 11(487).

Geymond, U., Ramanaidou, E., Lévy, D., Ouaya, A., & Moretti, I. (2022). Can Weathering of Banded Iron Formations Generate Natural Hydrogen? Evidence from Australia, Brazil and South Africa. *Minerals*, 12(2), 163. <https://doi.org/10.3390/min12020163>

Giardini, A. A., Salotti, C. A., & Lakner, J. F. (1968). Synthesis of Graphite and Hydrocarbons by Reaction between Calcite and Hydrogen. *Science*, 159(3812), 317–319. <https://doi.org/10.1126/science.159.3812.317>

Goodwin, A. M. (1996). *Principles of Precambrian Geology*. In Google Books. Elsevier.

Guélard, J., Beaumont, V., Rouchon, V., Guyot, F., Pillot, D., Jézéquel, D., Ader, M., Newell, K. D., & Deville, E. (2017). Natural H₂ in Kansas: Deep or shallow origin? *Geochemistry, Geophysics, Geosystems*, 18(5), 1841–1865. <https://doi.org/10.1002/2016gc006544>

Hirose, T., Kawagucci, S., & Suzuki, K. (2011). Mechanoradical H₂ generation during simulated faulting: Implications for an earthquake-driven subsurface biosphere. *Geophysical Research Letters*, 38(17), n/a-n/a. <https://doi.org/10.1029/2011gl048850>

Holloway, J. R. (1984). Graphite-CH₄-H₂O-CO₂ equilibria at low-grade metamorphic conditions. *Geology*, 12(8), 455. [https://doi.org/10.1130/0091-7613\(1984\)12%3C455:gealmc%3E2.0.co;2](https://doi.org/10.1130/0091-7613(1984)12%3C455:gealmc%3E2.0.co;2)

Horsfield, B., Mahlstedt, N., Weniger, P., Misch, D., Vranjes-Wessely, S., Han, S., & Wang, C. (2022). Molecular hydrogen from organic sources in the deep Songliao Basin, P.R. China. *International Journal of Hydrogen Energy*, 47(38), 16750–16774. <https://doi.org/10.1016/j.ijhydene.2022.02.208>

Ilyin, A. V. (2009). Neoproterozoic banded iron formations. *Lithology and Mineral Resources*, 44(1), 78–86. <https://doi.org/10.1134/s0024490209010064>

Klein, C., & Beukes, N. J. (1993). Sedimentology and geochemistry of the glaciogenic late Proterozoic Rapitan Iron-Formation in Canada. *Economic Geology*, 88(3), 542–565. <https://doi.org/10.2113/gsecongeo.88.3.542>

Klein, F., Bach, W., & McCollom, T. M. (2013). Compositional controls on hydrogen generation during serpentinization of ultramafic rocks. *Lithos*, 178, 55–69. <https://doi.org/10.1016/j.lithos.2013.03.008>

Klein, F., Tarnas, J. D., & Bach, W. (2020). Abiotic Sources of Molecular Hydrogen on Earth. *Elements*, 16(1), 19–24. <https://doi.org/10.2138/gselements.16.1.19>

Krumrei, T. V., Pernicka, E., Kaliwoda, M., & Markl, G. (2007). Volatiles in a peralkaline system: Abiogenic hydrocarbons and F–Cl–Br systematics in the naujaite of the Ilímaussaq intrusion, South Greenland. *Lithos*, 95(3), 298–314. <https://doi.org/10.1016/j.lithos.2006.08.003>

Kularatne, K., Sissmann, O., Guyot, F., & Martinez, I. (2023). Mineral carbonation of New Caledonian ultramafic mine slag: Effect of glass and secondary silicates on the carbonation yield. *Chemical Geology*, 618, 121282. <https://doi.org/10.1016/j.chemgeo.2022.121282>

Kularatne, K., Sissmann, O., Kohler, E., Chardin, M., Noirez, S., & Martinez, I. (2018). Simultaneous ex-situ CO₂ mineral sequestration and hydrogen production from olivine-bearing mine tailings. *Applied Geochemistry*, 95, 195–205. <https://doi.org/10.1016/j.apgeochem.2018.05.020>

Larin, N., Zgonnik, V., Rodina, S., Deville, E., Prinzhofer, A., & Larin, V. N. (2014). Natural Molecular Hydrogen Seepage Associated with Surficial, Rounded Depressions on the European Craton in Russia. *Natural Resources Research*, 24(3), 369–383. <https://doi.org/10.1007/s11053-014-9257-5>

Lefevre, N., Truche, L., Donzé, F., Ducoux, M., Barré, G., Fakoury, R., Calassou, S., & Gaucher, E. C. (2021). Native H₂ Exploration in the Western Pyrenean Foothills. *Geochemistry, Geophysics, Geosystems*, 22(8). <https://doi.org/10.1029/2021gc009917>

Lin, L.-H., Hall, J., Lippmann-Pipke, J., Ward, J. A., Sherwood Lollar, B., DeFlaun, M., Rothmel, R., Moser, D., Gihring, T. M., Mislowack, B., & Onstott, T. C. (2005). Radiolytic H₂ in continental crust: Nuclear power for deep subsurface microbial communities. *Geochemistry, Geophysics, Geosystems*, 6(7), n/a-n/a. <https://doi.org/10.1029/2004gc000907>

Mahlstedt, N. (2018). Thermogenic Formation of Hydrocarbons in Sedimentary Basins. *Hydrocarbons, Oils and Lipids: Diversity, Origin, Chemistry and Fate*, 1–30. https://doi.org/10.1007/978-3-319-54529-5_15-1

Mahlstedt, N., Horsfield, B., Weniger, P., Misch, D., Shi, X., Noah, M., & Boreham, C. (2022). Molecular hydrogen from organic sources in geological systems. *Journal of Natural Gas Science and Engineering*, 105, 104704. <https://doi.org/10.1016/j.jngse.2022.104704>

Malvoisin, B., Brunet, F., Carlut, J., Rouméjon, S., & Cannat, M. (2012). Serpentinization of oceanic peridotites: 2. Kinetics and processes of San Carlos olivine hydrothermal alteration.

Journal of Geophysical Research: Solid Earth, 117(B4), n/a-n/a.
<https://doi.org/10.1029/2011jb008842>

Marcaillou, C. (2011). Serpentinisation et production d'hydrogène en contexte de dorsale lente : approche expérimentale et numérique. In theses.hal.science. <https://theses.hal.science/tel-00676948/>

Marks, M. A. W., & Markl, G. (2017). A global review on agpaitic rocks. *Earth-Science Reviews*, 173, 229–258. <https://doi.org/10.1016/j.earscirev.2017.06.002>

McCollom, T. M., & Bach, W. (2009). Thermodynamic constraints on hydrogen generation during serpentinization of ultramafic rocks. *Geochimica et Cosmochimica Acta*, 73(3), 856–875. <https://doi.org/10.1016/j.gca.2008.10.032>

Moody, J. B. (1976). Serpentinization: a review. *Lithos*, 9(2), 125–138. [https://doi.org/10.1016/0024-4937\(76\)90030-x](https://doi.org/10.1016/0024-4937(76)90030-x)

Moretti, I., Brouilly, E., Loiseau, K., Prinzhofer, A., & Deville, E. (2021). Hydrogen Emanations in Intracratonic Areas: New Guide Lines for Early Exploration Basin Screening. *Geosciences*, 11(3), 145. <https://doi.org/10.3390/geosciences11030145>

Moretti, I., Geymond, U., Pasquet, G., Aimar, L., & Rabaute, A. (2022). Natural hydrogen emanations in Namibia: Field acquisition and vegetation indexes from multispectral satellite image analysis. *International Journal of Hydrogen Energy*, 47(84), 35588–35607. <https://doi.org/10.1016/j.ijhydene.2022.08.135>

Myagkiy, A., Brunet, F., Popov, C., Krüger, R., Guimarães, H., Sousa, R. S., Charlet, L., & Moretti, I. (2020). H₂ dynamics in the soil of a H₂-emitting zone (São Francisco Basin, Brazil): Microbial uptake quantification and reactive transport modelling. *Applied Geochemistry*, 112, 104474. <https://doi.org/10.1016/j.apgeochem.2019.104474>

Myagkiy, A., Moretti, I., & Brunet, F. (2020). Space and time distribution of subsurface H₂ concentration in so-called “fairy circles”: Insight from a conceptual 2-D transport model. *BSGF - Earth Sciences Bulletin*, 191, 13. <https://doi.org/10.1051/bsgf/2020010>

Neal, C., & Stanger, G. (1985). Past And Present Serpentinisation of Ultramafic Rocks; An Example from the Semail Ophiolite Nappe of Northern Oman. *The Chemistry of Weathering*, 249–275. https://doi.org/10.1007/978-94-009-5333-8_15

Newell, K. D., Doveton, J. H., Merriam, D. F., Lollar, B. S., Waggoner, W. M., & Magnuson, L. M. (2007). H₂-rich and Hydrocarbon Gas Recovered in a Deep Precambrian Well in

Northeastern Kansas. Natural Resources Research, 16(3), 277–292.
<https://doi.org/10.1007/s11053-007-9052-7>

Nivin, V. (2020). The Origin of Hydrocarbon Gases in the Lovozero Nepheline-Syenite Massif (Kola Peninsula, NW Russia), as Revealed from He and Ar Isotope Evidence. *Minerals*, 10(9), 830. <https://doi.org/10.3390/min10090830>

Nivin, V. A. (2016). Free hydrogen-hydrocarbon gases from the Lovozero loparite deposit (Kola Peninsula, NW Russia). *Applied Geochemistry*, 74, 44–55.
<https://doi.org/10.1016/j.apgeochem.2016.09.003>

Nivin, V. A. (2019). Occurrence Forms, Composition, Distribution, Origin and Potential Hazard of Natural Hydrogen–Hydrocarbon Gases in Ore Deposits of the Khibiny and Lovozero Massifs: A Review. *Minerals*, 9(9), 535. <https://doi.org/10.3390/min9090535>

Noël, J. (2018, November 21). Etude pétro-structurale et géochimique des processus de serpentinisation et de carbonatation des péridotites de l'ophiolite d'Oman. *Theses.hal.science*.
<https://theses.hal.science/tel-02053492/>

Nyberg, B., & Howell, J. A. (2015). Is the present the key to the past? A global characterization of modern sedimentary basins. *Geology*, 43(7), 643–646. <https://doi.org/10.1130/g36669.1>

Potter, J., Salvi, S., & Longstaffe, F. J. (2013). Abiogenic hydrocarbon isotopic signatures in granitic rocks: Identifying pathways of formation. *Lithos*, 182–183, 114–124.
<https://doi.org/10.1016/j.lithos.2013.10.001>

Prinzhofer, A., Moretti, I., Françolin, J., Pacheco, C., D'Agostino, A., Werly, J., & Rupin, F. (2019). Natural hydrogen continuous emission from sedimentary basins: The example of a Brazilian H₂-emitting structure. *International Journal of Hydrogen Energy*, 44(12), 5676–5685.
<https://doi.org/10.1016/j.ijhydene.2019.01.119>

Prinzhofer, A., Tahara Cissé, C. S., & Diallo, A. B. (2018). Discovery of a large accumulation of natural hydrogen in Bourakebougou (Mali). *International Journal of Hydrogen Energy*, 43(42), 19315–19326. <https://doi.org/10.1016/j.ijhydene.2018.08.193>

Ramanaidou, E. R., & Wells, M. A. (2014). *Sedimentary hosted iron ores*. Elsevier.

Salvi, S., & Williams-Jones, A. E. (1990). The role of hydrothermal processes in the granite-hosted Zr, Y, REE deposit at Strange Lake, Quebec/Labrador: Evidence from fluid inclusions. *Geochimica et Cosmochimica Acta*, 54(9), 2403–2418. [https://doi.org/10.1016/0016-7037\(90\)90228-D](https://doi.org/10.1016/0016-7037(90)90228-D)

Salvi, S., & Williams-Jones, A. E. (1992). Reduced orthomagmatic C-O-H-N-NaCl fluids in the Strange Lake rare-metal granitic complex, Quebec/Labrador, Canada. *European Journal of Mineralogy*, 4(5), 1155–1174. <https://doi.org/10.1127/ejm/4/5/1155>

Salvi, S., & Williams-Jones, A. E. (1996). The role of hydrothermal processes in concentrating high-field strength elements in the Strange Lake peralkaline complex, northeastern Canada. *Geochimica et Cosmochimica Acta*, 60(11), 1917–1932. [https://doi.org/10.1016/0016-7037\(96\)00071-3](https://doi.org/10.1016/0016-7037(96)00071-3)

Sato, M., Sutton, A. J., McGee, K. A., & Russell-Robinson, S. (1986). Monitoring of hydrogen along the San Andreas and Calaveras faults in central California in 1980-1984. *Journal of Geophysical Research: Solid Earth*, 91(B12), 12315–12326. <https://doi.org/10.1029/jb091ib12p12315>

Sherwood Lollar, B., Onstott, T. C., Lacrampe-Couloume, G., & Ballentine, C. J. (2014). The contribution of the Precambrian continental lithosphere to global H₂ production. *Nature*, 516(7531), 379–382. <https://doi.org/10.1038/nature14017>

Sherwood Lollar, B., Voglesonger, K., Lin, L.-H. ., Lacrampe-Couloume, G., Telling, J., Abrajano, T. A., Onstott, T. C., & Pratt, L. M. (2007). Hydrogeologic Controls on Episodic H₂ Release from Precambrian Fractured Rocks—Energy for Deep Subsurface Life on Earth and Mars. *Astrobiology*, 7(6), 971–986. <https://doi.org/10.1089/ast.2006.0096>

Sherwood, B., Fritz, P., Frape, S. K., Macko, S. A., Weise, S. M., & Welhan, J. A. (1988). Methane occurrences in the Canadian Shield. *Chemical Geology*, 71(1-3), 223–236. [https://doi.org/10.1016/0009-2541\(88\)90117-9](https://doi.org/10.1016/0009-2541(88)90117-9)

Sugisaki, R., Ido, M., Takeda, H., Isobe, Y., Hayashi, Y., Nakamura, N., Satake, H., & Mizutani, Y. (1983). Origin of Hydrogen and Carbon Dioxide in Fault Gases and Its Relation to Fault Activity. *The Journal of Geology*, 91(3), 239–258. <https://doi.org/10.1086/628769>

Tissot, B., & Welte, D. (1980). *Petroleum Formation and Occurrence A New Approach to Oil and Gas Exploration*. <https://link.springer.com/content/pdf/bfm%253A978-3-642-96446-6%252F1.pdf>

Truche, L., Bourdelle, F., Salvi, S., Lefeuvre, N., Zug, A., & Lloret, E. (2021). Hydrogen generation during hydrothermal alteration of peralkaline granite. *Geochimica et Cosmochimica Acta*, 308, 42–59. <https://doi.org/10.1016/j.gca.2021.05.048>

Truche, L., Joubert, G., Dargent, M., Martz, P., Cathelineau, M., Rigaudier, T., & Quirt, D. (2018). Clay minerals trap hydrogen in the Earth's crust: Evidence from the Cigar Lake

uranium deposit, Athabasca. *Earth and Planetary Science Letters*, 493, 186–197.
<https://doi.org/10.1016/j.epsl.2018.04.038>

Vacquand, C., Deville, E., Beaumont, V., Guyot, F., Sissmann, O., Pillot, D., Arcilla, C., & Prinzhofer, A. (2018). Reduced gas seepages in ophiolitic complexes: Evidences for multiple origins of the H₂-CH₄-N₂ gas mixtures. *Geochimica et Cosmochimica Acta*, 223, 437–461.
<https://doi.org/10.1016/j.gca.2017.12.018>

Ward, L. K. (1933). Inflammable Gases Occluded in the Pre-Palaeozoic Rocks of South Australia.

Warr, O., Giunta, T., Ballentine, C. J., & Sherwood Lollar, B. (2019). Mechanisms and rates of 4He, 40Ar, and H₂ production and accumulation in fracture fluids in Precambrian Shield environments. *Chemical Geology*, 530, 119322. <https://doi.org/10.1016/j.chemgeo.2019.119322>

Welhan, J. A., & Craig, H. (1979). Methane and hydrogen in East Pacific Rise hydrothermal fluids. *Geophysical Research Letters*, 6(11), 829–831. <https://doi.org/10.1029/gl006i011p00829>

Zgonnik, V. (2020). The occurrence and geoscience of natural hydrogen: A comprehensive review. *Earth-Science Reviews*, 203, 103140. <https://doi.org/10.1016/j.earscirev.2020.103140>

Zgonnik, V., Beaumont, V., Deville, E., Larin, N., Pillot, D., & Farrell, K. M. (2015). Evidence for natural molecular hydrogen seepage associated with Carolina bays (surficial, ovoid depressions on the Atlantic Coastal Plain, Province of the USA). *Progress in Earth and Planetary Science*, 2(1). <https://doi.org/10.1186/s40645-015-0062-5>

Zhu, X.-Q., Tang, H.-S., & Sun, X.-H. (2014). Genesis of banded iron formations: A series of experimental simulations. *Ore Geology Reviews*, 63, 465–469.
<https://doi.org/10.1016/j.oregeorev.2014.03.009>

III. Chapter 3

Ballentine, C. J., O’Nions, R. K., Oxburgh, E. R., Horvath, F., & Deak, J. (1991). Rare gas constraints on hydrocarbon accumulation, crustal degassing and groundwater flow in the Pannonian Basin. *Earth and Planetary Science Letters*, 105(1-3), 229–246. [https://doi.org/10.1016/0012-821x\(91\)90133-3](https://doi.org/10.1016/0012-821x(91)90133-3)

Ballentine, C. J., & Sherwood Lollar, B. (2002). Regional groundwater focusing of nitrogen and noble gases into the Hugoton-Panhandle giant gas field, USA. *Geochimica et Cosmochimica Acta*, 66(14), 2483–2497. [https://doi.org/10.1016/s0016-7037\(02\)00850-5](https://doi.org/10.1016/s0016-7037(02)00850-5)

Barbarin, B. (1999). A review of the relationships between granitoid types, their origins and their geodynamic environments. *Lithos*, 46(3), 605–626. [https://doi.org/10.1016/s0024-4937\(98\)00085-1](https://doi.org/10.1016/s0024-4937(98)00085-1)

Bickford, M. E., Harrower, K. L., Hoppe, W. J., Nelson, B. K., Nusbaum, R. L., & Thomas, J. J. (1981). Rb-Sr and U-Pb geochronology and distribution of rock types in the Precambrian basement of Missouri and Kansas. *GSA Bulletin*, 92(6), 323–341. [https://doi.org/10.1130/0016-7606\(1981\)92%3C323:RAUGAD%3E2.0.CO;2](https://doi.org/10.1130/0016-7606(1981)92%3C323:RAUGAD%3E2.0.CO;2)

Burberry, C. M., Joeckel, R. M., & Korus, J. T. (2015). Post-Mississippian tectonic evolution of the Nemaha Tectonic Zone and Midcontinent Rift System, SE Nebraska and N Kansas. *Archives.datapages.com*, 52(4), 47–73. https://archives.datapages.com/data/mountain-geologist-rmag/data/052/052004/47_rmag-mg520047.htm

Cannon, W. F. (1994). Closing of the Midcontinent rift-A far—field effect of Grenvillian compression. *Geology*, 22(2), 155. [https://doi.org/10.1130/0091-7613\(1994\)022%3C0155:cotmra%3E2.3.co;2](https://doi.org/10.1130/0091-7613(1994)022%3C0155:cotmra%3E2.3.co;2)

Carlson, M. L., & Treves, S. B. (2005). The Elk Creek Carbonatite, Southeast Nebraska—An Overview. *Natural Resources Research*, 14(1), 39–45. <https://doi.org/10.1007/s11053-005-4677-x>

Cole, V. B. (1976). Configuration of the top of Precambrian rocks in Kansas: Kansas Geological Survey, Map Ser. M-7, scale: 1:500 000 [Map]. Kansas Geological Survey .

Cole, V. B., & Watney, W. L. (1985). List of wells drilled into Precambrian rocks: Kansas Geol. Survey, Subsurface Geology Ser. 7, 139 p.

Coveney, R. M., Jr., Goebel, E. D., Zeller, E. J., Dreschhoff, G. A. M., & Angino, E. E. (1987). Serpentinization and the Origin of Hydrogen Gas in Kansas1. *AAPG Bulletin*, 71(1), 39–48. <https://doi.org/10.1306/94886D3F-1704-11D7-8645000102C1865D>

Dickas, A. B., & Mudrey, M. G. (1997). Middle Proterozoic to Cambrian rifting, central North America. In *Google Books. Geological Society of America.*

https://books.google.fr/books?hl=fr&lr=&id=YS_pAgAAQBAJ&oi=fnd&pg=PA37&dq=dikas+and+mudrey+1997&ots=SzGTRqXnza&sig=003oSHN4qPeTBKeD-lu0h09tliw

Dolton, G., & Finn, T. (1989). Petroleum geology of the Nemaha uplift, central midcontinent. US Geological Survey Open-File Report, 88, 1-18. <https://scholar.archive.org/work/k4lhfgzqgzemxehownqolk2ndq/access/wayback/https://pubs.usgs.gov/of/1988/0450d/report.pdf>

Goodwin, A. M. (1996). Principles of Precambrian Geology. In Google Books. Elsevier.

Guélard, J., Beaumont, V., Rouchon, V., Guyot, F., Pillot, D., Jézéquel, D., Ader, M., Newell, K. D., & Deville, E. (2017). Natural H₂ in Kansas: Deep or shallow origin? *Geochemistry, Geophysics, Geosystems*, 18(5), 1841–1865. <https://doi.org/10.1002/2016gc006544>

Guélard, J. (2016). Caractérisation des émanations de dihydrogène naturel en contexte intracratonique : exemple d'une interaction gaz/eau/roche au Kansas. In *theses.hal.science*. <https://theses.hal.science/tel-01609839/>

Hemsell, C. C. (1939). Geology of Hugoton Gas Field of Southwestern Kansas. *Bulletin of the American Association of Petroleum Geologist*, 23. <https://doi.org/10.1306/3d9330da-16b1-11d7-8645000102c1865d>

Hinze, W. J., & Braile, L. W. (1988). Geophysical aspects of the craton: US. *Sedimentary Cover—North American Craton: US*, 90, 5. The Geological Society of America.

Macfarlane, P. A. (2000). Revisions to the Nomenclature for Kansas Aquifers. *Current Research in Earth Sciences*, 1–14. <https://doi.org/10.17161/cres.v0i244.11815>

Merriam, D. F. (1963). The geologic history of Kansas. University of Kansas publications.

Miller, J. D. (2011). Layered intrusions of the Duluth Complex. In *Archean to Anthropocene: field guides to the Geology of the Mid-Continent of North-America* (pp. 171–201). Geological Society of America. [https://doi.org/10.1130/2011.0024\(09\)](https://doi.org/10.1130/2011.0024(09))

Newell, K. D., Doveton, J. H., Merriam, D. F., Lollar, B. S., Waggoner, W. M., & Magnuson, L. M. (2007). H₂-rich and Hydrocarbon Gas Recovered in a Deep Precambrian Well in Northeastern Kansas. *Natural Resources Research*, 16(3), 277–292. <https://doi.org/10.1007/s11053-007-9052-7>

Ojakangas, R. W., Morey, G. B., & Green, J. C. (2001). The Mesoproterozoic Midcontinent Rift System, Lake Superior Region, USA. *Sedimentary Geology*, 141-142, 421–442. [https://doi.org/10.1016/s0037-0738\(01\)00085-9](https://doi.org/10.1016/s0037-0738(01)00085-9)

Serpa, L., Setzer, T., & Brown, L. (1989). COCORP seismic-reflection profiling in northeastern Kansas. *Geophysics in Kansas*; Steeples, DW, Ed.; Kansas Geological Survey: Lawrence, KS,

USA, 226, 165-176. In www.kgs.ku.edu.
<http://www.kgs.ku.edu/Publications/Bulletins/226/Serpa/>

Serpa, L., Setzer, T., Farmer, H., Brown, L. R., Oliver, J. D., Kaufman, S. B., Sharp, J. G., & Steeples, D. W. (1984). Structure of the Southern Keweenawan Rift from COCORP Surveys across the midcontinent geophysical anomaly in northeastern Kansas. *Tectonics*, 3(3), 367–384. <https://doi.org/10.1029/tc003i003p00367>

Sherwood Lollar, B., Lacrampe-Couloume, G., Slatter, G. F., Ward, J., Moser, D. P., Gihring, T. M., Lin, L.-H. ., & Onstott, T. C. (2006). Unravelling abiogenic and biogenic sources of methane in the Earth's deep subsurface. *Chemical Geology*, 226(3-4), 328–339. <https://doi.org/10.1016/j.chemgeo.2005.09.027>

Steeples, D. W., DuBois, S. M., & Wilson, F. W. (1979). Seismicity, faulting, and geophysical anomalies in Nemaha County, Kansas: Relationship to regional structures. *Geology*, 7(3), 134–138. <https://pubs.geoscienceworld.org/gsa/geology/article/7/3/134/188742/Seismicity-faulting-and-geophysical-anomalies-in>

Van Schmus, W. R., Bickford, M. E., & Condie, K. C. (1993). Early Proterozoic transcontinental orogenic belts in the United States. *Geological Society of America, Abstracts with Programs; (United States)*, 25:1. <https://www.osti.gov/biblio/5932944>

Woelk, T. S., & Hinze, W. J. (1991). Model of the midcontinent rift system in northeastern Kansas. *Geology*, 19(3), 277–280. [https://doi.org/10.1130/0091-7613\(1991\)019%3C0277:MOTMRS%3E2.3.CO;2](https://doi.org/10.1130/0091-7613(1991)019%3C0277:MOTMRS%3E2.3.CO;2)

IV. Chapter 4

Andreani, M., Muñoz, M., Marcaillou, C., & Delacour, A. (2013). μ XANES study of iron redox state in serpentine during oceanic serpentinization. *Lithos*, 178, 70–83. <https://doi.org/10.1016/j.lithos.2013.04.008>

Ballentine, C. J., & Sherwood Lollar, B. (2002). Regional groundwater focusing of nitrogen and noble gases into the Hugoton-Panhandle giant gas field, USA. *Geochimica et Cosmochimica Acta*, 66(14), 2483–2497. [https://doi.org/10.1016/s0016-7037\(02\)00850-5](https://doi.org/10.1016/s0016-7037(02)00850-5)

Bernard, B. B., Brooks, J. M., & Sackett, W. M. (1976). Natural gas seepage in the Gulf of Mexico. *Earth and Planetary Science Letters*, 31(1), 48–54. [https://doi.org/10.1016/0012-821x\(76\)90095-9](https://doi.org/10.1016/0012-821x(76)90095-9)

Bourdelle, F. (2011). Thermobarométrie des phyllosilicates dans les séries naturelles : conditions de la diagénèse et du métamorphisme de bas degré. In *theses.hal.science*. <https://theses.hal.science/tel-00616543/>

Bourdelle, F., Benzerara, K., Beyssac, O., Cosmidis, J., Neuville, D. R., Brown, G. E., & Paineau, E. (2013). Quantification of the ferric/ferrous iron ratio in silicates by scanning transmission X-ray microscopy at the Fe L_{2,3} edges. *Contributions to Mineralogy and Petrology*, 166(2), 423–434. <https://doi.org/10.1007/s00410-013-0883-4>

Centrella, S., Austrheim, H., & Putnis, A. (2015). Coupled mass transfer through a fluid phase and volume preservation during the hydration of granulite: An example from the Bergen Arcs, Norway. *Lithos*, 236-237, 245–255. <https://doi.org/10.1016/j.lithos.2015.09.010>

Centrella, S., Beaudoin, N., Derluyn, H., Motte, G., Guilhem Hoareau, Lanari, P., Piccoli, F., Christophe Pécheyran, & Jean-Paul Callot. (2020). Micro-scale chemical and physical patterns in an interface of hydrothermal dolomitization reveals the governing transport mechanisms in nature: Case of the Layens anticline, Pyrenees, France. *Sedimentology*, 68(2), 834–854. <https://doi.org/10.1111/sed.12808>

Ciobanu, C. L., Cook, N. J., Utsunomiya, S., Pring, A., & Green, L. (2011). Focussed ion beam–transmission electron microscopy applications in ore mineralogy: Bridging micro- and nanoscale observations. *Ore Geology Reviews*, 42(1), 6–31. <https://doi.org/10.1016/j.oregeorev.2011.06.012>

de la Pena, F., Ostasevicius, T., Tonaas Fauske, V., Burdet, P., Jokubauskas, P., Nord, M., Sarahan, M., Prestat, E., Johnstone, D. N., Taillon, J., Jan Caron, Furnival, T., MacArthur, K. E., Eljarrat, A., Mazzucco, S., Migunov, V., Aarholt, T., Walls, M., Winkler, F., & Donval,

G. (2017). Electron Microscopy (Big and Small) Data Analysis With the Open Source Software Package HyperSpy. *Microscopy and Microanalysis*, 23(S1), 214–215. <https://doi.org/10.1017/s1431927617001751>

Deville, E., & Prinzhofer, A. (2016). The origin of N₂-H₂-CH₄-rich natural gas seepages in ophiolitic context: A major and noble gases study of fluid seepages in New Caledonia. *Chemical Geology*, 440, 139–147. <https://doi.org/10.1016/j.chemgeo.2016.06.011>

Evans, B. W., Kuehner, S. M., Joswiak, D. J., & Cressey, G. (2017). Serpentine, Iron-rich Phyllosilicates and Fayalite Produced by Hydration and Mg Depletion of Peridotite, Duluth Complex, Minnesota, USA. *Journal of Petrology*, 58(3), 495–512. <https://doi.org/10.1093/petrology/egx024>

Giggenbach, W. F. (1987). Redox processes governing the chemistry of fumarolic gas discharges from White Island, New Zealand. *Applied Geochemistry*, 2(2), 143–161. [https://doi.org/10.1016/0883-2927\(87\)90030-8](https://doi.org/10.1016/0883-2927(87)90030-8)

Gresens, R. L. (1967). Composition-volume relationships of metasomatism. *Chemical Geology*, 2, 47–65. [https://doi.org/10.1016/0009-2541\(67\)90004-6](https://doi.org/10.1016/0009-2541(67)90004-6)

Guélard, J. (2016). Caractérisation des émanations de dihydrogène naturel en contexte intracratonique : exemple d'une interaction gaz/eau/roche au Kansas. In theses.hal.science. <https://theses.hal.science/tel-01609839/>

Kak, A. C., & Slaney, M. (1988). Principles of Computerized Tomographic Imaging. In ieeexplore.ieee.org. IEEE Press, New York . <https://ieeexplore.ieee.org/iel1/36/173/x0440791.pdf>

Lanari, P., Vho, A., Bovay, T., Airaghi, L., & Centrella, S. (2019). Quantitative compositional mapping of mineral phases by electron probe micro-analyser. *Geological Society, London, Special Publications*, 478(1), 39–63. <https://doi.org/10.1144/sp478.4>

Lanari, P., Vidal, O., De Andrade, V., Dubacq, B., Lewin, E., Grosch, E. G., & Schwartz, S. (2014). XMapTools: A MATLAB©-based program for electron microprobe X-ray image processing and geothermobarometry. *Computers & Geosciences*, 62, 227–240. <https://doi.org/10.1016/j.cageo.2013.08.010>

Landis, E. N., & Keane, D. T. (2010). X-ray microtomography. *Materials Characterization*, 61(12), 1305–1316. <https://doi.org/10.1016/j.matchar.2010.09.012>

Le Guillou, C., Changela, H. G., & Brearley, A. J. (2015). Widespread oxidized and hydrated amorphous silicates in CR chondrites matrices: Implications for alteration conditions and H₂ degassing of asteroids. *Earth and Planetary Science Letters*, 420, 162–173. <https://doi.org/10.1016/j.epsl.2015.02.031>

Lévy, D., Callot, J.-P., Moretti, I., Duttine, M., Dubreuil, B., de Parseval, P., & Boudouma, O. (2022). Successive phases of serpentization and carbonation recorded in the Sivas ophiolite (Turkey), from oceanic crust accretion to post-obduction alteration. *BSGF - Earth Sciences Bulletin*, 193, 12. <https://doi.org/10.1051/bsgf/2022015>

Malvoisin, B., Auzende, A.-L., & Kelemen, P. B. (2021). Nanostructure of serpentisation products: Importance for water transport and low-temperature alteration. *Earth and Planetary Science Letters*, 576, 117212. <https://doi.org/10.1016/j.epsl.2021.117212>

Malvoisin, B., Brunet, F., Carlut, J., Rouméjon, S., & Cannat, M. (2012). Serpentinization of oceanic peridotites: 2. Kinetics and processes of San Carlos olivine hydrothermal alteration. *Journal of Geophysical Research: Solid Earth*, 117(B4), n/a-n/a. <https://doi.org/10.1029/2011jb008842>

McLaren, A. C. (1991). *Transmission Electron Microscopy of Minerals and Rocks*. In NASA ADS. Cambridge University Press. <https://ui.adsabs.harvard.edu/abs/1991temm.book.....M/abstract>

McNair, H. M., Miller, J. M., & Snow, N. H. (2019). *Basic Gas Chromatography*. In Google Books. John Wiley & Sons. <https://books.google.fr/books?hl=fr&lr=&id=VimjDwAAQBAJ&oi=fnd&pg=PP11&dq=gas+chromatography+method+&ots=QmKMZaEq1Y&sig=6oQxbxfgVBGKpvPgxcQaRrAkkdU#v=onepage&q=gas%20chromatography%20method&f=true>

Meunier, A., Mas, A., Beaufort, D., Patrier, P., & Dudoignon, P. (2008). Clay minerals in basalt-hawaiite rocks from Mururoa Atoll (French Polynesia). II. Petrography and geochemistry. *Clays and Clay Minerals*, 56(6), 730–750. <https://doi.org/10.1346/ccmn.2008.0560612>

Osselin, F., Pichavant, M., Champallier, R., Ulrich, M., & Raimbourg, H. (2022). Reactive transport experiments of coupled carbonation and serpentization in a natural serpentinite. Implication for hydrogen production and carbon geological storage. *Geochimica et Cosmochimica Acta*, 318, 165–189. <https://doi.org/10.1016/j.gca.2021.11.039>

- Pasquet, G., Houssein Hassan, R., Sissmann, O., Varet, J., & Moretti, I. (2022). An Attempt to Study Natural H₂ Resources across an Oceanic Ridge Penetrating a Continent: The Asal–Ghoubbet Rift (Republic of Djibouti). *Geosciences*, 12(1), 16. <https://doi.org/10.3390/geosciences12010016>
- Pownceby, M. I., C. Neil Macrae, & Wilson, N. H. F. (2007). Mineral characterisation by EPMA mapping. *Mineral Engineering*, 20(5), 444–451. <https://doi.org/10.1016/j.mineng.2006.10.014>
- Putnis, A. (2002). Mineral replacement reactions: from macroscopic observations to microscopic mechanisms. *Mineralogical Magazine*, 66(5), 689–708. <https://doi.org/10.1180/0026461026650056>
- Saur, H., Sénéchal, P., Boiron, T., Aubourg, C., Derluyn, H., & Moonen, P. (2020). First investigation of quartz and calcite shape fabrics in strained shales by means of X-ray tomography. *Journal of Structural Geology*, 130, 103905. <https://doi.org/10.1016/j.jsg.2019.103905>
- Sherwood Lollar, B., Frapé, S. K., Weise, S. M., Fritz, P., Macko, S. A., & Welhan, J. A. (1993). Abiogenic methanogenesis in crystalline rocks. *Geochimica et Cosmochimica Acta*, 57(23-24), 5087–5097. [https://doi.org/10.1016/0016-7037\(93\)90610-9](https://doi.org/10.1016/0016-7037(93)90610-9)
- Sissmann, O., Brunet, F., Martinez, I., Guyot, F., Verlaguet, A., Pinquier, Y., & Daval, D. (2014). Enhanced Olivine Carbonation within a Basalt as Compared to Single-Phase Experiments: Reevaluating the Potential of CO₂ Mineral Sequestration. *Environmental Science & Technology*, 48(10), 5512–5519. <https://doi.org/10.1021/es405508a>
- Tobias, H. J., Sacks, G. L., Zhang, Y., & Brenna, J. T. (2009). Progress towards comprehensive 2d gas chromatography combustion isotope ratio mass spectrometry (GCxGCC-IRMS).
- Truche, L., Bourdelle, F., Salvi, S., Lefeuvre, N., Zug, A., & Lloret, E. (2021). Hydrogen generation during hydrothermal alteration of peralkaline granite. *Geochimica et Cosmochimica Acta*, 308, 42–59. <https://doi.org/10.1016/j.gca.2021.05.048>
- Tutolo, B. M., Evans, B. W., Tosca, N. J., Ignatyev, K., & Kuehner, S. M. (2019). Hisingerite-forming serpentinization in the Duluth Complex (USA): A rare terrestrial analogue for serpentinization on Mars. *NASA ADS*, 2019, V31B05. <https://ui.adsabs.harvard.edu/abs/2019AGUFM.V31B..05T/abstract>

Vacquand, C. (2011). Genesis and mobility of natural hydrogen: energy source or storable energy carrier?; Genese et mobilite de l'hydrogene naturel: source d'energie ou vecteur energetique stockable? Wwww.osti.gov. <https://www.osti.gov/etdeweb/biblio/22143685>

Vacquand, C., Deville, E., Beaumont, V., Guyot, F., Sissmann, O., Pillot, D., Arcilla, C., & Prinzhofer, A. (2018). Reduced gas seepages in ophiolitic complexes: Evidences for multiple origins of the H₂-CH₄-N₂ gas mixtures. *Geochimica et Cosmochimica Acta*, 223, 437–461. <https://doi.org/10.1016/j.gca.2017.12.018>

Viennet, J.-C. ., Bernard, S., Le Guillou, C., Sautter, V., Schmitt-Kopplin, P., Beyssac, O., Pont, S., Zanda, B., Hewins, R., & Remusat, L. (2020). Tardi-magmatic precipitation of Martian Fe/Mg-rich clay minerals via igneous differentiation. *Geochemical Perspectives Letters*, 47–52. <https://doi.org/10.7185/geochemlet.2023>

Welton, J. (1984). SEM petrology atlas. The American Association of Petroleum Geologists.

Whiticar, M. J. (1999). Carbon and hydrogen isotope systematics of bacterial formation and oxidation of methane. *Chemical Geology*, 161(1-3), 291–314. [https://doi.org/10.1016/s0009-2541\(99\)00092-3](https://doi.org/10.1016/s0009-2541(99)00092-3)

Willich, P. (1992). EPMA—A Versatile Technique for the Characterization of Thin Films and Layered Structures. *Electron Microbeam Analysis*, 1–17. https://doi.org/10.1007/978-3-7091-6679-6_1

V. Chapter 5

Baker, I., & Haggerty, S. E. (1967). The alteration of olivine in basaltic and associated lavas. *Contributions to Mineralogy and Petrology*, 16(3), 233–257. <https://doi.org/10.1007/bf00371094>

Belkhou, R., Stanescu, S., Swaraj, S., Besson, A., Ledoux, M., Hajlaoui, M., & Dalle, D. (2015). HERMES: a soft X-ray beamline dedicated to X-ray microscopy. *Journal of Synchrotron Radiation*, 22(4), 968–979. <https://doi.org/10.1107/s1600577515007778>

Bernard, S., Benzerara, K., Beyssac, O., Brown, G. E., Stamm, L. G., & Düringer, P. (2009). Ultrastructural and chemical study of modern and fossil sporoderms by Scanning Transmission X-ray Microscopy (STXM). *Review of Palaeobotany and Palynology*, 156(156), 248–261. <https://doi.org/10.1016/j.revpalbo.2008.09.002>

Bickforf, M. E., Harrower, K. L., Hoppe, W. J., Nelson, B. K., Nusbaum, R. L., & Thomas, J. J. (1981). Rb-Sr and U-Pb geochronology and distribution of rock types in the Precambrian basement of Missouri and Kansas. *GSA Bulletin*, 92(6), 323–341. [https://doi.org/10.1130/0016-7606\(1981\)92%3C323:RAUGAD%3E2.0.CO;2](https://doi.org/10.1130/0016-7606(1981)92%3C323:RAUGAD%3E2.0.CO;2)

Bourdelle, F., Benzerara, K., Beyssac, O., Cosmidis, J., Neuville, D. R., Brown, G. E., & Paineau, E. (2013). Quantification of the ferric/ferrous iron ratio in silicates by scanning transmission X-ray microscopy at the Fe L_{2,3} edges. *Contributions to Mineralogy and Petrology*, 166(2), 423–434. <https://doi.org/10.1007/s00410-013-0883-4>

Coveney, J., Goebel, E. D., Zeller, E. J., Dreschhoff, G. a. M., & Angino, E. E. (1987). Serpentinization and the origin of hydrogen gas in Kansas. *Am. Assoc. Pet. Geol., Bull.; (United States)*, 71:1(71). <https://www.osti.gov/biblio/6532504>

Dalou, C., Le Losq, C., Mysen, B. O., & Cody, G. D. (2015). Solubility and solution mechanisms of chlorine and fluorine in aluminosilicate melts at high pressure and high temperature. *American Mineralogist*, 100(10), 2272–2283. <https://doi.org/10.2138/am-2015-5201>

de la Pena, F., Ostasevicius, T., Tonaas Fauske, V., Burdet, P., Jokubauskas, P., Nord, M., Sarahan, M., Prestat, E., Johnstone, D. N., Taillon, J., Caron, J., Furnival, T., MacArthur, K. E., Eljarrat, A., Mazzucco, S., Migunov, V., Aarholt, T., Walls, M., Winkler, F., & Donval, G. (2017). Electron Microscopy (Big and Small) Data Analysis With the Open Source Software Package HyperSpy. *Microscopy and Microanalysis*, 23(S1), 214–215. <https://doi.org/10.1017/s1431927617001751>

DePasquale, B. M., & Jenkins, D. M. (2022). The upper-thermal stability of an iron-rich smectite: Implications for smectite formation on Mars. *Icarus*, 374(374), 114816. <https://doi.org/10.1016/j.icarus.2021.114816>

- Edwards, A. B. (1938). The Formation of Iddingsite. *American Mineralogist*, 23(4), 277–281. <https://pubs.geoscienceworld.org/msa/ammin/article-abstract/23/4/277/536978/The-Formation-of-Iddingsite>
- Eggleton, R. A. (1984). Formation of Iddingsite Rims on Olivine: A Transmission Electron Microscope Study. *Clays and Clay Minerals*, 32(1), 1–11. <https://doi.org/10.1346/ccmn.1984.0320101>
- Filiberto, J., & Treiman, A. H. (2009a). Martian magmas contained abundant chlorine, but little water. *Geology*, 37(12), 1087–1090. <https://doi.org/10.1130/g30488a.1>
- Filiberto, J., & Treiman, A. H. (2009b). The effect of chlorine on the liquidus of basalt: First results and implications for basalt genesis on Mars and Earth. *Chemical Geology*, 263(1-4), 60–68. <https://doi.org/10.1016/j.chemgeo.2008.08.025>
- Guélard, J., Beaumont, V., Rouchon, V., Guyot, F., Pillot, D., Jézéquel, D., Ader, M., Newell, K. D., & Deville, E. (2017). Natural H₂ in Kansas: Deep or shallow origin? *Geochemistry, Geophysics, Geosystems*, 18(5), 1841–1865. <https://doi.org/10.1002/2016gc006544>
- Guélard, J. (2016). Caractérisation des émanations de dihydrogène naturel en contexte intracratonique : exemple d'une interaction gaz/eau/roche au Kansas. In theses.hal.science. <https://theses.hal.science/tel-01609839/>
- Harlov, D. E., Hansen, E. C., & Bigler, C. (1998). Petrologic evidence for K-feldspar metasomatism in granulite facies rocks. *Chemical Geology*, 151(1), 373–386. [https://doi.org/10.1016/S0009-2541\(98\)00090-4](https://doi.org/10.1016/S0009-2541(98)00090-4)
- Le Guillou, C., & Brearley, A. (2014). Relationships between organics, water and early stages of aqueous alteration in the pristine CR3.0 chondrite MET 00426. *Geochimica et Cosmochimica Acta*, 131(131), 344–367. <https://doi.org/10.1016/j.gca.2013.10.024>
- Mas, A., Meunier, A., Beaufort, D., Patrier, P., & Dudoignon, P. (2008). Clay minerals in basalt-hawaiite rocks from Mururoa Atoll (French Polynesia). I. Mineralogy. *Clays and Clay Minerals*, 56(6), 711–729. <https://doi.org/10.1346/ccmn.2008.0560611>
- Merriam, D. F. (1963). The geologic history of Kansas. *Proceedings of the United States National Museum*. <https://cir.nii.ac.jp/crid/1130282273276970240>
- Meunier, A., Mas, A., Beaufort, D., Patrier, P., & Dudoignon, P. (2008). Clay minerals in basalt-hawaiite rocks from Mururoa Atoll (French Polynesia). II. Petrography and geochemistry. *Clays and Clay Minerals*, 56(6), 730–750. <https://doi.org/10.1346/ccmn.2008.0560612>
- Newell, K. D., Doveton, J. H., Merriam, D. F., Lollar, B. S., Waggoner, W. M., & Magnuson, L. M. (2007). H₂-rich and Hydrocarbon Gas Recovered in a Deep Precambrian Well in

Northeastern Kansas. Natural Resources Research, 16(3), 277–292.
<https://doi.org/10.1007/s11053-007-9052-7>

Putnis, A., Hinrichs, R., Putnis, C. V., Golla-Schindler, U., & Collins, L. G. (2007). Hematite in porous red-clouded feldspars: Evidence of large-scale crustal fluid–rock interaction. *Lithos*, 95(1-2), 10–18. <https://doi.org/10.1016/j.lithos.2006.07.004>

Ross, C. S., & Shannon, E. V. (1925). The origin, occurrence, composition, and physical properties of the mineral iddingsite. https://repository.si.edu/bitstream/handle/10088/15362/1/USNMP-67_2579_1925.pdf

Smith, K. L. (1987). Weathering of Basalt: Formation of Iddingsite. *Clays and Clay Minerals*, 35(6), 418–428. <https://doi.org/10.1346/ccmn.1987.0350602>

Steeple, D. W., DuBois, S. M., & Wilson, F. W. (1979). Seismicity, faulting, and geophysical anomalies in Nemaha County, Kansas: Relationship to regional structures. *Geology*, 7(3), 134–138. [https://doi.org/10.1130/0091-7613\(1979\)7%3C134:SFAGAI%3E2.0.CO;2](https://doi.org/10.1130/0091-7613(1979)7%3C134:SFAGAI%3E2.0.CO;2)

Swaraj, S., Belkou, R., Stanescu, S., Rioult, M., Besson, A., & Hitchcock, A. P. (2017). *Journal of Physics: Conference Series*.

Truche, L., Joubert, G., Dargent, M., Martz, P., Cathelineau, M., Rigaudier, T., & Quirt, D. (2018). Clay minerals trap hydrogen in the Earth's crust: Evidence from the Cigar Lake uranium deposit, Athabasca. *Earth and Planetary Science Letters*, 493(493), 186–197. <https://doi.org/10.1016/j.epsl.2018.04.038>

Viennet, J.-C. ., Bernard, S., Le Guillou, C., Sautter, V., Schmitt-Kopplin, P., Beyssac, O., Pont, S., Zanda, B., Hewins, R., & Remusat, L. (2020). Tardi-magmatic precipitation of Martian Fe/Mg-rich clay minerals via igneous differentiation. *Geochemical Perspectives Letters*, 47–52. <https://doi.org/10.7185/geochemlet.2023>

Viennet, J.-C., Bernard, S., Le Guillou, C., Sautter, V., Grégoire, B., Jambon, A., Pont, S., Beyssac, O., Zanda, B., Hewins, R., & Remusat, L. (2021). Martian Magmatic Clay Minerals Forming Vesicles: Perfect Niches for Emerging Life? *Astrobiology*, 21(5), 605–612. <https://doi.org/10.1089/ast.2020.2345>

Wang, J., Morin, C., Li, L., Hitchcock, A. P., Scholl, A., & Doran, A. (2009). Radiation damage in soft X-ray microscopy. *Journal of Electron Spectroscopy and Related Phenomena*, 170(1-3), 25–36. <https://doi.org/10.1016/j.elspec.2008.01.002>

Wirth, R. (2009). Focused Ion Beam (FIB) combined with SEM and TEM: Advanced analytical tools for studies of chemical composition, microstructure and crystal structure in geomaterials on a nanometre scale. *Chemical Geology*, 261(3-4), 217–229. <https://doi.org/10.1016/j.chemgeo.2008.05.019>

Woelk, T. S., & Hinze, W. J. (1991). Model of the midcontinent rift system in northeastern Kansas. *Geology*, 19(3), 277–280. [https://doi.org/10.1130/0091-7613\(1991\)019%3C0277:MOTMRS%3E2.3.CO;2](https://doi.org/10.1130/0091-7613(1991)019%3C0277:MOTMRS%3E2.3.CO;2)

VI. Chapter 6

Ague, J. J. (1991). Evidence for major mass transfer and volume strain during regional metamorphism of pelites. *Geology*, 19(8), 855. [https://doi.org/10.1130/0091-7613\(1991\)019%3C0855:efmmta%3E2.3.co;2](https://doi.org/10.1130/0091-7613(1991)019%3C0855:efmmta%3E2.3.co;2)

Allen, D. E., & Seyfried, W. E. (2003). Compositional controls on vent fluids from ultramafic-hosted hydrothermal systems at mid-ocean ridges: An experimental study at 400°C, 500 bars. *Geochimica et Cosmochimica Acta*, 67(8), 1531–1542. [https://doi.org/10.1016/S0016-7037\(02\)01173-0](https://doi.org/10.1016/S0016-7037(02)01173-0)

Andreani, M., Muñoz, M., Marcaillou, C., & Delacour, A. (2013). μ XANES study of iron redox state in serpentine during oceanic serpentinization. *Lithos*, 178, 70–83. <https://doi.org/10.1016/j.lithos.2013.04.008>

Baptiste Debret, Andreani, M., Muñoz, M., Bolfan-Casanova, N., Carlut, J., Nicollet, C., Schwartz, S., & Trcera, N. (2014). Evolution of Fe redox state in serpentine during subduction. *Earth and Planetary Science Letters*, 400, 206–218. <https://doi.org/10.1016/j.epsl.2014.05.038>

Bickford, M. E., Harrower, K. L., Hoppe, W. J., Nelson, B. K., Nusbaum, R. L., & Thomas, J. J. (1981). Rb-Sr and U-Pb geochronology and distribution of rock types in the Precambrian basement of Missouri and Kansas. *GSA Bulletin*, 92(6), 323–341. [https://doi.org/10.1130/0016-7606\(1981\)92%3C323:RAUGAD%3E2.0.CO;2](https://doi.org/10.1130/0016-7606(1981)92%3C323:RAUGAD%3E2.0.CO;2)

Birle, J. D., Gibbs, G. V., Moore, P. B., & Smith, J. V. (1968). Crystal structures of natural olivines. *American Mineralogist*, 53(5-6), 807–824. <https://pubs.geoscienceworld.org/msa/ammin/article-abstract/53/5-6/807/542440>

Bischoff, J. L., & Dickson, F. W. (1975). Seawater-basalt interaction at 200°C and 500 bars: Implications for origin of sea-floor heavy-metal deposits and regulation of seawater chemistry. *Earth and Planetary Science Letters*, 25(3), 385–397. [https://doi.org/10.1016/0012-821x\(75\)90257-5](https://doi.org/10.1016/0012-821x(75)90257-5)

Brigatti, M. F., Lugli, C., Poppi, L., Foord, E. E., & Kile, D. E. (2000). Crystal chemical variations in Li- and Fe-rich micas from Pikes Peak batholith (central Colorado). *American Mineralogist*, 85(9), 1275–1286. <https://doi.org/10.2138/am-2000-8-920>

Burnham, C. W., Ohashi, Y., Hafner, S. S., & Virgo, D. (1971). Cation Distribution and Atomic Thermal Vibrations in an Iron-Rich Orthopyroxene. *American Mineralogist*, 56(5-6), 850–876. <https://pubs.geoscienceworld.org/msa/ammin/article-abstract/56/5-6/850/540882>

Campbell, A. C., Bowers, T. S., Measures, C. I., Falkner, K. K., Khadem, M., & Edmond, J. M. (1988). A time series of vent fluid compositions from 21°N, East Pacific Rise (1979, 1981, 1985), and the Guaymas Basin, Gulf of California (1982, 1985). *Journal of Geophysical Research: Solid Earth*, 93(B5), 4537–4549. <https://doi.org/10.1029/jb093ib05p04537>

Carlson, W. D., J. Steven Swinnea, & Miser, D. E. (1988). Stability of orthoenstatite at high temperature and low pressure. *American Mineralogist*, 73(11-12), 1255–1263. <https://pubs.geoscienceworld.org/msa/ammin/article-abstract/73/11-12/1255/42068>

Carmichael, D. M. (1969). On the mechanism of prograde metamorphic reactions in quartz-bearing pelitic rocks. *Contributions to Mineralogy and Petrology*, 20(3), 244–267. <https://doi.org/10.1007/bf00377479>

Carmichael, D. M. (1987). Induced Stress and Secondary Mass Transfer: Thermodynamic Basis for the Tendency toward Constant-Volume Constraint in Diffusion Metasomatism. *Chemical Transport in Metasomatic Processes*, 239–264. https://doi.org/10.1007/978-94-009-4013-0_10

Centrella, S., Austrheim, H., & Putnis, A. (2015). Coupled mass transfer through a fluid phase and volume preservation during the hydration of granulite: An example from the Bergen Arcs, Norway. *Lithos*, 236-237, 245–255. <https://doi.org/10.1016/j.lithos.2015.09.010>

Centrella, S., Austrheim, H., & Putnis, A. (2016). Mass transfer and trace element redistribution during hydration of granulites in the Bergen Arcs, Norway. *Lithos*, 262, 1–10. <https://doi.org/10.1016/j.lithos.2016.06.019>

Centrella, S., Beaudoin, N. E., Trebucq, C., Hoareau, G., Rivas, E. G., Martin-Martin, J. D., & Callot, J.-P. (2023). Textural and chemical evolution during dedolomitization: A case study of the Benassal Formation, Maestrat Basin, Spain. *Marine and Petroleum Geology*, 153, 106290. <https://doi.org/10.1016/j.marpetgeo.2023.106290>

Centrella, S., Beaudoin, N., Derluyn, H., Motte, G., Guilhem Hoareau, Lanari, P., Piccoli, F., Christophe Pécheyran, & Jean-Paul Callot. (2020). Micro-scale chemical and physical patterns in an interface of hydrothermal dolomitization reveals the governing transport mechanisms in nature: Case of the Layens anticline, Pyrenees, France. *Sedimentology*, 68(2), 834–854. <https://doi.org/10.1111/sed.12808>

Centrella, S., Hoareau, G., Beaudoin, N. E., Motte, G., Lanari, P., Piccoli, F., Callot, J. P., Gomez-Rivas, E., & Martín-Martín, J. D. (2023). Estimating the fluid composition after dolomitization using mass balance equation: comparison of examples from Spain, Canada and

France. Global and Planetary Change, 220, 104016.
<https://doi.org/10.1016/j.gloplacha.2022.104016>

Centrella, S., Putnis, A., Lanari, P., & Austrheim, H. (2018). Textural and chemical evolution of pyroxene during hydration and deformation: A consequence of retrograde metamorphism. *Lithos*, 296-299, 245–264. <https://doi.org/10.1016/j.lithos.2017.11.002>

Colville, A. A., & Ribbe, P. H. (1968). The crystal structure of an adularia and a refinement of the structure of orthoclase. *American Mineralogist*, 53(1-2), 25–37. <https://pubs.geoscienceworld.org/msa/ammin/article-abstract/53/1-2/25/542374>

Coveney, R. M., Jr., Goebel, E. D., Zeller, E. J., Dreschhoff, G. A. M., & Angino, E. E. (1987). Serpentinization and the Origin of Hydrogen Gas in Kansas1. *AAPG Bulletin*, 71(1), 39–48. <https://doi.org/10.1306/94886D3F-1704-11D7-8645000102C1865D>

Daval, D., Sissmann, O., Menguy, N., Saldi, G. D., Guyot, F., Martinez, I., Corvisier, J., Garcia, B., Machouk, I., Knauss, K. G., & Hellmann, R. (2011). Influence of amorphous silica layer formation on the dissolution rate of olivine at 90°C and elevated pCO₂. *Chemical Geology*, 284(1-2), 193–209. <https://doi.org/10.1016/j.chemgeo.2011.02.021>

Deer, W. A., Howie, R. A., & Zussman, J. (2013). An Introduction to the Rock-Forming Minerals. In [pubs.geoscienceworld.org](https://pubs.geoscienceworld.org/minersoc/books/book/952/An-Introduction-to-the-Rock-Forming-Minerals). Mineralogical Society of Great Britain and Ireland. <https://pubs.geoscienceworld.org/minersoc/books/book/952/An-Introduction-to-the-Rock-Forming-Minerals>

Dungan, M. (2009). A microprobe study of antigorite and some serpentine pseudomorphs. *Canadian Mineralogist*. https://hero.epa.gov/hero/index.cfm/reference/details/reference_id/6868956

Emmanuel, S., & Berkowitz, B. (2006). Suppression and stimulation of seafloor hydrothermal convection by exothermic mineral hydration. *Earth and Planetary Science Letters*, 243(3), 657–668. <https://doi.org/10.1016/j.epsl.2006.01.028>

Flatt, R. J. (2002). Salt damage in porous materials: how high supersaturations are generated. *Journal of Crystal Growth*, 242(3-4), 435–454. [https://doi.org/10.1016/s0022-0248\(02\)01429-x](https://doi.org/10.1016/s0022-0248(02)01429-x)

Foit, F. F., & Peacor, D. R. (1973). The anorthite crystal structure at 410 and 830°C. *American Mineralogist*, 58(7-8), 665–675. <https://pubs.geoscienceworld.org/msa/ammin/article-abstract/58/7-8/665/542843>

- Frery, E., Langhi, L., Maison, M., & Moretti, I. (2021). Natural hydrogen seeps identified in the North Perth Basin, Western Australia. *International Journal of Hydrogen Energy*, 46(61), 31158–31173. <https://doi.org/10.1016/j.ijhydene.2021.07.023>
- Geymond, U., Briollet, T., Combaudon, V., Sissmann, O., Martinez, I., Duttine, M., & Moretti, I. (2023). Reassessing the role of magnetite during natural hydrogen generation. *Frontiers in Earth Science*, 11(487).
- Godard, M., Yves Lagabrielle, Olivier Alard, & Harvey, J. T. (2008). Geochemistry of the highly depleted peridotites drilled at ODP Sites 1272 and 1274 (Fifteen-Twenty Fracture Zone, Mid-Atlantic Ridge): Implications for mantle dynamics beneath a slow spreading ridge. *Earth and Planetary Science Letters*, 267(3-4), 410–425. <https://doi.org/10.1016/j.epsl.2007.11.058>
- Grant, J. A. (1986). The isocon diagram; a simple solution to Gresens' equation for metasomatic alteration. *Economic Geology*, 81(8), 1976–1982. <https://doi.org/10.2113/gsecongeo.81.8.1976>
- Grant, J. A. (2005). Isocon analysis: A brief review of the method and applications. *Physics and Chemistry of the Earth, Parts A/B/C*, 30(17-18), 997–1004. <https://doi.org/10.1016/j.pce.2004.11.003>
- Gresens, R. L. (1967). Composition-volume relationships of metasomatism. *Chemical Geology*, 2, 47–65. [https://doi.org/10.1016/0009-2541\(67\)90004-6](https://doi.org/10.1016/0009-2541(67)90004-6)
- Grozeva, N. G., Klein, F., Seewald, J. S., & Sylva, S. P. (2017). Experimental study of carbonate formation in oceanic peridotite. *Geochimica et Cosmochimica Acta*, 199, 264–286. <https://doi.org/10.1016/j.gca.2016.10.052>
- Guélard, J., Beaumont, V., Rouchon, V., Guyot, F., Pillot, D., Jézéquel, D., Ader, M., Newell, K. D., & Deville, E. (2017). Natural H₂ in Kansas: Deep or shallow origin? *Geochemistry, Geophysics, Geosystems*, 18(5), 1841–1865. <https://doi.org/10.1002/2016gc006544>
- Hazen, R. M., & Burnham, C. W. (1973). The Crystal Structures of One-Layer Phlogopite and Annite. *American Mineralogist*, 58(9-10), 889–900. <https://pubs.geoscienceworld.org/msa/ammin/article-abstract/58/9-10/889/542895>
- Hendricks, S. B. (1939). Random structures of layer minerals as illustrated by cronstedite (2FeO.Fe₂O₃.SiO₂.2H₂O). Possible iron content of kaolin. *American Mineralogist*, 24(9), 529–539. <https://pubs.geoscienceworld.org/msa/ammin/article-abstract/24/9/529/537156>

- Hendricks, S. B., & Jefferson, M. E. (1939). Polymorphism of the micas with optical measurements. *American Mineralogist*, 24(12), 729–771. <https://pubs.geoscienceworld.org/msa/ammin/article-abstract/24/12/729/537187>
- Hermann, J., Zheng, Y.-F. ., & Rubatto, D. (2013). Deep Fluids in Subducted Continental Crust. *Elements*, 9(4), 281–287. <https://doi.org/10.2113/gselements.9.4.281>
- Lanari, P. (2018). An introduction to XMAPTOOLS 2.6 numerical tools for quantitative petrology. https://www.xmaptools.com/XMapTools.2.6_UserGuide.pdf
- Lanari, P., & Engi, M. (2017). Local Bulk Composition Effects on Metamorphic Mineral Assemblages. *Reviews in Mineralogy and Geochemistry*, 83(1), 55–102. <https://doi.org/10.2138/rmg.2017.83.3>
- Lanari, P., Vho, A., Bovay, T., Airaghi, L., & Centrella, S. (2019). Quantitative compositional mapping of mineral phases by electron probe micro-analyser. *Geological Society, London, Special Publications*, 478(1), 39–63. <https://doi.org/10.1144/sp478.4>
- Lanari, P., Vidal, O., De Andrade, V., Dubacq, B., Lewin, E., Grosch, E. G., & Schwartz, S. (2014). XMapTools: A MATLAB©-based program for electron microprobe X-ray image processing and geothermobarometry. *Computers & Geosciences*, 62, 227–240. <https://doi.org/10.1016/j.cageo.2013.08.010>
- Larin, N., Zgonnik, V., Rodina, S., Deville, E., Prinzhofer, A., & Larin, V. N. (2014). Natural Molecular Hydrogen Seepage Associated with Surficial, Rounded Depressions on the European Craton in Russia. *Natural Resources Research*, 24(3), 369–383. <https://doi.org/10.1007/s11053-014-9257-5>
- Le Maitre, R. W. (1981). GENMIX—A generalized petrological mixing model program. *Computers & Geosciences*, 7(3), 229–247. [https://doi.org/10.1016/0098-3004\(81\)90046-7](https://doi.org/10.1016/0098-3004(81)90046-7)
- Leake, B. E. (1978). Nomenclature of amphiboles. *American Mineralogist*, 63(11-12), 1023–1052. <https://pubs.geoscienceworld.org/msa/ammin/article-abstract/63/11-12/1023/40814>
- Leake, B. E., Woolley, A. R., Arps, C., Birch, W. D., M. Charles Gilbert, Grice, J. D., Hawthorne, F. C., Kato, A., Kisch, H. J., Krivovichev, V. G., Kees Linthout, Laird, J., Mandarino, J. A., Maresch, W. V., Nickel, E. H., Nicholas, Schumacher, J. C., Smith, D. C., Nick, & Ungaretti, L. (1997). Nomenclature of amphiboles; report of the subcommittee on amphiboles of the International Mineralogical Association, Commission on New Minerals and Mineral Names. *The Canadian Mineralogist*, 35(1), 219–246. <https://pubs.geoscienceworld.org/canmin/article-abstract/35/1/219/12862>

- Lécuyer, C., Brouxel, M., & Albarède, F. (1990). Elemental fluxes during hydrothermal alteration of the Trinity ophiolite (California, U.S.A.) by seawater. *Chemical Geology*, 89(1), 87–115. [https://doi.org/10.1016/0009-2541\(90\)90061-B](https://doi.org/10.1016/0009-2541(90)90061-B)
- Leong JA, Nielsen M, McQueen N, et al (2023) H₂ and CH₄ outgassing rates in the Samail ophiolite, Oman: Implications for low-temperature, continental serpentinization rates. *Geochimica et Cosmochimica Acta* 347:1–15. <https://doi.org/10.1016/j.gca.2023.02.008>
- Macdonald, A. H., & Fyfe, W. S. (1985). Rate of serpentinization in seafloor environments. *Tectonophysics*, 116(1), 123–135. [https://doi.org/10.1016/0040-1951\(85\)90225-2](https://doi.org/10.1016/0040-1951(85)90225-2)
- Maliva, R., & Siever, R. (1988). Diagenetic replacement controlled by force of crystallization. *Geology*, 16(8), 688–688. [https://doi.org/10.1130/0091-7613\(1988\)016%3C0688:drcbfo%3E2.3.co;2](https://doi.org/10.1130/0091-7613(1988)016%3C0688:drcbfo%3E2.3.co;2)
- McCollom, T. M., Klein, F., Robbins, M., Moskowitz, B., Berquó, T. S., Jöns, N., Bach, W., & Templeton, A. (2016). Temperature trends for reaction rates, hydrogen generation, and partitioning of iron during experimental serpentinization of olivine. *Geochimica et Cosmochimica Acta*, 181, 175–200. <https://doi.org/10.1016/j.gca.2016.03.002>
- Mellini, M. (1982). The crystal structure of lizardite 1T: hydrogen bonds and polytypism. *American Mineralogist*, 67(5-6), 587–598. <https://pubs.geoscienceworld.org/msa/ammin/article-abstract/67/5-6/587/41395>
- Merino, E., & Canals, A. (2011). Self-accelerating dolomite-for-calcite replacement: Self-organized dynamics of burial dolomitization and associated mineralization. *American Journal of Science*, 311(7), 573–607. <https://doi.org/10.2475/07.2011.01>
- Mével, C. (2003). Serpentinization of abyssal peridotites at mid-ocean ridges. *Comptes Rendus Geoscience*, 335(10-11), 825–852. <https://doi.org/10.1016/j.crte.2003.08.006>
- Moody, J. B. (1976). Serpentinization: a review. *Lithos*, 9(2), 125–138. [https://doi.org/10.1016/0024-4937\(76\)90030-x](https://doi.org/10.1016/0024-4937(76)90030-x)
- Ojakangas, R. W., Morey, G. B., & Green, J. C. (2001). The Mesoproterozoic Midcontinent Rift System, Lake Superior Region, USA. *Sedimentary Geology*, 141-142, 421–442. [https://doi.org/10.1016/s0037-0738\(01\)00085-9](https://doi.org/10.1016/s0037-0738(01)00085-9)
- Pens, M., Andreani, M., Daniel, I., Perrillat, J.-P., & Cardon, H. (2016). Contrasted effect of aluminum on the serpentinization rate of olivine and orthopyroxene under hydrothermal conditions. *Chemical Geology*, 441, 256–264. <https://doi.org/10.1016/j.chemgeo.2016.08.007>

Plümper, O., Røyne, A., Magrasó, A., & Bjørn Jamtveit. (2012). The interface-scale mechanism of reaction-induced fracturing during serpentinization. *Geology*, 40(12), 1103–1106. <https://doi.org/10.1130/g33390.1>

Prewitt, C. T., S. Sueno, & Papike, J. J. (1976). The crystal structures of high albite and monalbite at high temperatures. *American Mineralogist*, 61(11-12), 1213–1225. <https://pubs.geoscienceworld.org/msa/ammin/article-abstract/61/11-12/1213/40595>

Prinzhofer, A., Tahara Cissé, C. S., & Diallo, A. B. (2018). Discovery of a large accumulation of natural hydrogen in Bourakebougou (Mali). *International Journal of Hydrogen Energy*, 43(42), 19315–19326. <https://doi.org/10.1016/j.ijhydene.2018.08.193>

Putnis, A. (2002). Mineral replacement reactions: from macroscopic observations to microscopic mechanisms. *Mineralogical Magazine*, 66(5), 689–708. <https://doi.org/10.1180/0026461026650056>

Putnis, A. (2009). Mineral Replacement Reactions. *Reviews in Mineralogy and Geochemistry*, 70(1), 87–124. <https://doi.org/10.2138/rmg.2009.70.3>

Putnis, A., & Austrheim, H. (2010). Fluid-induced processes: metasomatism and metamorphism. *Geofluids*, 10. <https://doi.org/10.1111/j.1468-8123.2010.00285.x>

Shervais, J. W., Kolesar, P., & Andreasen, K. (2005). A Field and Chemical Study of Serpentinization—Stonyford, California: Chemical Flux and Mass Balance. *International Geology Review*, 47(1), 1–23. <https://doi.org/10.2747/0020-6814.47.1.1>

Shirozu, H., & Bailey, S. W. (1965). Chlorite polytypism: III. crystal structure of an orthohexagonal iron chlorite. *American Mineralogist*, 50(7-8), 868–885. <https://pubs.geoscienceworld.org/msa/ammin/article-abstract/50/7-8/868/540139>

Sissmann, O., Brunet, F., Martinez, I., Guyot, F., Verlaguet, A., Pinquier, Y., & Daval, D. (2014). Enhanced Olivine Carbonation within a Basalt as Compared to Single-Phase Experiments: Reevaluating the Potential of CO₂ Mineral Sequestration. *Environmental Science & Technology*, 48(10), 5512–5519. <https://doi.org/10.1021/es405508a>

Steeple, D. W., DuBois, S. M., & Wilson, F. W. (1979). Seismicity, faulting, and geophysical anomalies in Nemaha County, Kansas: Relationship to regional structures. *Geology*, 7(3), 134–138. [https://doi.org/10.1130/0091-7613\(1979\)7%3C134:SFAGAI%3E2.0.CO;2](https://doi.org/10.1130/0091-7613(1979)7%3C134:SFAGAI%3E2.0.CO;2)

Toft, P. B., Arkani-Hamed, J., & Haggerty, S. E. (1990). The effects of serpentinization on density and magnetic susceptibility: a petrophysical model. *Physics of the Earth and Planetary Interiors*, 65(1-2), 137–157. [https://doi.org/10.1016/0031-9201\(90\)90082-9](https://doi.org/10.1016/0031-9201(90)90082-9)

Van Schmus, W. R., Bickford, M. E., & Condie, K. C. (1993). Early Proterozoic transcontinental orogenic belts in the United States. *Geological Society of America, Abstracts with Programs; (United States)*, 25:1. <https://www.osti.gov/biblio/5932944>

Ward, L. (1933). Inflammable gases occluded in the pre-Palaeozoic rocks in South Australia. *Proceedings of the Royal Society of South Australia* .

Wicks, F. J., & Whittaker, W. (1977). Serpentine textures and serpentinization. *The Canadian Mineralogist*, 15(4), 459–488. <https://pubs.geoscienceworld.org/canmin/article-abstract/15/4/459/11203>

Wilson, C. (1996). Hydrothermal anomalies in the Lucky Strike segment on the Mid-Atlantic Ridge (37°17'N). *Earth and Planetary Science Letters*, 142(3-4), 467–477. [https://doi.org/10.1016/0012-821x\(96\)00100-8](https://doi.org/10.1016/0012-821x(96)00100-8)

Wilson, M. J. (2004). Weathering of the primary rock-forming minerals: processes, products and rates. *Clay Minerals*, 39(3), 233–266. <https://doi.org/10.1180/0009855043930133>

Woelk, T. S., & Hinze, W. J. (1991). Model of the midcontinent rift system in northeastern Kansas. *Geology*, 19(3), 277–280. [https://doi.org/10.1130/0091-7613\(1991\)019%3C0277:MOTMRS%3E2.3.CO;2](https://doi.org/10.1130/0091-7613(1991)019%3C0277:MOTMRS%3E2.3.CO;2)

VII. Chapter 7

Ballentine, C. J., O’Nions, R. K., Oxburgh, E. R., Horvath, F., & Deak, J. (1991). Rare gas constraints on hydrocarbon accumulation, crustal degassing and groundwater flow in the Pannonian Basin. *Earth and Planetary Science Letters*, 105(1-3), 229–246. [https://doi.org/10.1016/0012-821x\(91\)90133-3](https://doi.org/10.1016/0012-821x(91)90133-3)

Ballentine, C. J., & Sherwood Lollar, B. (2002). Regional groundwater focusing of nitrogen and noble gases into the Hugoton-Panhandle giant gas field, USA. *Geochimica et Cosmochimica Acta*, 66(14), 2483–2497. [https://doi.org/10.1016/s0016-7037\(02\)00850-5](https://doi.org/10.1016/s0016-7037(02)00850-5)

Campbell, A. C., Palmer, M. R., Klinkhammer, G. P., Bowers, T. S., Edmond, J. M., Lawrence, J. R., Casey, J. F., Thompson, G., Humphris, S., Rona, P., & Karson, J. A. (1988). Chemistry of hot springs on the Mid-Atlantic Ridge. *Nature*, 335(6190), 514–519. <https://doi.org/10.1038/335514a0>

Cannon, W. F. (1994). Closing of the Midcontinent rift—A far—field effect of Grenvillian compression. *Geology*, 22(2), 155. [https://doi.org/10.1130/0091-7613\(1994\)022%3C0155:cotmra%3E2.3.co;2](https://doi.org/10.1130/0091-7613(1994)022%3C0155:cotmra%3E2.3.co;2)

Deville, E., & Prinzhofer, A. (2016). The origin of N₂-H₂-CH₄-rich natural gas seepages in ophiolitic context: A major and noble gases study of fluid seepages in New Caledonia. *Chemical Geology*, 440, 139–147. <https://doi.org/10.1016/j.chemgeo.2016.06.011>

Douglas, P. M. J., Stolper, D. A., Eiler, J. M., Sessions, A. L., Lawson, M., Shuai, Y., Bishop, A., Podlaha, O. G., Ferreira, A. A., Santos Neto, E. V., Niemann, M., Steen, A. S., Huang, L., Chimiak, L., Valentine, D. L., Fiebig, J., Luhmann, A. J., Seyfried, W. E., Etiope, G., & Schoell, M. (2017). Methane clumped isotopes: Progress and potential for a new isotopic tracer. *Organic Geochemistry*, 113, 262–282. <https://doi.org/10.1016/j.orggeochem.2017.07.016>

Eickenbusch, P., Takai, K., Sissmann, O., Suzuki, S., Menzies, C., Sakai, S., Sansjofre, P., Tasumi, E., Bernasconi, S. M., Glombitza, C., Jorgensen, B. B., Morono, Y., & Lever, M. A. (2019). Origin of short-chain organic acids in serpentinite mud volcanoes of the Mariana convergent margin. *Frontiers in Microbiology*, 10.

Etiope, G., Ehlmann, B. L., & Schoell, M. (2013). Low temperature production and exhalation of methane from serpentinized rocks on Earth: A potential analog for methane production on Mars. *Icarus*, 224(2), 276–285. <https://doi.org/10.1016/j.icarus.2012.05.009>

Etiope, G., & Sherwood Lollar, B. (2013). Abiotic methane of Earth. *Reviews of Geophysics*, 51(2), 276–299. <https://doi.org/10.1002/rog.20011>

Evans, B. W., Kuehner, S. M., Joswiak, D. J., & Cressey, G. (2017). Serpentine, Iron-rich Phyllosilicates and Fayalite Produced by Hydration and Mg Depletion of Peridotite, Duluth Complex, Minnesota, USA. *Journal of Petrology*, 58(3), 495–512. <https://doi.org/10.1093/petrology/egx024>

Gerling, E., Mamyrin, B., Tolstikhin, I., & Yakovleva, S. (1971). Helium isotope composition in some rocks. *Geochemica Isotopica*. <https://pascal-francis.inist.fr/vibad/index.php?action=getRecordDetail&idt=GEODEBRGM722203127>

Giunta, T., Young, E. D., Warr, O., Kohl, I., Ash, J. L., Martini, A., Mundle, S. O. C., Rumble, D., Pérez-Rodríguez, I., Wasley, M., LaRowe, D. E., Gilbert, A., & Sherwood Lollar, B. (2019). Methane sources and sinks in continental sedimentary systems: New insights from paired clumped isotopologues $^{13}\text{CH}_3\text{D}$ and $^{12}\text{CH}_2\text{D}_2$. *Geochimica et Cosmochimica Acta*, 245, 327–351. <https://doi.org/10.1016/j.gca.2018.10.030>

Glückauf, E., & Paneth, F. (1946). The helium content of atmospheric air. *Proceedings of the Royal Society of London. Series A. Mathematical and Physical Sciences*, 185(1000), 89–98. <https://doi.org/10.1098/rspa.1946.0006>

Goldner, B. D. (2011). Igneous petrology of the Ni-Cu-PGE mineralized Tamarack intrusion, Aitkin and Carlton Counties, Minnesota [Master thesis]. In conservancy.umn.edu. <https://conservancy.umn.edu/handle/11299/104139>

Goodwin, A. (1968). *Evolution of the Canadian Shield*. Geological association of Canada.

Goodwin, A. M. (1996). *Principles of Precambrian Geology*. In Google Books. Elsevier. https://books.google.fr/books?hl=fr&lr=&id=kiyZt6IRmj8C&oi=fnd&pg=PP2&dq=goodwin+1996+precambrian+&ots=uty59okBLc&sig=ULN_CbkacGrwmhla-drTbxDPK0

Green, J., Miller, J., Severson, M., Chandler, V., Hauck, S., & Wahl, T. (2002). Volcanic and sedimentary rocks of the Keweenawan Supergroup in northeastern Minnesota. Miller, JD, Jr., Green, JC, Severson, MJ, Chandler, VW, Hauck, SA, and Wahl, TE, *Geology and mineral potential of the Duluth Complex and related rocks of northeastern Minnesota*. : Minnesota Geological Survey Report of Investigations, 58, 94–102.

Guélard, J., Beaumont, V., Rouchon, V., Guyot, F., Pillot, D., Jézéquel, D., Ader, M., Newell, K. D., & Deville, E. (2017). Natural H_2 in Kansas: Deep or shallow origin? *Geochemistry, Geophysics, Geosystems*, 18(5), 1841–1865. <https://doi.org/10.1002/2016gc006544>

Guélard, J. (2016). Caractérisation des émanations de dihydrogène naturel en contexte intracratonique : exemple d'une interaction gaz/eau/roche au Kansas. In theses.hal.science. <https://theses.hal.science/tel-01609839/>

Heaman, L. M., Easton, R. M., Thomas Robert Hart, Carole Anne MacDonald, Hollings, P., & Smyk, M. (2007). Further refinement to the timing of Mesoproterozoic magmatism, Lake Nipigon region, Ontario. *Journal of Earth Sciences*, 44(8), 1055–1086. <https://doi.org/10.1139/e06-117>

Holloway, J. R. (1984). Graphite-CH₄-H₂O-CO₂ equilibria at low-grade metamorphic conditions. *Geology*, 12(8), 455. [https://doi.org/10.1130/0091-7613\(1984\)12%3C455:gealmc%3E2.0.co;2](https://doi.org/10.1130/0091-7613(1984)12%3C455:gealmc%3E2.0.co;2)

Jirsa, M. A., Boerboom, T. J., Chandler, V. W., Mossler, J. H., Runkel, A. C., & Setterholm, D. R. (2011). S-21 Geologic Map of Minnesota-Bedrock Geology [Map]. In conservancy.umn.edu. Minnesota Geological Survey. <https://conservancy.umn.edu/handle/11299/101466>

Joslin, G. (2004). Stratiform palladium-platinum-gold mineralization in the Sonju Lake intrusion, Lake County, Minnesota [Doctoral dissertation].

Kelley, D. S., Karson, J., Fruh-Green, G., Yoerger, D., Shank, T., Butterfield, D., Hayes, J., Schrenk, M., Olson, E., Proskurowski, G., & Jakuba, M. (2005). A Serpentinite-Hosted Ecosystem: The Lost City Hydrothermal Field. *Science*, 307(5714), 1428–1434. <https://doi.org/10.1126/science.1102556>

Kohl, L., Cumming, E., Cox, A., Rietze, A., Morrissey, L., Lang, S. Q., Richter, A., Suzuki, S., Nealson, K. H., & Morrill, P. L. (2016). Exploring the metabolic potential of microbial communities in ultra-basic, reducing springs at The Cedars, CA, USA: Experimental evidence of microbial methanogenesis and heterotrophic acetogenesis. *Journal of Geophysical Research: Biogeosciences*, 121(4), 1203–1220. <https://doi.org/10.1002/2015jg003233>

Lancet, M. S., & Anders, E. (1970). Carbon Isotope Fractionation in the Fischer-Tropsch Synthesis and in Meteorites. *Science*, 170(3961), 980–982. <https://doi.org/10.1126/science.170.3961.980>

Lang, S. Q., & Brazelton, W. J. (2020). Habitability of the marine serpentinite subsurface: a case study of the Lost City hydrothermal field. *Philosophical Transactions of the Royal Society A: Mathematical, Physical and Engineering Sciences*, 378(2165), 20180429. <https://doi.org/10.1098/rsta.2018.0429>

- Lang, S. Q., Früh-Green, G. L., Bernasconi, S. M., Brazelton, W. J., Schrenk, M. O., & McGonigle, J. M. (2018). Deeply-sourced formate fuels sulfate reducers but not methanogens at Lost City hydrothermal field. *Scientific Reports*, 8(1). <https://doi.org/10.1038/s41598-017-19002-5>
- Martel, D. J., O’Nions, R. K., Hilton, D. R., & Oxburgh, E. R. (1990). The role of element distribution in production and release of radiogenic helium: the Carnmenellis Granite, southwest England. *Chemical Geology*, 88(3), 207–221. [https://doi.org/10.1016/0009-2541\(90\)90090-T](https://doi.org/10.1016/0009-2541(90)90090-T)
- Marty, B., & Jambon, A. (1987). C3He in volatile fluxes from the solid Earth: implications for carbon geodynamics. *Earth and Planetary Science Letters*, 83(1-4), 16–26. [https://doi.org/10.1016/0012-821x\(87\)90047-1](https://doi.org/10.1016/0012-821x(87)90047-1)
- McCollom, T. M. (2003). Formation of meteorite hydrocarbons from thermal decomposition of siderite (FeCO₃). *Geochimica and Cosmochimica Acta*, 67(2), 311–317. [https://doi.org/10.1016/s0016-7037\(02\)00945-6](https://doi.org/10.1016/s0016-7037(02)00945-6)
- McCollom, T. M. (2013). Laboratory Simulations of Abiotic Hydrocarbon Formation in Earth’s Deep Subsurface. *Reviews in Mineralogy and Geochemistry*, 75(1), 467–494. <https://doi.org/10.2138/rmg.2013.75.15>
- McCollom, T. M., & Seewald, J. S. (2007). Abiotic Synthesis of Organic Compounds in Deep-Sea Hydrothermal Environments. *Chemical Reviews*, 107(2), 382–401. <https://doi.org/10.1021/cr0503660>
- Miller, H. M., Chaudhry, N., Conrad, M. E., Bill, M., Kopf, S. H., & Templeton, A. S. (2018). Large carbon isotope variability during methanogenesis under alkaline conditions. *Geochimica et Cosmochimica Acta*, 237, 18–31. <https://doi.org/10.1016/j.gca.2018.06.007>
- Miller, J. H. (2011). Layered intrusions of the Duluth Complex (pp. 171–201). *The Geological Society of America*. [https://doi.org/10.1130/2011.0024\(09\)](https://doi.org/10.1130/2011.0024(09))
- Miller, J., Green, J., Severson, M., Chandler, V., Hauck, S., Peterson, D., & Wahl, T. (2002). Geology and mineral potential of the Duluth Complex and related rocks of northeastern Minnesota. *Minnesota Geological Survey* .
- Miller, J., & Vervoort, J. (1996). The latent magmatic stage of the Midcontinent rift: a period of magmatic underplating and melting of the lower crust. *Institute on Lake Superior Geology Proceedings* , 42, 33–35.

Moody, J. B. (1976). Serpentinization: a review. *Lithos*, 9(2), 125–138. [https://doi.org/10.1016/0024-4937\(76\)90030-x](https://doi.org/10.1016/0024-4937(76)90030-x)

Nelson, K., Inagaki, F., & Takai, K. (2005). Hydrogen-driven subsurface lithoautotrophic microbial ecosystems (SLiMEs): do they exist and why should we care? *Trends in Microbiology*, 13(9), 405–410.

Nier, A. O. (1950). A Redetermination of the Relative Abundances of the Isotopes of Carbon, Nitrogen, Oxygen, Argon, and Potassium. *Physical Review*, 77(6), 789–793. <https://doi.org/10.1103/physrev.77.789>

O’Nions, R. K., & Oxburgh, E. R. (1983). Heat and helium in the Earth. *Nature*, 306(5942), 429–431. <https://doi.org/10.1038/306429a0>

Ojakangas, R. W., Dickas, A. B., & Green, J. C. (1997). Middle Proterozoic to Cambrian rifting, central North America. In Google Books. Geological Society of America. https://books.google.fr/books?hl=fr&lr=&id=YS_pAgAAQBAJ&oi=fnd&pg=PA73&dq=Miller

Potter, J., Rankin, A., & Treloar, P. (2004). Abiogenic Fischer-Tropsch synthesis of hydrocarbons in alkaline igneous rocks; fluid inclusion, textural and isotopic evidence from the Lovozero complex, N.W. Russia. *Lithos*, 75(3-4), 311–330. <https://doi.org/10.1016/j.lithos.2004.03.003>

Proskurowski, G., Lilley, M. D., Seewald, J. S., Früh-Green, G. L., Olson, E. J., Lupton, J. E., Sylva, S. P., & Kelley, D. S. (2008). Abiogenic Hydrocarbon Production at Lost City Hydrothermal Field. *Science*, 319(5863), 604–607. <https://doi.org/10.1126/science.1151194>

Reeves, E. P., & Fiebig, J. (2020). Abiotic Synthesis of Methane and Organic Compounds in Earth’s Lithosphere. *Elements*, 16(1), 25–31. <https://doi.org/10.2138/gselements.16.1.25>

Reller, A., Padeste, C., & Hug, P. (1987). Formation of organic carbon compounds from metal carbonates. *Nature*, 329(6139), 527–529. <https://doi.org/10.1038/329527a0>

Schoell, M. (1988). Multiple origins of methane in the Earth. *Chemical Geology*, 71(1), 1–10. [https://doi.org/10.1016/0009-2541\(88\)90101-5](https://doi.org/10.1016/0009-2541(88)90101-5)

Seewald, J. S. (2003). Organic–inorganic interactions in petroleum-producing sedimentary basins. *Nature*, 426(6964), 327–333. <https://doi.org/10.1038/nature02132>

- Seewald, J. S., Zolotov, M. Yu., & McCollom, T. (2006). Experimental investigation of single carbon compounds under hydrothermal conditions. *Geochimica et Cosmochimica Acta*, 70(2), 446–460. <https://doi.org/10.1016/j.gca.2005.09.002>
- Sherwood Lollar, B., Frapre, S. K., Weise, S. M., Fritz, P., Macko, S. A., & Welhan, J. A. (1993). Abiogenic methanogenesis in crystalline rocks. *Geochimica et Cosmochimica Acta*, 57(23-24), 5087–5097. [https://doi.org/10.1016/0016-7037\(93\)90610-9](https://doi.org/10.1016/0016-7037(93)90610-9)
- Sherwood Lollar, B., Heuer, V. B., McDermott, J., Tille, S., Warr, O., Moran, J. J., Telling, J., & Hinrichs, K.-U. . (2021). A window into the abiogenic carbon cycle – Acetate and formate in fracture waters in 2.7 billion year-old host rocks of the Canadian Shield. *Geochimica et Cosmochimica Acta*, 294, 295–314. <https://doi.org/10.1016/j.gca.2020.11.026>
- Sherwood Lollar, B., Lacrampe-Couloume, G., Slatter, G. F., Ward, J., Moser, D. P., Gihring, T. M., Lin, L.-H. ., & Onstott, T. C. (2006). Unravelling abiogenic and biogenic sources of methane in the Earth's deep subsurface. *Chemical Geology*, 226(3-4), 328–339. <https://doi.org/10.1016/j.chemgeo.2005.09.027>
- Sherwood Lollar, B., Onstott, T. C., Lacrampe-Couloume, G., & Ballentine, C. J. (2014). The contribution of the Precambrian continental lithosphere to global H₂ production. *Nature*, 516(7531), 379–382. <https://doi.org/10.1038/nature14017>
- Sherwood, B., Fritz, P., Frapre, S. K., Macko, S. A., Weise, S. M., & Welhan, J. A. (1988). Methane occurrences in the Canadian Shield. *Chemical Geology*, 71(1-3), 223–236. [https://doi.org/10.1016/0009-2541\(88\)90117-9](https://doi.org/10.1016/0009-2541(88)90117-9)
- Stute, M., & Schlosser, P. (2000). Atmospheric Noble Gases. *Environmental Tracers in Subsurface Hydrology*, 349–377. https://doi.org/10.1007/978-1-4615-4557-6_11
- Taranovic, V., Ripley, E. M., Li, C., & Rossell, D. (2015). Petrogenesis of the Ni–Cu–PGE sulfide-bearing Tamarack Intrusive Complex, Midcontinent Rift System, Minnesota. *Lithos*, 212-215, 16–31. <https://doi.org/10.1016/j.lithos.2014.10.012>
- Truche, L., McCollom, T. M., & Martinez, I. (2020). Hydrogen and Abiogenic Hydrocarbons: Molecules that Change the World. *Elements*, 16(1), 13–18. <https://doi.org/10.2138/gselements.16.1.13>
- Vacquand, C. (2011). Genèse et mobilité de l'hydrogène naturel : source d'énergie ou vecteur énergétique stockable ? [Doctoral dissertation]. In [theses.fr](https://www.theses.fr/2011GLOB0002). <https://www.theses.fr/2011GLOB0002>

Vacquand, C., Deville, E., Beaumont, V., Guyot, F., Sissmann, O., Pillot, D., Arcilla, C., & Prinzhofer, A. (2018). Reduced gas seepages in ophiolitic complexes: Evidences for multiple origins of the H₂-CH₄-N₂ gas mixtures. *Geochimica et Cosmochimica Acta*, 223, 437–461. <https://doi.org/10.1016/j.gca.2017.12.018>

Warr, O., Giunta, T., Ballentine, C. J., & Sherwood Lollar, B. (2019). Mechanisms and rates of 4He, 40Ar, and H₂ production and accumulation in fracture fluids in Precambrian Shield environments. *Chemical Geology*, 530, 119322. <https://doi.org/10.1016/j.chemgeo.2019.119322>

Welhan, J. A. (1988). Origins of methane in hydrothermal systems. *Chemical Geology*, 71(1-3), 183–198. [https://doi.org/10.1016/0009-2541\(88\)90114-3](https://doi.org/10.1016/0009-2541(88)90114-3)

Welhan, J. A., & Craig, H. (1979). Methane and hydrogen in East Pacific Rise hydrothermal fluids. *Geophysical Research Letters*, 6(11), 829–831. <https://doi.org/10.1029/gl006i011p00829>

Whiticar, M. J., Faber, E., & Schoell, M. (1986). Biogenic methane formation in marine and freshwater environments: CO₂ reduction vs. acetate fermentation—Isotope evidence. *Geochimica et Cosmochimica Acta*, 50(5), 693–709. [https://doi.org/10.1016/0016-7037\(86\)90346-7](https://doi.org/10.1016/0016-7037(86)90346-7)

Woltemate, I., Whiticar, M. J., & Schoell, M. (1984). Carbon and hydrogen isotopic composition of bacterial methane in a shallow freshwater lake. *Limnology and Oceanography*, 29(5), 985–992. <https://doi.org/10.4319/lo.1984.29.5.0985>

VIII. Chapter 8

Alt, J. C., & Shanks, W. C. (2003). Serpentinization of abyssal peridotites from the MARK area, Mid-Atlantic Ridge: sulfur geochemistry and reaction modeling. *Geochimica et Cosmochimica Acta*, 67(4), 641–653. [https://doi.org/10.1016/s0016-7037\(02\)01142-0](https://doi.org/10.1016/s0016-7037(02)01142-0)

Anderson, R. R. (1992). The midcontinent rift of Iowa - ProQuest [Doctoral dissertation]. <https://www.proquest.com/openview/c684252101b6dc95ee4c2e9e00e42eaa/1?pq-origsite=gscholar&cbl=18750&diss=y>

Baker, I., & Haggerty, S. E. (1967). The alteration of olivine in basaltic and associated lavas. *Contributions to Mineralogy and Petrology*, 16(3), 233–257. <https://doi.org/10.1007/bf00371094>

Cannon, W. F., Green, A. I., D. Jean Hutchinson, Myung Gyoon Lee, Bernd Milkereit, Behrendt, J. C., Halls, H. C., Green, J., Dickas, A. B., Morey, G. B., Richard, & Spencer, C. (1989). The North American Midcontinent Rift beneath Lake Superior from Glimpce seismic reflection profiling. *Tectonics*, 8(2), 305–332. <https://doi.org/10.1029/tc008i002p00305>

Charlou, J. L., Donval, J. P., Fouquet, Y., Jean-Baptiste, P., & Holm, N. (2002). Geochemistry of high H₂ and CH₄ vent fluids issuing from ultramafic rocks at the Rainbow hydrothermal field (36°14'N, MAR). *Chemical Geology*, 191(4), 345–359. [https://doi.org/10.1016/s0009-2541\(02\)00134-1](https://doi.org/10.1016/s0009-2541(02)00134-1)

Coveney, R. M., Jr., Goebel, E. D., Zeller, E. J., Dreschhoff, G. A. M., & Angino, E. E. (1987). Serpentinization and the Origin of Hydrogen Gas in Kansas1. *AAPG Bulletin*, 71(1), 39–48. <https://doi.org/10.1306/94886D3F-1704-11D7-8645000102C1865D>

Deville, E., & Prinzhofer, A. (2016). The origin of N₂-H₂-CH₄-rich natural gas seepages in ophiolitic context: A major and noble gases study of fluid seepages in New Caledonia. *Chemical Geology*, 440, 139–147. <https://doi.org/10.1016/j.chemgeo.2016.06.011>

Dickas, A. B., & Mudrey, M. G. (1997). Middle Proterozoic to Cambrian rifting, central North America. In Google Books. *Geological Society of America*. https://books.google.fr/books?hl=fr&lr=&id=YS_pAgAAQBAJ&oi=fnd&pg=PA37&dq=dickas+and+mudrey+1997&ots=SzGTRqXnza&sig=003oSHN4qPeTBKeD-lu0h09tliw

Douglas, P. M. J., Stolper, D. A., Eiler, J. M., Sessions, A. L., Lawson, M., Shuai, Y., Bishop, A., Podlaha, O. G., Ferreira, A. A., Santos Neto, E. V., Niemann, M., Steen, A. S., Huang, L., Chimiak, L., Valentine, D. L., Fiebig, J., Luhmann, A. J., Seyfried, W. E., Etiope, G., &

- Schoell, M. (2017). Methane clumped isotopes: Progress and potential for a new isotopic tracer. *Organic Geochemistry*, 113, 262–282. <https://doi.org/10.1016/j.orggeochem.2017.07.016>
- Edge, J. S. (2015). Hydrogen adsorption and dynamics in clay minerals. In [discovery.ucl.ac.uk](https://discovery.ucl.ac.uk/id/eprint/1462102/). <https://discovery.ucl.ac.uk/id/eprint/1462102/>
- Edwards, A. B. (1938). The Formation of Iddingsite. *American Mineralogist*, 23(4), 277–281. <https://pubs.geoscienceworld.org/msa/ammin/article-abstract/23/4/277/536978/The-Formation-of-Iddingsite>
- Eggleton, R. A. (1984). Formation of Iddingsite Rims on Olivine: A Transmission Electron Microscope Study. *Clays and Clay Minerals*, 32(1), 1–11. <https://doi.org/10.1346/ccmn.1984.0320101>
- Etioppe, G., & Sherwood Lollar, B. (2013). Abiotic methane on Earth. *Reviews of Geophysics*, 51(2), 276–299. <https://doi.org/10.1002/rog.20011>
- Evans, B. W., Kuehner, S. M., Joswiak, D. J., & Cressey, G. (2017). Serpentine, Iron-rich Phyllosilicates and Fayalite Produced by Hydration and Mg Depletion of Peridotite, Duluth Complex, Minnesota, USA. *Journal of Petrology*, 58(3), 495–512. <https://doi.org/10.1093/petrology/egx024>
- Geymond, U., Briollet, T., Combaudon, V., Sissmann, O., Martinez, I., Duttine, M., & Moretti, I. (2023). Reassessing the role of magnetite during natural hydrogen generation. *Frontiers in Earth Science*, 11(487).
- Geymond, U., Ramanaidou, E., Lévy, D., Ouaya, A., & Moretti, I. (2022). Can Weathering of Banded Iron Formations Generate Natural Hydrogen? Evidence from Australia, Brazil and South Africa. *Minerals*, 12(2), 163. <https://doi.org/10.3390/min12020163>
- Goldner, B. D. (2011). Igneous petrology of the Ni-Cu-PGE mineralized Tamarack intrusion, Aitkin and Carlton Counties, Minnesota [Master thesis]. In conservancy.umn.edu. <https://conservancy.umn.edu/handle/11299/104139>
- Green, A. G., Cannon, W. F., B. Milkereit, Hutchinson, D. R., Davidson, A., Behrendt, J. C., Spencer, C., Lee, M. W., P. Morel-à-LáHuissier, & Agena, W. F. (1989). A “GLIMPCE” of the deep crust beneath the Great Lakes. *Geophysical Monograph*, 65–80. <https://doi.org/10.1029/gm051p0065>
- Gresens, R. L. (1967). Composition-volume relationships of metasomatism. *Chemical Geology*, 2, 47–65. [https://doi.org/10.1016/0009-2541\(67\)90004-6](https://doi.org/10.1016/0009-2541(67)90004-6)

Grozeva, N. G., Klein, F., Seewald, J. S., & Sylva, S. P. (2017). Experimental study of carbonate formation in oceanic peridotite. *Geochimica et Cosmochimica Acta*, 199, 264–286. <https://doi.org/10.1016/j.gca.2016.10.052>

Guélard, J., Beaumont, V., Rouchon, V., Guyot, F., Pillot, D., Jézéquel, D., Ader, M., Newell, K. D., & Deville, E. (2017). Natural H₂ in Kansas: Deep or shallow origin? *Geochemistry, Geophysics, Geosystems*, 18(5), 1841–1865. <https://doi.org/10.1002/2016gc006544>

Guélard, J. (2016). Caractérisation des émanations de dihydrogène naturel en contexte intracratonique : exemple d'une interaction gaz/eau/roche au Kansas. In *theses.hal.science*. <https://theses.hal.science/tel-01609839/>

Hinze, W. J., & Braile, L. W. (1988). Geophysical aspects of the craton: US. *Sedimentary Cover—North American Craton: US*, 90, 5. The Geological Society of America.

Hinze, W., Allen, D., Braile, L., Mariano, J., Ojakangas, R., Dickas, A., & Green, J. (1997). The Midcontinent rift system: A major Proterozoic continental rift. In *Geological Society of America*. https://books.google.fr/books?hl=fr&lr=&id=YS_pAgAAQBAJ&oi=fnd&pg=PA7&dq=hinze+1997+midcontinent+rift&ots=SzGWQmPqB7&sig=Ii6ncFbVLoTbhPwCpOPO-bCsdjc

Jirsa, M. A., Boerboom, T. J., Chandler, V. W., Mossler, J. H., Runkel, A. C., & Setterholm, D. R. (2011). S-21 Geologic Map of Minnesota-Bedrock Geology [Map]. In *conservancy.umn.edu*. *Minnesota Geological Survey*. <https://conservancy.umn.edu/handle/11299/101466>

Joslin, G. (2004). Stratiform palladium-platinum-gold mineralization in the Sonju Lake intrusion, Lake County, Minnesota [Doctoral dissertation].

Kelemen, P. B., Matter, J., Streit, E. E., Rudge, J. F., Curry, W. B., & Blusztajn, J. (2011). Rates and Mechanisms of Mineral Carbonation in Peridotite: Natural Processes and Recipes for Enhanced, in situ CO₂ Capture and Storage. *Annual Review of Earth and Planetary Sciences*, 39(1), 545–576. <https://doi.org/10.1146/annurev-earth-092010-152509>

Kelley, D. S., Karson, J., Fruh-Green, G., Yoerger, D., Shank, T., Butterfield, D., Hayes, J., Schrenk, M., Olson, E., Proskurowski, G., & Jakuba, M. (2005). A Serpentinite-Hosted Ecosystem: The Lost City Hydrothermal Field. *Science*, 307(5714), 1428–1434. <https://doi.org/10.1126/science.1102556>

Lévy, D., Callot, J.-P., Moretti, I., Duttine, M., Dubreuil, B., de Parseval, P., & Boudouma, O. (2022). Successive phases of serpentinization and carbonation recorded in the Sivas ophiolite

(Turkey), from oceanic crust accretion to post-obduction alteration. *BSGF - Earth Sciences Bulletin*, 193, 12. <https://doi.org/10.1051/bsgf/2022015>

Macfarlane, P. A. (2000). Revisions to the Nomenclature for Kansas Aquifers. *Current Research in Earth Sciences*, 1–14. <https://doi.org/10.17161/cres.v0i244.11815>

McCullom, T. M., Klein, F., Robbins, M., Moskowitz, B., Berquó, T. S., Jöns, N., Bach, W., & Templeton, A. (2016). Temperature trends for reaction rates, hydrogen generation, and partitioning of iron during experimental serpentinization of olivine. *Geochimica et Cosmochimica Acta*, 181, 175–200. <https://doi.org/10.1016/j.gca.2016.03.002>

Newell, K. D., Doveton, J. H., Merriam, D. F., Lollar, B. S., Waggoner, W. M., & Magnuson, L. M. (2007). H₂-rich and Hydrocarbon Gas Recovered in a Deep Precambrian Well in Northeastern Kansas. *Natural Resources Research*, 16(3), 277–292. <https://doi.org/10.1007/s11053-007-9052-7>

Noël, J. (2018, November 21). Etude pétro-structurale et géochimique des processus de serpentinisation et de carbonatation des péridotites de l'ophiolite d'Oman. *Tel.archives-Ouvertes.fr*. <https://tel.archives-ouvertes.fr/tel-02053492/>

Ojakangas, R. W., Morey, G. B., & Green, J. C. (2001). The Mesoproterozoic Midcontinent Rift System, Lake Superior Region, USA. *Sedimentary Geology*, 141-142, 421–442. [https://doi.org/10.1016/s0037-0738\(01\)00085-9](https://doi.org/10.1016/s0037-0738(01)00085-9)

Rasbury, E. T., & Cole, J. M. (2009). Directly dating geologic events: U-Pb dating of carbonates. *Reviews of Geophysics*, 47(3). <https://doi.org/10.1029/2007rg000246>

Ross, C. S., & Shannon, E. V. (1925). The origin, occurrence, composition, and physical properties of the mineral iddingsite. https://repository.si.edu/bitstream/handle/10088/15362/1/USNMP-67_2579_1925.pdf

Seewald, J. S., Zolotov, M. Yu., & McCollom, T. (2006). Experimental investigation of single carbon compounds under hydrothermal conditions. *Geochimica et Cosmochimica Acta*, 70(2), 446–460. <https://doi.org/10.1016/j.gca.2005.09.002>

Sherwood Lollar, B., Voglesonger, K., Lin, L.-H. ., Lacrampe-Couloume, G., Telling, J., Abrajano, T. A., Onstott, T. C., & Pratt, L. M. (2007). Hydrogeologic Controls on Episodic H₂ Release from Precambrian Fractured Rocks—Energy for Deep Subsurface Life on Earth and Mars. *Astrobiology*, 7(6), 971–986. <https://doi.org/10.1089/ast.2006.0096>

Smith, K. L. (1987). Weathering of Basalt: Formation of Iddingsite. *Clays and Clay Minerals*, 35(6), 418–428. <https://doi.org/10.1346/ccmn.1987.0350602>

Steeple, D. W., DuBois, S. M., & Wilson, F. W. (1979). Seismicity, faulting, and geophysical anomalies in Nemaha County, Kansas: Relationship to regional structures. *Geology*, 7(3), 134–138. <https://pubs.geoscienceworld.org/gsa/geology/article/7/3/134/188742/Seismicity-faulting-and-geophysical-anomalies-in>

Stein, C. A., Kley, J., Stein, S., Hindle, D., & Keller, G. R. (2015). North America's Midcontinent Rift: When rift met LIP. *Geosphere*, 11(5), 1607–1616. <https://doi.org/10.1130/ges01183.1>

Taranovic, V., Ripley, E. M., Li, C., & Rossell, D. (2015). Petrogenesis of the Ni–Cu–PGE sulfide-bearing Tamarack Intrusive Complex, Midcontinent Rift System, Minnesota. *Lithos*, 212–215, 16–31. <https://doi.org/10.1016/j.lithos.2014.10.012>

Truche, L., Joubert, G., Dargent, M., Martz, P., Cathelineau, M., Rigaudier, T., & Quirt, D. (2018). Clay minerals trap hydrogen in the Earth's crust: Evidence from the Cigar Lake uranium deposit, Athabasca. *Earth and Planetary Science Letters*, 493(493), 186–197. <https://doi.org/10.1016/j.epsl.2018.04.038>

Tutolo, B. M., Evans, B. W., & Kuehner, S. M. (2019). Serpentine–Hisingerite Solid Solution in Altered Ferroan Peridotite and Olivine Gabbro. *Minerals*, 9(1), 47. <https://doi.org/10.3390/min9010047>

Vacquand, C. (2011). Genèse et mobilité de l'hydrogène naturel : source d'énergie ou vecteur énergétique stockable ? [Doctoral dissertation]. In *theses.fr*. <https://www.theses.fr/2011GLOB0002>

Van Schmus, W. R., Bickford, M. E., & Condie, K. C. (1993). Early Proterozoic transcontinental orogenic belts in the United States. *Geological Society of America, Abstracts with Programs; (United States)*, 25:1. <https://www.osti.gov/biblio/5932944>

Woelk, T. S., & Hinze, W. J. (1991). Model of the midcontinent rift system in northeastern Kansas. *Geology*, 19(3), 277–280. [https://doi.org/10.1130/0091-7613\(1991\)019%3C0277:MOTMRS%3E2.3.CO;2](https://doi.org/10.1130/0091-7613(1991)019%3C0277:MOTMRS%3E2.3.CO;2)

IX. Chapter 9

Bickford, M. E., Harrower, K. L., Hoppe, W. J., Nelson, B. K., Nusbaum, R. L., & Thomas, J. J. (1981). Rb-Sr and U-Pb geochronology and distribution of rock types in the Precambrian basement of Missouri and Kansas. *GSA Bulletin*, 92(6), 323–341. [https://doi.org/10.1130/0016-7606\(1981\)92%3C323:RAUGAD%3E2.0.CO;2](https://doi.org/10.1130/0016-7606(1981)92%3C323:RAUGAD%3E2.0.CO;2)

Eborall, M. I., & Wright, J. B. (1974). Comments on experimental studies concerning the genesis of the Nigerian Younger Granites? by G.C. Brown and P.Bowden. *Contributions to Mineralogy and Petrology*, 43(2), 159–161. <https://doi.org/10.1007/bf00572717>

Green, A. G., Cannon, W. F., B. Milkereit, Hutchinson, D. R., Davidson, A., Behrendt, J. C., Spencer, C., Lee, M. W., P. Morel-à-LáHuissier, & Agena, W. F. (1989a). A “GLIMPCE” of the deep crust beneath the Great Lakes. *Geophysical Monograph*, 65–80. <https://doi.org/10.1029/gm051p0065>

Green, A. G., Cannon, W. F., B. Milkereit, Hutchinson, D. R., Davidson, A., Behrendt, J. C., Spencer, C., Lee, M. W., P. Morel-à-LáHuissier, & Agena, W. F. (1989b). A “GLIMPCE” of the deep crust beneath the Great Lakes. *Geophysical Monograph*, 65–80. <https://doi.org/10.1029/gm051p0065>

Guélard, J., Beaumont, V., Rouchon, V., Guyot, F., Pilot, D., Jézéquel, D., Ader, M., Newell, K. D., & Deville, E. (2017a). Natural H₂ in Kansas: Deep or shallow origin? *Geochemistry, Geophysics, Geosystems*, 18(5), 1841–1865. <https://doi.org/10.1002/2016gc006544>

Horsfield, B., Mahlstedt, N., Weniger, P., Misch, D., Vranjes-Wessely, S., Han, S., & Wang, C. (2022). Molecular hydrogen from organic sources in the deep Songliao Basin, P.R. China. *International Journal of Hydrogen Energy*, 47(38), 16750–16774. <https://doi.org/10.1016/j.ijhydene.2022.02.208>

Kelley, D. S., Früh-Green, G. L., Karson, J. A., & Ludwig, K. A. (2007). The Lost City Hydrothermal Field Revisited. *Oceanography*, 20(4), 90–99. <https://www.jstor.org/stable/24860149>

Kelley, D. S., Karson, J., Fruh-Green, G., Yoerger, D., Shank, T., Butterfield, D., Hayes, J., Schrenk, M., Olson, E., Proskurowski, G., & Jakuba, M. (2005). A Serpentinite-Hosted Ecosystem: The Lost City Hydrothermal Field. *Science*, 307(5714), 1428–1434. <https://doi.org/10.1126/science.1102556>

Krumrei, T. V., Pernicka, E., Kaliwoda, M., & Markl, G. (2007). Volatiles in a peralkaline system: Abiogenic hydrocarbons and F–Cl–Br systematics in the naujaite of the Ilímaussaq

intrusion, South Greenland. *Lithos*, 95(3), 298–314.
<https://doi.org/10.1016/j.lithos.2006.08.003>

Leila, M., Loiseau, K., & Moretti, I. (2022). Controls on generation and accumulation of blended gases (CH₄/H₂/He) in the Neoproterozoic Amadeus Basin, Australia. *Marine and Petroleum Geology*, 140, 105643. <https://doi.org/10.1016/j.marpetgeo.2022.105643>

Lévy, D., Callot, J.-P., Moretti, I., Duttine, M., Dubreuil, B., de Parseval, P., & Boudouma, O. (2022). Successive phases of serpentinization and carbonation recorded in the Sivas ophiolite (Turkey), from oceanic crust accretion to post-obduction alteration. *BSGF - Earth Sciences Bulletin*, 193, 12. <https://doi.org/10.1051/bsgf/2022015>

Lin, L.-H., Hall, J., Lippmann-Pipke, J., Ward, J. A., Sherwood Lollar, B., DeFlaun, M., Rothmel, R., Moser, D., Gihring, T. M., Mislowack, B., & Onstott, T. C. (2005). Radiolytic H₂ in continental crust: Nuclear power for deep subsurface microbial communities. *Geochemistry, Geophysics, Geosystems*, 6(7), n/a-n/a. <https://doi.org/10.1029/2004gc000907>

Macdonald, A. H., & Fyfe, W. S. (1985). Rate of serpentinization in seafloor environments. *Tectonophysics*, 116(1), 123–135. [https://doi.org/10.1016/0040-1951\(85\)90225-2](https://doi.org/10.1016/0040-1951(85)90225-2)

Mahlstedt, N., Horsfield, B., Weniger, P., Misch, D., Shi, X., Noah, M., & Boreham, C. (2022). Molecular hydrogen from organic sources in geological systems. *Journal of Natural Gas Science and Engineering*, 105, 104704. <https://doi.org/10.1016/j.jngse.2022.104704>

Maiga, O., Deville, E., Laval, J., Prinzhofer, A., & Diallo, A. B. (2023). Characterization of the spontaneously recharging natural hydrogen reservoirs of Bourakebougou in Mali. *Scientific Reports*, 13(1), 11876. <https://doi.org/10.1038/s41598-023-38977-y>

Miller, J., Green, J., Severson, M., Chandler, V., Hauck, S., Peterson, D., & Wahl, T. (2002). Geology and mineral potential of the Duluth Complex and related rocks of northeastern Minnesota. Minnesota Geological Survey .

Mücke, A. (2003). Fayalite, pyroxene, amphibole, annite and their decay products in mafic clots within Younger Granites of Nigeria: Petrography, mineral chemistry and genetic implications. *Journal of African Earth Sciences*, 36(1-2), 55–71. [https://doi.org/10.1016/s0899-5362\(03\)00015-0](https://doi.org/10.1016/s0899-5362(03)00015-0)

Nivin, V. (2020). The Origin of Hydrocarbon Gases in the Lovozero Nepheline-Syenite Massif (Kola Peninsula, NW Russia), as Revealed from He and Ar Isotope Evidence. *Minerals*, 10(9), 830. <https://doi.org/10.3390/min10090830>

Nivin, V. A. (2019). Occurrence Forms, Composition, Distribution, Origin and Potential Hazard of Natural Hydrogen–Hydrocarbon Gases in Ore Deposits of the Khibiny and Lovozero Massifs: A Review. *Minerals*, 9(9), 535. <https://doi.org/10.3390/min9090535>

Salvi, S., & Williams-Jones, A. E. (1992). Reduced orthomagmatic C-O-H-N-NaCl fluids in the Strange Lake rare-metal granitic complex, Quebec/Labrador, Canada. *European Journal of Mineralogy*, 4(5), 1155–1174. <https://doi.org/10.1127/ejm/4/5/1155>

Sherwood Lollar, B., Voglesonger, K., Lin, L.-H. ., Lacrampe-Couloume, G., Telling, J., Abrajano, T. A., Onstott, T. C., & Pratt, L. M. (2007). Hydrogeologic Controls on Episodic H₂ Release from Precambrian Fractured Rocks—Energy for Deep Subsurface Life on Earth and Mars. *Astrobiology*, 7(6), 971–986. <https://doi.org/10.1089/ast.2006.0096>

Sherwood-Lollar, B., Onstott, T. C., Lacrampe-Couloume, G., & Ballentine, C. J. (2014). The contribution of the Precambrian continental lithosphere to global H₂ production. *Nature*, 516(7531), 379–382. <https://doi.org/10.1038/nature14017>

Steeple, D. W., DuBois, S. M., & Wilson, F. W. (1979). Seismicity, faulting, and geophysical anomalies in Nemaha County, Kansas: Relationship to regional structures. *Geology*, 7(3), 134–138. <https://pubs.geoscienceworld.org/gsa/geology/article/7/3/134/188742/Seismicity-faulting-and-geophysical-anomalies-in>

Stein, C. A., Kley, J., Stein, S., Hindle, D., & Keller, G. R. (2015a). North America’s Midcontinent Rift: When rift met LIP. *Geosphere*, 11(5), 1607–1616. <https://doi.org/10.1130/ges01183.1>

Stein, C. A., Kley, J., Stein, S., Hindle, D., & Keller, G. R. (2015b). North America’s Midcontinent Rift: When rift met LIP. *Geosphere*, 11(5), 1607–1616. <https://doi.org/10.1130/ges01183.1>

Truche, L., Bourdelle, F., Salvi, S., Lefeuvre, N., Zug, A., & Lloret, E. (2021). Hydrogen generation during hydrothermal alteration of peralkaline granite. *Geochimica et Cosmochimica Acta*, 308, 42–59. <https://doi.org/10.1016/j.gca.2021.05.048>

Truche, L., Joubert, G., Dargent, M., Martz, P., Cathelineau, M., Rigaudier, T., & Quirt, D. (2018). Clay minerals trap hydrogen in the Earth’s crust: Evidence from the Cigar Lake uranium deposit, Athabasca. *Earth and Planetary Science Letters*, 493(493), 186–197. <https://doi.org/10.1016/j.epsl.2018.04.038>

Vasyukova, O. V., & Williams-Jones, A. E. (2019). Closed system fluid-mineral-mediated trace element behaviour in peralkaline rare metal pegmatites: Evidence from Strange Lake. *Chemical Geology*, 505, 86–99. <https://doi.org/10.1016/j.chemgeo.2018.12.023>

Woelk, T. S., & Hinze, W. J. (1991a). Model of the midcontinent rift system in northeastern Kansas. *Geology*, 19(3), 277–280. [https://doi.org/10.1130/0091-7613\(1991\)019%3C0277:MOTMRS%3E2.3.CO;2](https://doi.org/10.1130/0091-7613(1991)019%3C0277:MOTMRS%3E2.3.CO;2)

Woelk, T. S., & Hinze, W. J. (1991b). Model of the midcontinent rift system in northeastern Kansas. *Geology*, 19(3), 277–280. [https://doi.org/10.1130/0091-7613\(1991\)019%3C0277:MOTMRS%3E2.3.CO;2](https://doi.org/10.1130/0091-7613(1991)019%3C0277:MOTMRS%3E2.3.CO;2)

X. Supplementary 1

Ballentine, C. J., & Sherwood Lollar, B. (2002). Regional groundwater focusing of nitrogen and noble gases into the Hugoton-Panhandle giant gas field, USA. *Geochimica et Cosmochimica Acta*, 66(14), 2483–2497. [https://doi.org/10.1016/s0016-7037\(02\)00850-5](https://doi.org/10.1016/s0016-7037(02)00850-5)

Battani, A., Sarda, P., & Prinzhofer, A. (2000). Basin scale natural gas source, migration and trapping traced by noble gases and major elements: the Pakistan Indus basin. *Earth and Planetary Science Letters*, 181(1-2), 229–249. [https://doi.org/10.1016/s0012-821x\(00\)00188-6](https://doi.org/10.1016/s0012-821x(00)00188-6)

Bernard, B. B., Brooks, J. M., & Sackett, W. M. (1976). Natural gas seepage in the Gulf of Mexico. *Earth and Planetary Science Letters*, 31(1), 48–54. [https://doi.org/10.1016/0012-821x\(76\)90095-9](https://doi.org/10.1016/0012-821x(76)90095-9)

Etiope, G., Vadillo, I., Whiticar, M. J., Marques, J. M., Carreira, P. M., Tiago, I., Benavente, J., Jiménez, P., & Urresti, B. (2016). Abiotic methane seepage in the Ronda peridotite massif, southern Spain. *Applied Geochemistry*, 66, 101–113. <https://doi.org/10.1016/j.apgeochem.2015.12.001>

Guélard, J. (2016). Caractérisation des émanations de dihydrogène naturel en contexte intracratonique : exemple d'une interaction gaz/eau/roche au Kansas. In *theses.hal.science*. <https://theses.hal.science/tel-01609839/>

Ozima, M., & Podosek, F. A. (2002). *Noble Gas Geochemistry*. In Google Books. Cambridge University Press. https://books.google.fr/books?hl=fr&lr=&id=TMIAfSIe428C&oi=fnd&pg=PP1&dq=ozima+and+podosek+2002&ots=nebzMvARpq&sig=Bxtev_QKrWMh3MGjyTh6TIAmzS8

Sherwood Lollar, B., Frapé, S. K., Weise, S. M., Fritz, P., Macko, S. A., & Welhan, J. A. (1993). Abiogenic methanogenesis in crystalline rocks. *Geochimica et Cosmochimica Acta*, 57(23-24), 5087–5097. [https://doi.org/10.1016/0016-7037\(93\)90610-9](https://doi.org/10.1016/0016-7037(93)90610-9)

Whiticar, M. J. (1999). Carbon and hydrogen isotope systematics of bacterial formation and oxidation of methane. *Chemical Geology*, 161(1-3), 291–314. [https://doi.org/10.1016/s0009-2541\(99\)00092-3](https://doi.org/10.1016/s0009-2541(99)00092-3)

Table of illustrations

Figure 1: Illustration of the methodology used in this thesis	21
Figure 2: Map locating the various Precambrian cratons (outcropping and buried) correlated with known H ₂ emissions (Sherwood-Lollar et al., 2014).....	25
Figure 3: Map synthesizing the different occurrences of peralkaline rocks or similar mineralogical assemblages (EGM is for eudialyte-group minerals, for a more detailed legend please refer to Marks and Markl., 2017; see references).	27
Figure 4: Map of the intracratonic areas (in dark grey) and Banded Iron Formations (Geymond et al., 2022).....	28
Figure 5: Location of sedimentary basins in the function of their structural regime. Intracratonic basins are represented in orange (modified from Nyberg and Howell., 2015) ...	30
Figure 6: Synthetic map of the Kansas state with lithologies of each known portion of the Kansas basement (modified from Bickford et al., 1981).....	38
Figure 7: Simplified geological map of the Mid-Rift System gravimetric anomalies (modified from Ojakangas et al., 2001; Dickas and Mudrey, 1997).....	39
Figure 8: Simplified geological map (of the Kansas state) of the basement top with the location of the H ₂ -bearing wells and DR1-A well (modified from Bickford et al., 1981; Coveney et al., 1987 and Guélard et al., 2017).	41
Figure 9: West-East cross-section of Kansas with the location of the H ₂ -bearing wells and the DR1-A well (modified from Bickford et al., 1981, Kansas Geological Survey (1984), Coveney et al., 1987, and Guélard et al., 2017).....	42
Figure 10: Schematization of the interactions between the beam and the sample and their associated emitted particles.....	50

Figure 11: FIB preparation of a sample of the Kansas Precambrian basement, 1- Selection of a zone of several micrometers; 2- Deposition of a platinum layer to maintain the FIB thin section during the rest of the preparation; 3- The ion beam is used to dig around the selected area; 4- The FIB thin section is thinned by the ion beam; 5- The area around the FIB thin section is widened in order to prevent any damage during the next step; 6- The FIB thin section is extracted from the sample and fixed on a sample holder. 52

Figure 12: Schematic stacks of acquired images (STXM) and extracted average X-ray absorption spectra with peaks of the Fe L3 edge and the Fe L2 edge (XANES) (This image originates from a personal communication of S. Bernard). 53

Figure 13: Schematic illustrations of the different architectures of the SEM and TEM (in imaging and diffraction modes). 55

Figure 14: Bruker Skyscan 1172 and architecture of the source-object-detector. In this scanner, the sample is mobile. 58

Figure 15: Hydrogen quantification workflow with 1- the Fe³⁺ map for a mineral of interest (here the serpentine), 2- the volume determination for each mineral by performing XCT (green is oxide, blue is for mafic minerals, and pink is for the felspathic matrix), and 3- the H₂ calculation applied for the whole rock. 60

Figure 16: Schematic view of the gas chromatograph architecture (modified from Chemlys communication). 64

Figure 17: Injection setup coupled with the Gas chromatograph 65

Figure 18: Thin sections of each sample of the DR1-A well in function of depth with the location of the top of the basement at 350 meters deep..... 70

Figure 19: Scans of the thin sections of K0 (454m), K2(450m), and K1(442m) samples and associated optical micrographs in non-analyzed polarized light showing their mineralogical assemblages (K-F is for K-felspar, Plg is for plagioclase, Ol is for olivine, Px is for pyroxene, Amp is for amphibole, and Idd is for iddingsite)..... 72

Figure 20: Scans of the thin sections of K3 (446m) and K5 (437m) samples and associated optical micrographs in non-analyzed polarized light showing their mineralogical assemblages (K-F is for K-felspar, Plg is for plagioclase, Ol is for olivine, Px is for pyroxene, Amp is for amphibole, Idd is for iddingsite, Clay is for clay minerals, Bt is for biotite, Qtz is for quartz, and Cbt is for carbonates)..... 73

Figure 21: Scan of the thin section of K6 (381m); A- Cathodoluminescence showing the different generations of carbonates; B- associated optical micrograph in non-analyzed polarized light showing its mineralogical assemblages (Clay is for clay minerals and Cbt is for carbonates).74

Figure 22: Scan of the thin section of K7 (372m) and associated optical micrographs in non-analyzed polarized light showing its mineralogical assemblages (K-F is for K-felspar, Clay is for clay minerals, Ox is for oxide, and Cbt is for carbonates)..... 75

Figure 23: Scan of the thin sections of K11 (350m) and K12 (349.9m) and their associated optical micrographs in non-analyzed polarized light showing its mineralogical assemblages (K-F is for K-felspars, Clay is for clay minerals, Ox is for oxide)..... 76

Figure 24: Simplified geological map of the basement top with the location of the H₂-bearing wells and DR1-A well (modified from Bickford et al., 1981, Coveney et al., 1987 and Guélard et al., 2017) and West-East cross-section of Kansas with the location of the H₂-bearing wells and the DR1-A well (modified from Bickford et al., 1981, Kansas Geological Survey (1984), Coveney et al., 1987, and Guélard et al., 2017)..... 80

Figure 25: A- Optical micrographs in plane polarized light showing the K2 sample gabbroic mineralogical assemblage; B- Optical micrographs in plane polarized light zoomed on an olivine crystal and its associated aggregates of light yellow to dark brown colors clay mineral seen in A; C- Optical micrograph showing K2 olivine and associated mafic minerals inside the feldspar matrix; D- Optical micrographs in plane polarized light zoomed on the olivine – orthopyroxene association seen in C; E- Optical micrographs in plane polarized light showing the K1 sample gabbroic mineralogical assemblage; F- Optical micrographs in plane polarized light zoomed on the olivine and clays seen in E (Ab is for albite, Or is for orthoclase, Ol is for olivine, Opx is for orthopyroxene, Amp is for amphibole, Mag is for magnetite. Abbreviations have been defined by Whitney and Evans., 2010)..... 83

Figure 26: SEM images of A- The mineralogical assemblage of the K2 sample with an aggregate of mafic minerals; B- Veins of clay minerals going through an olivine grain, associated with apatite and iron oxide with the location of the FIB thin-section; C- The mineralogical assemblage of K1 sample with a rim of orthopyroxene and plagioclase in a feldspars mesostasis; D- Veins of clay minerals inside a fayalite crystal, clay minerals are associated to iron oxide and quartz; E- The mineralogical assemblage in K1 with the propagation of the veins in the plagioclase; F- Zoom on the veins within the plagioclase and localization of the K1 FIB thin-section (Or is for orthoclase, Ab is for albite, Ol is for olivine, Opx is for orthopyroxene, Amp is for amphibole, Mag is for magnetite, Ap is for apatite, Qx is for quartz, Prth is for perthite).
 85

Figure 27: A- High-resolution SEM image of the olivine grain in the K2 sample and the propagation of the veins inside the rim and the mesostasis (see black arrows); B- Phase mapping (hyperspy) of the propagation of the veins; C- Mapping of the Fe/Si ratio signal, the color scale represents the ratio of the intensity of the X-ray signal, i.e., the number of counts. 86

Figure 28: SEM images of the K1 sample, A- A fayalite crystal with its rim of mafic minerals (Opx and Amp) and plagioclase; B- A zoom on one vein inside the fayalite showing intergrowth of clay minerals, quartz, and iron oxide and mafic minerals such as amphibole and orthopyroxene, at the right of the image iron oxide can also be found at the border of the orthopyroxene..... 87

Figure 29: A- TEM image of the K2 FIB thin-section with the area mapped; B- Quantitative map of iron(III) in the K2 FIB thin section, each pixel corresponds to the percentage of iron(III) on total iron (Fa is for fayalite, E.v. is for external vein, C.v. is for central vein); C- Global X-ray absorption spectra for each part of the FIB thin section (blue spectra is for the fayalite, red spectra is for the external vein and green spectra is for the central vein), D- TEM image of the K1 FIB-thin section with the area mapped; E- Quantitative map of iron(III) in the K1 FIB thin-section (Ab is for albite, E.v. is for external vein, C.v. is for central vein); F- Global X-ray absorption spectra for each part of the area mapped (light green spectra is for the center of the vein, red spectra is for the border of the vein in direct contact with the plagioclase and dark green spectra is for the part between the border and the center mineral). 88

Figure 30: A- STEM image of the K2 FIB thin-section showing the multiple veins inside the fayalite. The black square is for the localization of the TEM image in B (Fa is for fayalite, C.v. is for central vein and E.v. is for external vein); B- TEM image of the filling of the vein with multiple zooms on areas of interest; a- TEM high-resolution image of the fayalite and its associated electron diffraction; b- TEM high-resolution image of the clay mineral in contact

with the fayalite, its associated electron diffraction, and location of zooms b1 and b2 on the clay sheets; b1- Zoom on the clay mineral in direct contact with the fayalite; b2- Zoom on the well-crystallized sheets of the clay mineral in contact with the fayalite; c- TEM high-resolution image of the clay mineral with no direct contact with the fayalite and its associated electron diffraction and location of zoom c1; c1- Zoom on the sheets of the central clay mineral; d- TEM image of the contact between the two clay minerals; e- TEM image of the contact between the fayalite and the clay mineral; C- STEM-EDS maps of the Fe/Si ratio, atomic percent of K, and atomic percent of Ca of the clays going through the olivine (scale is in atomic percent); D- (M+; 4Si; 3R2+) ternary diagram representing the endmembers of clay minerals and the studied clay minerals in function of M+, the interlayer cationic charge, 3R2+, the number of divalent cations in octahedral position and 4Si, the amount of silica. It highlights the mixing of the phases between the chlorite, the smectite, and the serpentine endmembers. 91

Figure 31: A- TEM image of K1 FIB thin-section; B- TEM image of the contact between the plagioclase and the vein; b1- the electron diffraction of the plagioclase; b2- The electron diffraction of the mineral filling the vein; C- HRTEM image of the center of the vein; C1- Zoom on the layers of the clay mineral filling the vein; D- HRTEM image of the border of the vein, D1- Zoom on the layers of the clay mineral that are in contact with the plagioclase; E- STEM-EDS maps of the Fe/Si ratio, the K and Ca contents (in atomic percent); F- (M+; 4Si; 3R2+) ternary diagram representing the endmembers of clay minerals and the studied clay minerals in function of M+, the interlayer cationic charge, 3R2+, the number of divalent cations in octahedral position and 4Si, the amount of silica. It highlights the mixing of the phases between the serpentine, the chlorite, and the micas endmembers. 92

Figure 32: Synthesis sketches of the crystallization sequence in the K1 and K2 samples and zooms on veins formation; A- Fayalite, pyroxene, amphibole, and plagioclase in rims around the mafic minerals; B- Circulation of a differentiated residual liquid which give perthites of K-feldspars and leads to the crystallization of the center serpentine and the exsolution of water. Apatite and iron oxides also crystallize at that time. The serpentine is cross cutting every previous mineral. Associated are zoom and sketches of the filling of the vein (1 is for fayalite crystallization and 2 for serpentine crystallization); C- Deuteric alteration of the fayalite by the exsolved water leading to the crystallization of the chlorite and then of the serpentine in direct contact with the fayalite while the temperature is decreasing. These two clay minerals are only found in fayalite. Associated are zoom and sketches of the filling of the vein (1 is for fayalite crystallization, 2 for serpentine crystallization, 3 for chlorite crystallization, and 3' for serpentine of the border vein crystallization). 96

Figure 33: A- BSE-SEM image of the area studied; B- Phases map of the studied area obtained from WDS element maps using the software XMapTools 4.1. (Lanari et al., (2014, 2019). (Ap is for apatite, Serp is for serpentine, Qtz is for quartz, Plg is for plagioclase, Opx is for orthopyroxene, Ol is for olivine, Bt is for biotite, Mgt is for magnetite, K-F is for K-feldspar, Amph is for amphibole)..... 111

Figure 34: A- Compositional map of FeO in olivine (in oxide weight percent); B- Compositional map of FeO in orthopyroxene (in ox.wt.%); C- Compositional map of Fe₂O₃ in serpentine (in ox.wt.%), and D- Compositional map of Fe₂O₃ in amphibole (in ox.wt.%). The phase map is presented in Figure 1..... 113

Figure 35: Sum of gains and losses of elements as a function of the volume change during the three reactions. When minimizing the mass transfer, reaction 1 of orthopyroxene being replaced by amphibole induces a volume change of +20.8%. When minimizing the mass transfer, reaction 2 of olivine being replaced by serpentine induces a volume change of +3.7%. When minimizing the mass transfer, reaction 3 of (olivine + orthopyroxene) being replaced by (amphibole + serpentine) induces a volume change of +11.1%. These volume variations represent the optimal solid volume variation accompanying the density change induced by the mineral replacement considered..... 115

Figure 36: A- Mass transfer diagram for the three possible reactions with the assumptions of minimizing the mass transfer and with no volume variation. These diagrams compare the element composition of the product with its original parent. A and B are for reaction 1, amphibole replaces orthopyroxene. C and D are for reaction 2, serpentine replaces olivine. E and F are for reaction 3, serpentine and amphibole replace olivine and orthopyroxene. Red line indicates the 0% of mass change, and the dashed line the % of mass change. 116

Figure 37: Graphical representation of the amount of H₂ produced (by mol of H₂/ ton of rock) in the function of the different scenarios (in dark blue Opx → Amp by considering the amount of Fe³⁺ gained and in light blue Opx → Amp by considering the amount of Fe²⁺ lost ; in dark purple Ol → Serp (Fe³⁺) and in light purple Ol → Serp (Fe²⁺) ; in dark green Ol + Opx → Amp + Serp (Fe³⁺) and in light green Ol + Opx → Amp + Serp (Fe²⁺) ; in red data is from Geymond et al., 2023, in orange data is from Groveza et al., 2017, in yellow data is from McCollom et al., 2016, and in brown data is from Leong et al., 2023. 125

Figure 38: Simplified geological map of Minnesota with the location and zoom on our study zone with the major geological complexes and the location of the studied wells (gis data are from the Minnesota Geological Survey, see the complete description of the geological map in Jirsa et al., 2011)..... 137

Figure 39: Gas composition in H₂, CH₄, CO₂, and C₂H₆ acquired by gas chromatography for Tamarack wells and DMK wells# 1-2, 2, and 3..... 142

Figure 40: Gas composition in He, H₂, CH₄, CO₂, Ar, O₂, N₂, and C₂+ acquired by gas chromatography for Tamarack wells and DMK wells# 1-2, 2, and 3. 143

Figure 41: Relative abundance of the air-normalized isotope composition of noble gases (⁴He, ²⁰Ne, ³⁶Ar, ⁸⁴Kr, ⁴⁰Ar/³⁶Ar, and ³He/⁴He) for each studied well. Also plotted is the relative abundance isotope composition of noble gas for the air-equilibrated water. Noble gases above the air average composition (black dashed line) are enriched compared to air, while all noble gases below the air average composition are depleted compared to air..... 146

Figure 42: ²⁰Ne/⁴He in the function of R/Ra (³He/⁴He air normalized) for each well with air, crustal, and mantellic endmembers (Additional points in grey and black are from Christel Vacquand’s Ph.D. dissertation (2011), Julia Guélard’s Ph.D. dissertation (2016), and Vacquand et al., 2018)..... 149

Figure 43: Schoell diagram of deuterium isotopic values of methane versus carbon isotopic values of methane for the Tamarack wells, the DMK wells# 1, 1-2, 2, and 3, as well as BC well#1. The dots are for the first set of analyses. The squares are for the second set of analyses (modified from Giunta et al., 2019)..... 152

Figure 44: Bernard diagram of carbon isotopic values of methane versus C1/C2+ ratios for the Tamarack wells, the DMK wells# 1, 1-2, 2, and 3, as well as BC well#1. The dots are for the first set of analyses. The squares are for the second set of analyses. 153

Figure 45: A- Intermediate species forming experimentally during CO₂ and H₂ interactions in water, along the reaction pathways to CH₄ (McCollom and Seewald, 2007); B- Chemical compounds detected within the lost city hydrothermal fluids, listed with decreasing redox potential (from Lang et al., 2020) 155

Figure 46 : Formate and acetate concentrations in brines collected at H₂ and CH₄ producing sites. High concentrations suggest abiotic synthesis. Data from this study, Sherwood-Lollar et al., 2021, Kohl et al., 2016, Eickenbusch et al., 2019 and Lang et al., 2018. 156

Figure 47: Schematic vertical profile of the DR1-A well. The K2, K3, K6, K7, and K11 are schematized (at the micrometric scale) and localized in the profile as they are characteristic of the basement at their respective depths. They clearly display an alteration gradient increasing up to the basement top. Of note, different clay minerals are represented in these schemes as we have identified several generations of them (I. is the late magmatic event, II. is the second and posterior potential event of fluid circulation). In the K11 schema, the unknown part represents the mineral(s) lost during the thin-section realization as the sample is very brittle. We infer that the clay mineral is missing in these parts. The first sedimentary rocks, in direct contact with the basement, are also schematized as they could represent potential seals for the hydrogen generated in the basement. 165

Figure 48: A- Simplified geological map of the gravimetric anomalies of the MRS (modified from Ojakangas et al., 2001 after Dickas and Mudrey., 1997) with the location of B-Geological map of the northern part of the Mid-Rift System with 1) the location of Evans et al., 2016; Tutolo et al., 2019; and 2) Joslin, 2004 studies (modified from Ojakangas et al., 2001 after Hinze et al., 1997). 171

Figure 49: A- Geologic interpretation of the seismic profile COCORP Kansas Line 1 acquired during the eighties (modified from Woelk and Hinze., 1991), B- Geologic interpretation of the seismic profile GLIMPCE line C acquired at the end of the eighties in Minnesota (modified from Stein et al., 2015 after Green et al., 1989). Locations of both seismic lines can be found in the two smaller maps at the bottom right. Of note, both seismic profile are dated from nineties and their geological interpretation must be treated with caution.)..... 172

Figure 50: Simplified regional map of the Precambrian rocks of the Northeastern part of Minnesota with the North Shore Volcanic Group, the Duluth Complex, the Beaver Bay Complex, and the Miscellaneous intrusions of the MRS, intruded into the Paleoproterozoic rocks of the Rove, Virginia and Thomson formations, the BIF of Gunflint and Biwabik, and the Archean granitoid intrusions, and supracrustal rocks (modified from Miller et al., 2002). 173

Figure 51: A- Regional geological map with the location of Tamarack intrusion (from Taranovic et al., 2015, after the Geological Map of Minnesota from Jirsa et al., 2011), B- Geological map of the intrusion (from Taranovic et al., 2015, after an unpublished Rio Tinto Exploration map), C- W-E cross-section of the Dike (from Taranovic et al., 2015). 176

Figure 52: A- Geologic interpretation of the seismic profile COCORP Kansas Line 1 acquired during the eighties (modified from Woelk and Hinze., 1991) in addition, the main characteristics of the H₂ system are represented, B- Geologic interpretation of the seismic profile GLIMPCE line C acquired at the end of the eighties in Minnesota (modified from Stein et al., 2015 after Green et al., 1989) in addition, the main characteristics of the H₂ system are represented. Locations of both seismic lines can be found in the two smaller maps at the bottom right..... 183

Figure 53: Schematic view of a GC-C-IRMS (Tobias et al., 2009)..... 187

Figure 54: Schematic architecture of the noble gases analyzer (modified from Julia Guélard 2026 doctoral dissertation) 188

Table of tables

Table 1: H ₂ -generating reactions occurring in the intracratonic areas (1- Marcaillou., 2011; 2- Lin et al., 2005; Sherwood-Lollar et al., 2007; 3- Horsfield et al., 2022; Mahlstedt., 2018, Mahlstedt et al., 2022; 4- Sugisaki et al., 1983).....	30
Table 2: H ₂ -bearing wells in Kansas (modified after Coveney et al., 1987)	41
Table 3: Wells in Eastern Kansas drilled more than 300m into the Precambrian basement. AL, Allen; BR, Brown; BT, Butler; CS, Chase; DK, Dickinson; EW, Ellsworth; GW, Greenwood; MS, Marshall; NE, Nemaha; RL, Riley; WA, Washington; WO, Woodson (Newell et al., 2007)	43
Table 4: Summary of the detectors used during SEM analysis.	50
Table 5: Synthesis of the imaging techniques used during this thesis. (Abbreviation: OM=optical microscopy, SEM=Scanning Electron Microscopy, TEM=Transmitted Electron Microscopy, STXM-XANES=Scanning Transmitted X-ray Microscopy – X-ray Absorption Near Edges Structures, EPMA=Electron Probe Micro Analyzer, and XCT=X-ray Computed Tomography).....	59
Table 6: Average microprobe analyses of minerals constitutive of the sample studied (in ox.wt.%). Olivine, orthopyroxene, amphibole, serpentine, and biotite density were calculated on the basis of a linear combination of end members assuming an ideal solid solution. FeO* is iron total. Estimation of Fe ₂ O ₃ in amphibole was made following Leake’s work (1997). Fe ₂ O ₃ in serpentine was obtained with STXM-XANES in Combaudon et al., 2023. XFo = XForsterite, XFa = XFayalite, XTep = XTephroide, XEs = XEnstatite, XFs = XFerrosilite, XChry = Xchrysotile, XGreen = XGreenalite, XAn = XAnnite, XPhl = XPhlogopite, XSid = XSiderophyllite, XAb = XAlbite, XAn = XAnorthite, and XOrth = XOrthose.	112
Table 7: H ₂ production calculation for each reaction by considering the Bruker and the Tescan μ CT scans and their associated volume characterization	125
Table 8: Summary of the analyses performed for each sample (X is for samples analyzed twice).	140

Table 9: Physico-chemical parameters of water at the wellhead. 140

Table 10: Gas composition in H₂, CH₄, CO₂, and C₂H₆ analyzed as trace components, C1/C2 ratio. Blank spaces indicate no values were recorded. 141

Table 11: Gas composition in He, H₂, CH₄, CO₂, Ar, O₂, N₂, and C₂+ acquired by gas chromatography with a TCD and FID columns for Tamarack wells and DMK wells# 1-2, 2, 2-2, and 3. 143

Table 12: Relative abundance of noble gases and isotopic ratios (⁴He, calculated ³He, ²⁰Ne, ³⁶Ar, calculated ⁴⁰Ar, ⁸⁴Kr, ¹²⁹Xe, ⁴⁰Ar/³⁶Ar, ³⁸Ar/³⁶Ar, ³He/⁴He, ²⁰Ne/⁴He,) for each well, air normalized values and uncertainties. 145

Table 13: Gas composition and isotopic ratios of δ¹³C of CH₄ per mil versus SMOW and δD of CH₄ per mil versus VPDB, with calculated standard deviation, for the first set of analysis (gas from exetenairs). Blank spaces indicate no values were recorded. 147

Table 14: Gas composition and isotopic ratios of δ¹³C of CH₄ per mil versus SMOW and δD of CH₄ per mil versus VPDB for the second set of analysis (gas from inox tubes). No standard deviation is calculated for these results as only one injection and analysis were done for each sample. Blank spaces indicate no values were recorded. 147

Table 15: Acetate and formate concentrations in sampled fluids. Blank space indicates compounds were below the detection limit. 148

Table of equations

(Equation 1): $30\text{Mg}_{1.8}\text{Fe}_{0.2}\text{SiO}_4 + 41\text{H}_2\text{O} \rightarrow 15\text{Mg}_3\text{SiO}_5(\text{OH})_4 + 9\text{Mg}(\text{OH})_2 + 2\text{Fe}_3\text{O}_4 + 2\text{H}_2$	24
(Equation 2): $15\text{Mg}_{1.8}\text{Fe}_{0.2}\text{Si}_2\text{O}_6 + 19\text{H}_2\text{O} \rightarrow 9\text{Mg}_3\text{SiO}_5(\text{OH})_4 + \text{Fe}_3\text{O}_4 + 12\text{SiO}_2 + 2\text{H}_2$	24
(Equation 3): $\text{Fe}^{2+} + \text{H}_2\text{O} \rightarrow 12 \text{H}_2 + \text{iron oxides}$	31
(Equation 4): $2(\text{Mg},\text{Fe}^{2+})\text{SiO}_4 + 3\text{H}_2\text{O} \rightarrow 2\text{Mg}_2\text{Fe}^{3+}(\text{Fe}^{3+},\text{Si})\text{O}_5(\text{OH})_4 + \text{SiO}_2 + \text{H}_2$	31
(Equation 5): $3 \text{Fe}_2\text{SiO}_4 + 2 \text{H}_2\text{O} \rightarrow 2 \text{Fe}_3\text{O}_4 + 3 \text{SiO}_2 + 2 \text{H}_2$	31
(Equation 6) : $\text{Si} \cdot + \text{H}_2\text{O} \rightarrow \text{Si} - \text{OH} + \text{H} \cdot$ and $2\text{H} \cdot \rightarrow \text{H}_2$	32
(Equation 7): $n\text{CO}_2 + (3n+1)\text{H}_2 = \text{C}_n\text{H}_{2n+2} + 2n\text{H}_2\text{O}$	34
(Equation 8): $\text{CO}_2 + \text{H}_2\text{O} = \text{H}_2\text{CO}_3 = \text{CO}_3^{2-} + 2\text{H}^+$	35
(Equation 9): $I = I_0 \times \exp - \mu d$	57
(Equation 10): $fv \text{ dmineral } 2\text{dmineral } 1\text{cnmineral } 2 - c \text{ nmineral } 1 = xn$	61
(Equation 12): $fv \text{ dmineral } 2\text{dmineral } 1\text{cnmineral } 2 - c \text{ nmineral } 1 = xn$	108
(Equation 13): $d = i = 1nd1 \times x1 + \dots + dn \times xn$	108
(Equation 14): Solid volume variation (%) = $(-1 + fv) \times 100$	109
(Equation 15): $\text{Fe}^{2+} + \text{H}_2\text{O} \rightarrow 12 \text{H}_2 + \text{iron oxides}$	110
(Equation 16, $\Delta V = 20.8\%$): 100g of orthopyroxene + 0.002g Si + 0.43g Ti + 5.92g Al + 3.63g Fe ³⁺ + 8.12g Ca + 1.38g Na + 1.54g K + 1.27g P + 0.25g H = 108.32 g of amphibole + 13.13g Fe ²⁺ + 0.96g Mn + 0.12g Mg	117
(Equation 17, $\Delta V = 0\%$): 100g of orthopyroxene + 0.35g Ti + 4.87g Al + 3.01g Fe ³⁺ + 6.65g Ca + 1.13g Na + 1.26g K + 1.05g P + 0.2g H = 96.27g of amphibole + 3.82g Si + 16.73g Fe ²⁺ + 1.06g Mn + 0.65g Mg	117
(Equation 18, $\Delta V = 3.7\%$): 100g of olivine + 0.01g Ti + 1.11g Al + 6.46g Fe ³⁺ + 0.29g Ca + 0.59g Na + 0.09g K + 0.003g P + 0.79g H = 74.51g of serpentine + 0.001g Si + 32.90g Fe ²⁺ + 1.31g Mn + 0.61g Mg	118
(Equation 19, $\Delta V = 0\%$): 100g of olivine + 0.01g Ti + 1.07g Al + 6.23g Fe ³⁺ + 0.28g Ca + 0.57g Na + 0.08g K + 0.003g P + 0.64g H = 72.88g of serpentine + 0.50g Si + 33.53g Fe ²⁺ + 1.33g Mn + 0.64g Mg	118
(Equation 20, $\Delta V = 11.1\%$): 100g of olivine and orthopyroxene + 0.01g of Si + 0.23g Ti + 2.65g Al + 6.28g Fe ³⁺ + 2.87g Ca + 0.84g Na + 0.51g K + 0.05g P + 0.59g H = 86.90g of serpentine and amphibole + 25.54g Fe ²⁺ + 1.03g Mn + 0.56g Mg	118
(Equation 21, $\Delta V = 0\%$): 100g of olivine and orthopyroxene + 0.21g Ti + 2.37g Al + 5.65g Fe ³⁺ + 2.56g Ca + 0.75g Na + 0.46g K + 0.05g P + 0.53g H = 81.65g of serpentine and amphibole + 1.72g of Si + 27.40g Fe ²⁺ + 1.10g Mn + 0.70g Mg	118
(Equation 22): $\text{RCH}_2\text{CH}_2\text{CH}_3 + 4\text{H}_2\text{O} \rightarrow \text{R} + 2\text{CO}_2 + \text{CH}_4 + 5\text{H}_2$ (Seewald., 2003)	149
(Equation 23): $\text{CO}_2 + 2\text{H}_2\text{O} = \text{CH}_4 + 2\text{O}_2$ i.e., late magmatic despeciation of C-O-H fluids during magma cooling (Etiope and Sherwood-Lollar., 2013)	150

(Equation 24): $\text{CO}_2 + \text{H}_2 \rightarrow \text{HCOOH}$ (formic acid), $\text{HCOOH} + \text{H}_2 - \text{H}_2\text{O} \rightarrow \text{CH}_2\text{O}$ (formaldehyde), $\text{CH}_2\text{O} + \text{H}_2 \rightarrow \text{CH}_3\text{OH}$ (methanol), $\text{CH}_3\text{OH} + \text{H}_2 - \text{H}_2\text{O} \rightarrow \text{CH}_4$ *i.e.*, *uncatalyzed aqueous CO₂ reduction (Seewald et al., 2006)*..... 150

(Equation 25): $\text{CO}_2 + 4\text{H}_2 = \text{CH}_4 + 2\text{H}_2\text{O}$ *i.e.*, *methanation*..... 150

(Equation 26): $\text{CaCO}_3 + 4\text{H}_2 = \text{CH}_4 + \text{Ca}(\text{OH})_2 + \text{H}_2\text{O}$ *i.e.*, *carbonate methanation (Reller et al., 1987)*..... 150

(Equation 27): $1.67\text{Mg}_{1.2}\text{Fe}_{0.8}\text{SiO}_4 + 2.32\text{H}_2\text{O} + 0.8\text{H}^+ + 0.07 \text{Ca}^{2+} + 0.39\text{Si}^{4+} = \text{Mg}_{0.75}\text{Fe}^{3+}_{1.34}\text{Ca}_{0.07}\text{Si}_{2.06}\text{O}_5(\text{OH})_4 + 1.25\text{Mg}^{2+} + 0.72\text{H}_2$ (Evans et al., 2017) 174

